



HAL
open science

Synthesis, crystallographic and magnetic studies of lanthanide-based molecular edifices

Gang Huang

► **To cite this version:**

Gang Huang. Synthesis, crystallographic and magnetic studies of lanthanide-based molecular edifices. Cristallography. INSA de Rennes, 2017. English. NNT : 2017ISAR0008 . tel-01784113

HAL Id: tel-01784113

<https://theses.hal.science/tel-01784113>

Submitted on 3 May 2018

HAL is a multi-disciplinary open access archive for the deposit and dissemination of scientific research documents, whether they are published or not. The documents may come from teaching and research institutions in France or abroad, or from public or private research centers.

L'archive ouverte pluridisciplinaire **HAL**, est destinée au dépôt et à la diffusion de documents scientifiques de niveau recherche, publiés ou non, émanant des établissements d'enseignement et de recherche français ou étrangers, des laboratoires publics ou privés.

Thèse

UNIVERSITE
BRETAGNE
LOIRE

THESE INSA Rennes
sous le sceau de l'Université Bretagne Loire
pour obtenir le titre de
DOCTEUR DE L'INSA RENNES
Spécialité : Chimie

présentée par

Gang HUANG

ECOLE DOCTORALE : *SDLM*

LABORATOIRE : *ISCR/CSM*

**Synthesis,
crystallographic and
magnetic studies of
lanthanide-based
molecular edifices**

Thèse soutenue le 31.03.2017
devant le jury composé de :

Pr. Stéphane Rigaut

Professeur à l'Université de Rennes 1 / Président

Pr. Corine Mathonière

Professeur à l'Université de Bordeaux / Rapporteur

Pr. Smail Triki

Professeur à l'Université de Bretagne Occidentale / Rapporteur

Pr. Laure Catala

Professeur à l'Université Paris-Sud 11 / Examineur

Dr. Kevin Bernot

Maitre de Conférences à l'INSA de Rennes / Co-encadrant de thèse

Pr. Olivier Guillou

Professeur à l'INSA de Rennes / Directeur de thèse

Synthesis, crystallographic and magnetic studies of lanthanide-based molecular edifices

Gang HUANG



En partenariat avec



Acknowledgement

First of all, I would like offer my sincere gratitude to my supervisor Pr. Olivier Guillou who gives me the opportunity to complete my doctor degree. In his direction, our group has a better academic environment and everyone is in harmony. I am very happy to work with in such a group.

It is my honor to work with my co-supervisor Dr. Kevin Bernot, who directs me the work in the past forty two months. He has profound knowledge in chemistry, magnetism and other skills. Thanks for his enlightening instructions and encouraging guidance to let me make progress. During the work, he always renders me the novel ideas to give me a hand. What's more, he has taught me think independently. With his guidance, now I have learned to analyze some problems by myself. I should thank him for his patience in the discussion of my work.

I want to give my sincere thanks to Xiaohui Yi, he has given me many helps no matter in life or in the research work, though we have just worked together for only six months. At the beginning of my life in France, he has introduced me many about this country. Most importantly, he has taught me how to use the research tools that we have used in our work, for example how to use SHELX to solve the crystal structure, it is a really hard job sometimes in our work. Thanks for his kindness and patient to help me use it. In addition, he has also offered me many proposals on the crystal synthesis and magnetic measurement analysis.

I would like to express my gratitude all my colleagues, they are so kind and so nice. I would like to thank François Le Nature, thanks for the period of time that he has passed with me. He always likes to talk with me about the subject of my work, and he has given me many useful ideas to synthesize different types of complexes. I am impressed by his rich reservoir of knowledge in chemistry. I will thank Stéphane Freslon, Florence Le Dret and Guillaume Calvez for their support in the experimental manipulations. They also tell me many interesting histories happened in France. Their efforts to improve my level of French are fully appreciated. I will also thank Isabelle Morlais, thanks for quantities of trivial affairs that she has done for me. When I have any difficulties in life, they have given me the useful ideas to solve the problems. I thank them together again. I will thank Carole Daiguebonne, I clearly remembered that she received me in the train station of Rennes the first day that I arrived in Rennes. And thanks for offering me the help in my work and giving me the chance to take the TP. I enjoy this feeling to work with her and the young students. I will also thank Yan Suffren, Christophe Lescop for their support in the measurements.

I would like to thank Haiyun Yao, Jinzeng Wang, Xiao Fan, Marin Puget, Vincent Roguet, INSA Badiane, Albert Badiane and Christelle Neaime, Hamad Abdallah for their help in my work. In addition, I also enjoyed the time that I worked with Mélissa Laurans, Bérenger Aranda, Camille Tandé, Nicolas Kerbellec, Aurélien Dif and Romain Guerandel.

Of course I cannot forget Aurore Gouin, she always smiles to us and patiently gives us the help as much as possible.

I would like to thank Smail Triki, Laure Catala, Corine Mathoniere and Stéphane Rigaut for accepting to examine and judge my work as reportors.

I want to thank Mr. Thierry Roisnel and Mr. Vincent Dorcet for their aids in the single crystal measurement. I also want to thank Mr. Thierry Guizouarn for his kindness in the help of magnetic measurement. Moreover, when I have the questions about the Squid measurement, he is always patient to answer my questions. Mr. Olivier Cador, Mr. Boris Le Guennic and their doctor students are gratefully acknowledged for the theoretical calculation in this thesis.

I gratefully acknowledge the funding sources that made my Ph.D. work possible. I was funded by the China Scholarship Council fellowship for 42 months. Without their financial support, I would not have been finished my work of thesis.

I must thank all my family for their forever support and encouragement.

Last but not least, I would like to thank for all the friends that I have encountered in these three and a half years. I cherish very much this precious period of time with all of you. With your company, I find my life is colorful.

Abstract

Single-molecule-magnet (SMM) has attracted increasing attention in recent years due to their appealing potential for high-density storage devices. Much effort has been made to improve the magnetic performance through flexible coordination chemistry strategy.

In this thesis, the work is organized in two main parts. The first part is constituted of chapter 2 and chapter 3, primarily focus on the Ln-Radical families aiming at designing zero-dimensional and one-dimensional single-molecule-magnet (SMM). The second part contains chapter 4 and chapter 5, in which the ligands are replaced by diamagnetic ones for the purpose of designing the multifunctional materials.

In the first part, nine TEMPO-R (R represents the substituent) radicals are employed to construct zero-dimensional and one-dimensional complexes. These kinds of compounds were prepared by reactions in the dichloromethane/n-heptane co-solvents between the precursor $[\text{Ln}(\text{hfac})_3(\text{H}_2\text{O})_2]$ and TEMPO radicals. Subsequently their molecular structure as well as magnetic properties have been characterized and described. In chapter 2, four radicals (TEMPO-OCH₃, TEMPO-NH₂, TEMPO-Acetamido and TEMPO-OCH₂CCH) are used to synthesize monometallic or dimetallic complexes, among which three are successful to construct the SMM. For the special case of TEMPO-OCH₃ a rare light lanthanide ions (Ce^{III}, Pr^{III} and Nd^{III}) SMM behavior is reported. The Pr^{III} derivative is the first Pr^{III}-based SMM ever reported. In chapter 3, the target is to design SMM in one dimension by using another five radicals: TEMPO-Methacrylate, TEMPO-OCOPh, TEMPO-Oxo, TEMPO-OH and TEMPO-CN. Among all the chains, $[\text{Pr}(\text{hfac})_3(\text{H}_2\text{O})(\text{TEMPO-OH})]_n$ (**17**), $[\text{Dy}(\text{hfac})_3\text{-TEMPO-OH}]_n$ (**18**) and $[\text{Tb}(\text{hfac})_3(\text{TEMPO-CN})]_n$ (**22**) are identified as chains of SMM. **22** exhibits the slowest magnetic relaxation among all the 4f-2p SMMs obtained in this thesis, with a small opening of magnetic hysteresis. Its analogue of $[\text{Gd}(\text{hfac})_3(\text{TEMPO-CN})]_n$ (**23**) even exhibits one of the largest exchange values in Gd-2p compounds. Last a very rare example of bidimensional 4f-2p network of formula $[(\text{Ce}(\text{hfac})_3)_3(\text{Oxo-TEMPO})_4]_n$ (**15**) is obtained.

In chapter 4, the salt of a photo-switchable carboxylic ligand was reacted with Ln^{III} ions to afford a chain-like arrangement of dinuclear complexes of formula $[\text{Ln}_2(\text{AZO})_6(\text{DMSO})_2(\text{H}_2\text{O})_2] \cdot 4\text{DMSO}$. Photo-sensitivity of the ligand under the irradiation of UV has been tested together with magnetic measurements in solution. In chapter 5, a Metal-Organic-Framework (MOF) (**28**) has been designed and characterized. Ln-Ln ferromagnetic interaction has been observed and diamagnetic doping highlight that, contrary to what observed on $[\text{Ln}_2(\text{AZO})_6(\text{DMSO})_2(\text{H}_2\text{O})_2] \cdot 4\text{DMSO}$, this interaction promote SMM behavior in a so-called MOF-SMM.

Résumé

Les molécules-aimants ou Single-Molécule Magnets (SMM) ont attiré une attention croissante au cours des dernières années en raison de leur potentiel attrayant en tant que dispositifs de stockage magnétique à haute densité. Beaucoup d'efforts ont été faits pour améliorer la performance magnétique de ces molécules à l'aide des techniques de chimie de coordination.

Dans cette thèse, le travail est organisé en deux parties principales. La première partie est constituée des chapitres 2 et 3 qui se concentrent principalement sur les familles Lanthanide-radicaux zéro- et mono-dimensionnelles. La deuxième partie contient les chapitres 4 et 5, où des ligands diamagnétiques sont utilisés afin concevoir des matériaux multifonctionnels.

Dans la première partie, neuf radicaux TEMPO-R (R représente le substituant) sont utilisés. Leur structure cristalline, ainsi que leurs propriétés magnétiques ont été caractérisées. Dans le chapitre 2, quatre radicaux (TEMPO-OCH₃, TEMPO-NH₂, TEMPO-Acetamido et TEMPO-OCH₂CCH) sont utilisés pour synthétiser des complexes zéro-dimensionnels, dont trois présentent des propriétés de SMM. Dans le cas particulier de TEMPO-OCH₃, un très rare comportement de SMM avec lanthanides légers est observé (Ce^{III}, Pr^{III} et Nd^{III}). La première SMM à base de Pr^{III} est ainsi reportée. Dans le chapitre 3, l'objectif est de concevoir des SMM organisés mono-dimensionnellement dans l'empilement cristallin. Cinq autres radicaux sont utilisés: TEMPO-Méthacrylate, TEMPO-OCOPh, TEMPO-oxo, TEMPO-OH et TEMPO-CN. Parmi toutes les chaînes obtenues, [Pr(hfac)₃(H₂O)(TEMPO-OH)]_n (**17**), [Dy(hfac)₃-TEMPO-OH]_n (**18**) et [Tb(hfac)TEMPO-CN]_n (**22**) sont identifiés comme SMM. **22** présente la relaxation magnétique la plus lente parmi tous les SMM 4f-2p obtenues dans cette thèse, avec une d'hystérèse magnétique à basse température. Son analogue à base Gd^{III} (**23**) présente une des plus grandes valeurs d'échange dans les composés de Gd-2p. Enfin un très rare exemple de réseau bidimensionnel 4f-2p de formule [(Ce(hfac)₃)₃(Oxo-TEMPO)₄]_n (**15**) est obtenu.

Dans la deuxième partie, une chaîne de dimère est obtenue par réaction d'un ligand carboxylique photo-commutable avec des sels d'ions Ln^{III}. La photo-sensibilité du ligand sous irradiation UV a été testée et des mesures magnétiques en solution ont été entreprises. En outre, un composé de type Metal-Organic-Framework (MOF) présentant un comportement de SMM de {[Dy₂(o-PDA)₃(H₂O)₂]₂H₂O}_n (**28**) a été conçu et caractérisé. Une interaction ferromagnétique Ln-Ln a été observée dans ce MOF-SMM et le dopage diamagnétique démontre que, contrairement à ce qui est observé sur [Ln₂(AZO)₆(DMSO)₂(H₂O)₂].4DMSO, cette interaction favorise le comportement de SMM.

Résumé étendu

A la suite du premier molécules-aimant à based d'ion de lanthanide rapporté en 2003, ce type de matériaux attire de plus en plus d'attention avec propriétés magnétiques super intéressantes grâce à la forte anisotropie intrinsèque d'ions de lanthanide. Actuellement de nombres exemples sont été réalisés afin de comprendre les comportements magnétiques.

Points de nos travaux

Nous nous penchons sur la recherche de molécules-aimant à base de lanthanides dans cette thèse. Afin de comprendre des phénomènes magnétiques profondément et afin d'améliorer leur performance, ce travail est organisé en deux parties d'après les ligands que nous avons utilisés. Deux types de ligands ont été choisis: radicaux paramagnétiques pour la première partie et acides carboxyliques diamagnétiques pour la deuxième partie.

Pour chacun des composés les points suivants ont été discutés :

- Construction des composés par les radicaux TEMPO-R qui hébergent un groupe R non coordinant et coordinant respectivement.
- Etudier des molécules-aimants à base de lanthanides légers et lourds.
- Estimation de l'échange magnétique entre Gd^{III} et radical.
- Analyse des processus de relaxation magnétique.
- Dilution magnétique pour comprendre l'effet des interactions intra et intermoléculaire sur la relaxation magnétique.

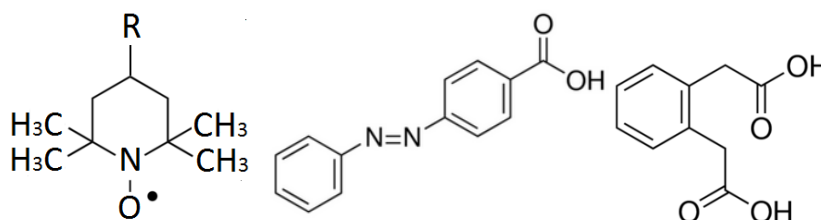


Figure R1. Les ligands utilisés dans le cadre de cette thèse. R représente le substituant.

Edifice en 0D dans la famille de 4f-TEMPO.

La réaction de précurseur de lanthanides et de radicaux non-coordinant donne les composés en 0D quel que soit la stœchiométrie utilisée.

Le radical TEMPO-OCH₃ permet de former un composé en 0D. Les dérivés de Ce^{III}(**1**), Pr^{III}(**2**) et Nd^{III} (**3**) ont présentés des modestes comportements de molécule-aimant. Il est le premier exemple de SMM à base de Pr^{III}.

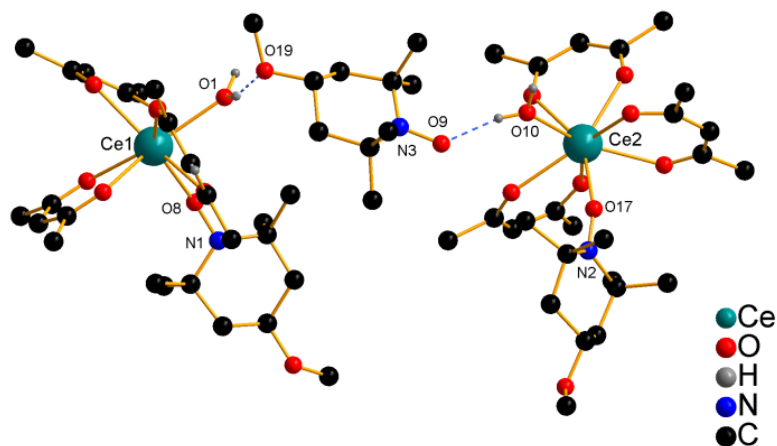


Figure R2. Représentation du composé $\{[(\text{Ce}(\text{hfac})_3)(\text{TEMPO-OMe})(\text{H}_2\text{O})_2]_2 \cdot \text{TEMPO-OMe}\}$ (1).

Pour $\text{R} = \text{NH}_2$, $\{[\text{Dy}(\text{hfac})_3(\text{H}_2\text{O})_2](\text{TEMPO-NH}_2)_2\}$ (6) forme un dimère similaire à $\text{Dy}(\text{Stilbene})$ rapporté par notre équipe, mais avec un comportement de molécule-aimant légèrement dégradé.

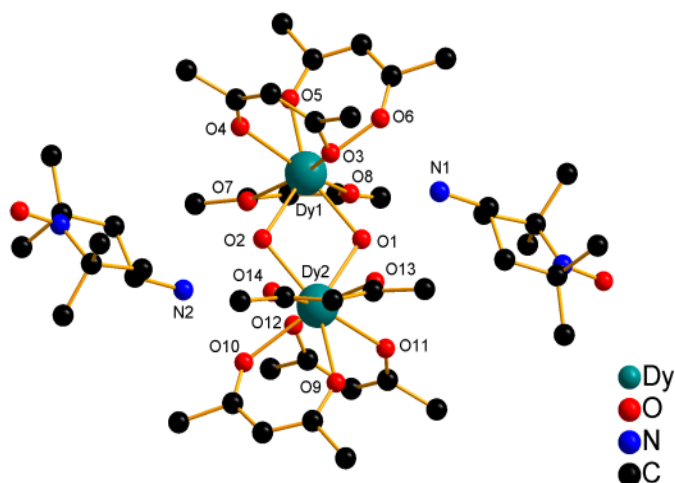


Figure R3. Représentation du composé $\{[\text{Dy}(\text{hfac})_3(\text{H}_2\text{O})_2](\text{TEMPO-NH}_2)_2\}$ (6).

Pour $\text{R} = \text{acétamido}$, deux radicaux de TEMPO-Acétamido sont accrochés à un ion de Dy^{III} via leur groupe $\text{C}=\text{O}$ plutôt que NO , pour former un système de trois spins. Dans ce cas, il n'y a pas d'interaction entre Dy^{III} et radicaux. Cette combinaison ne donne pas de comportement de molécules-aimant.

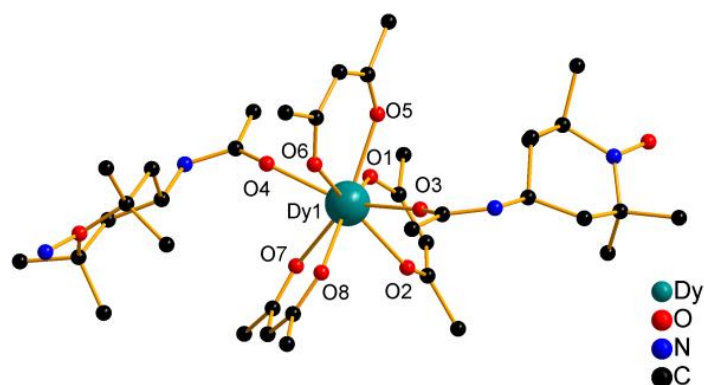


Figure R4. Représentation du composé $[\text{Dy}(\text{hfac})_3(\text{TEMPO-Acétamido})_2]$ (**8**).

Pour $\text{R} = \text{OCH}_2\text{CCH}$, le radical n'est coordonné qu'à un seul ion Dy^{III} pour former $[\text{Dy}(\text{hfac})_3(\text{TEMPO-OCH}_2\text{CCH})(\text{H}_2\text{O})]$ (**9**). Pour le dérivé de Gd^{III} (**11**) une forte interaction d'échange gadolinium-radical est identifiée. Mais cette interaction AF ne mène qu'à un modest comportement de SMM sur **9**. Le dérivé de Tb^{III} (**10**) démontre un comportement de molécule-aimant meilleur que (**9**).

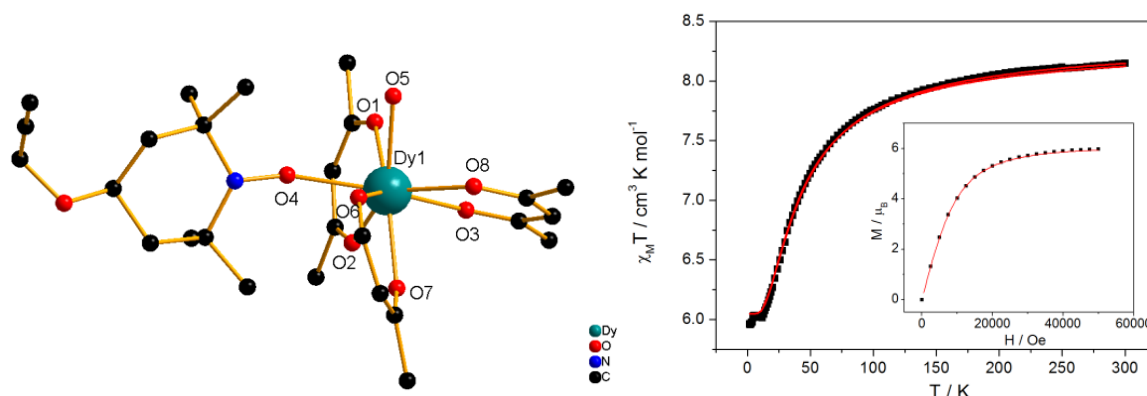


Figure R5. Représentation du composé $[\text{Dy}(\text{hfac})_3(\text{TEMPO-OCH}_2\text{CCH})(\text{H}_2\text{O})]$ (**9**) (gauche) et susceptibilité magnétique de $[\text{Gd}(\text{hfac})_3(\text{TEMPO-OCH}_2\text{CCH})(\text{H}_2\text{O})]$ (**11**) obtenues expérimentalement (points noirs), simulée avec le modèle de 'spin Hamiltonian' $H = -J S_{\text{Rad}} S_{\text{Gd}}$ pour une valeur de J de -9.98 K (-6.84 cm^{-1}) (ligne rouge) (droite).

Chaîne en 1D dans la famille de 4f-TEMPO.

L'association de radicaux TEMPO-R ($\text{R} = \text{Méthacrylate}, \text{OCOPh}, \text{oxo}, \text{OH}$ et CN) donne des chaînes dans les trois premiers cas. Mais tous les trois chaînes ne montrent aucun caractère de SMM. Cependant, dans le cas de la réaction de TEMPO-Oxo avec Ce^{III} un réseau 2D est obtenu qui malheureusement, ne montre pas de comportement de molécules-aimant.

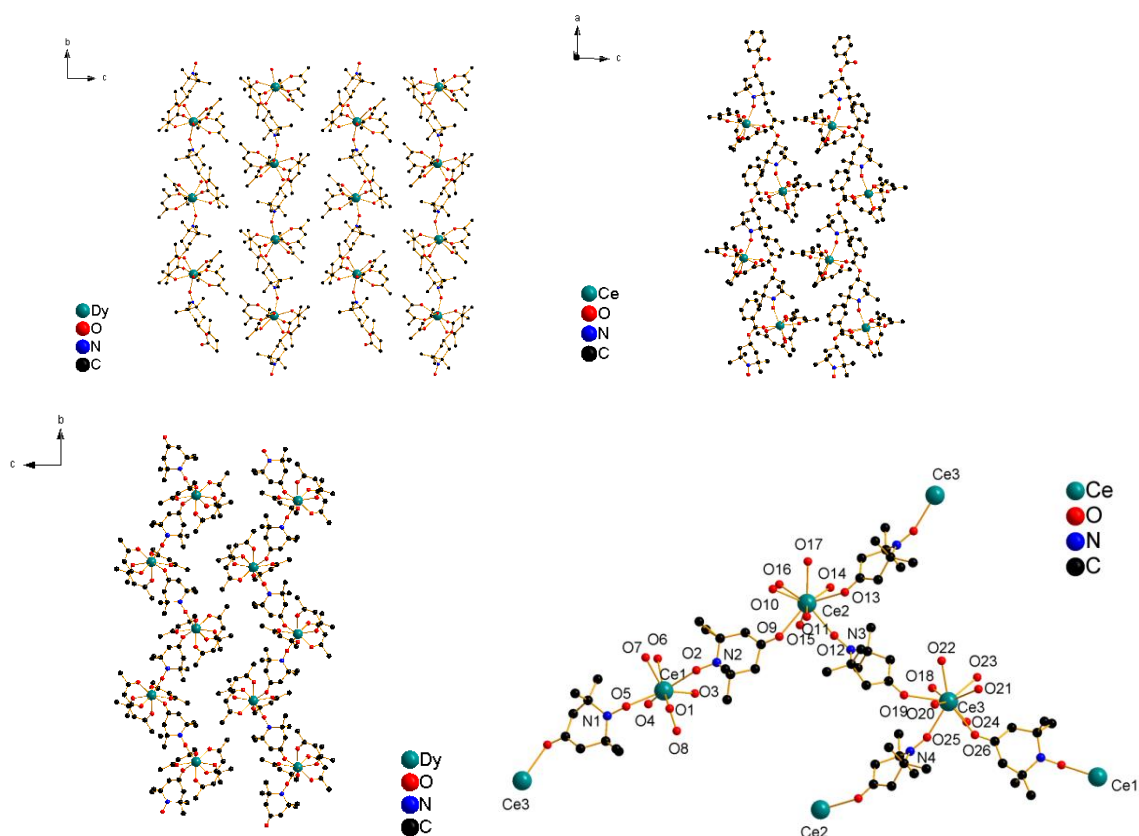


Figure R6. Représentation du composé $[\text{Dy}(\text{hfac})_3(\text{TEMPO-methacrylate})]_n$ (**12**) (haut gauche), $[\text{Ce}(\text{hfac})_3(\text{TEMPO-OCOPh})]_n$ (**13**) (haut droite), $[\text{Dy}(\text{hfac})_3(\text{Oxo-TEMPO})]_n$ (**14**) (bas gauche) et $\text{Ce}(\text{hfac})_3(\text{Oxo-TEMPO})_4$ (**15**) (bas droite).

Le radical TEMPO-OH permet de construire deux type de chaînes $[\text{Pr}(\text{hfac})_3(\text{TEMPO-OH})(\text{H}_2\text{O})]_n$ (**17**) et $[\text{Dy}(\text{hfac})_3(\text{TEMPO-OH})]_n$ (**18**). Par rapport à **18**, les ions de Pr^{III} sur **17** sont en coordination 9. **17** est le deuxième exemple de molécule-aimant à base de Pr^{III} . Comme le composé **2**, il montre le modest comportement de SMM. Du point de vue magnétique, **18** peut être considéré comme un SMM isolé car le ligand n'a qu'un groupe de mono-NO. Cela permet de quantifier l'interaction magnétique sur son dérivé de Gd(**19**) comme ce que nous avons fait sur **11**.

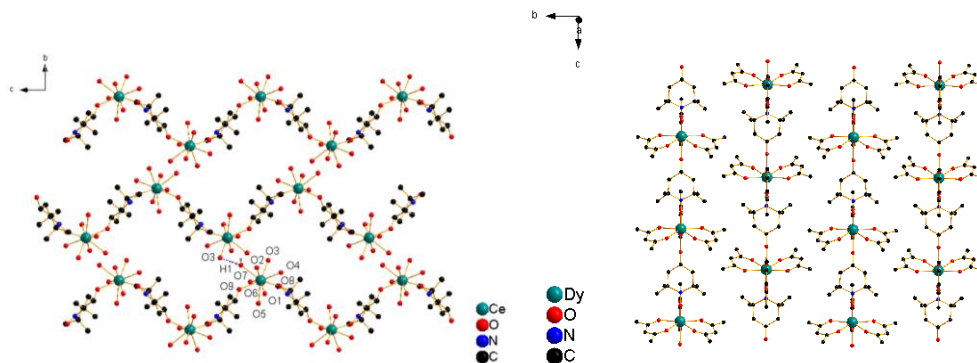


Figure R7. Représentation du composé $[\text{Ce}(\text{hfac})_3(\text{TEMPO-OH})(\text{H}_2\text{O})]_n$ (**16**) (gauche) et $[\text{Dy}(\text{hfac})_3(\text{TEMPO-OH})]_n$ (**18**) (droite).

Le radical TEMPO-CN est très versatile et permet d'obtenir plusieurs edifices moléculaires différents. Combiné avec Ce^{III} , un système de tri-spin $[\text{Ce}(\text{hfac})_3(\text{Tempo-CN})_2]$ (**20**) est été obtenu. Différent de **8**, **20** is coordonné par les groupes NO qui va donner l'interaction intramoléculaire. Ce composé est été identifié comme un SMM.

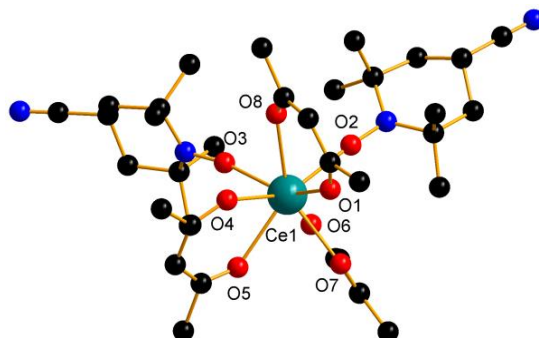


Figure R8. Représentation du composé $\text{Ce}(\text{hfac})_3(\text{TEMPO-CN})_2$ (**20**).

Pourtant la combinaison avec Dy^{III} donne deux type de structures donc la première est très compliqué qui est constituée de deux précurseurs $\text{Dy}(\text{hfac})_3(\text{H}_2\text{O})_2$ et une molécule avec deux radicaux coordonné. Les molécules se contactent par la liaison d'hydrogène pour former un système de penta-spin. $\{[\text{Dy}(\text{hfac})_3(\text{TEMPO-CN})_2][\text{Dy}(\text{hfac})_3(\text{H}_2\text{O})_2]_2\}$ (**21**) montre un comportement de SMM contenant deux série de pics de hors phase de la susceptibilité magnétique.

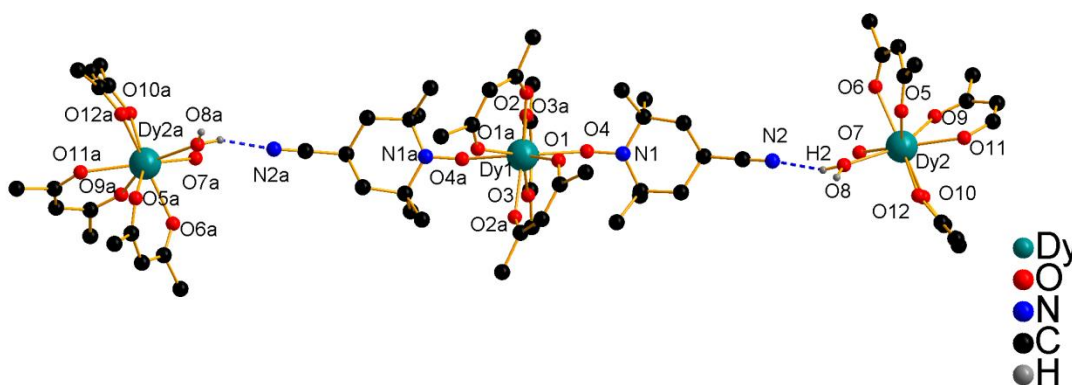


Figure R9. Représentation du composé $\{[\text{Dy}(\text{hfac})_3(\text{TEMPO-CN})_2][\text{Dy}(\text{hfac})_3(\text{H}_2\text{O})_2]_2\}$ (**21**).

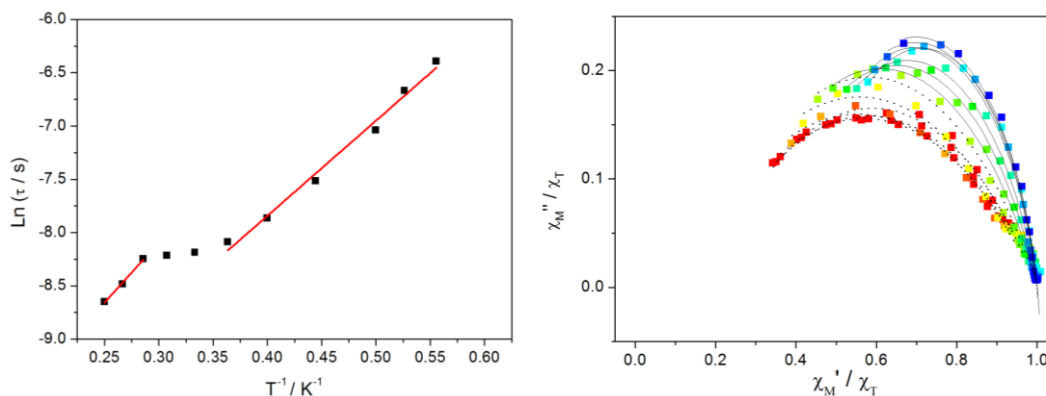


Figure R10. Graphique de temps de relaxation en fonction de T^{-1} (gauch) et Graphique de Cole-Cole (droite) de (21)..

La deuxième structure is une chaîne 1D de formule $[\text{Tb}(\text{hfac})_3(\text{TEMPO-CN})]_n$ (22) et $[\text{Gd}(\text{hfac})_3(\text{TEMPO-CN})]_n$ (23). Le composé 23 a montré le plus fort couplage ($J = -22.4 \text{ K}$ or 15.3 cm^{-1}) mesuré dans cette thèse. En même temps, c'est plus grand que la plupart de composés de Gd-NIT (Nitronyl nitroxide radical). Ce fort couplage fait montrer d'excellentes propriétés magnétiques sur 22. Une grande barrière énergétique est observée (65.8 K), parmi les plus fortes valeurs reportées pour les systèmes 4f-radicaux.

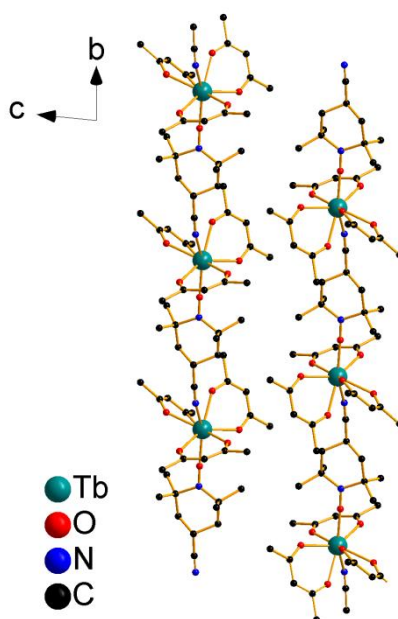


Figure R11. Représentation du composé $[\text{Tb}(\text{hfac})_3(\text{TEMPO-CN})]_n$ (22).

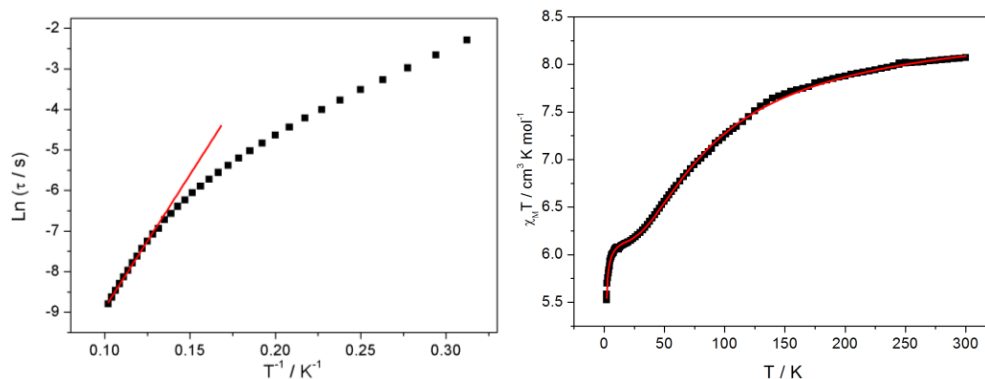


Figure R12. Graphique de $\ln(\tau)$ en fonction de T^{-1} à 2000 Oe de $[\text{Tb}(\text{hfac})_3(\text{TEMPO-CN})]_n$ (**22**) (gauche) et graphique de susceptibilité magnétique de $[\text{Gd}(\text{hfac})_3(\text{TEMPO-CN})]_n$ (**23**) obtenues expérimentalement (points noirs), simulée avec le modèle de ‘spin Hamiltonian’ $H = -J S_{\text{Rad}} S_{\text{Gd}}$ pour une valeur de J de -22.4 K (ligne rouge) (droite).

Pseudo chaîne en1D à base de ligand HAZO

Le ligand HAZO est un ligand carboxylique photo-commutable. Il forme des ions Ln^{III} pour donner une chaîne de dimères par réaction avec des sels de Ln^{III} . Grâce à la technique de dilution magnétique, nous comprenons que l’interaction $\text{Dy}^{\text{III}}\text{-Dy}^{\text{III}}$ a accéléré la relaxation parce que l’hystérèse est éte ouverte sur l’échantillon dopé, mais elle est fermée sur celui pur. La photosensibilité du ligand sous irradiation UV a été testée et des mesures magnétiques en solution ont été entreprises.

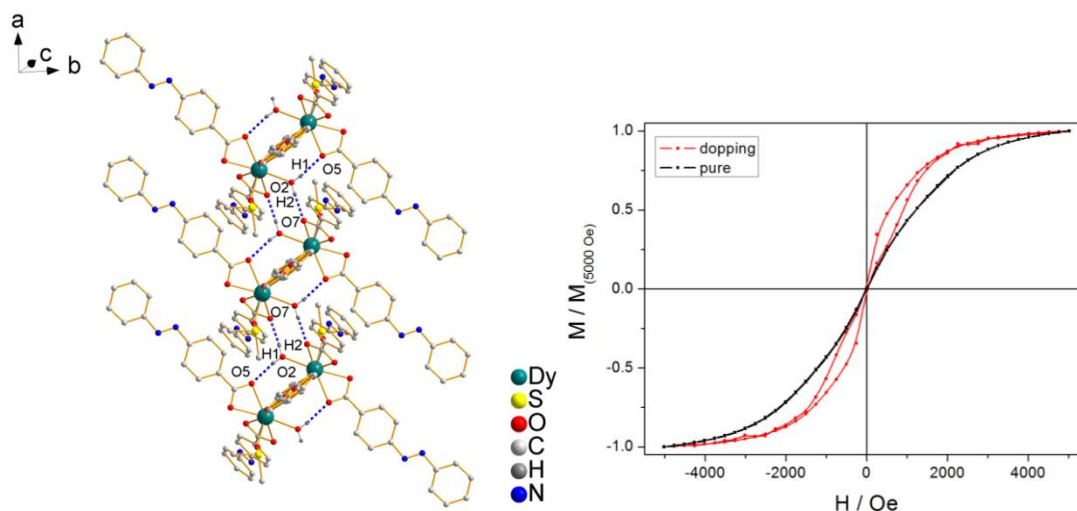


Figure R13. Représentation du composé $[\text{Ln}_2(\text{AZO})_6(\text{DMSO})_2(\text{H}_2\text{O})_2] \cdot 4\text{DMSO}$ (**24**) (gauch). Hystérèse mesuré à 0.5 K selon une variation de champ de 15.5 Oe/s.

$\text{H}_2\text{-o-PDA}$ a deux groupements carboxyliques qui peuvent être coordonnés avec des cations métallique afin de fabriquer des structures étendu. Un MOF-SMM $\{[\text{Dy}(\text{o-PDA})_3(\text{H}_2\text{O})_2]_2\text{H}_2\text{O}\}_n$ (**28**) a été conçu et caractérisé. Une interaction ferromagnétique Ln-Ln a été observée et le dopage diamagnétique démontre que, contrairement à ce qui est observé

sur $[\text{Ln}_2(\text{AZO})_6(\text{DMSO})_2(\text{H}_2\text{O})_2] \cdot 4\text{DMSO}$, cette interaction favorise le comportement de SMM.

En outre, le dérivé de Nd^{III} démontre une relaxation lente aussi.

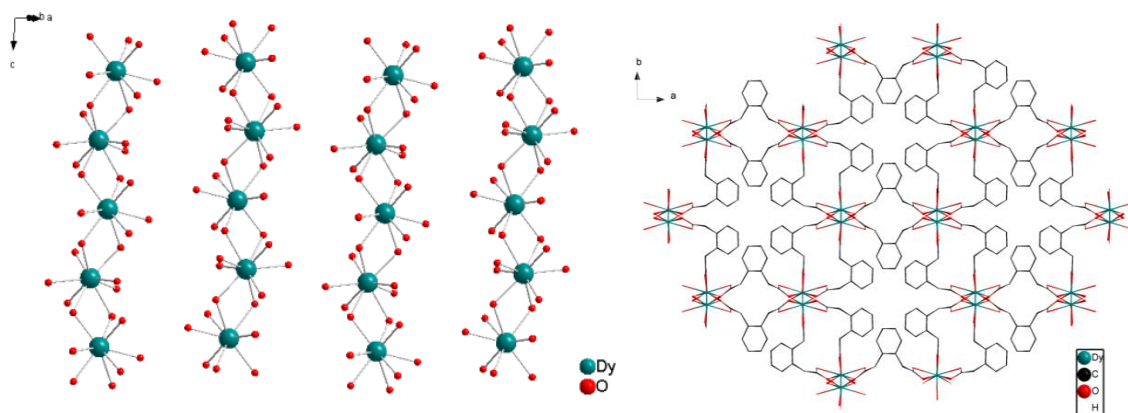


Figure R14. Représentation du composé $\{[\text{Dy}(\text{o-PDA})_3(\text{H}_2\text{O})_2] \cdot 2\text{H}_2\text{O}\}_n$ (**28**).

Dans ce travail, nous avons présenté plusieurs composés à base d'ions de lanthanide. Certains composés ont démontrés un comportement magnétique intéressant, cela nous permet de mieux comprendre les phénomènes existant dans les molécules-aimant. Au stade suivant, les résultats peut être utilisé comme une base pour enfin améliorer le comportement de molécule-aimant.

List of reported compounds

- $\{[\text{Ln}(\text{hfac})_3(\text{TEMPO-OCH}_3)(\text{H}_2\text{O})]_2 \cdot \text{TEMPO-OCH}_3\}$ (Ln=Ce**(1)**, Pr**(2)**, Nd**(3)**, Gd**(4)**, Dy**(5)**)
- $[\text{Ln}(\text{hfac})_3(\text{H}_2\text{O})]_2(\text{TEMPO-NH}_2)_2$ (Ln = Dy**(6)**, Gd**(7)**)
- $[\text{Ln}(\text{hfac})_3(\text{TEMPO-Acetamido})_2]$ (Ln= Dy**(8)**)
- $[\text{Ln}(\text{hfac})_3(\text{TEMPO-OCH}_2\text{CCH})(\text{H}_2\text{O})]$ (Ln = Dy**(9)**, Tb**(10)**, Gd**(11)**)
- $[\text{Ln}(\text{hfac})_3(\text{TEMPO-methacrylate})]_n$ (Ln = Dy**(12)**)
- $[\text{Ln}(\text{hfac})_3(\text{TEMPO-OCOPh})]_n$ (Ln = Ce**(13)**)
- $[\text{Ln}(\text{hfac})_3(\text{Oxo-TEMPO})]_n$ (Ln = Dy**(14)**)
- $[\text{Ln}(\text{hfac})_3(\text{Oxo-TEMPO})_4]_n$ (Ln = Ce**(15)**)
- $[\text{Ln}(\text{hfac})_3(\text{TEMPO-OH})(\text{H}_2\text{O})]_n$ (Ln = Ce**(16)**, Pr**(17)**)
- $[\text{Ln}(\text{hfac})_3(\text{TEMPO-OH})]_n$ (Ln = Dy**(18)**, Gd**(19)**)
- $[\text{Ln}(\text{hfac})_3(\text{TEMPO-CN})_2]$ (Ln = Ce **(20)**)
- $\{[\text{Ln}(\text{hfac})_3(\text{TEMPO-CN})_2][\text{Ln}(\text{hfac})_3(\text{H}_2\text{O})_2]_2\}$ (Ln = Dy**(21)**)
- $[\text{Ln}(\text{hfac})_3(\text{TEMPO-CN})]_n$ (Ln = Tb**(22)**, Gd**(23)**)
- $[\text{Ln}_2(\text{AZO})_6(\text{DMSO})_2(\text{H}_2\text{O})_2] \cdot 4\text{DMSO}$ (Ln = Dy**(24)**)
- $\{[\text{Ln}(\text{o-PDA})_3(\text{H}_2\text{O})_2] \cdot 2\text{H}_2\text{O}\}_n$ (Ln= Ce**(25)**, Nd**(26)**, Gd**(27)**, Dy**(28)**)

Table of content

Introduction.....	21
1 Basics of Lanthanide elements and Single-Molecule-Magnets.....	23
1.1 Introduction to Lanthanide trivalent ions-electronic configurations	23
1.2 Introduction to molecular magnetism of Ln^{III} ions	25
1.2.1 Magnetism of free lanthanide ions.....	25
1.2.2 Single-Molecule Magnets (SMMs) and related behavior	26
1.3 Rules to design lanthanide-based Single-Molecule-Magnets.....	29
1.3.1 Maximize the anisotropy of lanthanide ions-oblate/prolate model.....	29
1.3.2 Tune the electrostatic charge distribution	31
1.3.3 Avoiding Quantum Tunneling of the magnetization	33
1.3.3.1 Introduction to Quantum Tunneling (QT).....	33
1.3.3.2 Strategies to avoid (QT)	33
1.3.4 Avoiding three dimensional (3D) ordering.....	34
1.3.5 Improving the blocking temperature.....	35
1.4 Selected examples of lanthanide-based Single-Molecule-Magnets	36
1.4.1 Selected examples of heavy lanthanides-based SMMs (diamagnetic ligands)....	36
1.4.2 Selected examples of lanthanides-Radicals (4f-2p) based SMMs (paramagnetic ligands).....	39
1.4.3 Selected examples of light lanthanides-based SMMs (diamagnetic ligands).....	44
1.5 Objectives of current thesis	48
References.....	49
2 (TEMPO-R)-4f based zero dimensional complexes: synthesis and magnetic properties.....	53
2.1 Introduction.....	53

2.2 SMM behavior on light lanthanides derivatives in: $\{[(Ln(hfac)_3)(TEMPO-OMe)(H_2O)]_2 \cdot TEMPO-OMe\}$ (Ln=Ce(1), Pr(2), Nd(3), Gd(4), Dy(5))	54
2.2.1 Structural description	54
2.2.2 Static magnetic properties	56
2.2.3 Dynamic magnetic properties	60
2.2.4 Determination of energy barrier and other dynamic parameters	63
2.2.5 Conclusion	64
2.3 μ_2-H₂O bridged dimer: $\{[Dy(hfac)_3(H_2O)]_2(TEMPO-NH_2)_2\}$ (6)	64
2.3.1 Structural description	64
2.3.2 Static magnetic properties	66
2.3.3 Dynamic magnetic properties	68
2.3.4 Conclusion	70
2.4 $[Ln(hfac)_3(TEMPO-acetamido)]_2$ (Ln = Dy(8))	70
2.4.1 Structural description	70
2.5 A family of monometallic compounds $[Ln(hfac)_3(TEMPO-OCH_2CCH)(H_2O)]$ (Ln =Dy(9), Tb(10) and Gd(11))	71
2.5.1 Structural description	71
2.5.2 Static magnetic properties	73
2.5.3 Dynamic magnetic properties	76
2.5.4 Determination of energy barrier and other dynamic parameters	78
2.5.5 Conclusion	78
2.6 Conclusion	79
References	80
3 (TEMPO-R)-4f based multi-dimensional complexes: synthesis and magnetic properties	83
3.1 Introduction	83

3.2 [Ln(hfac)₃(TEMPO-methacrylate)]_n (Dy(12))	84
3.2.1 Structural description	84
3.3 [Ln(hfac)₃(TEMPO-OCOPh)]_n (Ln = Ce(13)).....	85
3.3.1 Structural description	85
3.4 Structural diversity in combination with Oxo-TEMPO radical	87
3.4.1.1D zig-zag chain [Ln(hfac) ₃ (Oxo-TEMPO)] _n (Ln = Dy(14))	87
3.4.1.1 Structural description	87
3.4.2 Two-dimensional 4f-2p network: [(Ce(hfac) ₃) ₃ (Oxo-TEMPO) ₄] _n (15)	88
3.4.2.1 Structural description	88
3.5 Structural diversity in combination with TEMPO-OH radical	91
3.5.1 [Ln(hfac) ₃ (TEMPO-OH)(H ₂ O)] _n (Ln = Ce(16), Pr(17))	91
3.5.1.1 Structural description	91
3.5.1.2 Static magnetic properties	92
3.5.1.3 Dynamic magnetic properties	93
3.5.1.4 Comparison of SMM behaviors of compounds based on Pr ^{III}	94
3.5.2 [Ln(hfac) ₃ (TEMPO-OH)] _n (Ln = Dy(18) and Gd(19))	95
3.5.2.1 Structural description	95
3.5.2.2 Static magnetic properties	97
3.5.2.3 Dynamic magnetic properties	99
3.5.3 Conclusion	100
3.6 Structural diversity in combination with TEMPO-CN radical	101
3.6.1 Tri-spin monometallic SMM based on light lanthanide: [Ce(hfac) ₃ (TEMPO-CN) ₂] (20).....	101
3.6.1.1 Structural description	101
3.6.1.2 Static magnetic properties	102

3.6.1.3 Dynamic magnetic properties	103
3.6.2 Trinuclear compound: {[Dy(hfac) ₃ (TEMPO-CN) ₂]·[Dy(hfac) ₃ (H ₂ O) ₂] ₂ } (21)	104
3.6.2.1 Structural description	104
3.6.2.2 Static magnetic properties	106
3.6.2.3 Dynamic magnetic properties	106
3.6.3 One dimensional 4f-2p chain, strong interaction and large energy barrier in: [Ln(hfac) ₃ (TEMPO-CN)] _n (Ln =Tb(22) and Gd(23)).....	108
3.6.3.1 Structural description	108
3.6.3.2 Static magnetic properties	109
3.6.3.3 Dynamic magnetic properties	112
3.6.3.4 Comparison of Gd ^{III} -Radical exchange interaction between 11 , 19 and 23	114
3.6.4 Conclusion	115
3.7 Conclusion	115
References.....	116
4 Single-Molecule-Magnets based on photo-active ligand:	
[Ln₂(AZO)₆(DMSO)₂(H₂O)₂]·4DMSO.....	119
4.1 Introduction.....	119
4.2 [Dy₂(AZO)₆(DMSO)₂(H₂O)₂]·4DMSO (24)	119
4.2.1 Structural description	119
4.2.2 Static magnetic properties	122
4.2.3 Dynamic magnetic properties	122
4.3 Influence of magnetic dilution	125
4.4 Influence of isomerization on SMM behavior.....	129
4.5 Conclusion	131
References.....	132

5 Slow relaxation and magnetic ordering in a three dimensional metal organic framework	133
5.1 Introduction.....	133
5.2 Structural description	133
5.3 Static magnetic properties	135
5.3.1 {[Nd(o-PDA) ₃ (H ₂ O) ₂]·2H ₂ O} _n (26)	135
5.3.2 {[Gd ₂ (o-PDA) ₃ (H ₂ O) ₂]·2H ₂ O} _n (27)	136
5.3.3 {[Dy(o-PDA) ₃ (H ₂ O) ₂]·2H ₂ O} _n (28).....	136
5.4 Theoretical calculation	138
5.5 Dynamic magnetic properties.....	138
5.5.1 {[Nd(o-PDA) ₃ (H ₂ O) ₂]·2H ₂ O} _n (26).....	138
5.5.2 {[Dy(o-PDA) ₃ (H ₂ O) ₂]·2H ₂ O} _n (28).....	139
5.5.3 {[Dy _{0.08} Y _{0.92} (o-PDA) ₃ (H ₂ O) ₂]·2H ₂ O} _n (28@Y)	141
5.6 Characterization of magnetic hysteresis.....	145
5.7 Conclusion	146
References.....	147
General conclusion.....	151
Appendix A1. Synthesis Information.....	153
Reference	162
Appendix A2. Supplementary information for Chapter 2	163
Appendix A3. Supplementary information for Chapter 3	175
Appendix A4. Supplementary information for Chapter 4	187
Appendix A5. Supplementary information for Chapter 5	197
Appendix A6. Experimental set-up.....	207

Appendix A7. Additional structural information.....	211
List of publications	247

Introduction

Single-molecule-magnets (SMM) studies is an intense field of research in the recent decade because these molecules have exhibited appealing potential in spintronic, quantum computing and data storage. With the help of coordination chemistry, this field develops quite fast. Owing to the flexible design of small edifices, the SMM library can be continuously enriched. Contrary to most transition metal ions, lanthanide ions have large magnetic anisotropy and strong spin-orbit coupling, which are very suitable to build the SMM.

The ligands used to design lanthanide-based SMM can be phthalocyanine,^{1,2} β -Diketonate,³⁻⁵ carboxylic acids,⁶⁻⁸ Schiff base,^{9,10} radicals¹¹⁻¹³ and other ligands.^{14,15} Except for Polycarboxylic acids ligands, other ligands favor the construction of mono or dinuclear compounds that can show SMM behavior.

Several approaches are used in this work to synthesize Ln-based SMMs:

- using radicals ligands (TEMPO) to maximize exchange interaction (chapter 2 and 3)
- using photoisomerizable ligand to afford multifunctionality to the SMMs (chapter 4)
- using carboxylate –based ligand to provide 3D edifices of SMMs

In chapter 2, the 0D Ln-radical building blocks are our target to seek for the possible SMM behavior and simultaneously research the magnetic interaction. We used four TEMPO-R radicals with non-coordinating R group to start our trip. A wide variety of compound has been obtained and we focus our study on the possible magnetic slow magnetic relaxation and the Ln-Ln, Ln-radical or radical-radical interaction on the Gd^{III} derivatives. Unexpectedly SMM behavior has been identified on light lanthanide derivatives.

In chapter 3, we focus on our attention on the TEMPO-R radicals with R coordinating groups. We selected five radicals to satisfy our needs. A wide variety of chain and even two dimensional structure have been obtained. Striking SMM behavior is observed on Tb-based chains;

In chapter 4, a photo sensitive ligand HAZO is employed to build a chain-like compound. This compound shows significant SMM behavior that is further enhanced by magnetic dilution. Magnetic studies in solutions are also presented.

In chapter 5, efforts have been made to design a multidimensional edifice by using carboxylic acid H₂-o-PDA. A Metal-Organic Framework (MOF) material is obtained and show significant magnetic properties with both SMM behavior and 3D ordering on the Dy^{III} derivative.

1. N. Ishikawa, *Polyhedron*, 2007, 26, 2147-2153.
2. N. Ishikawa, M. Sugita, T. Ishikawa, S.-y. Koshihara and Y. Kaizu, *Journal of the American Chemical Society*, 2003, 125, 8694-8695.
3. X. Yi, K. Bernot, O. Cadoret, J. Luzon, G. Calvez, C. Daugebonne and O. Guillou, *Dalton Transactions*, 2013, 42, 6728-6731.
4. X. Yi, K. Bernot, F. Pointillart, G. Poneti, G. Calvez, C. Daugebonne, O. Guillou and R. Sessoli, *Chemistry – A European Journal*, 2012, 18, 11379-11387.
5. P. Chen, H. Li, W. Sun, J. Tang, L. Zhang and P. Yan, *CrystEngComm*, 2015, 17, 7227-7232.

6. P. C. Andrews, W. J. Gee, P. C. Junk and J. G. MacLellan, *Dalton Transactions*, 2011, 40, 12169-12179.
7. Y. Gao, G.-F. Xu, L. Zhao, J. Tang and Z. Liu, *Inorganic Chemistry*, 2009, 48, 11495-11497.
8. C.-M. Liu, D.-Q. Zhang, X. Hao and D.-B. Zhu, *Crystal Growth & Design*, 2012, 12, 2948-2954.
9. L. Zou, L. Zhao, P. Chen, Y.-N. Guo, Y. Guo, Y.-H. Li and J. Tang, *Dalton Transactions*, 2012, 41, 2966-2971.
10. J. Tang, I. Hewitt, N. T. Madhu, G. Chastanet, W. Wernsdorfer, C. E. Anson, C. Benelli, R. Sessoli and A. K. Powell, *Angewandte Chemie International Edition*, 2006, 45, 1729-1733.
11. K. Bernot, L. Bogani, R. Sessoli and D. Gatteschi, *Inorganica Chimica Acta*, 2007, 360, 3807-3812.
12. X. Wang, X. Bao, P. Xu and L. Li, *European Journal of Inorganic Chemistry*, 2011, 2011, 3586-3591.
13. Y.-L. Wang, N. Zhou, Y. Ma, Z.-X. Qin, Q.-L. Wang, L.-C. Li, P. Cheng and D.-Z. Liao, *CrystEngComm*, 2012, 14, 235-239.
14. X. Yi, K. Bernot, V. Le Corre, G. Calvez, F. Pointillart, O. Cador, B. Le Guennic, J. Jung, O. Maury, V. Placide, Y. Guyot, T. Roisnel, C. Daiguebonne and O. Guillou, *Chemistry – A European Journal*, 2014, 20, 1569-1576.
15. S. Hino, M. Maeda, K. Yamashita, Y. Kataoka, M. Nakano, T. Yamamura, H. Nojiri, M. Kofu, O. Yamamuro and T. Kajiwara, *Dalton Transactions*, 2013, 42, 2683-2686.

1 Basics of Lanthanide elements and Single-Molecule-Magnets

In the element periodic table, elements from the lanthanide series plus Sc and Y are collectively called “rare earth elements”. In fact, they are not really rare, on the contrary, most of them are fairly common. For example, cerium is the 25th most abundant element in the earth’s crust and is as abundant as copper. The discovery of rare earth elements started in the year 1751, and because of their remarkable luminescent, magnetic and electronic properties they have attracted great attention in the scientific community.

Periodic Table of the Elements

1 H Hydrogen 1.008																	2 He Helium 4.003
3 Li Lithium 6.941	4 Be Beryllium 9.012											5 B Boron 10.811	6 C Carbon 12.011	7 N Nitrogen 14.007	8 O Oxygen 15.999	9 F Fluorine 18.998	10 Ne Neon 20.180
11 Na Sodium 22.990	12 Mg Magnesium 24.305											13 Al Aluminum 26.982	14 Si Silicon 28.086	15 P Phosphorus 30.974	16 S Sulfur 32.066	17 Cl Chlorine 35.453	18 Ar Argon 39.948
19 K Potassium 39.098	20 Ca Calcium 40.078	21 Sc Scandium 44.956	22 Ti Titanium 47.867	23 V Vanadium 50.942	24 Cr Chromium 51.996	25 Mn Manganese 54.938	26 Fe Iron 55.845	27 Co Cobalt 58.933	28 Ni Nickel 58.693	29 Cu Copper 63.546	30 Zn Zinc 65.38	31 Ga Gallium 69.723	32 Ge Germanium 72.631	33 As Arsenic 74.922	34 Se Selenium 78.971	35 Br Bromine 79.904	36 Kr Krypton 84.738
37 Rb Rubidium 84.468	38 Sr Strontium 87.62	39 Y Yttrium 88.906	40 Zr Zirconium 91.224	41 Nb Niobium 92.906	42 Mo Molybdenum 95.95	43 Tc Technetium 98.907	44 Ru Ruthenium 101.07	45 Rh Rhodium 102.905	46 Pd Palladium 106.42	47 Ag Silver 107.868	48 Cd Cadmium 112.414	49 In Indium 114.818	50 Sn Tin 118.710	51 Sb Antimony 121.760	52 Te Tellurium 127.6	53 I Iodine 126.904	54 Xe Xenon 131.294
55 Cs Cesium 132.905	56 Ba Barium 137.328	57-71 Lanthanides	72 Hf Hafnium 178.49	73 Ta Tantalum 180.948	74 W Tungsten 183.84	75 Re Rhenium 186.207	76 Os Osmium 190.23	77 Ir Iridium 192.222	78 Pt Platinum 195.085	79 Au Gold 196.967	80 Hg Mercury 200.592	81 Tl Thallium 204.383	82 Pb Lead 207.2	83 Bi Bismuth 208.980	84 Po Polonium [209]	85 At Astatine [209]	86 Rn Radon [222]
87 Fr Francium [223]	88 Ra Radium [226]	89-103 Actinides	104 Rf Rutherfordium [261]	105 Db Dubnium [262]	106 Sg Seaborgium [266]	107 Bh Bohrium [264]	108 Hs Hassium [265]	109 Mt Meitnerium [268]	110 Ds Darmstadtium [268]	111 Rg Roentgenium [272]	112 Cn Copernicium [277]	113 Uut Ununtrium [288]	114 Fl Flerovium [289]	115 Uup Ununpentium [289]	116 Lv Livermorium [293]	117 Uus Ununseptium [293]	118 Uuo Ununoctium [294]
57 La Lanthanum 138.905	58 Ce Cerium 140.116	59 Pr Praseodymium 140.908	60 Nd Neodymium 144.243	61 Pm Promethium 144.913	62 Sm Samarium 150.36	63 Eu Europium 151.964	64 Gd Gadolinium 157.25	65 Tb Terbium 158.925	66 Dy Dysprosium 162.500	67 Ho Holmium 164.930	68 Er Erbium 167.259	69 Tm Thulium 168.934	70 Yb Ytterbium 173.055	71 Lu Lutetium 174.967			
89 Ac Actinium [227]	90 Th Thorium [232]	91 Pa Protactinium [231]	92 U Uranium [238]	93 Np Neptunium [237]	94 Pu Plutonium [244]	95 Am Americium [243]	96 Cm Curium [247]	97 Bk Berkelium [247]	98 Cf Californium [251]	99 Es Einsteinium [254]	100 Fm Fermium [257]	101 Md Mendelevium [258]	102 No Nobelium [259]	103 Lr Lawrencium [262]			

Figure 1.1 Periodic table of the elements.

1.1 Introduction to Lanthanide trivalent ions-electronic configurations

Lanthanide elements refer to the elements ranging from La to Lu. Their electronic ground state configurations are determined by their principal quantum number n and angular quantum number l . According to the principle of low energy, there are two types of electronic configurations for the lanthanide elements: $[\text{Xe}]4f^n6s^2$ or $[\text{Xe}]4f^{n-1}5d^16s^2$. Here $[\text{Xe}]$ stands for the electronic configuration of xenon and n represents the number from 1 to 14. Lanthanum, cerium, gadolinium and lutetium belong to the $[\text{Xe}]4f^n6s^2$ type, while praseodymium, neodymium, promethium, samarium, europium, terbium, dysprosium, holmium, erbium, thulium, ytterbium, and lutetium have the $[\text{Xe}]4f^{n-1}5d^16s^2$ pattern.¹ Scandium and Yttrium do not have 4f electrons but they have similar chemical properties to lanthanide elements, because their outermost electrons have the $(n-1)d^1ns^2$ configuration. For this reason, they are generally regarded as being lanthanide elements (they are often called

“lanthanoids”). Lanthanide elements can lose three electrons and adopt the configuration of $[\text{Xe}]4f^n$. Lanthanide ions except La^{III} and Lu^{III} all have the unfilled 4f orbitals, due to the different configuration of the electrons, they will have different energy levels. The electronic configurations of all the lanthanides plus Y are listed in Table 1.1.

Table 1.1 The electronic configurations of lanthanide elements.

Z	Element	Electronic configurations of neutral atoms					Electronic configurations of trivalent ions	Atomic radius
		4f	5s	5p	5d	6s		
57	La	0	2	6	1	2	$[\text{Xe}]4f^0$	187.91
58	Ce	1	2	6	1	2	$[\text{Xe}]4f^1$	182.47
59	Pr	3	2	6		2	$[\text{Xe}]4f^2$	182.80
60	Nd	4	2	6		2	$[\text{Xe}]4f^3$	182.14
61	Pm	5	2	6		2	$[\text{Xe}]4f^4$	181.0
62	Sm	6	2	6		2	$[\text{Xe}]4f^5$	180.41
63	Eu	7	2	6		2	$[\text{Xe}]4f^6$	204.20
64	Gd	7	2	6	1	2	$[\text{Xe}]4f^7$	180.13
65	Tb	9	2	6		2	$[\text{Xe}]4f^8$	178.33
66	Dy	10	2	6		2	$[\text{Xe}]4f^9$	177.40
67	Ho	11	2	6		2	$[\text{Xe}]4f^{10}$	176.61
68	Er	12	2	6		2	$[\text{Xe}]4f^{11}$	175.66
69	Tm	13	2	6		2	$[\text{Xe}]4f^{12}$	174.62
70	Yb	14	2	6		2	$[\text{Xe}]4f^{13}$	193.92
71	Lu	14	2	6	1	2	$[\text{Xe}]4f^{14}$	173.49
		3d	4s	4p	4d	5s		
39	Y	10	2	6	1	2	$[\text{Kr}]$	180.12

The 4f electronic transition is possible to generate spectral term, which is usually described by ^{2S+1}L , in which S denotes the total spin quantum number and L the total orbital quantum number. Spin-orbit coupling splits the ^{2S+1}L state into multiplets with different values of J. Here, the J values are defined as $L-S$ for light Ln^{III} ions and $L+S$ for heavy Ln^{III} ions. The

spin-orbit coupling constant ζ ranges from 600 to 3,000 cm^{-2} . In most cases the multiplets are well separated in energy and so only the lowest lying is populated at room temperature.

The ligand field continues to split the ground state into $2J+1$ sublevels (M_J) in the order of a few hundreds of cm^{-1} (Figure 1.2). The sublevels can also be called Stark levels. The arrangement of the M_J levels is different in different ligand field, unlike the spin-orbit coupling term which is arranged in sequential, for example, $^{2S+1}L_J$ lies in the lowest levels, then $^{2S+1}L_{J-1}$ the second lowest, finally $^{2S+1}L_{J-n}$ the highest levels. The sublevels can mix to certain extent and the largest sublevels are not ensured to populate at ground state. The sublevels may be singlets or grouped as doublets, generally depending on whether the ion is of Kramers (odd number of unpaired electrons, i.e. Dy^{III}) or non-Kramers (even number of unpaired electrons, i.e. Tb^{III}) type.

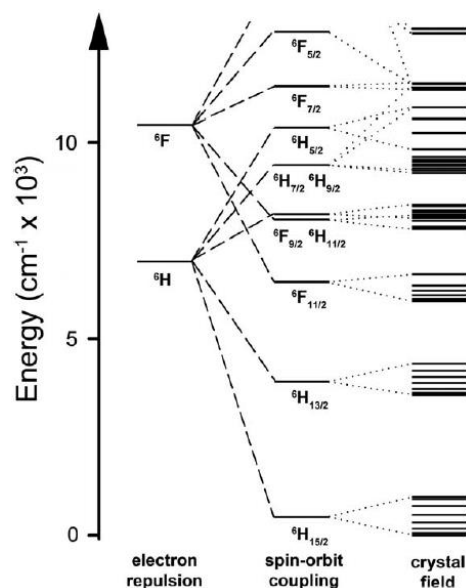


Figure 1.2 Representation of electronic structure of lanthanide trivalent ion with sequential perturbations of electron-electron repulsions, spin-orbit coupling, and the crystal field.³

The 4f electrons are shielded by 5d and 6s orbitals and the spin-orbit coupling of lanthanide ions is much stronger than that of the transition metal ions. The $^{2S+1}L_J$ multiplets pattern of Ln^{III} ions is derived from Pauli Principle and Hund's Rule by taken the Coulombic interaction and the spin-orbit coupling into consideration.

1.2 Introduction to molecular magnetism of Ln^{III} ions

1.2.1 Magnetism of free lanthanide ions

The degeneracy of the $(2J + 1)$ levels in each $^{2S+1}L_J$ multiplet can be removed by applying a magnetic field, providing a series of levels identified by their M_J value, with $-J \leq M_J \leq +J$. The energy can be written in terms of a Landé splitting factor, g_J , depending on J , L and S . The corresponding magnetic moment will be

$$\mu_J = \mu_B g_J J = \mu_B (g_J L + g_S S) \quad \text{equ (1.1)}$$

where g_J is given as:

$$g_J = 1 + \frac{J(J+1+S(S+1)-L(L+1))}{2J(J+1)} \quad \text{equ (1.2)}$$

The magnetic susceptibility of the free ion will follow the Curie law and can be obtained as:

$$\chi = \frac{NgJ^2\beta^2}{3KT} J(J+1) \quad \text{equ (1.3)}$$

where χ is the molar magnetic susceptibility and N is the Avogadro number. The free limit of $\chi_M T$ is listed in Table 1.2. The values of $\chi_M T$ are calculated at room temperature.

Table 1.2 Basic magnetic information for Ln^{3+} ions.²

Ion	$4f^n$	$^{2S+1}L_J$	g_J	ζ (cm ⁻¹)	$\chi_M T$	μ_{eff}	M (μ_B)
Ce ³⁺	1	² F _{5/2}	6/7	644	0.80	2.54	2.14
Pr ³⁺	2	³ H ₄	4/5	730	1.60	3.58	3.20
Nd ³⁺	3	⁴ I _{9/2}	8/11	844	1.64	3.13	3.27
Pm ³⁺	4	⁵ I ₄	3/5	1070	0.90	2.68	2.4
Sm ³⁺	5	⁶ H _{5/2}	2/7	1200	0.09	0.85	0.71
Eu ³⁺	6	⁷ F ₀	5	1320	0.00	—	—
Gd ³⁺	7	⁸ S _{7/2}	2	1583	7.88	7.94	7
Tb ³⁺	8	⁷ F ₆	3/2	1705	11.82	9.72	9
Dy ³⁺	9	⁶ H _{15/2}	4/3	1900	14.17	10.65	10
Ho ³⁺	10	⁵ I ₈	5/4	2163	14.07	10.61	10
Er ³⁺	11	⁴ I _{15/2}	6/5	2393	11.48	9.58	9
Tm ³⁺	12	³ H ₆	7/6	2656	7.15	7.56	7
Yb ³⁺	13	² F _{7/2}	8/7	2883	2.57	4.54	4

1.2.2 Single-Molecule Magnets (SMMs) and related behavior

The traditional magnets consist of a number of molecules or atoms with stable magnetic moment. These magnetic moments interact with each other to induce a 3D long range ordering of magnetic moment, which is stronger than the thermal agitation which tends to give a disordered state. A permanent magnetization of the sample is then achievable.

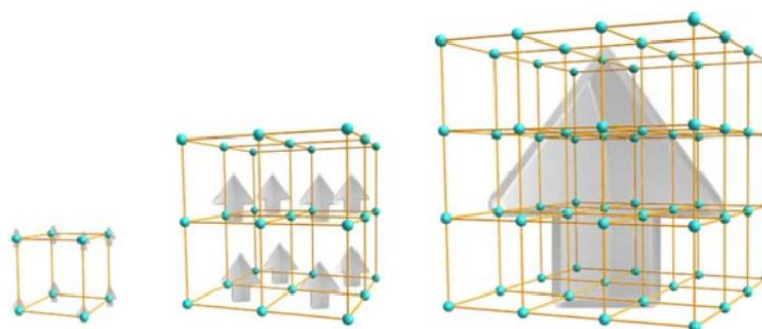


Figure 1.3 3D ordering in a traditional magnet.⁴

In 1993, the discovery of anomalous magnetic behavior in $[\text{Mn}_{12}\text{O}_{12}(\text{OAc})_{16}(\text{H}_2\text{O})_4]$ ⁵ wrote a new page in the search for magnetic materials. In this system, the magnetic domains do not exist anymore, or more precisely, each domain only contains one magnetic molecule. The intermolecular interaction is very weak, therefore, the molecules are magnetically isolated and non-interacting. These molecules have been called Single-molecule-magnets (SMM). Although there are no domain walls between the molecules per se, SMMs still exhibit the properties associated with traditional macroscopic magnets—specifically retention of magnetization and thus hysteresis—but on a molecular scale, and to date only at very low temperatures. The nanoscale of the magnet causes many quantum phenomena different from that of the traditional one.

The interaction of the ground spin-orbit coupled J state of lanthanide ions with the crystal field generates the magnetic anisotropy barrier Δ separating opposite orientations of the spin ground state, described as double-well potential in Figure 1.4. The passage from the ground M_J state to the $+M_J$ state can be due to different relaxation pathways:

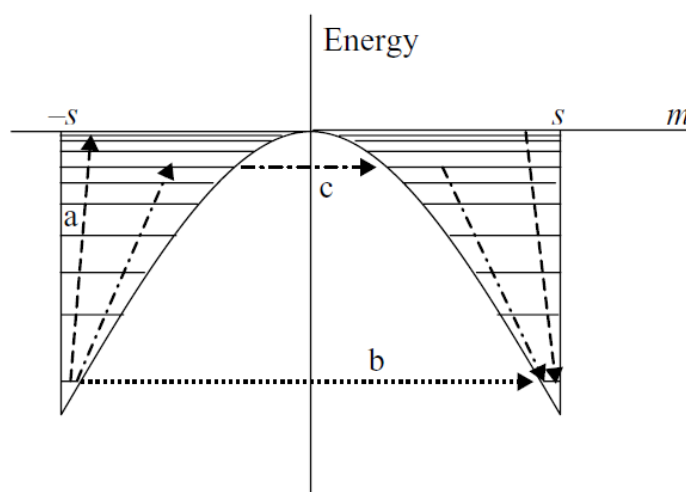


Figure 1.4 Depiction of the double energy well. Three possible relaxation processes are presented.

Thermal regime (pathway a). This process takes place in two steps. At high temperature, the spin absorbs the phonon and flips above the highest level which is delocalized, so that the spin can de-excite into the other side of well.

Quantum tunneling regime (QTM) (pathway b). At low temperature, the spins at the low-lying states go through the energy barrier to the other side without energy cost. This short cuts the energy barrier. That is why the effective barrier U_{eff} is employed to characterize the SMM rather than U . This process takes place in one step, from M_J to $-M_J$ ground state directly.

Thermal-assisted Quantum tunneling regime (pathway c). QTM only begins to compete with the thermal relaxation process at intermediate temperature range. When both the thermal and quantum regimes are contributing to the magnetic relaxation, the process is known as the ‘thermally-assisted quantum tunneling’ or ‘photon-assisted quantum tunneling’. The spin reversal of this pathway is consist of three steps, firstly the spin excites from ground state M_J to one low lying excited state M_{J-N} , secondly it traverses the energy barrier to $-M_{J-N}$ state, thirdly it falls into the $-M_J$ ground state.

In the thermal relaxation process, the emitted or released phonons usually have an exchange of energy with lattice. All these processes are termed spin-lattice relaxation. They can be described as:

Direct process: A transition occurs from energy level a to level b of the spin system directly, where the energy difference δ_{ab} is taken up by (or released to) the lattice as a single quantum of a long-wavelength lattice vibration, which is also viewed as single-phonon process. Direct process often occurs between the non-degenerate M_J levels in the presence of high field, causing the acceleration of relaxation.

Raman process: This process is realized by a transition from the initial state a to an upper intermediate virtual state c , accompanying by the absorption of a phonon, then a release of another phonon occurs to let the system fall into level b . It involves a two-photon process with an energy difference matches δ_{ab} .

Orbach process: The spin system absorbs a phonon and is excited from one of the two lowest states to an upper real state with energy Δ , then it relaxes to the other ground state by emission of another phonon. This process can be viewed as a concerted two-phonon process.

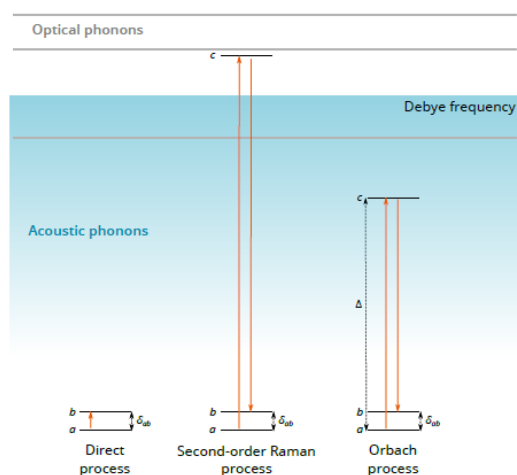


Figure 1.5 Schematic overview over the different magnetisation relaxation (spin–lattice relaxation) processes. The blue lines indicate levels of the lattice, while red lines are CF levels of the lanthanide ion.⁶

The three spin-lattice regimes dominate in different temperature domains. Orbach process prevails generally at high temperature due to the adequate sources of phonons.⁷ The Raman and Direct process govern the relaxation at intermediate temperature where a curvature can be observed. They can co-exist with QT. The full formula for the relaxation rate of the magnetisation is then a sum of all the above mentioned process and is given in equation (1.5)⁸:

$$\tau^{-1} = A_1 H^4 T + A_2 H^2 T + \frac{B_1}{1 + B_2 H^2} + C T^n + \tau_0^{-1} \exp(-U_{eff} / kT) \quad (\text{equ. 1.5})$$

Where the first two terms stand for the direct process for a Kramers ion without and with hyperfine interactions respectively. The last three represent quantum tunneling, Raman process and Orbach process, respectively. Here A_1 , A_2 , C and τ_0 are parameters that contain the spin-phonon coupling matrix element and the speed of sound in the considered material. B_1 and B_2 are the constants associated with tunnel splitting, transition times between levels on the separate sides of the energy barrier as well as the energy difference between the levels on both side of the energy barrier. $n = 7$ for a non-Kramers ion, $n = 9$ for a Kramers ion, $n = 5$ in the presence of very low lying states of the spin system, $n = 2$ at temperatures much higher than the Debye temperature.

1.3 Rules to design lanthanide-based Single-Molecule-Magnets

1.3.1 Maximize the anisotropy of lanthanide ions-oblate/prolate model

As mentioned above, the energy barrier is related to the anisotropy of the magnetic ion. In these systems the magnetic anisotropy typically arises from the extensive splitting of M_J ground state of the lanthanide ion caused by the ligand field.⁹ For the lanthanide-based SMMs, the g -factor is commonly used to quantitatively characterize the anisotropy. The values of this factor in three directions characterize both the shape of the ions and the amplitude of anisotropy.

In many SMMs, there is an energetically most favorable anisotropic axis in which to orient the magnetization, a plane perpendicular to that axis which is the least favorable orientation for the magnetization. The anisotropic axis is known as the ‘easy axis’ and the plane as the ‘hard plane’. There can also be ‘intermediate’ axes.¹⁰

If the magnetic axis of the metal ion is aligned with the easy axis, the value of g_z will be maximized. For example, for Dy^{III} g_z tends to be close to 20, and g_x and g_y close to 0. This anisotropy is the so-called Ising-type magnetic anisotropy. Ising anisotropy will induce a stronger anisotropy, and the different substates will be separate from each other, only the largest $\pm M_J$ Kramer’s doublets are populated at low temperature. The pure Ising magnetic anisotropy is the ideal state for a SMM, but it has not been realized yet, because the values of

g_x and g_y are not strictly 0. The extent to which the higher excited state is ‘pure’, the larger the effective energy barrier will be obtained.¹¹

In some cases, the ‘easy’ direction can be a plane, instead of an axis, if there is a two-dimensional region of space in which it is preferable to find the magnetization. Let us call it ‘easy plane’, in which $g_z < g_x \approx g_y$.

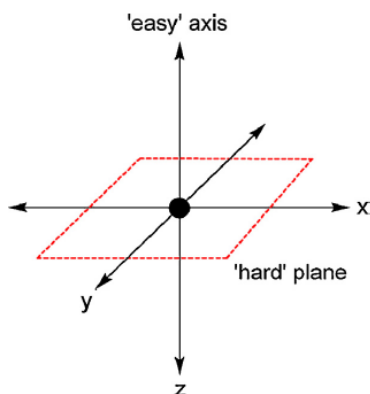


Figure 1.6 Representation of the easy axis and hard plane in three dimensional space.¹⁰

Achieving the Ising anisotropy is hence a key point, but how to do it becomes a question. In 2011, Jeffrey R. Long *et al.*³ have published a constructive work. They modeled the basic shapes of the lowest J states mathematically by the quadrupole moment of the f-electron charge cloud after approximate the distribution of the free-ion f-electron density for each ion. Thus the lanthanide trivalent ions are described as oblate (axially elongated), prolate (equatorially expanded), or isotropic (spherical), respectively.

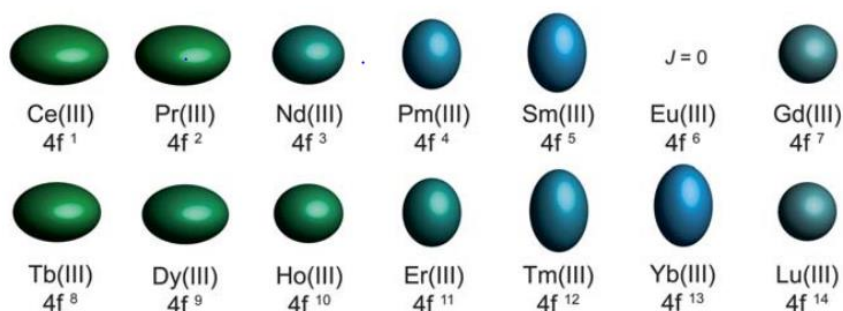


Figure 1.7 Representation of quadrupole approximations of the 4f-shell electron distribution for all the Ln^{III} except La^{III} . Eu^{III} is also not depicted due to a $J=0$ ground state.³

Except isotropic Gd^{III} and Lu^{III} ions ($g_x=g_y=g_z$), other ions are divided into two groups, oblate one and prolate one. Ce^{III} , Pr^{III} , Nd^{III} , Tb^{III} , Dy^{III} and Ho^{III} are of the former type, while Pm^{III} , Sm^{III} , Er^{III} , Tm^{III} and Yb^{III} are of the latter type, among which Ce^{III} , Pr^{III} , Tb^{III} , Dy^{III} , Sm^{III} , Tm^{III} and Yb^{III} have large intrinsic anisotropy. To maximize the anisotropy of an oblate ion, the distribution of a crystal field in the axial z direction should guarantee bistable orientations of $\pm M_J$ parallel and antiparallel to the molecular axis so as to minimize repulsive

contacts between ligand and f-electron charge clouds. Accordingly the equatorial crystal field will maximize the anisotropy of the prolate ions.

The square antiprism geometry (D_{4d})^{12, 13} and the recent flourish of pentagonal bipyramidal (D_{5h})¹⁴⁻¹⁶ are quite suitable for oblate Dy^{III} ions. The trigonal bipyramidal geometry (D_{3h}) is exploited to fit well with the oblate ones.¹⁷ Complex in the real ‘as isolated’ material often has lower symmetry, then molecular vibrations cause momentary deviations from high symmetry, producing a large transverse component of anisotropy to allow the fast relaxation.

This model has simultaneously explained why the Dy^{III} ion represents the best candidates for single-molecule magnetism. Because it is a Kramer’s ion, so a doubly degenerate mJ ground state is ensured regardless of what the ligand field symmetry is. It combines a large moment ${}^6H_{15/2}$ ground state with significant anisotropy of the 4f shell to make it very appealing. Conversely the Tb^{III} ion offers similar properties with an even greater electronic anisotropy, however a bistable ground state requires that rigorous axial symmetry been maintained or the magnetic exchange is present, since bistability is not always guaranteed for a non-Kramer’s ion.¹⁸ This is why Tb based SMM are very scarce.

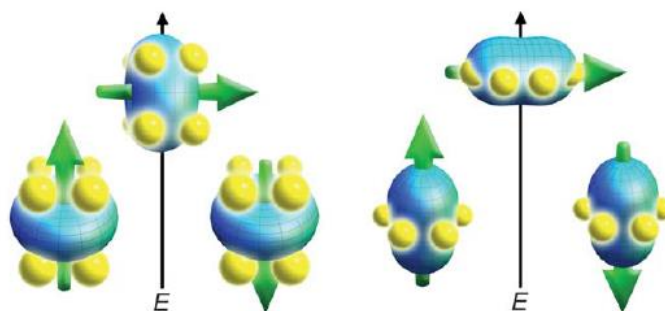


Figure 1.8 Representation of low- and high-energy configurations of the f-orbital electron density with respect to the crystal field environment for a 4f ion of oblate (left) and prolate (right) electron density. The green arrow represents the orientation of the spin angular momentum coupled to the orbital moment.³

Thereby, efforts to achieve high symmetry to reduce the transverse component are currently undertaken, mainly by coordination chemistry techniques.

1.3.2 Tune the electrostatic charge distribution

‘Simple’ prolate/oblate models are not suitable for seeking explanations of important changes in magnetic properties for complexes in which the symmetry of the coordination mode and ligands remains almost unaltered. The distribution of charge should be a key point to account for these changes. Thereby, more precise models considering this factor are needed. We take the most used Dy^{III} as the example, also because the models of Dy^{III} are calculated in detail by Gómez-Coca et al.²⁰ The models take the coordination geometry, number and the distribution of charge of the ligands into account to explore the best conditions to enhance the energy barrier and magnetic anisotropy, as seen in Figure 1.9.

From the histogram we can gain further insight into the rationalization on SMM. For a given geometry, the distribution of charge will greatly influence the energy barrier and anisotropy. The coordination number of Ln^{III} mainly concentrates on 7-9, considering the obtained anisotropy and the main relaxation regime, a number of models are interesting, such as 7_1 , 8_4 , 8_5 etc. The model 7_1 was successfully realized in 2016²¹ showing both large energy barrier and Ising anisotropy, as discussed in the following text. With these models in hand, chemists can rationalize the ligand field by flexible coordination chemistry strategy in spite of a still challenging target.

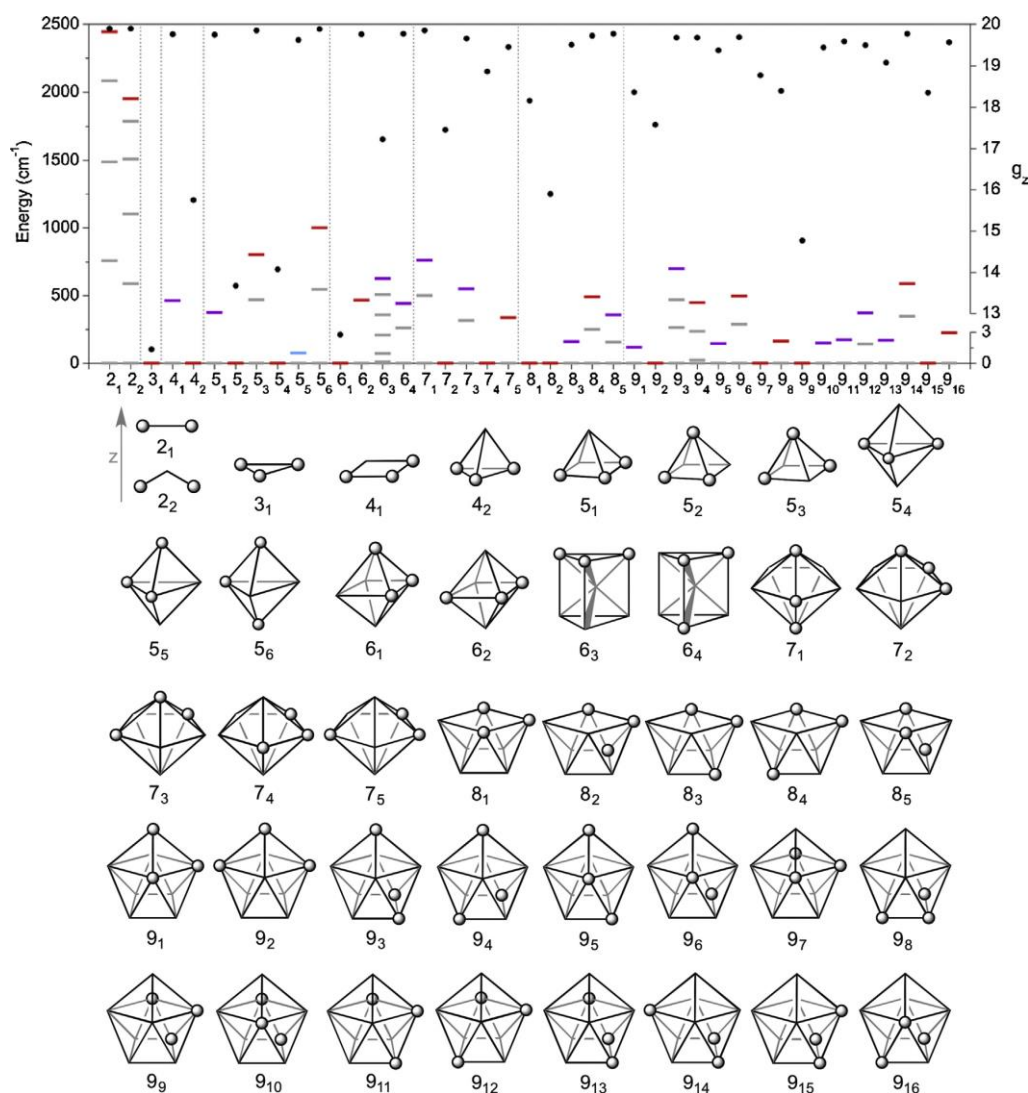


Figure 1.9 Reproduction of histogram for all the $[\text{Dy}(\text{OH})_3(\text{H}_2\text{O})^{n-3}]$ complexes showing their calculated g_z value (black points) at CASSCF + RASSI level; the systems are labeled as n_x where n is the coordination number. The horizontal lines correspond to the Kramer's doublet energies under the level involved in the spin relaxation mechanism (as criterion, a matrix element of the transition magnetic moment above 0.1 was considered). The color of the highest level indicates the main mechanism of the spin relaxation: red indicates quantum tunneling or thermally-assisted quantum tunneling, blue to a Orbach mechanism while violet represents a mixture of Orbach and tunneling mechanisms. (below) Structural description of the Dy^{III} complexes; the circles correspond to the OH^- ligands.²⁰

1.3.3 Avoiding Quantum Tunneling of the magnetization

1.3.3.1 Introduction to Quantum Tunneling (QT)

From the synthetic point of view, the above models are enough to design or rationalize a SMM, but quantum tunneling (QT) is still an issue as many Ln-SMMs can lose the magnetic slow relaxation capabilities through this process.

In theory, the occurrence of QT is determined by the bistability of lanthanide ions. It is normal for full-integer spin systems to show QT. Strictly according to Kramers' spin-parity theorem, QTM is forbidden in half-integer spin systems, which dictates that no matter how asymmetric the crystal field, ions with an odd number of electrons have to have at least a doubly degenerate ground state. But in the real system, many factors can break this ideal state, such as the perturbations deriving from dipole-dipole interaction and exchange interaction and non-local symmetry, rendering QT possible by allowing the mixing of the two states.²² But the real physical origin of the QT remains still unclear.²³⁻²⁴

QT is technically detectable in several ways. From the static point of view, the presence of QT can be evidenced as characteristic 'steps' in the field dependence of magnetization measurements. The steps arising from the transitions between mixed sublevels can be observed in a subtle magnitude of field strength.²³ From the dynamic point view, the $\ln(\tau)$ versus $1/T$ plot features a series of consecutive data points for which relaxation time is independent of the temperature well correspond to QTM. Moreover, a tail at low temperature is also viewed as a hint of this effect.²⁵ From the anisotropy point of view, the deviation from the pure Ising type anisotropy can often cause QT.

1.3.3.2 Strategies to avoid (QT)

The presence of QT accelerates the magnetic relaxation and cut down the energy barrier for spin reversal, which hampers the SMMs into practical application. How to reduce the QT is a challenging and interesting work. The following measures could be taken to modulate the QT.

(1) *Applying a dc field.* The application of the dc field reduces the extent of sublevel mixing, which results in a lower rate of tunneling and allows the magnetization to relax predominately through the thermal regime down to lower temperatures. One should be aware that, indeed, a dc field is applied to suppress the QT. However, tunneling can also take place in the presence of magnetic fields. If a magnetic field is applied parallel to z axis the energies of the M_J levels will change rapidly and lose their degeneracy. The rise of the m_J state in one side probably coincide in energy with certain low lying state in the other side and hence restore the conditions for resonant tunneling.²⁶

(2) *Magnetic site dilution.* Dispersion of the paramagnetic spin carriers in an isomorphous diamagnetic matrix, where there is no distribution of the molecular geometry and where dipolar coupling, often taken as a perturbation to enhance the tunneling process, is suppressed, is by far the best optimization. The increase in diamagnetic species determines more efficient relaxation, thus improve the memory effect. But this method sometimes can be useless if the relaxation is of intermolecular nature rather than the molecular one, though very rare, may lead to the shrink of the hysteresis loop on further dilution, occurring in $U(H_2BPz_2)_3$.²⁷

(3) *Metal-centered Isotope enrichment.* In some cases, QT of the magnetization is brought by hyperfine coupling and transverse internal field created in condensed phases by neighboring molecules. To minimize the two factors, a strategy can be achieved by using metal-centered isotopic enrichment. This approach may offer the possibility to intrinsically improve the magnetic bistability of existing SMMs, by decreasing the number of relaxation pathways.²⁸

(4) *Magnetic interaction.* Strong exchange coupling can serve to isolate the spin ground state and to quench quantum tunneling of the magnetization, finally shut down quantum tunneling processes within a single spin state manifold. The use of paramagnetic ligand is particularly suitable for this purpose.

1.3.4 Avoiding three dimensional (3D) ordering

For the single-molecule-magnet (SMM) or single-chain-magnet (SCM), the spin carriers are often composed of paramagnetic phase, some of them, especially the chain-like structure, can undergo phase transition to the antiparamagnetic ordered phase (in most cases). In 2009, Coulon *et al.*²⁹ have reported the famous SCM $[Mn_2(5-MeOsaltmen)_2Ni(pao)_2(phen)](PF_6)_2$ and depicted the phase diagram with a two-sublattice model (m_i) seen in Figure 1.10. The two sublattices have opposite values in zero field, as the field increases, the magnitude of one sublattice decreases to zero at the dashed line. Then the orientation has changed and the value increases to be positive and equal to another sublattice at the continuous line. The two mentioned lines are referred to “inversion field” (H_{inv}) and “antiferromagnetic-paramagnetic phase transition” (at HC), respectively. This research first proposed that slow relaxation of the magnetization exists in the ordered phase.

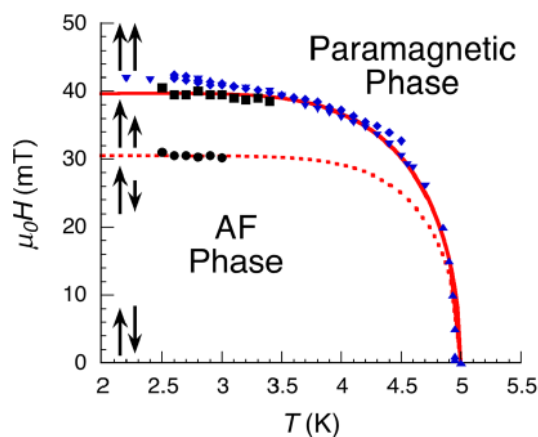


Figure 1.10 Location of the maximum of susceptibility from $M(H)$: (◆) single crystal, (▼) powder measurements, or (▲) from the T dependence of the powder ac susceptibility at a given dc field. Experimental points deduced from the dynamic measurements: (■) location on the main maximum of the relaxation time and (●) location of the second maximum (inversion point). The continuous line is the theoretical estimation of the AF-paramagnetic phase transition, and the dashed line gives the line of inversion points. The arrows are schematizing the orientation and magnitude of the two order parameters (m_1 and m_2).

The underlying reason of the 3D ordering phenomenon is generally believed to be the intermolecular interaction, such as through space dipolar interaction.^{30, 31} When the transition of 3D ordering takes place, the zero-field-cooled (ZFC) and field-cooled (FC) magnetization will show a bifurcation point at low temperature and the $\chi_M T$ product slumps at certain low temperature. Ac measurements down to very low temperatures also allowed us to observe the crossover from a dynamic spin reversal of the magnetization, first via a thermal pathway, then by a quantum tunneling pathway, to a 3D ordered state.³⁰

1.3.5 Improving the blocking temperature

To achieve the goal of practical application, one should enhance the blockage of the SMM to high temperature. Firstly we introduce the definition of blocking temperature, T_B . Two different definitions were proposed, T_{B1}) the highest temperature at which an SMM displays hysteresis in plots of magnetization (M) versus magnetic field (H). This defined T_B is strongly influenced by the sweep rate of the magnetic field, resulting in a troublesome comparison between the SMMs. T_{B2}) the temperature at which the time (τ) taken for the magnetization to relax is 100 s ³² is gradually widely accepted.

The efforts to augment the energy barrier do not necessarily guarantee the high blocking temperature. The reason is that the energy separation between the ground state and excited states is directly correlated to the strength of exchange coupling; small exchange coupling or small energy separation will permit a fast relaxation.

According to the interacting species, there can be two types of exchange interaction pathways.

Indirect exchange interaction. When the metal ions are bridged by diamagnetic atoms, they can interact with each other by indirect exchange interaction. In these complexes, superexchange interaction is the only pathway of indirect regime, which is a short-range regime permitting the interaction transmission by the p electrons of the bridging diamagnetic atoms. This superexchange magnetic coupling can be either ferromagnetic or antiferromagnetic. Since the 4f electrons are deeply masked by other orbitals, superexchange magnetic coupling between metal centers is often relatively weak, especially when the bridging atoms are non-single. The strength depends on the Ln^{III}-Ln^{III} distances and the species of bridging units (i.e. The H₂O molecule is less efficient in promoting strong exchanges than traditional oxido O²⁻ bridges;³³ The different bridging atoms also impact on the interaction strength).³⁴

The intramolecular exchange-biased interaction is able to suppress the QTM and play the decisive role of the exchange interaction in dinuclear or polynuclear systems despite its small magnitude.³⁵ But this strategy has a finite ceiling for improvement of T_B.

Direct exchange interaction. This interaction originates from the direct overlapping of the orbitals of neighboring spin carriers. The spin pairs are consist of the alternative paramagnetic metal ions and paramagnetic bridging ligands (radical), can give rise to much stronger exchange coupling between the metals and the S=1/2 spins. This is because the orbitals of paramagnetic ligands can easily penetrate into the 4f shell of Ln^{III}. Of course, it is much easier for one radical spin to diffuse into the orbitals of another radical spin, offering the J_{rad-rad} extremely larger than the J_{rad-Ln}.

The amplitude of the exchange coupling is proportional to the spin density at the nitrogen and oxygen atoms.³⁶ Electron-withdrawing groups will decrease the amount of electron density on the oxygen atoms, resulting in weaker magnetic coupling. In contrast, introducing the electron-donating substituents will provide stronger exchange, stabilizing the spin ground states of Ln^{III}. This strategy is much effective in the pursuit of improving the T_B relative to the superexchange one.

1.4 Selected examples of lanthanide-based Single-Molecule-Magnets

Since 2003, a tremendous amount of SMMs has been reported in the literature. We propose here a survey of the most representative examples of Ln-based SMMs.

1.4.1 Selected examples of heavy lanthanides-based SMMs (diamagnetic ligands)

In 2003, Ishikawa *et al*³⁷ reported the first example of SMM containing lanthanide ions ([Pc₂Ln]⁻·TBA⁺; Pc = phthalocyanine; Ln = Dy, Tb; TBA⁺ = N(C₄H₉)⁴⁺). This was also the first example of single-ion SMM. The arrangement of the Pc ligands around the lanthanide induces a double-decker or sandwich structure in which the Ln^{III} ions are in a D_{4d} symmetry environment. Their energy barriers for spin reversal are reported to be 28 and 230 cm⁻¹ for

the Dy^{III} and Tb^{III} adducts respectively. Solution ¹H NMR studies of the electronic spin dynamics of [Pc₂Tb]⁻ molecules revealed a much larger barrier of $U_{\text{eff}} = 584 \text{ cm}^{-1}$, and solid samples diluted with the diamagnetic salt (Bu₄N)Br also displayed considerably high barriers of 641 cm^{-1} .³⁷

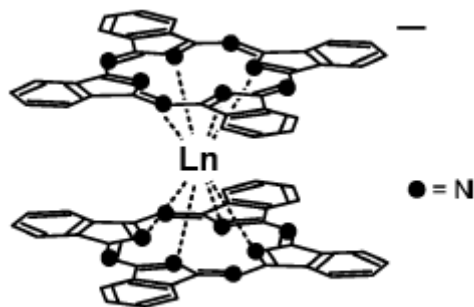


Figure 1.11 Structure of [Pc₂Ln]⁻·TBA⁺ (Pc=dianion of phthalocyanine; TBA⁺= N(C₄H₉)₄⁺).³⁷

[LnPc₂]⁻ is susceptible to one and two electron oxidation to give [LnPc₂] and [LnPc₂]⁺, respectively. The oxidations can change the molecular structure of the sandwich unit, which should impact on the ligand field, and which should, in turn, result in greater energetic separation of the ground M_J sublevel from the excited states. For example, the radical analogue [TbPc₂] has shown a strong frequency dependence of out-of-phase signal, with a peak maximum observed at 50 K. The resulting Arrhenius analysis produced a remarkable $U_{\text{eff}} = 410 \text{ cm}^{-1}$, which is considerably higher than any analogous value extracted for [Pc₂Ln]⁻ from ac susceptibility data.³⁸

After the work of Ishikawa, many types of Ln-SMMs have been reported. To main features are continuously optimized: the energy barrier value (U_{eff}) and the blocking temperature (T_B). Before 2016, the largest record of energy barrier was 938 K,³⁹ and the highest blocking temperature was 14 K.⁴⁰ In 2016 the most striking developments is that the value of energy barrier is pushed forwards two times.

Firstly, the complex [Dy(bbpen)Br] (H₂bbpen = N,N'-bis(2-hydroxybenzyl)-N,N'-bis(2-methylpyridyl)ethylenediamine) synthesized by Liu *et al.*²¹ breaks the record of energy barrier, overpassing 1000 K. The Dy^{III} ions is in a pseudo-D_{5h} symmetry surrounded by four neutral N atoms and one Br⁻ anion (negative charge) in the equatorial plane, and two charged oxygen atoms occupying the capping positions. The spin flips from the ground state to the 3rd excited doublet, which enhance the effective energy barrier dramatically to 1025 K, accompanied by an opening of the magnetic hysteresis up to 14 K. Ab initio calculations predict that the value of g_z is as high as 19.88, very close to the theoretical $g_z=20.00$ value for a purely anisotropic Dy^{III} ion. On a topologic point of view this molecule is very close to the 7₁ model (Figure 1.9).

The second compound, of formula [Dy(O^tBu)₂(py)₅][BPh₄], further enhanced the record to 1815 K. In this compound, five neutral pyridine molecules are placed in the equatorial pentagonal plane, two anions are placed below and above, resulting in a nearly perfect D_{5h} symmetry with strong axial crystal-field but weak equatorial crystal field. Besides, the

nitrogen is less electronegative than oxygen, the axially is strengthened again. Another record is that the ac signals appear at as high as 100 K. Both the two examples highlight the strongest axially of D_{5h} symmetry.

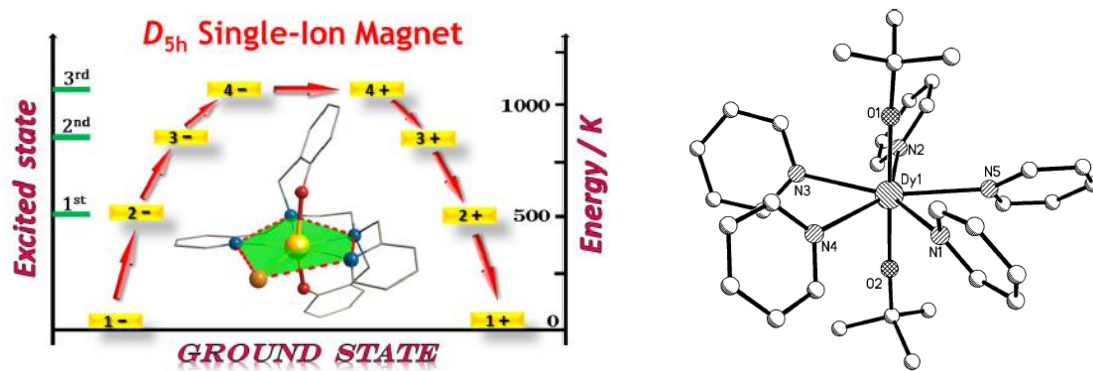


Figure 1.12 Representation of the structure of $[\text{Dy}(\text{bbpen})\text{X}]$ ($\text{X} = \text{Cl}$ or Br) (left) and $[\text{Dy}(\text{OtBu})_2(\text{py})_5]^+$ cation (right).^{14, 21}

Among the oblate ions, Er^{III} is the most used. The great success of Er-based SMM principally concentrates on organo-erbium complexes, such as $(\text{Cp}^*)\text{Er}(\text{COT})$,⁴¹ $[\text{K}(18\text{-crown-6})][\text{Er}(\text{COT})_2] \cdot 2\text{THF}$,⁴² $[\text{K}(18\text{-crown-6})(\text{THF})_2][\text{Er}(\text{COT})_2]$,⁴² $[\text{Li}(\text{DME})_3][\text{Er}^{\text{III}}(\text{COT}'')_2]$,⁴³ $[\text{Er}^{\text{III}}_2(\text{COT}'')_3]$ and $\text{K}_2(\text{THF})_4[\text{Er}^{\text{III}}_2(\text{COT})_4]$ (with $[\text{Cp}^*]^-$ = pentamethylcyclopentadienide anion, COT = cyclooctatetraenyl dianion, COT'' = 1,4-bis(trimethylsilyl)cyclooctatetraenyl dianion; THF = tetrahydrofuran).

Among them the last two SMMs $[\text{Er}^{\text{III}}_2(\text{COT}'')_3]$ and $\text{K}_2(\text{THF})_4[\text{Er}^{\text{III}}_2(\text{COT})_4]$ ⁴⁴ show very interesting behavior. Ac susceptibility data indicates a 100s relaxation times for temperatures of 12.5 and 12.9 K, respectively, which are among the highest values in all the Ln-SMMs. In zero applied field, a thermally activated relaxation with $U_{\text{eff}} = 323(3)$ K (231 cm^{-1}), with $\tau_0 = 5.7 \times 10^{-10}$ s was characterized for the former compound, and solution studies show slightly enhanced ac susceptibility dynamics with an effective energy barrier of $335(13)$ K (239 cm^{-1}) with a $\tau_0 = 1.9 \times 10^{-10}$ s. An effective energy barrier of $306(1)$ K (219 cm^{-1}) with a $\tau_0 = 5.0 \times 10^{-9}$ s was obtained for the latter compound.

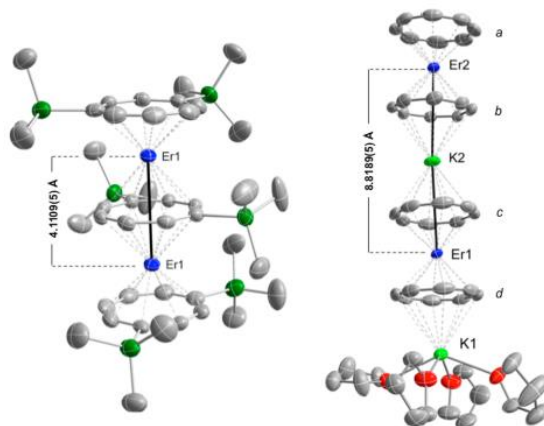


Figure 1.13 Representation of the structure of $[\text{Er}^{\text{III}}_2(\text{COT}'')_3]$ (left) and $\text{K}_2(\text{THF})_4[\text{Er}^{\text{III}}_2(\text{COT})_4]$ (right).⁴⁴

The group of Tang¹⁷ has reported the first equatorially coordinated mononuclear Er-based molecular species $\text{Er}[\text{N}(\text{SiMe}_3)_2]_3$ behaving as an effective SMM. The three-coordinate lanthanide compound demonstrates an equatorially coordinating crystal-field with a perfect C_3 axis around lanthanide ions, which meets the criteria of oblate/prolate theory, giving an effective barrier of 122 K.

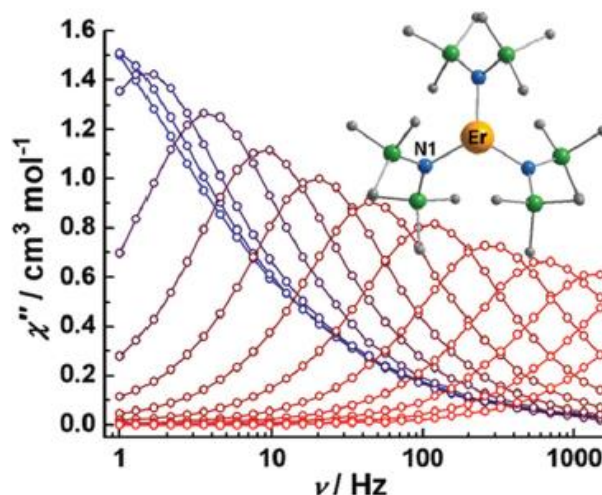


Figure 1.14 Representation of the structure of $\text{Er}[\text{N}(\text{SiMe}_3)_2]_3$ and its relaxation dynamics.¹⁷

Among the heavy lanthanides, Ho^{III} , Tm^{III} and Yb^{III} are less explored, while in which Yb^{III} ion is relatively the most popular amongst the minority group.

The first Yb^{III} -based $\text{K}_{13}[\text{Yb}(\text{SiW}_{11}\text{O}_{39})_2]$ SMM in which the lanthanide ion is surrounded by a fully oxygenated environment, was reported in 2009 by Coronado *et al.*⁴⁵ The X-ray structure revealed the encapsulation of the Yb^{III} ion by two $(\beta_2\text{-SiW}_{11}\text{O}_{39})_8^-$ anionic units leading to a distorted square-antiprism coordination sphere. An out-of-phase component of the magnetic susceptibility below 10 K. Unfortunately no quantitative dynamic parameters are given for this system.

Afterwards, many other examples are subsequently reported.^{11, 46-50} In general, Yb^{III} based SMM have less excellent magnetic performances than the commonly researched Dy^{III} , Er^{III} and Tb^{III} based ones. Other two ions, to date, only few examples have been reported.^{26, 45, 51-53}

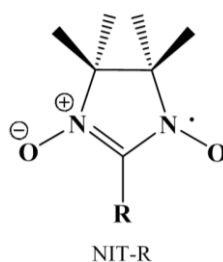
1.4.2 Selected examples of lanthanides-Radicals (4f-2p) based SMMs (paramagnetic ligands)

The 4f-2p systems are another branch of molecular magnetism. In these systems, paramagnetic ligands have been introduced in order to interact with the buried 4f shells of Ln^{III} . Thanks to organic chemistry techniques, a great number of radical ligands have been synthesized and coordinated with Ln^{III} ions.

Nitronyl nitroxide (NIT) A tremendous effort has been directed toward the synthesis and characterization of 4f-NIT (NIT = nitronyl nitroxide) compounds. Since 1987, Gatteschi and co-workers⁵⁴ have started studies on exchange coupling in Gd-NIT complexes and chains. In

2007, the first lanthanide-based single-molecule magnet incorporating a radical ligand was reported.⁵⁵ The bridging capability of the pyridine-functionalized nitronyl nitroxide ligand, NIT4Py, was exploited by linking two Dy^{III} centers to afford the single-molecule magnet [Dy(hfac)₃(NIT4Py)]₂, which exhibits an energy barrier of $U_{\text{eff}} = 9.2(5) \text{ cm}^{-1}$ under zero dc field and $U_{\text{eff}} = 9.5(1) \text{ cm}^{-1}$ under a 2000 Oe dc field. The Gd analogue exhibits weak ferromagnetic coupling between the Gd^{III} and radical centers with $J = +0.89 \text{ cm}^{-1}$.

Nitronyl Nitroxide



Scheme 1.1 Schematic representation of Nitronyl Nitroxide (NIT) radical.

Consequently, numerous NITs have been used in to improve the exchange coupling and to develop new Ln-SMMs. A summary of the 4f-NIT compounds are listed in Table 1.3 and 1.4.

Table 1.3 Summary of magnetic exchange coupling constants (K) for nitronyl nitroxide radical-containing complexes.

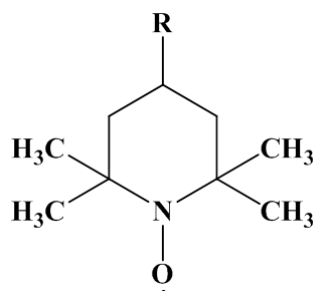
Compound	$J_{\text{rad-Ln}}$ (K)	$J_{\text{rad-rad}}$ (K)	Ref
{Gd(dca) ₂ (OH)(NIT-p-Py) ₂ } ₂	16.6		56
[Dy(hfac) ₃ (NIT-p-Py)] ₂	19.4		55
Ho(NO ₃) ₃ (NITTrz) ₂	6.5	-9.8 / La	57, 58
{Gd(hfac) ₃ (NITet)} _n	16.6/48.3		59
{Tm(hfac) ₃ (NITPhOPh)} _n	3.7		60
((Me ₃ Si) ₂ Ng ₂ (THF)Gd) ₂ (μ-N ₂ ³⁻)	-56.0		61
Gd(hfac) ₃ (NITPh) ₂	-1.8	7.4	62
{Gd(dca) ₂ (OH)(NIT-p-Py) ₂ } ₂	16.6		56
[Dy(hfac) ₃ (NIT-p-Py)] ₂	19.4		55
Gd(hfac) ₃ (NIT-o-Py)	-4.4		63
Gd(hfac) ₃ (NITPh-3-Br-4-OH) ₂	4.5	-17.6	64
Dy(hfac) ₃ (NITPhOEt) ₂	-19.4	22.815.8 / Y	65

Table 1.4 Dynamic relaxation parameters for lanthanide-radical (NIT) single-molecule magnets.

Compound	H _{dc} (KOe)	U _{eff} (K)	τ ₀ (s)	Ref
[Tb(hfac) ₃ (NIT-3BrPhOMe)] _n	0	58.75	2.25 × 10 ⁻⁷	66
[Dy(hfac) ₃ (NIT-3BrPhOMe)] _n	0	39.84	2.43 × 10 ⁻¹⁰	66
[Tb(hfac) ₃ (NITPhSCH3)] _n	0	29.96	2 × 10 ⁻⁹	67
[Tb(hfac) ₃ (NITPhCOOMe)] _n	1	36	2 × 10 ⁻⁸	68
[Tb(picNN) ₃]·6H ₂ O	0	22.8	5.5 × 10 ⁻⁹	69
[Dy(hfac) ₃ (NIT-PhNO ₂) ₂]·0.5C ₇ H ₁₆	0	33.7	3.55 × 10 ⁻¹⁰	70
[{Dy(hfac) ₃ NitPhIm ₂ }Dy(hfac) ₃] ^a	3	17.1/82.7	17.5×10 ⁻⁶ /8.8×10 ⁻⁸	71
Tb(hfac) ₃ (NITPhOEt) ₂	0	20	3.0 × 10 ⁻⁸	72
[Tb(hfac) ₃ (NIT-5-Py-3Br)] ₂	0	20	5.9 × 10 ⁻⁹	73
Tb(acac) ₃ NIT2Py·0.5H ₂ O	1/3.5	15/18	1.0 × 10 ⁻⁷ /3 × 10 ⁻⁸	74
[Tb(Phtfac) ₃ (NIT4Py)] ₂	0	18	4.1 × 10 ⁻⁸	75
[Tb(hfac) ₃ (NITPhPO(OEt) ₂) ₂] ₂	2	17	3.4 × 10 ⁻⁹	76
Tb(NITpic) ₃	2	16	5.5 × 10 ⁻⁹	69
[Dy(acac) ₃ (NIT2Py)]·0.5NIToPy	0	15	1.5 × 10 ⁻⁸	77
[Tb(hfac) ₃ (NITPhPO(OEt) ₂) ₂] ₂	2	15	1.8 × 10 ⁻⁹	76
[Dy(Phtfac) ₃ (NIT4Py)] ₂	3	14	1.8 × 10 ⁻⁶	75
[Tb(hfac) ₃ (NIT3Py)] ₂	3	13	8.8 × 10 ⁻⁸	78
[Tb(hfac) ₃ (NIT2Py)]·0.5C ₇ H ₁₆	0	12	9.6 × 10 ⁻⁷	79
Tb(tfa) ₃ NITBzImH	0	10	4.6 × 10 ⁻⁷	80
[Dy(hfac) ₃ (NIT4Py)] ₂ ^b	2	10/9.2	6.7×10 ⁻⁷ / 2.3×10 ⁻⁸	55
[Dy(hfac) ₃ (NIT-mbis)] ₂	0	8.1	2.3 × 10 ⁻⁸	81
[Dy(hfac) ₂ (NITPhO)] ₂	0	5.3	3.0 × 10 ⁻⁶	82
Dy(tfa) ₃ (NITBzImH)	0	3.2	3.6 × 10 ⁻⁷	80

^a Dual relaxation.^b Data obtained in the absence and presence of dc field.

Aliphatic nitroxide Aliphatic nitroxides are other paramagnetic ligands that in some cases induce higher magnetic coupling with lanthanides than NITs. The spin localization at the N-O group is indicated by the hyperfine coupling constant a_N, and nitroxide N and O atoms carry comparable spin densities. The constant a_N > 1.0 mT for aliphatic nitroxides, such as di-*t*-butyl nitroxide (DTBN), *t*-butyl 2-pyridyl nitroxide (2PyNO), 2,2,6,6-tetramethylpiperidin-1-oxyl (TEMPO)⁸³⁻⁸⁵ is larger than those for typical nitronyl nitroxides (ca. 0.75 mT).^{86, 87}



Scheme 1.2 Schematic representation of TEMPO-R radical.

The simplest TEMPO radical has been reacted with lanthanide ions to afford $\text{Ln}(\text{hfac})_3(\text{TEMPO})_2$ ($\text{Ln} = \text{Y}, \text{La}, \text{Gd}$).⁹⁶ In chapter 2 and 3 of this manuscript, the TEMPO-R radicals used are the derivatives of this one. Two radical ligands coordinate to the metal center in a trans mode. Variable-temperature dc susceptibility and low-temperature magnetization data for the Gd^{III} complex suggested a ground state of $S = 7/2$ for this molecule. This ground state indicates that the TEMPO radical spins cancel one another at low temperature. Similarly, strong superexchange interactions across diamagnetic lanthanide ions were first observed for radical-radical interactions across Y^{III} and La^{III} centers, with $J_{\text{TEMPO1-TEMPO2}} = -5.2$ (1) and -17.3 (2) cm^{-1} , respectively. Taking the isomorphous yttrium complex into account, the exchange interactions between Gd and the organic radicals have been evaluated to be $J_{\text{Gd-TEMPO}} = -4.5$ (1) and $+2.8$ (1) cm^{-1} . Er-TEMPO_2 , exhibits relatively slow magnetization relaxation with the effective activation energy $U_{\text{eff}}/k_{\text{B}} = 18.2$ (19) K and the pre-exponential factor $\tau_0 = 9(5) \times 10^{-8}$ s.⁹⁷

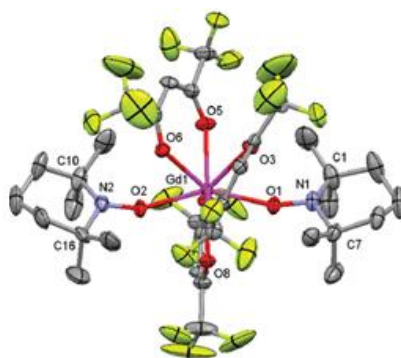


Figure 1.15 Representation of molecular structure of $\text{Re}(\text{hfac})_3(\text{TEMPO})_2$.³⁶

The second and third TEMPO-R based SMM are $[\text{Ln}_2(\text{hfac})_6(\text{H}_2\text{O})_2(\text{dppnTEMPO})]$ ($\text{Ln}^{\text{III}} = \text{Dy}^{\text{III}}$ and Tb^{III}). The two compounds show strong field-induced SMM signals and strong Ln^{III} -radical coupling. Moreover, the Gd^{III} analogue also shows sizable exchange coupling, as shown in Table 1.4.

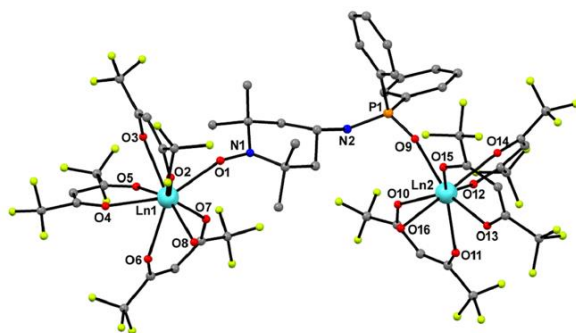
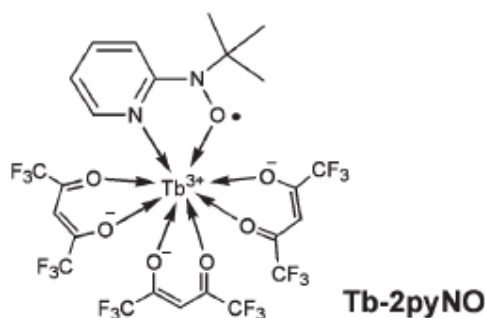


Figure 1.16 Representation of molecular structure of $[\text{Ln}_2(\text{hfac})_6(\text{H}_2\text{O})_2(\text{dppnTEMPO})]$.⁸⁸

$\text{Gd}(\text{hfac})_3(2\text{PyNO})(\text{H}_2\text{O})$ (abbreviated as Gd-2PyNO) has shown the highest exchange coupling of -13.8 K in the Gd containing aliphatic nitroxides compounds. Its Tb analogue has a different structure, which consist in two crystallographically independent molecules in a unit

cell. The magnetic study clarified that every molecule behaved as a single molecule magnet. Two series of the out-of-phase ac susceptibility signals appeared around 10 K even at zero dc field. The activation energies (Δ) for the magnetization reversal were estimated as $U_{\text{eff}}(1)/k_B = 39.2(3)$ K with $\tau_0(1) = 4.2 \times 10^{-8}$ s and $U_{\text{eff}}(2)/k_B = 36$ K with $\tau_0(2) = 4.1 \times 10^{-7}$ s. Magnetic hysteresis was recorded at 1.6 K by means of a pulsed-field technique. The relatively high U_{eff} is thought to be related to the presence of strong exchange coupling.



Scheme 1.3 Schematic representation of Tb-2PyNO.⁸⁹

Other Aliphatic nitroxides are also explored, most of them have shown strong Ln^{III} -radical coupling, the results are shown in Table 1.5.

Table 1.5 Summary of magnetic exchange coupling constants (K) for aliphatic nitroxide radical-containing complexes.

Compound	$J_{\text{rad-Ln}}$ (K)	$J_{\text{rad-rad}}$ (K)	Ref
Gd(hfac) ₃ (2PyNO)(H ₂ O)	-6.9		90
Tb(hfac) ₃ (2PyNO)	AFM		89
Gd(hfac) ₃ (DTBN)(H ₂ O)	-5.8		91
Gd(hfac) ₃ (6bpyNO)	-5.6		92
Gd(hfac) ₃ (TMIO) ₂	-6.3	-27	93
[Gd(hfac) ₃ (MeOH)(TEMPO)]	-1.8		94
[Gd ₂ (hfac) ₆ (H ₂ O) ₂ (dppnTEMPO)]	3.9		88
[Tb ₂ (hfac) ₆ (H ₂ O) ₂ (dppnTEMPO)]	16.4		88
[Dy ₂ (hfac) ₆ (H ₂ O) ₂ (dppnTEMPO)]	2.4		88
Gd(hfac) ₃ (TEMPO) ₂	-6.5/4.0 ¹	49.8 / Y	36
	-10.0/7.5 ¹	15.0 / La	34
[Gd(hfac) ₃ (phNO)(H ₂ O)]	9		95
[Gd(hfac) ₃ (3tolNO)(H ₂ O)]	8.4		95
[Gd(hfac) ₃ (4tbphNO)(H ₂ O)]·0.25C ₇ H ₁₆	3.8		95

¹ $J_{\text{Gd1-Rad}}$ is different from $J_{\text{Gd2-Rad}}$.

Radical N₂³⁻ The most successful use of radical in Ln-radical compound is a N₂³⁻ bridged complex [K(18-crown-6)]{[(Me₃Si)₂N]₂(THF)Tb)₂(N₂)⁴⁰ which represents the best hard-

magnets among the SMMs. The N_2^{3-} radical ligand serves to bridge the Ln^{III} and gives the strongest magnetic coupling of $J = -27 \text{ cm}^{-1}$ between a Gd^{III} center and paramagnetic ligand observed for a gadolinium compound. For the Tb^{III} derivative, the strong ferromagnetic interaction successfully suppresses the majority of QT, reaching an energy barrier of 327 K and the largest blocking temperature of 13.9 K. In the compound of Dy^{III} , an effective relaxation barrier of $U_{\text{eff}} = 177 \text{ K}$ is obtained. Replacing the N_2^{3-} by non-magnetic N_2^{2-} dramatically cut down the energy barrier to only 25.9 K. The obvious difference indicates that the blocking originates from the concerted effect of the anisotropic Dy^{III} ground states and the strong magnetic coupling through the radical N_2^{3-} bridge. The results demonstrate that a joint contribution, combining strong magnetic coupling with single-ion anisotropy, may ultimately lead to higher relaxation barrier SMMs capable of retaining their magnetization at higher temperatures.

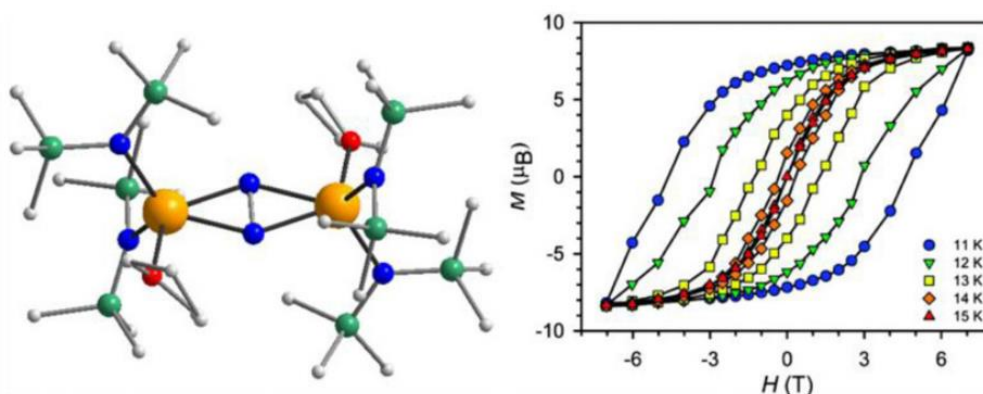


Figure 1.17 Molecular structure of N_2^{3-} -Dy₂ (left). Field dependence of the normalized magnetization for N_2^{3-} -Tb₂ (right).⁴⁰

1.4.3 Selected examples of light lanthanides-based SMMs (diamagnetic ligands)

Among the lanthanide series, light lanthanides elements have been the most used in hard magnetic materials such as in $SmCo_5$ and $Nd_2Fe_{14}B$.⁹⁶ However very few magnetic molecules have been reported with these elements, and even fewer show SMM behavior.. The main reason for this scarce use of light lanthanides is the difficulty to maximize their anisotropy under a given ligand field, because 1) they possess smaller amount of unpaired electrons and lower anisotropy relative than those of the heavier lanthanide analogues;⁹⁷ 2) they have larger ion radius than the heavier ones, and definitely larger coordination number (9 or 10), which increases the difficulty to reduce the equatorial ligand field.

Although being oblate ions like Dy^{III} , light lanthanide ions seem to be more finicky in choosing the appropriate environment geometry. For example, the typical square antiprism geometry (D_{4d} symmetry), which is demonstrated to be efficient with Dy^{III} ions by providing the axial crystal-field, is reported in only one Nd^{III} -based SMM.

In 2013, Hino *et al.*⁹⁶ have reported the first Ce-based SMMs, but the thematic still progresses sluggishly with few Ce-based complexes reported as SMMs.⁹⁸⁻¹⁰¹ There are a little bit more Nd-based SMMs were reported, and continue to enrich its family. To the best of our knowledge no SMM have been reported with Pr^{III} and Sm^{III}.¹⁰²

The first Ce-based SMM $[\text{Ce}^{\text{III}}\{\text{Zn}^{\text{II}}\text{I}(\text{L})\}_2(\text{MeOH})]\text{BPh}_4$ (Figure 1.18) was rationally designed as a linear CeZn_2 trinuclear structure, where Ce^{III} ion is sandwiched by two sets of two phenoxo oxygen donors in a $\{\text{Zn}(\text{L})\}$ moiety in the axial direction, other oxygen atoms of the two moieties and one ethanol molecule complete the equatorial plane.⁹⁶ The coordination geometry of Ce^{III} is a distorted spherical capped square antiprism, more close to a pseudo-pentagonal bipyramidal geometry, resulting in the enhancement of the anisotropy of Ce^{III} ion. The resulting stabilization of the largest m_J substates as the ground state, favor the slow relaxation in the absence of field. This is the only case of zero-field SMM constructed by Ce^{III} .

Consecutively, a similar strategy have been employed to yield a new field-induced SMM $[\text{Ce}(\text{NO}_3)\{\text{Zn}(\text{L})(\text{SCN})\}_2]\cdot\text{CH}_3\text{CN}$ (H_2L is a Schiff base ligand derived from *o*-vanillin and ethylenediamine) with $U_{\text{eff}} = 35.7(6)$ K and $\tau_0 = 2.2(3) \times 10^{-7}$ s (Figure 1.18).

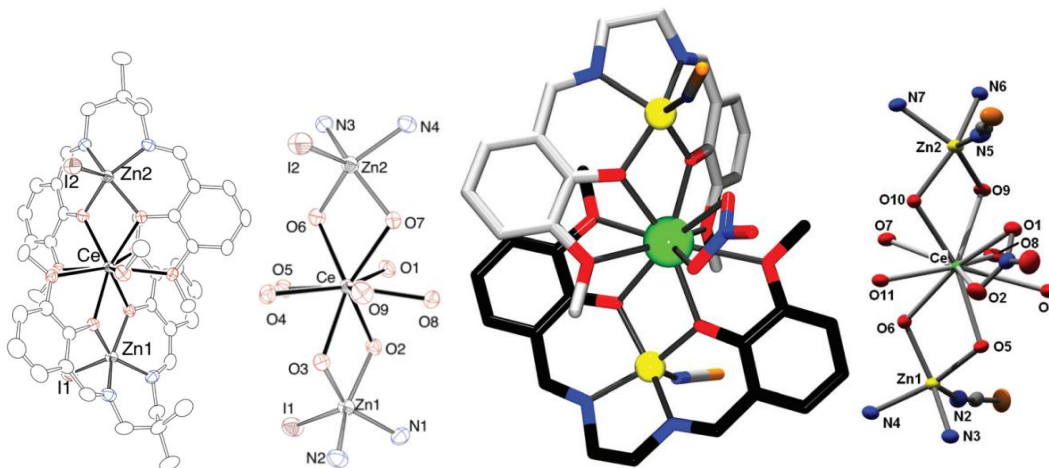


Figure 1.18 Representation of the structure of the molecular structure of $[\text{Ce}^{\text{III}}\{\text{Zn}^{\text{III}}(\text{L})\}_2(\text{MeOH})]\text{BPh}_4$ ⁹⁶ with magnetic skeleton (left) and $[\text{Ce}(\text{NO}_3)\{\text{Zn}(\text{L})(\text{SCN})\}_2]\cdot\text{CH}_3\text{CN}$ (right).¹⁰⁰

In the macrocyclic 18-crown-6 and 1,10-diaza-18-crown-6 ligated complex $[\text{Ln}(\text{NO}_3)_3(18\text{-crown-6})]$ ($\text{Ln} = \text{Ce}, \text{Pr}$ and Nd) and $[\text{Ln}(\text{NO}_3)_3(1,10\text{-diaza-18-crown-6})]$ ($\text{Ln} = \text{Ce}, \text{Pr}$ and Nd), the macrocyclic ligands occupy the equatorial positions and are slightly bent, with one and two chelating nitrate anions coordinating the Ce^{III} ion above and below, respectively. (fiure 1.17). The Ce^{III} ion is in a dodeca-coordination and is sandwiched by three negatively charged nitrate anions, which is preferable for Ising-type magnetic anisotropy of oblate-type lanthanide ions. Arrhenius analyses give the best fit parameters of $U_{\text{eff}} = 30.3(3)$ K, $\tau_0 = 2.20(17) \times 10^{-7}$ s for $\text{Ce}(\text{NO}_3)_3(18\text{-crown-6})$, $U_{\text{eff}} = 29.9(4)$ K and $\tau_0 = 2.9(4) \times 10^{-9}$ s for $\text{Nd}(\text{NO}_3)_3(18\text{-crown-6})$, $U_{\text{eff}} = 44(1)$ K and $\tau_0 = 2.3(5) \times 10^{-8}$ s for $[\text{Ce}(\text{NO}_3)_3(1,10\text{-diaza-18-crown-6})]$, and $U_{\text{eff}} = 69(1)$ K and $\tau_0 = 2.1(4) \times 10^{-10}$ s for $[\text{Nd}(\text{NO}_3)_3(1,10\text{-diaza-18-crown-6})]$ under dc field. Pr^{III} derivatives do not show maxima in the $\chi''(\text{T})$ plots.

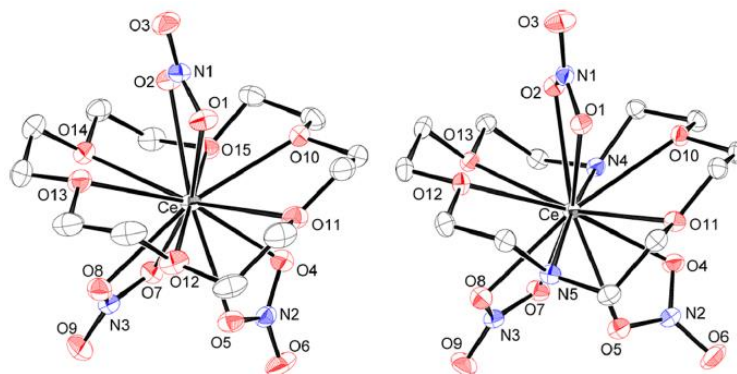


Figure 1.19 Representation molecular structure of $\text{Ce}(\text{NO}_3)_3(18\text{-crown-6})$ (left) and $[\text{Ce}(\text{NO}_3)_3(1,10\text{-diaz-18-crown-6})]$ (right).¹⁰¹

Our team recently reported the first SMM made of Ce^{III} and polyoxometalate. There are two crystallographic-independent Ce^{III} ions. Ce2 is isotropically surrounded by neutral DMSO molecules, precluding the SMM behavior from the electrostatic point of view. While, Ce1 is coordinated by oxygen atoms from two nitrate anions, four oxygen atoms from four DMSO molecules and one oxygen atom from $(\alpha\text{-Mo}_8\text{O}_{26})^{4-}$ anion. The strong axial ligand field of Ce1 induces SMM behavior in a very small dc field (200 Oe), $U_{\text{eff}}=24$ K and $\tau_0 = 2.5 \times 10^{-7}$ s.⁹⁹

Another nice example is a sandwich-type complex $\text{Li}(\text{DME})_3[\text{Ce}^{\text{III}}(\text{COT}^{\text{III}})_2]$ that displays an energy barrier of 30 K with a pre-exponential factor (τ_0) of 1.2×10^{-6} s.¹⁰⁹

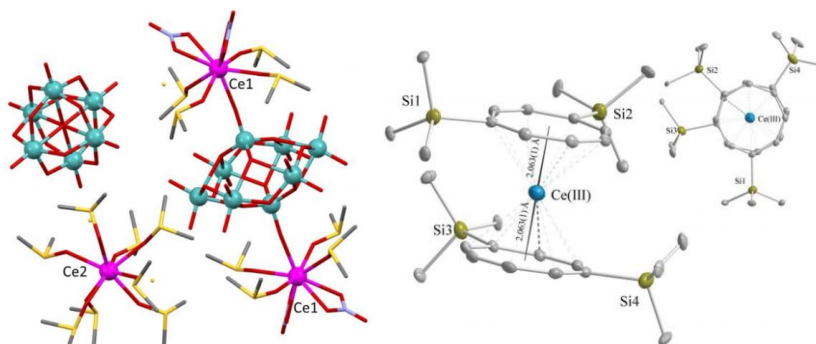


Figure 1.20 Representation of the structure of $[\text{Ce}(\text{dmsO})_8][\text{Ce}(\eta_2\text{-NO}_3)_2(\text{dmsO})_4(\alpha\text{-Mo}_8\text{O}_{26})_{0.5}][\text{Mo}_6\text{O}_{19}]$ ⁹⁹ (left) and $\text{Li}(\text{DME})_3[\text{Ce}^{\text{III}}(\text{COT}^{\text{III}})_2]$ (right).⁹⁸

S. K. Singh *et al.*¹⁰³ have conducted *ab initio* studies on Ce-based SMMs. As an oblate ion, the stronger axial and weaker equatorial ligation is likely to help build SMMs with larger U_{eff} values as stated earlier. According to the calculation, three models considering the coordination number (C.N) and geometries are favorable to construct the Ce-based SMMs. In the C.N = 2 model, the anisotropy is of pure Ising type, which causes stabilisation of $M_J = 5/2$ as the ground state. Moreover, all excited-state Kramer's doublets are collinear with the ground-state g_{zz} axis, leading to very large U_{calcd} values. For C.N = 5, square-pyramidal and trigonal bipyramidal (TBP) geometries were modeled and the TBP structure was found to be

superior because there are two axial ligands in the model. For $C.N = 7$ (pentagonal bipyramidal geometry), the presence of two axial ligands and unique C_5 axis leads to a significant barrier for reorientation of magnetization and collinearity among all g_z axes. Additionally, this structure yields only a small transverse anisotropy in the ground-state KD. Rational modulation of the ligand field to approach to these models will generate a high magnetic performance in combination with the Ce^{III} ion.

The first Nd-based SMM was reported in 2012, however, only a small value of energy barrier of 4.08 K under 100 Oe, was achieved. This value is far lower than those suggested by the electronic structure, which is calculated as 165 K. The large discrepancy is ascribed to intermolecular dipolar interactions, nuclear coupling, and mixing of low-lying excited states. The group of J. J. Baldov had augmented the value of energy barrier to 74 K under 1000 Oe. This is a new record for Nd-based SMM.¹⁰⁴

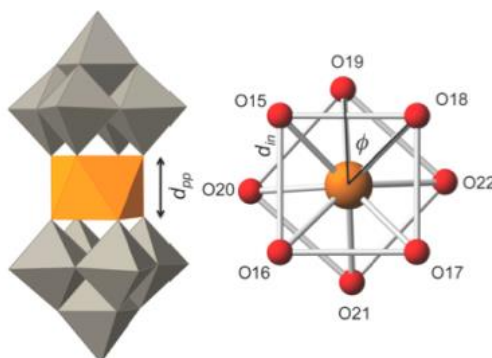


Figure 1.21 Representation of the structure of $[Nd(W_3O_{18})_2]^{9-}$ (left) and view of its square-antiprismatic coordination sphere (right).

In complex $[LNd(H_2O)_5]-[I]_3L(H_2O)$, (L= phosphonic diamide ligands) a high D_{5h} symmetry was achieved. Combination of a strong axial phosphonic diamide ligand field with a weak equatorial plane coordinating by water molecules leads to a SMM behavior in the absence of external field. From the electrostatic point of view, the water molecules induce a poor equatorial ligand field which corresponds to an hard plane of magnetization, while the easy axis is strengthened by the charge of O1 and O2. The zero-field anisotropy barriers are estimated to be 16.08 K and 24.69 K for fast and slow relaxation process respectively.

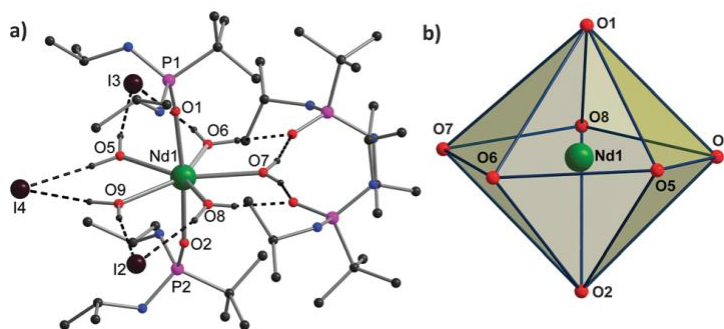


Figure 1.22 Representation of molecular structure (left) and Polyhedron (right) of $[LNd(H_2O)_5]^{1-}[I]_3L(H_2O)$ reported by Gupta, where L stands for phosphonic diamide ligands.¹⁰⁵

Table 1.6 Summary of the geometry of the ions in light lanthanide SMM.

Compound	Geometry	Shape factor	Reference
{[Nd(μ_2 -3,5-dinitrobenzoic acids) ₃ (H ₂ O) ₂] \cdot C ₂ H ₃ N _n }	Spherical capped square antiprism(Nd1)	1.359	106
	Spherical capped square antiprism(Nd2)	1.472	106
[Nd(μ_2 -2,4-dinitrobenzoic acids)(2,4-dinitrobenzoic acids) (CH ₃ COO)(H ₂ O) ₂] _n	Biaugmented trigonal prism	0.766	106
{[Nd ₂ (CNCH ₂ COO) ₆ (H ₂ O) ₄] \cdot 2H ₂ O} _n	Biaugmented trigonal prism(Nd1)	4.784	107
	Biaugmented trigonal prism(Nd2)	1.098	107
[Nd(W ₅ O ₁₈) ₂] ⁹⁻	Square antiprism	0.080	104
[Li(DME) ₃][Nd ^{III} (COT ^{'''}) ₂]	Double-decker		108
NdTp ₃ (Tp ⁻ = trispyrazolylborate)	Tricapped trigonal prism	0.905	109, 110
[phosphonic diamideNd(H ₂ O) ₅]-[I] ₃ phosphonic diamide (H ₂ O)	Pentagonal bipyramid	0.286	106
{[Ln(ant) _{1.5} (DMF) ₂] \cdot (DMF)} _n (H ₂ ant =9,10-anthracenedicarboxylic acid)	Spherical capped square antiprism	2.049	111
[Ce(dmsO) ₈][Ce(η_2 -NO ₃) ₂ (dmsO) ₄ (α -Mo ₈ O ₂₆) _{0.5}][Mo ₆ O ₁₉]	Spherical tricapped trigonal prism(Ce1)	2.042	99
	Biaugmented trigonal prism	0.920	99
[Ce ^{III} {Zn ^{II} I(L)} ₂ (MeOH)]BPh ₄	Spherical capped square antiprism	2.091	96
Li(DME) ₃ [Ce ^{III} (COT ^{'''}) ₂]	Double-decker		98
[Ln(NO ₃) ₃ {Zn(L)(SCN)} ₂](L=N,N'-bis-(3-methoxysalicylidene)ethylene-1,2-diamine)	Sphenocorona	4.245	100
Ce(NO ₃) ₃ (18-crown-6)	Augmented pentagonal prism	2.037	101
[Ce(NO ₃) ₃ (1,10-diaza-18-crown-6)]	Icosahedron	1.765	101

1.5 Objectives of current thesis

Since the first discovery of SMM, researchers have studied the structural-magneto relationship of 3d based SMMs, then 4f family, and established many models to explain the magnetic phenomena, but the origin of some of them remains still unclear. For example, the low-symmetry can also give rise to large energy barrier, which is contradicted with the commonly accepted high-symmetry strategy. Hence, more SMMs should be synthesized to enrich the data base so that we can build the more precise models systematically to predict the magnetic behaviors and enhance the magnetic properties.

In this work, we have two main objectives: seeking for the light lanthanide ions based SMM and studying the magnetic properties of a family of 4f-2p (TEMPO radicals) systematically. In addition, other interesting SMMs are reported for further understanding of

the magneto-structural relationship and the effect of $\text{Ln}^{\text{III}} - \text{Ln}^{\text{III}}$ exchange coupling on SMM behavior.

References

1. C. Huang, *John Wiley & Sons (Asia) Pte Ltd*, 2010.
2. D. G. Cristiano Benelli, *Wiley VCH*, 2015.
3. J. D. Rinehart and J. R. Long, *Chemical Science*, 2011, 2, 2078-2085.
4. Q. Zhou, *Synthesis and magnetic investigation of 3d-4f and 4f clusters*, 2012
5. R. Sessoli, H. L. Tsai, A. R. Schake, S. Wang, J. B. Vincent, K. Folting, D. Gatteschi, G. Christou and D. N. Hendrickson, *Journal of the American Chemical Society*, 1993, 115, 1804-1816.
6. S. T. Liddle and J. van Slageren, *Chemical Society Reviews*, 2015, 44, 6655-6669.
7. K. Katoh, R. Asano, A. Miura, Y. Horii, T. Morita, B. K. Breedlove and M. Yamashita, *Dalton Transactions*, 2014, 43, 7716-7725.
8. E. Lucaccini, L. Sorace, M. Perfetti, J.-P. Costes and R. Sessoli, *Chemical Communications*, 2014, 50, 1648-1651.
9. J. J. Baldoví, E. Coronado, A. Gaita-Ariño, C. Gamer, M. Giménez-Marqués and G. Mínguez Espallargas, *Chemistry – A European Journal*, 2014, 20, 10695-10702.
10. H. L. C. Feltham and S. Brooker, *Coordination Chemistry Reviews*, 2014, 276, 1-33.
11. M.-E. Boulon, G. Cucinotta, J. Luzon, C. Degl'Innocenti, M. Perfetti, K. Bernot, G. Calvez, A. Caneschi and R. Sessoli, *Angewandte Chemie*, 2013, 125, 368-372.
12. S.-D. Jiang, B.-W. Wang, G. Su, Z.-M. Wang and S. Gao, *Angewandte Chemie International Edition*, 2010, 49, 7448-7451.
13. Y. Bi, Y.-N. Guo, L. Zhao, Y. Guo, S.-Y. Lin, S.-D. Jiang, J. Tang, B.-W. Wang and S. Gao, *Chemistry – A European Journal*, 2011, 17, 12476-12481.
14. Y.-S. Ding, N. F. Chilton, R. E. P. Winpenny and Y.-Z. Zheng, *Angewandte Chemie International Edition*, 2016, DOI: 10.1002/anie.201609685, n/a-n/a.
15. M. Ren, S.-S. Bao, B.-W. Wang, R. A. S. Ferreira, L.-M. Zheng and L. D. Carlos, *Inorganic Chemistry Frontiers*, 2015, 2, 558-566.
16. X.-C. Huang, M. Zhang, D. Wu, D. Shao, X.-H. Zhao, W. Huang and X.-Y. Wang, *Dalton Transactions*, 2015, 44, 20834-20838.
17. P. Zhang, L. Zhang, C. Wang, S. Xue, S.-Y. Lin and J. Tang, *Journal of the American Chemical Society*, 2014, 136, 4484-4487.
18. Y.-Z. Tong, C. Gao, Q.-L. Wang, B.-W. Wang, S. Gao, P. Cheng and D.-Z. Liao, *Dalton Transactions*, 2015, 44, 9020-9026.
19. A. J. Brown, D. Pinkowicz, M. R. Saber and K. R. Dunbar, *Angewandte Chemie*, 2015, 127, 5962-5966.
20. S. Gómez-Coca, D. Aravena, R. Morales and E. Ruiz, *Coordination Chemistry Reviews*, 2015, 289-290, 379-392.
21. J. Liu, Y.-C. Chen, J.-L. Liu, V. Vieru, L. Ungur, J.-H. Jia, L. F. Chibotaru, Y. Lan, W. Wernsdorfer, S. Gao, X.-M. Chen and M.-L. Tong, *Journal of the American Chemical Society*, 2016, 138, 5441-5450.
22. V. E. Campbell, H. Bolvin, E. Rivière, R. Guillot, W. Wernsdorfer and T. Mallah, *Inorganic Chemistry*, 2014, 53, 2598-2605.
23. J. Long, F. Habib, P.-H. Lin, I. Korobkov, G. Enright, L. Ungur, W. Wernsdorfer, L. F. Chibotaru and M. Murugesu, *Journal of the American Chemical Society*, 2011, 133, 5319-5328.
24. K. Liu, X. Zhang, X. Meng, W. Shi, P. Cheng and A. K. Powell, *Chemical Society Reviews*, 2016, 45, 2423-2439.
25. F. Habib, P.-H. Lin, J. Long, I. Korobkov, W. Wernsdorfer and M. Murugesu, *Journal of the American Chemical Society*, 2011, 133, 8830-8833.

26. N. Ishikawa, M. Sugita and W. Wernsdorfer, *Journal of the American Chemical Society*, 2005, 127, 3650-3651.
27. K. R. Meihaus, J. D. Rinehart and J. R. Long, *Inorganic Chemistry*, 2011, 50, 8484-8489.
28. F. Pointillart, K. Bernot, S. Golhen, B. Le Guennic, T. Guizouarn, L. Ouahab and O. Cador, *Angewandte Chemie International Edition*, 2015, 54, 1504-1507.
29. R. C. Claude Coulon, Wolfgang Wernsdorfer, Thierry Colin, and Hitoshi Miyasaka, *PHYSICAL REVIEW LETTERS*, 2009, 102, 167204.
30. E. Bartolome, J. Bartolome, S. Melnic, D. Prodius, S. Shova, A. Arauzo, J. Luzon, F. Luis and C. Turta, *Dalton Transactions*, 2013, 42, 10153-10171.
31. R. Liu, Y. Ma, P. Yang, X. Song, G. Xu, J. Tang, L. Li, D. Liao and S. Yan, *Dalton Transactions*, 2010, 39, 3321-3325.
32. R. S. D. Gatteschi, J. Villain, , *Oxford University Press, Oxford*, , 2006.
33. Y.-N. Guo, G.-F. Xu, W. Wernsdorfer, L. Ungur, Y. Guo, J. Tang, H.-J. Zhang, L. F. Chibotaru and A. K. Powell, *Journal of the American Chemical Society*, 2011, 133, 11948-11951.
34. F. Tuna, C. A. Smith, M. Bodensteiner, L. Ungur, L. F. Chibotaru, E. J. L. McInnes, R. E. P. Winpenny, D. Collison and R. A. Layfield, *Angewandte Chemie International Edition*, 2012, 51, 6976-6980.
35. J. Xiong, H.-Y. Ding, Y.-S. Meng, C. Gao, X.-J. Zhang, Z.-S. Meng, Y.-Q. Zhang, W. Shi, B.-W. Wang and S. Gao, *Chemical Science*, 2017, DOI: 10.1039/C6SC03621J.
36. R. Murakami, T. Nakamura and T. Ishida, *Dalton Transactions*, 2014, 43, 5893-5898.
37. N. Ishikawa, M. Sugita, T. Ishikawa, S.-y. Koshihara and Y. Kaizu, *Journal of the American Chemical Society*, 2003, 125, 8694-8695.
38. N. Ishikawa, M. Sugita, N. Tanaka, T. Ishikawa, S.-y. Koshihara and Y. Kaizu, *Inorganic Chemistry*, 2004, 43, 5498-5500.
39. L. Ungur and L. F. Chibotaru, *Physical Chemistry Chemical Physics*, 2011, 13, 20086-20090.
40. J. D. Rinehart, M. Fang, W. J. Evans and J. R. Long, *Journal of the American Chemical Society*, 2011, 133, 14236-14239.
41. S.-D. Jiang, B.-W. Wang, H.-L. Sun, Z.-M. Wang and S. Gao, *Journal of the American Chemical Society*, 2011, 133, 4730-4733.
42. K. R. Meihaus and J. R. Long, *Journal of the American Chemical Society*, 2013, 135, 17952-17957.
43. J. J. Le Roy, I. Korobkov and M. Murugesu, *Chemical Communications*, 2014, 50, 1602-1604.
44. J. J. Le Roy, L. Ungur, I. Korobkov, L. F. Chibotaru and M. Murugesu, *Journal of the American Chemical Society*, 2014, 136, 8003-8010.
45. M. A. Aldamen, S. Cardona-Serra, J. M. Clemente-Juan, E. Coronado, A. Gaita-Ariño, C. Martí-Gastaldo, F. Luis and O. Montero, *Inorganic Chemistry*, 2009, 48, 3467-3479.
46. X. Yi, K. Bernot, V. Le Corre, G. Calvez, F. Pointillart, O. Cador, B. Le Guennic, J. Jung, O. Maury, V. Placide, Y. Guyot, T. Roisnel, C. Daiguebonne and O. Guillou, *Chemistry – A European Journal*, 2014, 20, 1569-1576.
47. P.-H. Lin, W.-B. Sun, Y.-M. Tian, P.-F. Yan, L. Ungur, L. F. Chibotaru and M. Murugesu, *Dalton Transactions*, 2012, 41, 12349-12352.
48. K. S. Pedersen, J. Dreiser, H. Weihe, R. Sibille, H. V. Johannesen, M. A. Sørensen, B. E. Nielsen, M. Sigrist, H. Mutka, S. Rols, J. Bendix and S. Piligkos, *Inorganic Chemistry*, 2015, 54, 7600-7606.
49. F. Pointillart, B. L. Guennic, S. Golhen, O. Cador, O. Maury and L. Ouahab, *Chemical Communications*, 2013, 49, 615-617.
50. T.-Q. Liu, P.-F. Yan, F. Luan, Y.-X. Li, J.-W. Sun, C. Chen, F. Yang, H. Chen, X.-Y. Zou and G.-M. Li, *Inorganic Chemistry*, 2015, 54, 221-228.
51. R. J. Blagg, F. Tuna, E. J. L. McInnes and R. E. P. Winpenny, *Chemical Communications*, 2011, 47, 10587-10589.
52. S. Cardona-Serra, J. M. Clemente-Juan, E. Coronado, A. Gaita-Ariño, A. Camón, M. Evangelisti, F. Luis, M. J. Martínez-Pérez and J. Sesé, *Journal of the American Chemical Society*, 2012, 134, 14982-14990.

53. Y.-S. Meng, Y.-S. Qiao, Y.-Q. Zhang, S.-D. Jiang, Z.-S. Meng, B.-W. Wang, Z.-M. Wang and S. Gao, *Chemistry – A European Journal*, 2016, 22, 4704-4708.
54. C. Benelli, A. Caneschi, D. Gatteschi, J. Laugier and P. Rey, *Angewandte Chemie International Edition in English*, 1987, 26, 913-915.
55. G. Poneti, K. Bernot, L. Bogani, A. Caneschi, R. Sessoli, W. Wernsdorfer and D. Gatteschi, *Chemical Communications*, 2007, DOI: 10.1039/B617898G, 1807-1809.
56. C.-F. Hsu, S.-H. Lin and H.-H. Wei, *Inorganic Chemistry Communications*, 2005, 8, 1128-1132.
57. M. L. Kahn, R. Ballou, P. Porcher, O. Kahn† and J.-P. Sutter, *Chemistry – A European Journal*, 2002, 8, 525-531.
58. J.-P. Sutter, M. L. Kahn and O. Kahn, *Advanced Materials*, 1999, 11, 863-865.
59. C. Benelli, A. Caneschi, D. Gatteschi and R. Sessoli, *Journal of Applied Physics*, 1993, 73, 5333-5337.
60. K. Bernot, L. Bogani, R. Sessoli and D. Gatteschi, *Inorganica Chimica Acta*, 2007, 360, 3807-3812.
61. J. D. Rinehart, M. Fang, W. J. Evans and J. R. Long, *Nat Chem*, 2011, 3, 538-542.
62. C. Benelli, A. Caneschi, D. Gatteschi, L. Pardi, P. Rey, D. P. Shum and R. L. Carlin, *Inorganic Chemistry*, 1989, 28, 272-275.
63. C. Benelli, A. Caneschi, D. Gatteschi and L. Pardi, *Inorganic Chemistry*, 1992, 31, 741-746.
64. F.-X. Du, P. Hu, Y.-Y. Gao, F.-P. Xiao and Y.-N. Wu, *Inorganic Chemistry Communications*, 2014, 48, 166-170.
65. K. Bernot, J. Luzon, L. Bogani, M. Etienne, C. Sangregorio, M. Shanmugam, A. Caneschi, R. Sessoli and D. Gatteschi, *Journal of the American Chemical Society*, 2009, 131, 5573-5579.
66. P. Hu, X. Wang, Y. Ma, Q. Wang, L. Li and D. Liao, *Dalton Transactions*, 2014, 43, 2234-2243.
67. X. Wang, X. Bao, P. Xu and L. Li, *European Journal of Inorganic Chemistry*, 2011, 2011, 3586-3591.
68. L. Li, S. Liu, H. Li, W. Shi and P. Cheng, *Chemical Communications*, 2015, 51, 10933-10936.
69. E. Coronado, C. Giménez-Saiz, A. Recuenco, A. Tarazón, F. M. Romero, A. Camón and F. Luis, *Inorganic Chemistry*, 2011, 50, 7370-7372.
70. J. Wang, M. Zhu, C. Li, J. Zhang and L. Li, *European Journal of Inorganic Chemistry*, 2015, 2015, 1368-1375.
71. R. Liu, L. Li, X. Wang, P. Yang, C. Wang, D. Liao and J.-P. Sutter, *Chemical Communications*, 2010, 46, 2566-2568.
72. N. Zhou, Y. Ma, C. Wang, G. Feng Xu, J.-K. Tang, J.-X. Xu, S.-P. Yan, P. Cheng, L.-C. Li and D.-Z. Liao, *Dalton Transactions*, 2009, DOI: 10.1039/B908639K, 8489-8492.
73. J.-X. Xu, Y. Ma, D.-z. Liao, G.-F. Xu, J. Tang, C. Wang, N. Zhou, S.-P. Yan, P. Cheng and L.-C. Li, *Inorganic Chemistry*, 2009, 48, 8890-8896.
74. A. Lannes, M. Intissar, Y. Suffren, C. Reber and D. Luneau, *Inorganic Chemistry*, 2014, 53, 9548-9560.
75. X.-L. Mei, R.-N. Liu, C. Wang, P.-P. Yang, L.-C. Li and D.-Z. Liao, *Dalton Transactions*, 2012, 41, 2904-2909.
76. F. Pointillart, K. Bernot, G. Poneti and R. Sessoli, *Inorganic Chemistry*, 2012, 51, 12218-12229.
77. X.-L. Mei, Y. Ma, L.-C. Li and D.-Z. Liao, *Dalton Transactions*, 2012, 41, 505-511.
78. H. Tian, R. Liu, X. Wang, P. Yang, Z. Li, L. Li and D. Liao, *European Journal of Inorganic Chemistry*, 2009, 2009, 4498-4502.
79. X.-L. Wang, L.-C. Li and D.-Z. Liao, *Inorganic Chemistry*, 2010, 49, 4735-4737.
80. P. Hu, M. Zhu, X. Mei, H. Tian, Y. Ma, L. Li and D. Liao, *Dalton Transactions*, 2012, 41, 14651-14656.
81. K. Bernot, F. Pointillart, P. Rosa, M. Etienne, R. Sessoli and D. Gatteschi, *Chemical Communications*, 2010, 46, 6458-6460.
82. R. Liu, C. Zhang, L. Li, D. Liao and J.-P. Sutter, *Dalton Transactions*, 2012, 41, 12139-12144.

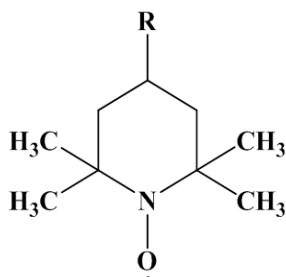
83. O. H. Griffith, D. W. Cornell and H. M. McConnell, *The Journal of Chemical Physics*, 1965, 43, 2909-2910.
84. A. Okazawa, Y. Nagaichi, T. Nogami and T. Ishida, *Inorganic Chemistry*, 2008, 47, 8859-8868.
85. A. Okazawa, R. Watanabe, H. Nojiri, T. Nogami and T. Ishida, *Polyhedron*, 2009, 28, 1808-1813.
86. J. Goldman, T. E. Petersen, K. Torssell and J. Becher, *Tetrahedron*, 1973, 29, 3833-3843.
87. E. F. Ullman, J. H. Osiecki, D. G. B. Boocock and R. Darcy, *Journal of the American Chemical Society*, 1972, 94, 7049-7059.
88. S. G. Reis, M. Briganti, S. Soriano, G. P. Guedes, S. Calancea, C. Tiseanu, M. A. Novak, M. A. del Águila-Sánchez, F. Totti, F. Lopez-Ortiz, M. Andruh and M. G. F. Vaz, *Inorganic Chemistry*, 2016, 55, 11676-11684.
89. R. Murakami, T. Ishida, S. Yoshii and H. Nojiri, *Dalton Transactions*, 2013, 42, 13968-13973.
90. T. Ishida, R. Murakami, T. Kanetomo and H. Nojiri, *Polyhedron*, 2013, 66, 183-187.
91. T. Kanetomo and T. Ishida, *Chemical Communications*, 2014, 50, 2529-2531.
92. T. Kanetomo and T. Ishida, *Inorganic Chemistry*, 2014, 53, 10794-10796.
93. T. Nakamura and T. Ishida, *Polyhedron*, 2015, 87, 302-306.
94. T. Nakamura and T. Ishida, *AIP Conference Proceedings*, 2016, 1709, 020016.
95. T. Kanetomo, T. Yoshitake and T. Ishida, *Inorganic Chemistry*, 2016, 55, 8140-8146.
96. S. Hino, M. Maeda, K. Yamashita, Y. Kataoka, M. Nakano, T. Yamamura, H. Nojiri, M. Kofu, O. Yamamuro and T. Kajiwara, *Dalton Transactions*, 2013, 42, 2683-2686.
97. S. K. Gupta, T. Rajeshkumar, G. Rajaraman and R. Murugavel, *Chemical Communications*, 2016, DOI: 10.1039/C6CC03066A.
98. J. J. Le Roy, I. Korobkov, J. E. Kim, E. J. Schelter and M. Murugesu, *Dalton Transactions*, 2014, 43, 2737-2740.
99. A. B. Khelifa, M. S. Belkhiria, G. Huang, S. Freslon, O. Guillou and K. Bernot, *Dalton Transactions*, 2015, 44, 16458-16464.
100. C. Takehara, P. L. Then, Y. Kataoka, M. Nakano, T. Yamamura and T. Kajiwara, *Dalton Transactions*, 2015, 44, 18276-18283.
101. H. Wada, S. Ooka, T. Yamamura and T. Kajiwara, *Inorganic Chemistry*, 2016, DOI: 10.1021/acs.inorgchem.6b01764.
102. F. Pointillart, O. Cador, B. Le Guennic and L. Ouahab, *Coordination Chemistry Reviews*, DOI: <http://dx.doi.org/10.1016/j.ccr.2016.12.017>.
103. S. K. Singh, T. Gupta, L. Ungur and G. Rajaraman, *Chemistry – A European Journal*, 2015, 21, 13812-13819.
104. J. J. Baldoví, J. M. Clemente-Juan, E. Coronado, Y. Duan, A. Gaita-Ariño and C. Giménez-Saiz, *Inorganic Chemistry*, 2014, 53, 9976-9980.
105. S. K. Gupta, T. Rajeshkumar, G. Rajaraman and R. Murugavel, *Chemical Communications*, 2016, 52, 7168-7171.
106. A. K. Jassal, N. Aliaga-Alcalde, M. Corbella, D. Aravena, E. Ruiz and G. Hundal, *Dalton Transactions*, 2015, 44, 15774-15778.
107. A. Arauzo, A. Lazarescu, S. Shova, E. Bartolome, R. Cases, J. Luzon, J. Bartolome and C. Turta, *Dalton Transactions*, 2014, 43, 12342-12356.
108. J. J. Le Roy, S. I. Gorelsky, I. Korobkov and M. Murugesu, *Organometallics*, 2015, 34, 1415-1418.
109. J. D. Rinehart and J. R. Long, *Dalton Transactions*, 2012, 41, 13572-13574.
110. C. Apostolidis, J. Rebizant, B. Kanellakopulos, R. von Ammon, E. Dornberger, J. Müller, B. Powietzka and B. Nuber, *Polyhedron*, 1997, 16, 1057-1068.
111. A. J. Calahorra, I. Oyarzabal, B. Fernandez, J. M. Seco, T. Tian, D. Fairen-Jimenez, E. Colacio and A. Rodriguez-Dieguez, *Dalton Transactions*, 2016, 45, 591-598.

2 (TEMPO-R)-4f based zero dimensional complexes: synthesis and magnetic properties

2.1 Introduction

As described in chapter 1, a wide variety of 4f-2p heterospin systems have been reported so far. Among them, aliphatic nitroxides show high coupling constants specially when combined with 4f ions. The most representative ligand of this family is the TEMPO (2,2,6,6-tetramethylpiperidin-1-oxyl).

Surprisingly, and to the best of our knowledge, only two examples of 4f-TEMPO system has ever been reported. Murakami *et al.*¹ has published a Ln-TEMPO₂ family of compound where the Gd^{III} analogue exhibit strong magnetic exchange and the Er^{III} analogue² is the first pure 4f-Tempo SMM. Successively, two isostructural SMMs with a modified TEMPO ligand, [Ln₂(hfac)₆(H₂O)₂(dppnTEMPO)] (Ln=Dy and Tb),³ also show SMM behavior.



Scheme 2.1 Schematic representation of TEMPO-R radical.

The first part of our study of 4f-based TEMPO compounds aims to investigate the nature and strength of the 4f-radical interaction and the possible occurrence of SMM behavior in 4f-TEMPO based compounds.

To do so, we first focus our work on TEMPO radicals that host a non-coordinating R group in para position of the N-oxide group (work with coordinating R groups will be reported in chapter 3). The expected zero-dimensional compound should be easier to investigate for the first step of this study.

The variation over the different R groups is also expected to lead to different organization of the 4f-(TEMPO-R) entities in the crystal packing and to afford structural diversity to our study.

With this in mind, we selected four TEMPO-R radicals (scheme 2.2):

-R= O-CH₃, as in 4-Methoxy-TEMPO (abbreviated TEMPO-OMe)

-R= NH₂, as in 4-Amino-TEMPO (abbreviated TEMPO-NH₂)

-R= NHCOCH₃, as in 4-Acetamido-TEMPO (abbreviated TEMPO-Acetamido)

-R= OCH₂CCH, as in 2,2,6,6-Tetramethyl-4-(2-propynyloxy)piperidine 1-Oxyl (abbreviated TEMPO-OCH₂CCH).

We have obtained crystalline materials for 11 compounds with formula:

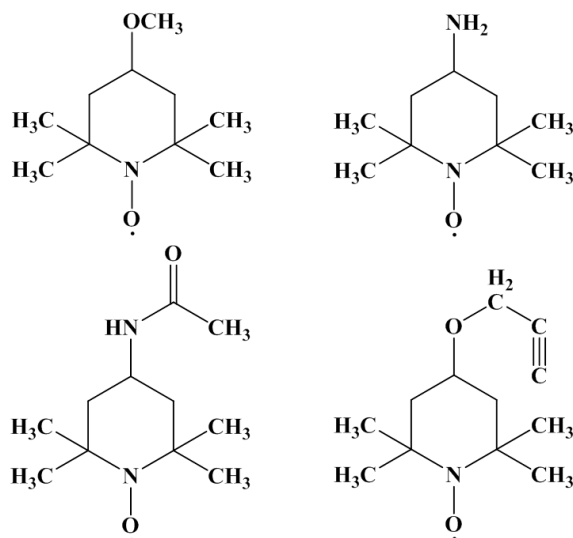
-{[(Ln(hfac)₃)(TEMPO-OCH₃)(H₂O)]₂·TEMPO-OCH₃} (Ln=Ce(**1**), Pr(**2**), Nd(**3**), Gd(**4**), Dy(**5**))

-{[Ln(hfac)₃(H₂O)]₂(TEMPO-NH₂)₂} (Ln = Dy(**6**), Gd(**7**))

- [Ln(hfac)₃(TEMPO-Acetamido)₂] (Ln= Dy(**8**))

- and [Ln(hfac)₃(TEMPO-OCH₂CCH)(H₂O)] (Ln = Dy(**9**), Tb(**10**), Gd(**11**)).

Their structural analysis and magnetic properties are reported in this chapter.



Scheme 2.2 Schematic representation of the different radicals used in this chapter: TEMPO-OMe (top left), TEMPO-NH₂ (top right), TEMPO- Acetamido (bottom left) and TEMPO-OCH₂CCH (bottom right).

2.2 SMM behavior on light lanthanides derivatives in: {[Ln(hfac)₃](TEMPO-OMe)(H₂O)]₂·TEMPO-OMe} (Ln=Ce(**1**), Pr(**2**), Nd(**3**), Gd(**4**), Dy(**5**))

2.2.1 Structural description

Crystal structure investigation of this family of derivatives has been performed on **1**. The main structural information is listed in Table 2.1. The isostructurality of the other derivatives have been assessed on the basis of their X-ray powder diffraction patterns and compared with simulated result of **1** as depicted in Figure A2.1.

Complex **1** crystallizes in P2₁/n space group. The asymmetric unit is made of two Ce(hfac)₃(TEMPO-OMe)H₂O entities and one uncoordinated radical lying between them (see Figure 2.1). Each Ce^{III} ion is then directly linked to a NO group of a TEMPO radical. The uncoordinated radical is interacting through H-bonds with two different Ce(hfac)₃(TEMPO-OMe)H₂O moieties. Overall, a penta-spin unit is formed (Figure 2.1).

Each Ce^{III} ion is coordinated by six oxygen atoms that arise from three hfac⁻ anions, one oxygen atom from the NO group of a radical and one coordinated water molecule. The Ce-O bond lengths are in the range of 2.42(5) to 2.49(5) Å, this is slightly longer than the Dy-O

bond lengths, reported in the literature.^{4, 5} Additional bonds and angles are listed in Table A2.1.

The geometry of the lanthanide ions could be treated by continuous shape measurement (CSM) which assesses quantitatively the degree of deviation to a regular symmetry indicating by a factor.⁶⁻⁸ The coordination polyhedron of each Ce^{III} ion is close to a triangular dodecahedron (D_{2d} symmetry) with slight differences between of Ce1 and Ce2 centers (CSM factors are 0.437 and 0.564, respectively). The shortest Ce-Ce inter-molecular distance is 10.71(1) Å.

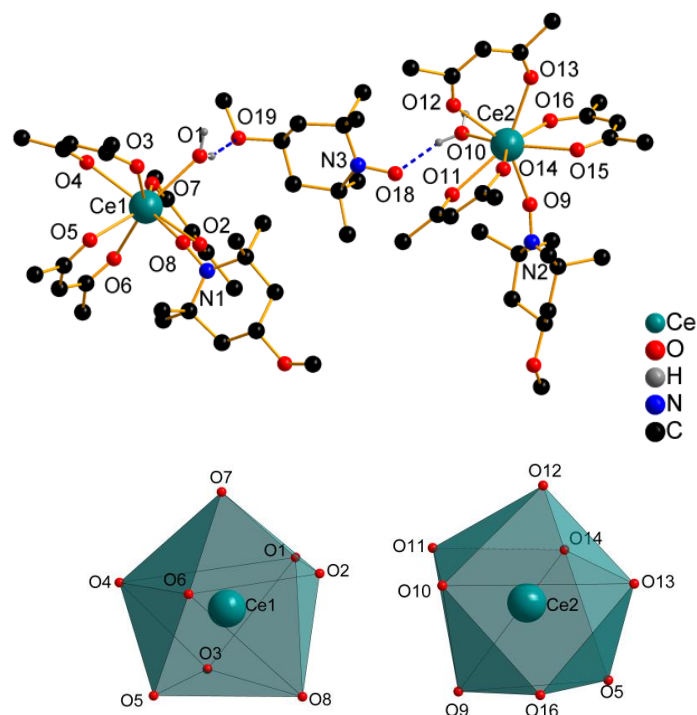


Figure 2.1 Representation of the asymmetric unit of Ce(1) (top) and coordination polyhedra of the two Ce^{III} ion (bottom). Fluorine and part of hydrogen atoms are omitted for clarity.

Table 2.1 Main crystallographic parameters for **1**.

Formula	C ₆₀ H ₄₀ Ce ₂ F ₃₆ N ₃ O ₂₀
M[g.mol ⁻¹]	2117.43
Crystal system	Monoclinic
Space group	P 21/n
a(Å)	9.70985(5)
b(Å)	44.0196(18)
c(Å)	20.3879(8)
α[°]	90
β[°]	102.454(2)
γ[°]	90
V[Å ³]	8509.2(7)
Z	4
T(K)	150(2)
2θ range	2.03-27.490
Reflns collected	62871
Independent reflns	19407
Observed reflns	16555
Parameters	1109
R1/ωR ²	0.0838/0.2399
Goof	1.058

2.2.2 Static magnetic properties

Static magnetic measurement has been carried out on polycrystalline powders of **1**, **2**, **3**, **4** and **5**.

$\{[(Ce(hfac)_3)(TEMPO-OMe)(H_2O)]_2 \cdot TEMPO-OMe\}$ (**1**)

The room temperature value of the $\chi_M T$ product for **1** is 2.58 cm³.K.mol⁻¹, which is close to the theoretical value of $\chi_M T_{300K} = 2.725$ cm³.K.mol⁻¹ considering three radical spin centers and two isolated Ce^{III} ion ($J = 5/2$, $g = 6/7$ and $\chi_M T_{300K} = 0.8$ cm³.K.mol⁻¹) at the non-interacting limit (see Figure 2.2).

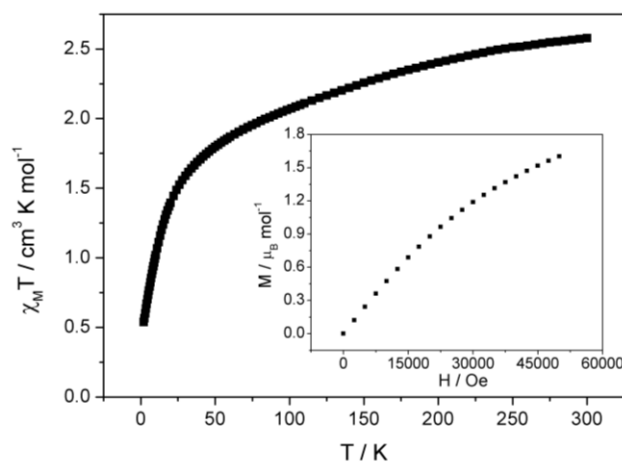


Figure 2.2 Temperature dependence of the $\chi_M T$ product for Ce(**1**). The inset shows the magnetization curve measured at 2.0 K.

The $\chi_M T$ product decreases gradually upon cooling to around with a more abrupt drop below 40 K and reaches a minimum of $0.51 \text{ cm}^3 \cdot \text{K} \cdot \text{mol}^{-1}$ at 2 K. The overall trend of the curve is expected to be a consequence of the progressive depopulation of the Stark sub-levels⁹ and a possible Ce^{III} -radical interaction. The magnetization at 2 K is shown in the inset of Figure 2.2.

{[Pr(hfac)₃(TEMPO-OCH₃)(H₂O)]₂·TEMPO-OCH₃} (2)

The room temperature value of the $\chi_M T$ product for **2** is $4.24 \text{ cm}^3 \cdot \text{K} \cdot \text{mol}^{-1}$, which is close to the expected value of $\chi_M T_{300\text{K}} = 4.325 \text{ cm}^3 \cdot \text{K} \cdot \text{mol}^{-1}$ considering three radical spin centers and two non-interacting Pr^{III} ion ($J = 4$, $g = 4/5$ and $\chi_M T_{300\text{K}} = 1.6 \text{ cm}^3 \cdot \text{K} \cdot \text{mol}^{-1}$) at the non-interacting limit (see Figure 2.3). The $\chi_M T$ product decreases gradually upon cooling and reaches a minimum of $1.18 \text{ cm}^3 \cdot \text{K} \cdot \text{mol}^{-1}$ at 2 K for the same reason as for **1**. The experimental magnetization is shown in the inset of Figure 2.3.

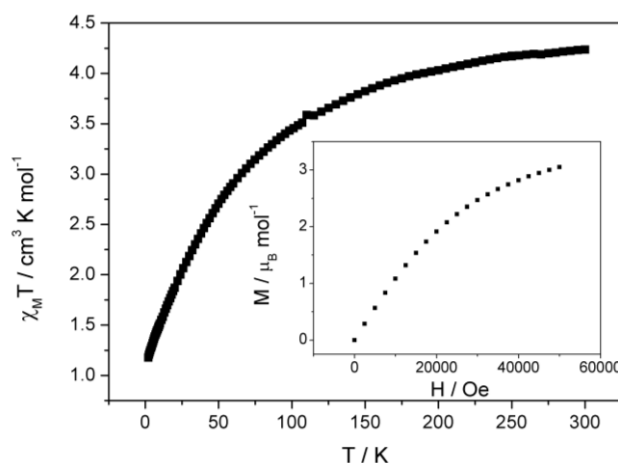


Figure 2.3 Temperature dependence of the $\chi_M T$ product for Pr(2). The inset shows the magnetization curve measured at 2.0 K.

{[Nd(hfac)₃(TEMPO-OCH₃)(H₂O)]₂·TEMPO-OCH₃} (3)

The room temperature value of the $\chi_M T$ product for **3** is $4.34 \text{ cm}^3 \cdot \text{K} \cdot \text{mol}^{-1}$, which is close to the theoretical value of $\chi_M T_{300\text{K}} = 4.405 \text{ cm}^3 \cdot \text{K} \cdot \text{mol}^{-1}$ considering three radical spin centers and two non-interacting Nd^{III} ions ($J = 9/2$, $g = 8/11$ and $\chi_M T_{300\text{K}} = 1.64 \text{ cm}^3 \cdot \text{K} \cdot \text{mol}^{-1}$) at the non-interacting limit (see Figure 2.4). The $\chi_M T$ product decreases gradually upon cooling and reaches a minimum of $0.61 \text{ cm}^3 \cdot \text{K} \cdot \text{mol}^{-1}$ at 2K for same reason as for **1**. The experimental magnetization is shown in the inset of Figure 2.4.

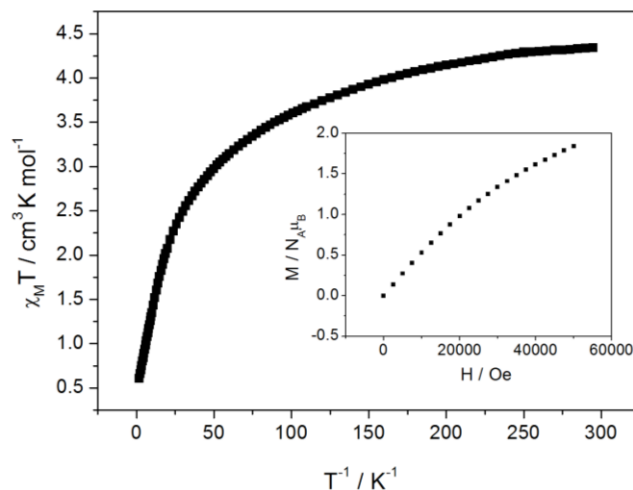


Figure 2.4 Temperature dependence of the $\chi_M T$ product for Nd(3). The inset shows the magnetization curve measured at 2.0 K.

$\{[(Gd(hfac)_3)(TEMPO-OMe)(H_2O)]_2 \cdot TEMPO-OMe\}$ (4)

The room temperature value of the $\chi_M T$ product for **4** is $16.84 \text{ cm}^3 \cdot \text{K} \cdot \text{mol}^{-1}$, which is close to the theoretical value of $\chi_M T_{300\text{K}} = 16.885 \text{ cm}^3 \cdot \text{K} \cdot \text{mol}^{-1}$ considering three radical spin centers and two non-interacting Gd^{III} ions ($J = 7/2$, $g = 2$ and $\chi_M T_{300\text{K}} = 7.88 \text{ cm}^3 \cdot \text{K} \cdot \text{mol}^{-1}$) (see Figure 2.5). The $\chi_M T$ product decreases gradually upon cooling and reaches a minimum of $14.86 \text{ cm}^3 \cdot \text{K} \cdot \text{mol}^{-1}$ at 13 K and then increases abruptly to reach $15.76 \text{ cm}^3 \cdot \text{K} \cdot \text{mol}^{-1}$ at 2 K. The magnetization curve is recorded at 2 K in the inset of Figure 2.5 and the value reaches $15.2 \mu_B$ at 5 T, far to the expected saturation magnetization value of $17 \mu_B$ for a fully ferromagnetically coupled system.

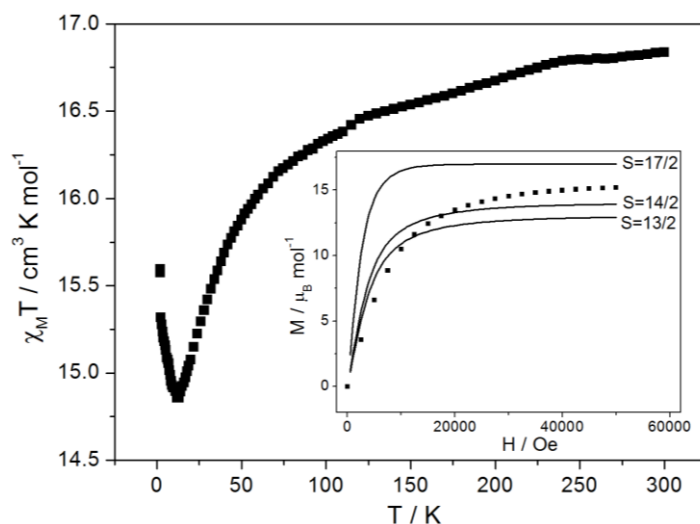


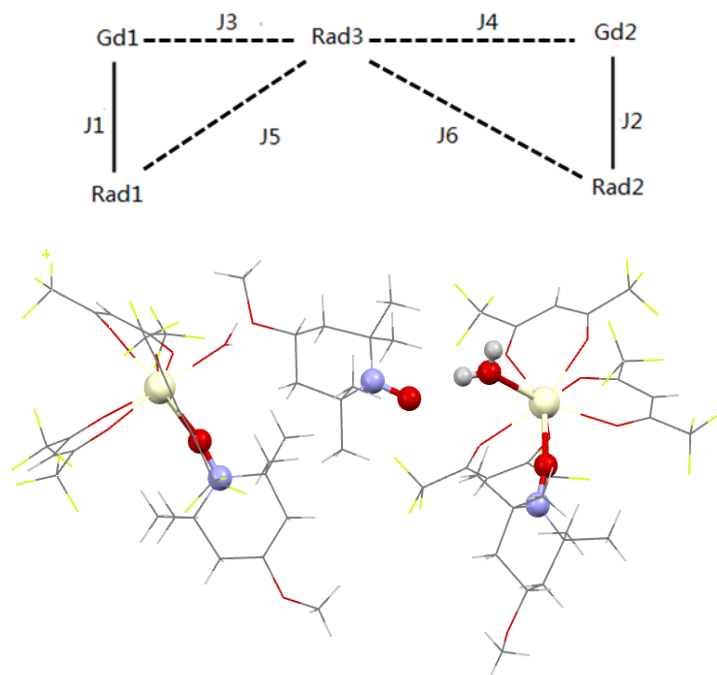
Figure 2.5 Temperature dependence of the $\chi_M T$ product for Gd(4). The inset shows the magnetization curve measured at 2.0 K with Simulated Brillouin curve with $S = 17/2$ (full ferro-), $14/2$ (J_1 ferro-, J_2 antiferro-), $13/2$ (J_1 antiferro-, J_2 antiferro- and J_4 ferromagnetic).

Several competing interactions are then expected in this system (scheme 2.3). Two strong interactions (J1 and J2) may occur between the Gd^{III} ions that are directly connected to the NO group of the TEMPO ligand. Additional but weaker interactions can take place between the free TEMPO ligand and the Gd^{III} ions (J3 and J4) or its coordinated TEMPO (J5 and J6). The overall spin picture of the system is quite complex but the topologic arrangement of the different moieties let suspect extremely weak contributions of J3, J5 and J6. We have thus two possible phenomenological schemes:

-the intramolecular interactions J1 and J2 are strongly antiferromagnetic and intermolecular interaction J4 is ferromagnetic. This can be supported by a relatively short NO...Gd^{III} distance (4.61Å), mediated by a strong H bond (NO...H=1.84 Å)

-J4 is negligible and the slight differences in the coordination geometry and bonding of the two Gd^{III} ions with the TEMPO radical may be enough to change the sign and magnitude of J1 and J2 as seen on nitronyle-nitroxide radicals for example (NO-Gd1=2.42Å, NOGd1=151.1° and NO-Gd2=2.43Å, NOGd2=156.2°).¹⁰

Unfortunately, at this stage of the study we have not been able to distinguish between the two hypotheses (simulation with Brillouin curve do not provide additional evidences).



Scheme 2.3 Exchange coupling scheme (top) and possible interaction pathway (bottom).

[(Dy(hfac)₃)(TEMPO-OMe)(H₂O)]₂·TEMPO-OMe (**5**)

The room temperature value of the $\chi_M T$ product for **5** is 29.25 cm³.K.mol⁻¹, which is lower than the theoretical value of $\chi_M T_{300K}=29.47$ cm³.K.mol⁻¹ for three radical spin centers and two non-interacting Dy^{III} ions ($J = 15/2$, $g = 4/3$ and $\chi_M T_{300K}=14.17$ cm³.K.mol⁻¹) at the non-interacting limit (Figure 2.6). The $\chi_M T$ product decreases gradually upon cooling and reaches

a minimum of $20.07 \text{ cm}^3 \cdot \text{K} \cdot \text{mol}^{-1}$ at 2 K, for the same reason as in Ce(1). The magnetization vs field measurement is reported in the inset of Figure 2.6.

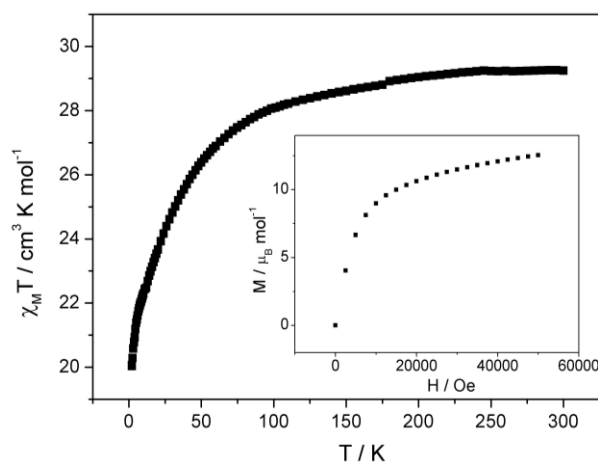


Figure 2.6 Temperature dependence of the $\chi_M T$ product of compound Dy(5). The inset shows the magnetization curve measured at 2.0 K.

2.2.3 Dynamic magnetic properties

Alternating current (ac) magnetic susceptibility data were collected for Ce(1), Pr(2), Nd(3) and Dy(5). None of the compounds show magnetic slow relaxation in zero-field. However, as a field is applied, the degeneracy of ground state sub-levels is removed and magnetic slow relaxation is promoted. This is due to the suppression of quantum tunneling relaxation processes, a common feature on Ln-based magnetic molecules.¹¹⁻¹³ The ac measurements at constant temperature (2 K) and variable field are presented in appendix A2. Among all samples, 1, 2 and 3 corresponding to the Ce^{III}, Pr^{III} and Nd^{III} derivatives depict in-field magnetic relaxation, whereas 5 (the Dy^{III} derivative) does not. The fields at which the slowest relaxation is observed are 800, 3600, 3600 Oe, respectively.

This is a quite remarkable feature as Dy^{III} derivatives are commonly the most likely to show magnetic slow relaxation. Lanthanide's magnetic relaxation is mainly due to the electrostatic environment generated around the ion.¹⁴⁻¹⁸ However in the present case the coordination of the TEMPO radical with the lanthanide significantly affect the electronic scheme of the molecule. Hence, its relaxation cannot be rationalized with the classic oblate/prolate description⁹ (all Ce^{III}, Pr^{III}, Nd^{III} and Dy^{III} are oblate ions) and Ln-radical magnetic coupling generates a new magnetic object with its own electrostatic and magnetic features.^{19, 20}

$\{[(\text{Ce}(\text{hfac})_3)(\text{TEMPO-OMe})(\text{H}_2\text{O})]_2 \cdot \text{TEMPO-OMe}\}$ (1)

For compound Ce(1), the intensities of χ' and χ'' measured with a 800 Oe field are comparable to the few existing previous reports on Ce^{III}-based SMMs.²¹⁻²³

The distribution of the relaxation times is obtained by plotting the Cole-Cole curves normalized over χ_T . The parameter of α (represents the distribution of relaxation times, when

α is close to 0, it indicates a single relaxation process; when α is close to 1, it implies a behavior of spin glass) is almost constant at 0.07, which indicates a nearly perfect single relaxation process. The non-relaxation fraction (χ_S/χ_T) of the sample is about 37%, a standard value on Ln-Based SMMs.^{24, 25} Although the coordination polyhedrons of two Ln^{III} ions are slightly different, they do not cause any clear distortion of the semi-circles. This means the local ligand field does not lead to different energies scheme for the two Ce^{III} ion.

This, together with the similar CSM values, indicates that even if Ce1 and Ce2 are crystallographically different, these centers are quite similar on the magnetic point of view. Discussion about the magnetic slow relaxation of Ce(1) is detailed in section 2.2.4.

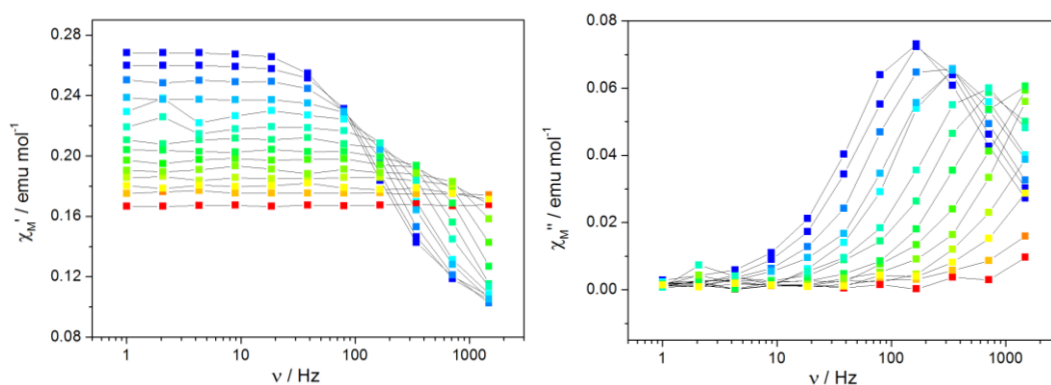


Figure 2.7 Frequency dependence of in-phase (left) and out-of-phase (right) ac susceptibilities under 800 Oe dc field for Ce(1). Temperatures range from 1.8 K (blue) to 3.5 K (red). Temperature plots of these data are available in Figure.A2.5. Lines are guides to the eye.

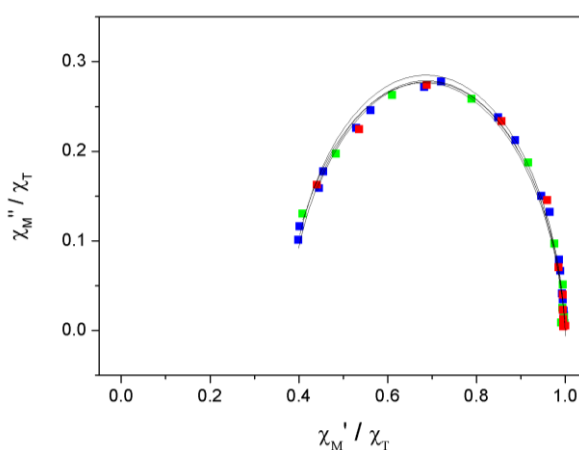


Figure 2.8 Normalized Cole-Cole plot for complex Ce(1) under 800 Oe dc field for some selected temperatures. Color mapping from 1.8 K (blue) to 2.1 K (red). Lines represent the best fits as calculated with an extended Debye model.

$\{[(Pr(hfac)_3)(TEMPO-OMe)(H_2O)]_2 \cdot TEMPO-OMe\} (2)$

Ac frequency-dependent signals have been observed for quite high dc field (3600Oe) and in the same temperature ranges as for Ce(1). This is a rare example of a Pr^{III}-based magnetic

molecule that presents magnetic slow relaxation. This is also one of the few examples where Ce^{III} derivative relax slowly.²⁶⁻²⁸

The maximum α value is 0.267 (at 1.8 K), much higher than that of Ce(1), suggesting a moderate distribution times. However the non-relaxing fraction of the sample is smaller with χ_s/χ_T that ranges from 0.23 at 1.8 K to 0.34 at 2.2 K. Discussion about the magnetic slow relaxation of Pr(2) is detailed in section 2.2.4.

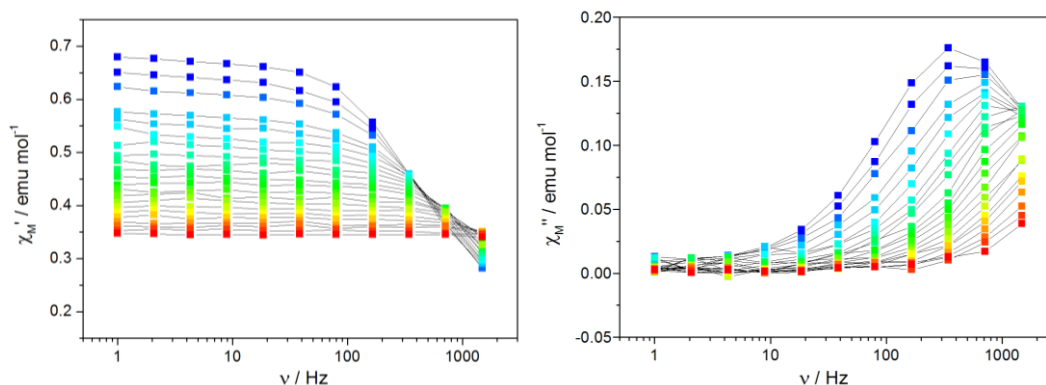


Figure 2.9 Frequency dependence of in-phase (left) and out-of-phase (right) ac susceptibilities under 3600 Oe dc field for Pr(2). Temperatures range from 1.8 K (blue) to 4 K (red). Temperature plots of these data are available in Figure.A2.6. Lines are guides to the eye.

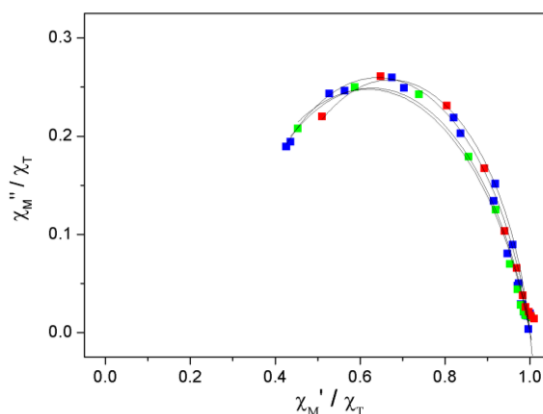


Figure 2.10 Normalized Cole-Cole plot for some selected temperatures for complex Pr(2) under 3600 Oe dc field. Color mapping from 1.8 K (blue) to 2.2 K (red). Lines represent the best fits as calculated with an extended Debye model.

$\{[(\text{Nd}(\text{hfac})_3)(\text{TEMPO-OMe})(\text{H}_2\text{O})]_2 \cdot \text{TEMPO-OMe}\}$ (3)

As for **2**, a quite strong dc field (3600 Oe) is needed to observed magnetic slow relaxation on **3**. The temperature window at which the relaxation is observed is slightly wider (1.8-5 K) and the α values are smaller (around 0.2). A comparable amount of non-relaxing fraction χ_s/χ_T is found. Discussion about the magnetic slow relaxation is detailed in section 2.2.4.

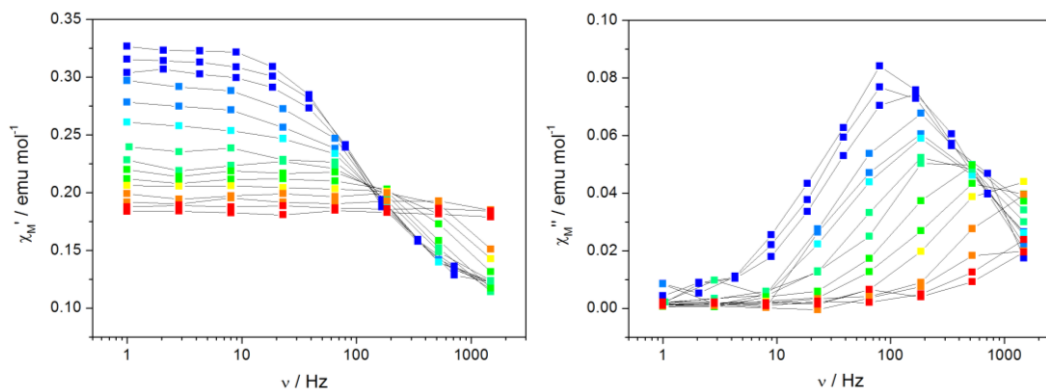


Figure 2.11 Frequency dependence of in-phase (left) and out-of-phase (right) ac susceptibilities under 3600 Oe dc field for Nd(3). Temperatures range from 1.8 K (blue) to 5 K (red). Temperature plots of these data are available in Figure.A2.7. Lines are guides to the eye.

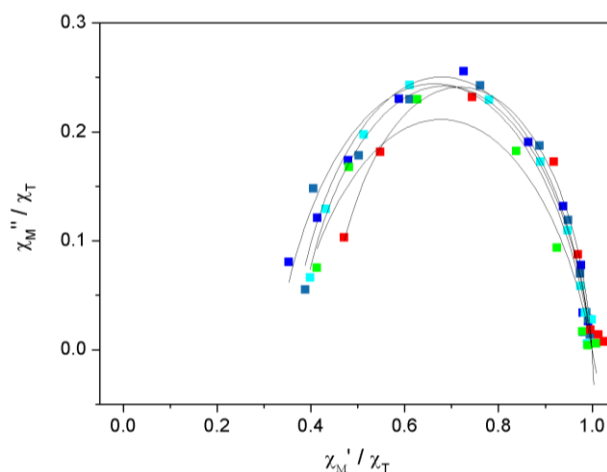


Figure 2.12 Normalized Cole-Cole plot for Nd(3) under 3600 Oe dc field for some selected temperatures. Color mapping from 1.8 K (blue) to 2.75 K (red). Lines represent the best fits as calculated with an extended Debye model.

2.2.4 Determination of energy barrier and other dynamic parameters

The extracted relaxation times (τ) are plotted as a function of T^{-1} for Ce(1), Pr(2) and Nd(3) and depicted in Figure 2.13. Tentative fits of the plots have been made considering that only the Orbach process is operating. Fitting by the fifth term of equation (1.5) (see chapter 1) gives the energy barrier of 9.46 ± 0.63 K (1), 6.3 ± 0.61 K (2) and 6.0 ± 0.72 K (3), with the pre-exponential factor of 4.08×10^{-6} s (1), 1.24×10^{-5} s (2), and 6.77×10^{-5} s (3), respectively. These energy barrier values are small indicating a small energy difference between the ground state and the first excited state.²⁹

$$\tau^{-1} = A_1 H^4 T + A_2 H^2 T + \frac{B_1}{1 + B_2 H^2} + CT^n + \tau_0^{-1} \exp(-U_{\text{eff}}/kT) \quad (\text{equ. 1.5})$$

However, the high τ_0 let suspect possible Raman (fourth term) or thermally independent processes (first three terms).

Whereas attempts to fit the curves of Ce(1) and Pr(2) considering these additional terms were not successful, a good fit has been obtained for Nd(3). This provides the values of $C = 2.14 \pm 0.19 \times 10^{-2} \text{ s}^{-1} \text{ K}^{-9}$, $n = 9$, $U_{\text{eff}} = 3.05 \pm 0.33 \text{ K}$ and $\tau_0 = 2.70 \pm 0.44 \times 10^{-4} \text{ s}$ ($R^2 = 0.999$).

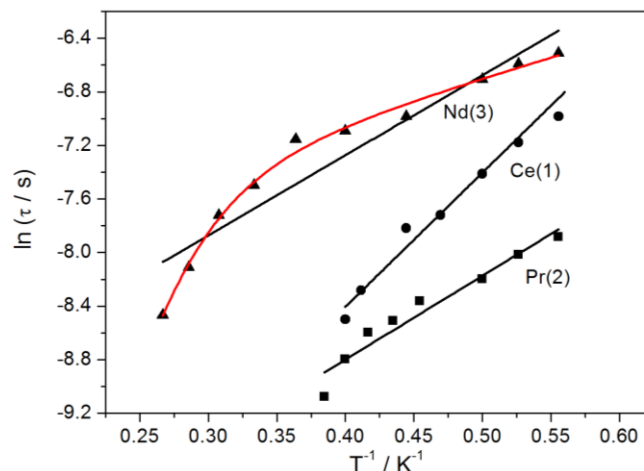


Figure 2.13 Relaxation times (τ) plotted against T^{-1} for Ce(1) (circles), Pr(2) (squares) and Nd(3) (triangles). The black lines represent the fit with only Orbach process, while the red line represents the fit with direct and Orbach processes.

2.2.5 Conclusion

In conclusion, reaction of $\text{Ln}(\text{hfac})_3$ with the TEMPO-OMe radical, affords as expected, zero-dimensional compounds where the lanthanide is coupled to the radical. However, the presence of one uncoordinated radical and two crystallographically Ln-radical moieties in the asymmetric unit makes more complex the magnetic picture. Indeed combined AF and F magnetic couplings have been observed on Gd(4). Interestingly, the light-lanthanide derivatives made of Ce^{III} (1), Nd^{III} (2) and Pr^{III} (3) all display SMM behavior whereas Dy^{III} (5) does not. This may be a consequence of interplay between the electrostatic environment around the Ln^{III} ion and the Ln-radical magnetic interaction.

2.3 μ_2 -H₂O bridged dimer: $\{[\text{Dy}(\text{hfac})_3(\text{H}_2\text{O})]_2(\text{TEMPO-NH}_2)_2\}$ (6)

2.3.1 Structural description

The reaction of $\text{Ln}(\text{hfac})_3 \cdot 2\text{H}_2\text{O}$ with TEMPO-NH₂ affords an unexpected lanthanide dimer. In fact, the hfac^- ancillary ligand provides to the $\text{Ln}(\text{hfac})_3$ building block a Lewis acid character. The lanthanide is then more likely to coordinate to electron-donor groups. However, in TEMPO-NH₂ the non-aromaticity of the TEMPO ring avoid an electronic delocalization. The NH₂ group cannot acts as a donor and its hydrogen atoms are then likely to be involved in hydrogen bonding as this is the case here.

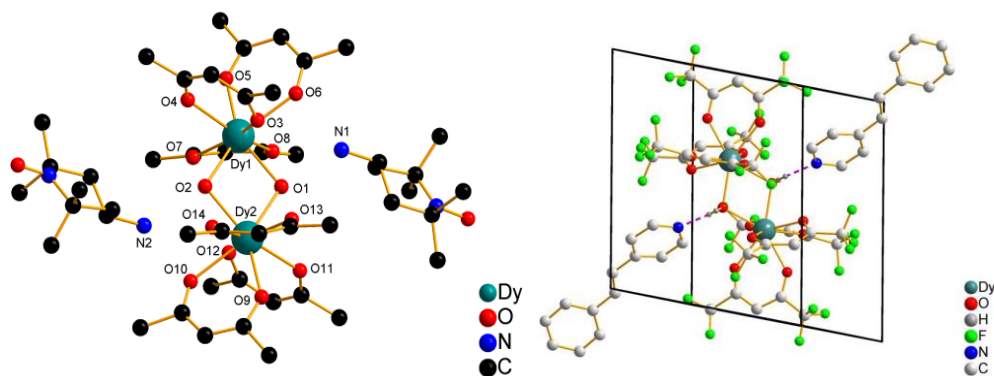


Figure 2.14 Representation of the asymmetric unit of **6** with fluorine and hydrogen atoms omitted for clarity (left). Representation of Dy(Stilbene) used for comparison (right).³⁰

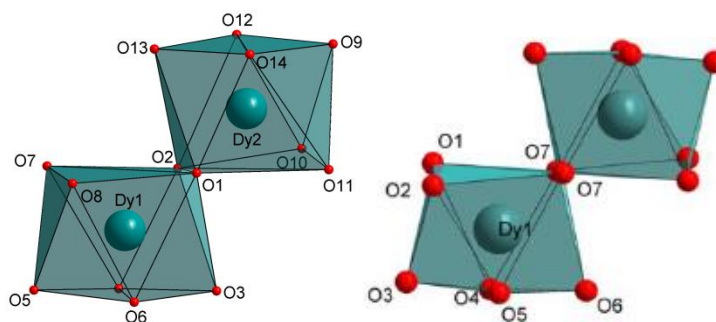


Figure 2.15 Coordination polyhedra of the two Dy^{III} ions of **6** (left). Representation of Dy(Stilbene) used for comparison (right).

The compound crystallizes in the $P2_1/c$ space group. The main structural information is listed in Table 2.2. The asymmetric unit is made of two Dy^{III} ions and two uncoordinated TEMPO-NH₂ radicals. Each Dy^{III} ion is coordinated by eight oxygen atoms: six from three hfac⁻ ancillary ligands and two others (O1 and O2) that connect the neighboring Dy^{III} atom in μ_2 mode. The neutrality of the overall molecule let suspect that these oxygen atoms belong to water molecules. However, no Q-peaks expected for the H atoms have been found and these latter have been refined on calculated positions. This motif is close to the one observed in a previous work from our team (named Dy(Stilbene)) (see Figure 2.14).³⁰

The Dy-O bond lengths are in the 2.30(3)-2.43(3) Å range. The Dy1-O1-Dy2 and Dy1-O2-Dy2 angles are 107.75(12)° and 107.60(12)°, respectively. The Dy1-Dy2 distance is 3.72(7) Å (see details in Table A2.8). All these distances are highly similar to the one observed in Dy(Stilbene). The two uncoordinated radicals ligands lies in between the dimers with the NO-groups that host the radical that are not directed toward the dimer but are interacting with the H atoms of the NH₂ group of a neighboring radical. This produces a chain-like arrangement of the radicals along the “a” direction. The coordination polyhedron of each Dy^{III} ions are estimated by using SHAPE software. The result suggests a very slightly distorted square antiprism (D_{4d} site symmetry) with the CSM = 0.617 and 0.814.

The isostructurality of the Gd derivative has been assessed on the basis of its X-ray powder diffraction patterns and compared with simulated result of Dy(**6**) as depicted in Figure A2.9.

Table 2.2 Main crystallographic parameters for Dy(**6**).

Formula	C ₄₈ H ₄₄ Dy ₂ F ₃₆ N ₄ O ₁₆
M[g.mol ⁻¹]	1941.87
Crystal system	monoclinic
Space group	P 21/c
a(Å)	11.780 (3)
b(Å)	26.797 (6)
c(Å)	23.720 (4)
α[°]	90
β[°]	90.794 (1)
γ[°]	90
V[Å ³]	7487.2 (3)
Z	4
T(K)	150(2)
2θ range	2.03-27.507
Reflns collected	33047
Independent reflns	17173
Observed reflns	13408
Parameters	1031
R1/ωR ²	0.0392/0.1310
Goof	1.067

2.3.2 Static magnetic properties

***{[Dy(hfac)₃(H₂O)]₂(TEMPO-NH₂)₂}* (**6**)**

At room temperature the value of $\chi_M T$ for Dy(**6**) is 28.69 cm³.K.mol⁻¹, in agreement with the expected value (29.09 cm³.K.mol⁻¹) for two uncoupled Dy^{III} ions (⁶H_{15/2}, $g = 4/3$) and two organic radicals ($S = 1/2$), as depicted in Figure 2.16. When the temperature is lowered, the value of $\chi_M T$ decreases quickly to reach a minimum around 20 K. It is then followed by a sudden increase upon further cooling. This increase is significantly smaller than the one observed on Dy(Stilbene) where single-crystal magnetic measurements and fitting with Stevens operators techniques give $J_{\text{eff}} = 2.26 \text{ cm}^{-1}$ considering an effective spin $1/2$ for the Dy^{III} ion. In our case the interaction is thus expected to be smaller than this value; however no reliable estimation has been possible up to date. The magnetization value of Dy(**6**) reaches 11.79 μ_B at 50 kOe far from a complete saturation of the magnetization of the system (22 μ_B) (inset of Figure 2.16).

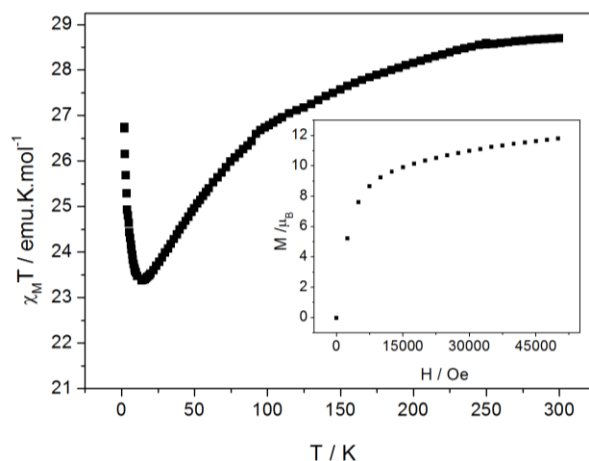


Figure 2.16 Temperature dependence of the $\chi_M T$ product for Dy(6). The inset shows the magnetization curve measured at 2.0 K.

$\{[Gd(hfac)_3(H_2O)]_2(TEMPO-NH_2)_2\}$ (7)

At room temperature the value of $\chi_M T$ for Gd(7) is $16.49 \text{ cm}^3 \cdot \text{K} \cdot \text{mol}^{-1}$, in agreement with the expected value ($16.51 \text{ cm}^3 \cdot \text{K} \cdot \text{mol}^{-1}$) for two uncoupled Gd^{III} ions ($^8S_{7/2}$, $g = 2$) and two organic radicals ($S = 1/2$), as depicted in Figure 2.17. When the temperature is lowered, the value of $\chi_M T$ keeps constant until 25 K, followed by a quick drop to reach $12.06 \text{ cm}^3 \cdot \text{K} \cdot \text{mol}^{-1}$. The magnetization value of **6** reaches $12.99 \mu_B$ at 40 kOe, lower than a complete saturation of the magnetization of the system ($16 \mu_B$) (inset of Figure 2.17).

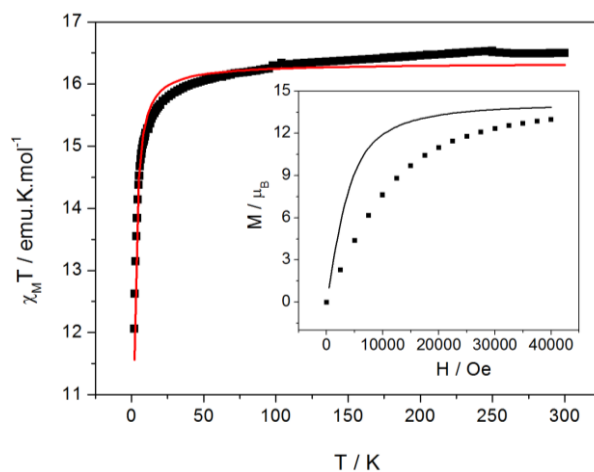


Figure 2.17 Temperature dependence of the $\chi_M T$ product for Gd(7). The red solid line represents the best fit. The inset shows the magnetization curve measured at 2.0 K and the Brillouin function for two non-interacting Gd^{III} ions.

The Gd-Gd interaction can be fitted using the following equation:³¹

$$\chi_M T = \frac{N_A \mu_B^2 g^2}{k_B} \times \frac{6e^x + 30e^{3x} + 84e^{6x} + 180e^{10x} + 330e^{15x} + 546e^{21x} + 840e^{28x}}{1 + 3e^x + 5e^{3x} + 7e^{6x} + 9e^{10x} + 11e^{15x} + 13e^{21x} + 15e^{28x}} \quad (\text{equ 2.1})$$

With $\chi = J_{\text{exch}}/T$, where N_A is the Avogadro constant, μ_B the Bohr magneton, g the Landé factor, k_B the Boltzmann constant, T the absolute temperature and J_{exch} the exchange constant. For compound **7**, $J_{\text{exch}} = -0.11 \pm 0.01 \text{ cm}^{-1}$ and $g = 1.871 \pm 0.001$, $R^2 = 0.974$.

2.3.3 Dynamic magnetic properties

To examine the spin dynamics of Dy(**6**), alternating current (ac) measurements were carried out at various fields and optimum dc field for the ac measurement is estimated to be between 800 and 1200 Oe (Figure 2.18). The field dependence of the magnetic slow relaxation is much more sensitive on Dy(**6**) than on the previous samples of this chapter.

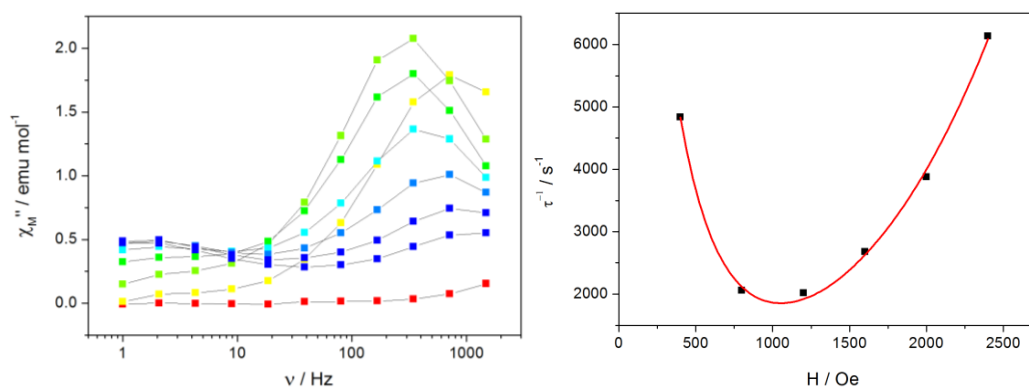


Figure 2.18 Frequency dependence of the out-of-phase components of the magnetization for various dc fields for Dy(**6**). Color mapping from 0 Oe (red) to 2400 Oe (blue) with 400 Oe step (left). Field dependence of the extracted values of τ^{-1} (right).

For $H_{\text{dc}} = 800$ Oe, magnetic slow relaxation is observed between 1.8 K and 5 K (Figure 2.19). The distribution of the relaxation times is moderate with $\alpha_{\text{max}} = 0.27$ for $T = 1.9$ K (Figure 2.20 and Table A2.10) but the relaxing fraction of the sample fluctuates around 60% ($\chi_s/\chi_T = 0.4$ at 1.8 K and $\chi_s/\chi_T = 0.47$ at 4.4 K).

Compound Dy(**6**) is also measured in a different field (2400 Oe) with a totally different SMM behavior. Specifically a set of dual peaks are observable. Consequently we can exclude pure ‘‘Raman+Orbach’’ process as those ones are field-independent.

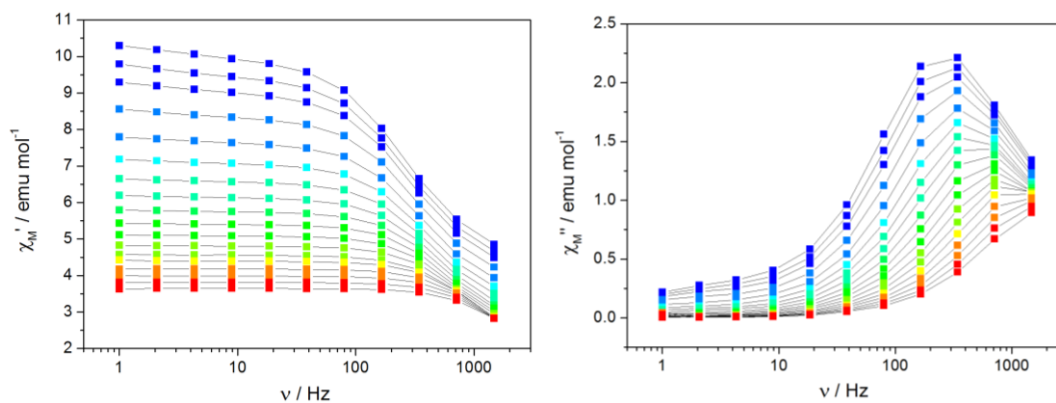


Figure 2.19 Frequency dependence of the in-phase (left) and out-of-phase (right) components of ac susceptibility for **6** under 800 Oe dc field. Color mapping from 1.8 K (blue) to 4 K (red). Temperatures range from 1.8K (blue) to 5 K (red). Temperature plots of these data are available in Figure.A2.10. Lines are guides to the eye.

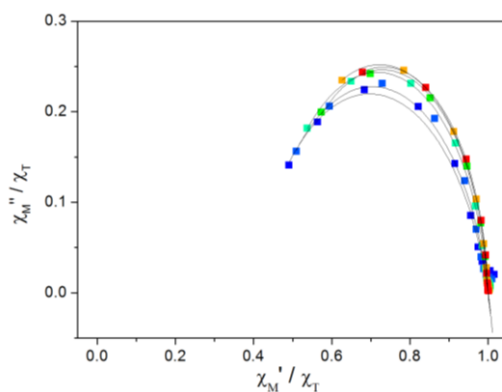


Figure 2.20 Normalized Cole-Cole diagram in selected temperatures in the 1.8-4 K temperature range for Dy(**6**). Lines represent the best fits as calculated with an extended Debye model.

Firstly, we can fit the τ^{-1} vs H curve (Figure 2.18) to estimate the parameters of the first three terms. The best fit gives: $A1 = 2.69 \pm 0.81 \times 10^{-11} \text{ s}^{-1} \text{ K}^{-1} \text{ Oe}^{-4}$, $A2 = 3.56 \pm 0.43 \times 10^{-4} \text{ s}^{-1} \text{ K}^{-1} \text{ Oe}^{-2}$, $B1 = (126.17 \pm 30.98) \times 10^2 \text{ s}^{-1}$, $B2 = 1.05 \pm 0.40 \times 10^{-5} \text{ Oe}^{-2}$ ($R^2 = 0.999$). Then the obtained parameters are fixed during the fitting of the τ^{-1} vs T^{-1} curve to determine the other parameters. This provides the $C = 3.47 \pm 0.54 \times 10^{-3} \text{ s}^{-1} \text{ K}^{-9}$, $n = 9$, $U_{\text{eff}} = 8.70 \pm 0.25 \text{ K}$, $\tau_0 = 4.03 \pm 0.39 \times 10^{-5} \text{ s}$ ($R^2 = 0.999$).

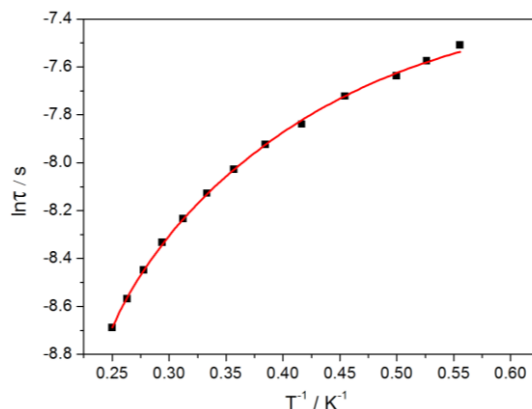


Figure 2.21 Relaxation times $\ln(\tau)$ plotted against T^{-1} for Dy(**6**). Lines represent best fitted curves.

2.3.4 Conclusion

In conclusion, the reaction of $\text{Ln}(\text{hfac})_3 \cdot 2\text{H}_2\text{O}$ with the TEMPO-NH₂ radical afford a crystalline material only if Ln=Gd or Dy. It do not lead to a Ln-radical compound but to a Ln^{III} dimer. If Ln=Gd^{III} an antiferromagnetic interaction is observed ($J=-0.11\text{cm}^{-1}$). If Ln=Dy^{III} a ferromagnetic interaction is observed as well as SMM behavior. The magnetic slow relaxation is found to be a mix of several different relaxing processes.

2.4 [Ln(hfac)₃(TEMPO-acetamido)₂ (Ln = Dy(8))

2.4.1 Structural description

The reaction of $\text{Ln}(\text{hfac})_3 \cdot 2\text{H}_2\text{O}$ with TEMPO-acetamido affords a trimer with general formula Radical-Ln-radical. Single-crystal X-ray diffraction reveals that the compound Dy(8) crystallizes in the Pbc_a space group with $Z = 8$. The main structural parameters are listed in Table 2.3

Table 2.3 Main crystallographic parameters for Dy(8).

Formula	$\text{C}_{39} \text{H}_{47} \text{Cl}_6 \text{Dy} \text{F}_{18} \text{N}_4 \text{O}_{10}$
$M[\text{g} \cdot \text{mol}^{-1}]$	1449.01
Crystal system	orthorhombic
Space group	Pbc _a
$a(\text{Å})$	17.6083 (7)
$b(\text{Å})$	24.3710 (12)
$c(\text{Å})$	26.6822 (12)
$\alpha[^\circ]$	90
$\beta[^\circ]$	90
$\gamma[^\circ]$	90
$V[\text{Å}^3]$	11450.2 (2)
Z	8
T(K)	150
2θ range	2.03-27.504
Reflns collected	9870
Independent reflns	13025
Observed reflns	10614
Parameters	723
$R1/\omega R^2$	0.0521/0.1535
Goof	1.033

The asymmetric unit is made of one Dy^{III} ion coordinated by two TEMPO-acetamido radical through the carbonyl group of the acetamido substituent (Figure 2.22). Despite numerous attempts with varying stoichiometries and reaction conditions it has not been possible to coordinate the NO group of the radical on the lanthanide. In other word the reactivity of the carbonyl group toward the lanthanide is always found better than the one of the NO group.

The Dy^{III} ion is then eight coordinated by six oxygen atoms from the hfac⁻ ligand and two oxygen atoms from the carbonyl group of two radicals. The geometry of the Dy^{III} coordination polyhedron is close to a square antiprism (D_{4d} site symmetry) with CSM = 0.786. Two dichloromethane molecules complete the asymmetric unit. Additional bond lengths and angles for Dy(**8**) are listed in Table A2.11.

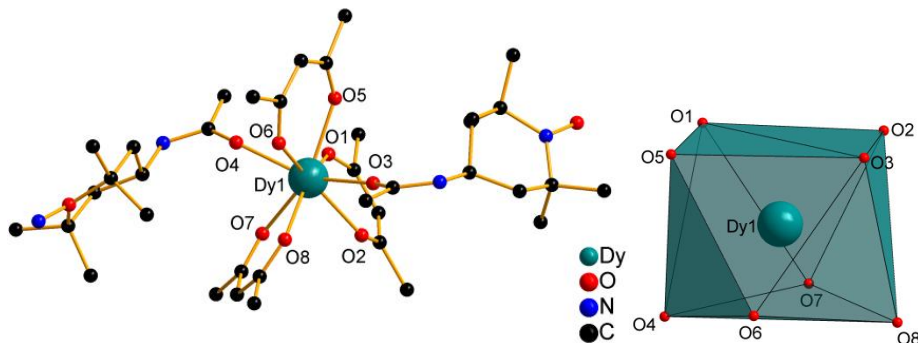


Figure 2.22 Representation of the asymmetric unit for Dy(**8**) (left) and coordination polyhedron of the Dy^{III} (right). All hydrogen and fluorine atoms are omitted for clarity.

To check whether this series of complexes are SMM or not, dynamic magnetic behavior has been investigated on the Dy(**8**) but no magnetic slow relaxation either with or without dc field has been observed.

2.5 A family of monometallic compounds [Ln(hfac)₃(TEMPO-OCH₂CCH)(H₂O)] (Ln =Dy(**9**), Tb(**10**) and Gd(**11**))

2.5.1 Structural description

The reaction of Ln(hfac)₃·2H₂O with TEMPO-OCH₂CCH afford a Ln^{III}-radical two-spin system as targeted at the beginning of this chapter. The R=OCH₂CCH substituting group seems to be particularly suitable to provide the expected compound. In fact:

- contrary to “acetamido”, it is strictly non-coordinating.
- contrary to “OMe” and “NH₂”, it is bulky enough and hydrogen poor enough to avoid hydrogen bonding possibilities that by a consequent diminish the affinity of the NO group for the lanthanide. In other words, with some R groups, the creation of hydrogen bonds network can be at the expenses of the radical-Ln^{III} coordination (see TEMPO-NH₂).

The crystal structure has been solved on the Dy^{III} derivative (**9**). Compound **9** crystallize in the monoclinic $P2_1/n$ space group. The main structural information is listed in Table 2.4. The asymmetric unit is made of one Dy(hfac)₃·H₂O unit and one radical ligand, as shown in Figure 2.23. Dy^{III} is coordinated by six oxygen atoms from three hfac⁻ ligands, one oxygen atom from the NO group of the radical and one water molecule. The latter interacts weakly with the oxygen atom of the neighboring OCH₂CCH group and “organizes” the molecules along the “a” axis (see Figure.A2.11). The geometry of the coordination polyhedron of the

Dy^{III} ion is close to a square antiprism (D_{4d} site symmetry, CSM= 0.855) but also not too far from a triangular dodecahedron (D_{2d} site symmetry, CSM= 1.045). The Dy-O_{hfac} bond lengths are in the 2.32(6)-2.36(6) Å range, while the Dy-O_{rad} and Dy-O_{H2O} bond lengths are 2.33(6) and 2.38(7) Å, respectively. The Dy-O-N angle is 154.48(5)°. Other important bond lengths and angles are listed in Table A2.12. The Dy^{III} ions are well separated in the crystal packing with a closest inter Dy^{III}-Dy^{III} distance of 11.53(2) Å, precluding the existence of intermolecular interaction.

Table 2.4 Main crystallographic parameters for Dy(9).

Formula	C ₂₇ H ₂₅ Dy F ₁₈ N O ₉
M[g.mol ⁻¹]	1011.98
Crystal system	monoclinic
Space group	P21/n
a(Å)	9.599(2)
b(Å)	20.804(4)
c(Å)	18.822(3)
α[°]	90
β[°]	94.701(7)
γ[°]	90
V[Å ³]	3746.1(12)
Z	4
T(K)	150
2θ range	2.35-27.537
Reflns collected	16747
Independent reflns	8596
Observed reflns	6404
Parameters	517
R1/ωR ²	0.0422/0.1082
Goof	0.969

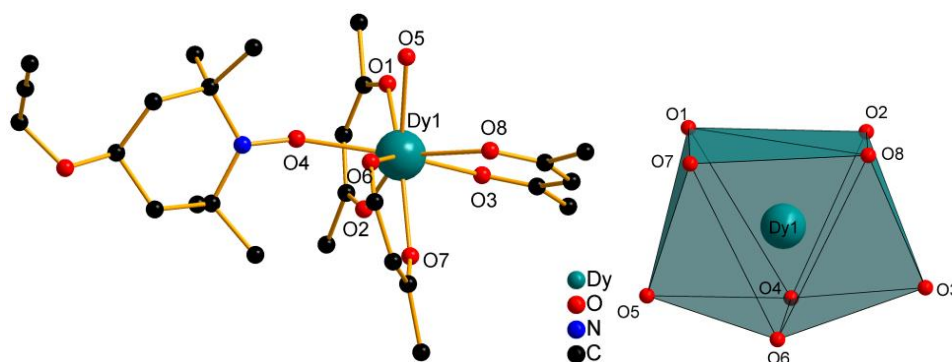


Figure 2.23 Representation of the asymmetric unit for Dy(9) (left) and coordination polyhedron of the Dy^{III} (right). All hydrogen and fluorine atoms are omitted for clarity.

The isostructurality of Dy(9), Tb(10) and Gd(11) derivatives has been assessed on the basis of their powder X-ray diffraction patterns (Figure A2.12).

2.5.2 Static magnetic properties

[Dy(hfac)₃(TEMPO-OCH₂CCH)(H₂O)] (9)

Variable-temperature magnetic susceptibility measurement reveals that the room temperature $\chi_M T$ value of Dy(9) is 15.32 cm³.K.mol⁻¹, slightly higher than the theoretical value of $\chi_M T_{300K} = 14.55$ cm³.K.mol⁻¹ that corresponds to one Dy^{III} ion (⁶H_{15/2}) plus one radical (S = 1/2) at the non-interacting limit (Figure 2.24). As the temperature is lowered, the $\chi_M T$ value slowly decreases to reach 9.74 cm³.K.mol⁻¹ at 1.8 K. The magnetization value reaches 5.17 μ_B at 50 kOe (see the inset of Figure 2.24).

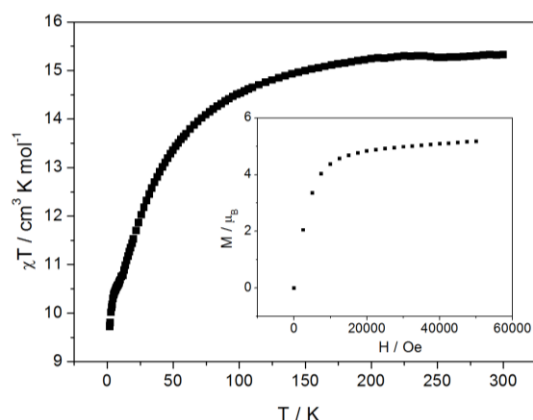


Figure 2.24 Temperature dependence of the $\chi_M T$ product for Dy(9). Inset: Field dependence of the magnetization at 2 K.

[Tb(hfac)₃(TEMPO-OCH₂CCH)(H₂O)] (10)

Variable-temperature magnetic susceptibility measurement reveals that the room temperature $\chi_M T$ value of Tb(10) is 13.18 cm³.K.mol⁻¹, slightly higher than the theoretical value of $\chi_M T_{300K} = 12.19$ cm³.K.mol⁻¹ that corresponds to one Tb^{III} ion (⁷F₆) plus one radical (S = 1/2) at the non-interacting limit (Figure 2.25).

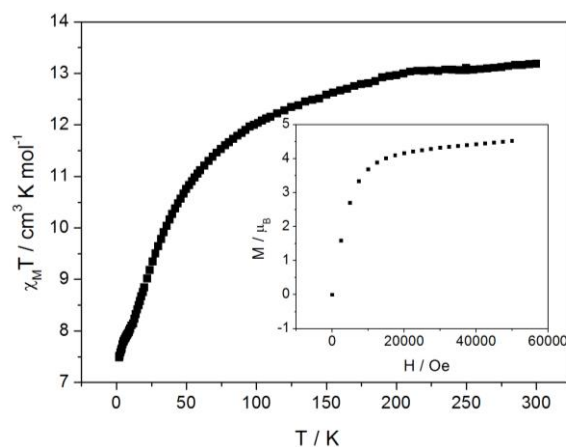


Figure 2.25 Temperature dependence of the $\chi_M T$ product for Tb(10). Inset: Field dependence of the magnetization at 2K.

As the temperature is lowered, the $\chi_M T$ value slowly decreases to reach $7.49 \text{ cm}^3 \cdot \text{K} \cdot \text{mol}^{-1}$ at 1.8 K. The magnetization value reaches $4.51 \mu_B$ at 50 kOe (see the inset of Figure 2.25).

[Gd(hfac)₃(TEMPO-OCH₂CCH)(H₂O)] (11)

Variable-temperature magnetic susceptibility measurement reveals that the room $\chi_M T$ value of Gd(**11**) is $8.15 \text{ cm}^3 \cdot \text{K} \cdot \text{mol}^{-1}$, slightly lower than the theoretical value of $\chi_M T_{300\text{K}} = 8.25 \text{ cm}^3 \cdot \text{K} \cdot \text{mol}^{-1}$ for one Gd^{III} ion ($^8S_{7/2}$) plus one radical ($S = 1/2$) at the non-interacting limit (Figure 2.26). As the temperature is lowered, the $\chi_M T$ value decreases progressively and drops quickly below 70 K to reach a plateau at $5.96 \text{ cm}^3 \cdot \text{K} \cdot \text{mol}^{-1}$ at 1.8K. This value is close to the one that corresponds to an antiferromagnetic $S_{\text{total}} = 3$ state.³² The exchange coupling parameter (J) between the Gd^{III} and the TEMPO radical can be determined by using the following expression (equ (2.2)) derived from a Heisenberg spin Hamiltonian, $H = -J_{\text{Gd-rad}} \mathbf{S}_{\text{Gd}} \cdot \mathbf{S}_{\text{rad}}$.

$$\chi_M T = \frac{4N_A g^2 \mu_B^2}{k_B} \frac{7 + 15 \exp(4J_{\text{Gd-rad}} / k_B T)}{7 + 9 \exp(4J_{\text{Gd-rad}} / k_B T)} \quad \text{equ (2.2)}^{33}$$

The best fit was obtained with $J_{\text{Gd-rad}}/k_B = -9.98 \pm 0.11 \text{ K}$ (that is -6.84 cm^{-1}), $g = 2.00 \pm 0.01$ with $R^2 = 0.998$ and considering negligible intermolecular interaction. This antiferromagnetic coupling is rather strong and in any case stronger than most 4f-radical interaction observed in nitronyle-nitroxide-based compounds (see Table 2.5 for comparison).

Table 2.5 Summary of magnetic exchange coupling constants (K) for Gd complexes.

Compound	$J_{\text{rad-Ln}}$ (K)	$J_{\text{rad-rad}}$ (K)	Ref
$\{\text{Gd}(\text{dca})_2(\text{OH})(\text{NIT-p-Py})_2\}_2$	8.3		34
$((\text{Me}_3\text{Si})_2\text{Ng}_2(\text{THF})\text{Gd})_2(\mu\text{-N}_2^{3-})$	-38.8		20
$\text{Gd}(\text{hfac})_3(\text{NITPh})_2$	-1.8	7.4	35
$\text{Gd}(\text{hfac})_3(\text{NIT-o-Py})$	-4.4		36
$\text{Gd}(\text{hfac})_3(\text{NITPh-3-Br-4-OH})_2$	4.5	-17.6	37
$\text{Gd}(\text{hfac})_3(2\text{PyNO})(\text{H}_2\text{O})$	-6.9		38
$\text{Gd}(\text{hfac})_3(\text{DTBN})(\text{H}_2\text{O})$	-5.8		39
$\text{Gd}(\text{hfac})_3(6\text{bpyNO})$	-5.6		32
$\text{Gd}(\text{hfac})_3(\text{TMIO})_2$	-6.3	-27	40
$[\text{Gd}(\text{hfac})_3(\text{MeOH})(\text{TEMPO})]$	-1.8		41
$[\text{Gd}_2(\text{hfac})_6(\text{H}_2\text{O})_2(\text{dppnTEMPO})]$	3.9		3
$\text{Gd}(\text{hfac})_3(\text{TEMPO})_2$	-6.5/4.0 ¹	49.8 / Y	1
	-10.0/7.5 ¹	15.0 / La	34
$[(\text{Cp}^*\text{Ln})_2(\mu\text{-bpym}^{\cdot})]^+$	-14.4		42
Compound (11)	-10.0		this work

At low temperature a plateau is observed that is possibly the consequence of the strong antiferromagnetic coupling between $7/2$ and $1/2$ spins. The field dependence of the magnetization at 2 K is then simulated by the Brillouin function considering $S=3$. The experimental data are very well reproduced ($R^2 = 0.998$). (see the inset of Figure 2.26).

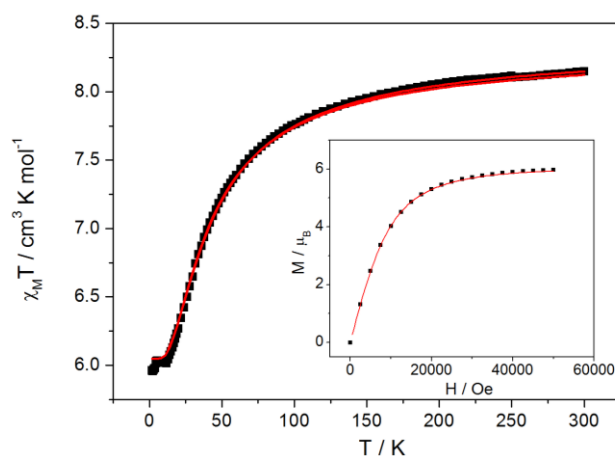


Figure 2.26 Temperature dependence of the $\chi_M T$ product for Gd(**11**). Inset: Field dependence of the magnetization at 2K. Red lines represent the best fits.

2.5.3 Dynamic magnetic properties

[Dy(hfac)₃(TEMPO-OCH₂CCH)(H₂O)] (9)

To further explore the spin dynamics, the alternating current (ac) magnetic susceptibilities were performed on Dy(9) under zero dc field and external field dc field, respectively. The results show that frequency-independent peaks were observed in part of the temperature range (Figure.A2.14). A very small dc field (400 Oe) is enough to activate a thermally dependent relaxation above 5 K whereas thermally independent relaxation is still present at lower temperature.

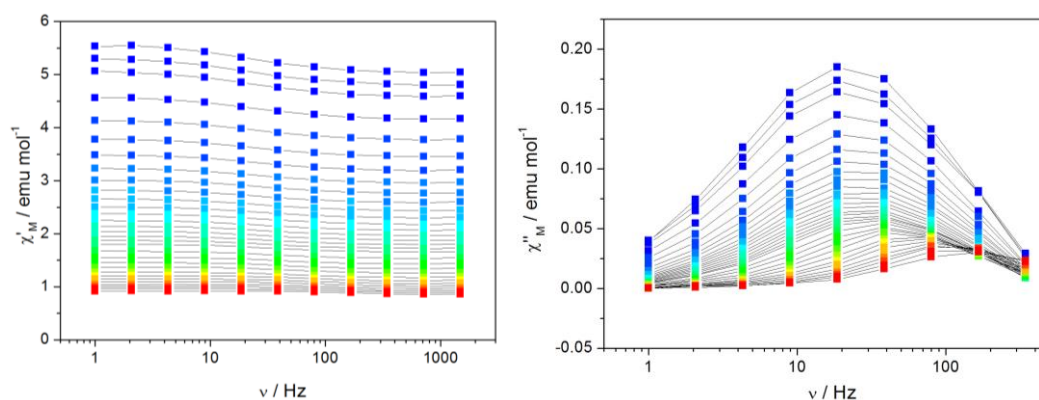


Figure 2.27 Frequency dependence of the in-phase (left) and out-of-phase (right) components of ac susceptibility for Dy(9) under 400 dc field. Color mapping from 1.8 K (blue) to 12 K (red). Temperature plots of these data are available in Figure.A2.15. Lines are guides to the eye.

The normalized Cole-Cole plots (Figure 2.28) display a very small semi-circle with a relatively narrow distribution of the relaxation times ($\alpha = 0.24$ at 2 K). However, the very high χ_s/χ_T value highlights that almost 90% of the sample is not able to relax slowly.

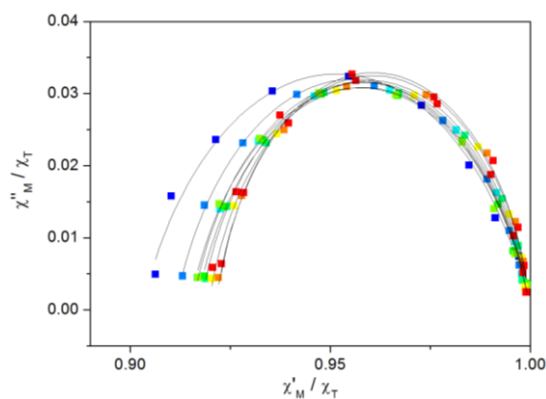


Figure 2.28 Normalized Cole-Cole plot for Dy(9) under 400 Oe dc field. Color mapping from 2.0 K (blue) to 6.5 K (red). Lines represent the best fits as calculated with an extended Debye model.

In the present case the coordination of the radical on the Dy^{III} ion seems to have a very bad impact on its magnetic slow relaxation properties.

[Tb(hfac)₃(TEMPO-OCH₂CCH)(H₂O)] (10)

Compound Tb(10) displays totally different magnetic behavior. No magnetic slow relaxation is observed with a zero dc field but with a 1600 Oe field a significant temperature-dependent slow relaxation is observed on a wide temperature range (1.8 K-6 K) and with a good χ''/χ' ratio.

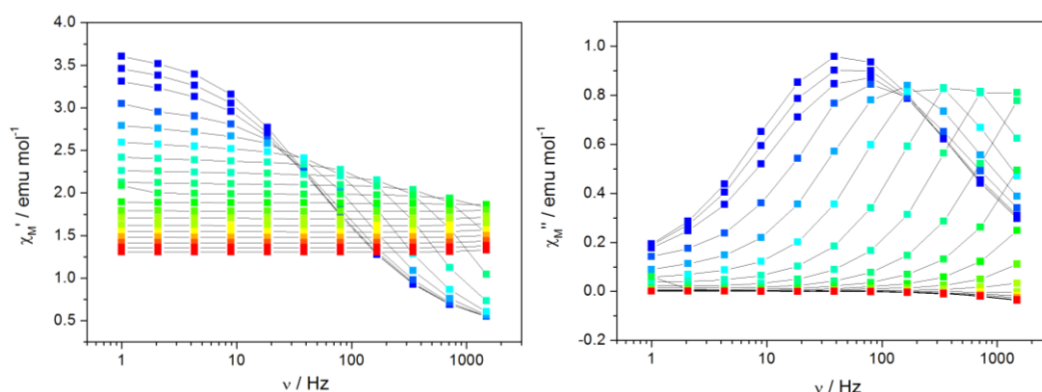


Figure 2.29 Normalized Cole-Cole plot for Tb(10) under 1600 Oe dc field. Color mapping from 1.8 K (blue) to 6.0 K (red). Temperature plots of these data are available in Figure.A2.17. Lines are guides to the eye.

The difference is even greater on the Cole-Cole plots (Figure 2.30) as good α values are observed. (from 0.06 at 3.25 K to 0.33 at 1.8 K) and most of all, almost all the sample relaxes slowly (χ_S/χ_T is in the range 0.09 at 1.8 K to 0.17 at 3.25 K)

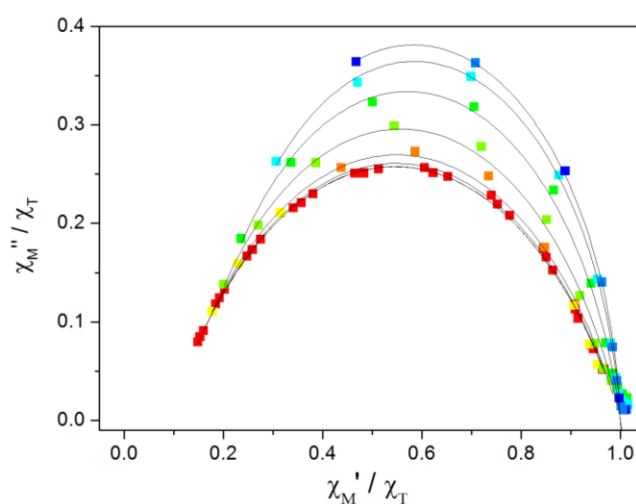


Figure 2.30 Normalized Cole-Cole plot for Tb(10) under 1600 Oe dc field. Color mapping from 1.8 K (blue) to 3.25 K (red). Lines represent the best fits as calculated with an extended Debye model.

In this case the coordination of the radical on the Tb^{III} ion seems to have a very positive impact on its magnetic slow relaxation properties.

2.5.4 Determination of energy barrier and other dynamic parameters

The extracted relaxation times of Dy(**9**) and Tb(**10**) are plotted in function of T^{-1} in Figure 2.31.

For **9**, several relaxation processes are clearly operating. Tentative fits of the linear region of the plot give $U_{\text{eff}}/k_B = 17.5 \pm 1.25$ K with $\tau_0 = 3.46 \times 10^{-4}$ s. The high value of τ_0 ^{49, 50} may highlight the contribution of the second and third terms (direct process) or the fourth term (Raman process) of equation 1.5. However, attempts to consider these processes in the fitting procedure fail.

Similarly, for **10**, we attempted to describe the relaxation considering all the five terms, but this was not successful. Finally, only the Orbach and direct processes have been taken into account to give a good fit with $A_2 = 7.34 \pm 0.31 \times 10^{-5} \text{ s}^{-1} \text{ K}^{-1} \text{ Oe}^{-4}$, $\tau_0 = 6.92 \pm 3.08 \times 10^{-8}$ s, $U_{\text{eff}} = 25.6 \pm 1.3$ K.

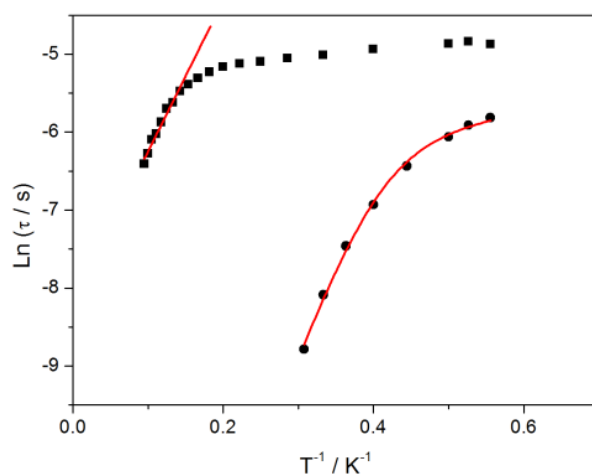


Figure 2.31 Plot of $\ln(\tau)$ versus (T^{-1}) for Dy(**9**) (squares) and Tb(**10**) (circles). The solid lines represent the best fits.

2.5.5 Conclusion

The TEMPO-OCH₂CCH has been found particularly suitable to provide isolated Ln-radical units with strong magnetic coupling.

This coupling has been evidenced to be of the order of -9.98K (-6.84cm⁻¹) on the Gd derivative (**11**). Such coupling is strong enough to lead to a totally antiferromagnetically coupled system of S=3 at 2K.

We have not been able to estimate the Ln-radical coupling with the derivatives based on anisotropic ions but they can potentially be on the same sign and same order of magnitude.³

The Dy^{III} and Tb derivatives are impacted totally differently by this coupling with SMM properties annihilated on the former and promoted on the latter.

2.6 Conclusion

In this chapter, we have used four monodentate TEMPO radicals in order to build isolated Ln-TEMPO entities.

Table 2.5 Summary of the conditions of the synthesis and measurement.

Ligand	Dimension	Ce	Pr	Nd	Sm	Gd	Tb	Dy	Ho	Er	Tm	Yb
TEMPO-OCH ₃	0D	1	2	3		4		5				
TEMPO-NH ₂	0D					7		6				
TEMPO-Acetamido	0D							8				
TEMPO-OCH ₂ CCH	0D					11	10	9				

Only DC data	Non SMM	SMM	oil		amorph	Synthese not done
--------------	---------	-----	-----	--	--------	-------------------

With TEMPO-OMe (section 2.2) we have obtained a five spin system made of three Ln-TEMPO entities and one free TEMPO. The rationalization of the magnetic coupling was then quite difficult but combined AF and F have been identified on the Gd^{III} analogue (**4**). Unexpectedly SMM behaviors with modest activation energies have been found for the Ce^{III} (**1**), Nd^{III} (**2**) and Pr^{III} (**3**) derivatives (independent of the Kramer or non-Kramer ion character) whereas the Dy^{III} one (**5**) remains silent. To the best of our knowledge this is the first time that concomitant SMM behavior is observed on these three light lanthanides concomitantly.

With TEMPO-NH₂ (section 2.3) no Ln-radical compound has been obtained but an antiferromagnetically connected Gd^{III} ($J = -0.11 \text{ cm}^{-1}$) dimer (**7**) and a ferromagnetically connected Dy^{III} dimer (**6**) that we compare with one of our previous report (Dy(Stilbene)).

With TEMPO-Acetamido (section 2.4) a trimeric radical-Dy-radical system (**8**) is obtained but do not lead to any SMM behavior.

Finally, with TEMPO-OCH₂CCH (section 2.5) a dimeric and isolated Ln-radical system has been obtained. It permitted to highlight a strong Ln-TEMPO AF interaction (-9.98 K or -6.84 cm^{-1}) on the Gd^{III} derivative (**11**). Such interaction also permitted to observe a SMM behavior on the usually silent Tb^{III} derivative (**10**) whereas Dy^{III} (**9**) was a poor SMM. In fact, Tb^{III} ion provides good SMM behavior in two cases:

-if it is confined in a very symmetrical ligand field environment, that fits with the oblate nature of its ground state electronic density. This is particularly spectacular on TbPc₂ derivatives for example.⁵¹⁻⁵³

-if it is combined with 2p spin carriers, as observed with Cu^{II} ions,⁵⁴⁻⁵⁷ nitronyl-nitroxide radicals,^{29, 58-61} or other radicals.⁶⁰ This should deserve a deeper magnetic study in particular on the theoretical point of view.

In summary, Tb-based TEMPO molecules should be of interest to build SMMs. In the following chapter we will use such building block to generate one dimensional compounds or extended networks.

References

1. R. Murakami, T. Nakamura and T. Ishida, *Dalton Transactions*, 2014, 43, 5893-5898.
2. M. Karbowiak, C. Rudowicz, T. Nakamura, R. Murakami and T. Ishida, *Chemical Physics Letters*, 2016, 662, 163-168.
3. S. G. Reis, M. Briganti, S. Soriano, G. P. Guedes, S. Calancea, C. Tiseanu, M. A. Novak, M. A. del Águila-Sánchez, F. Totti, F. Lopez-Ortiz, M. Andruh and M. G. F. Vaz, *Inorganic Chemistry*, 2016, 55, 11676-11684.
4. D. Zeng, M. Ren, S.-S. Bao and L.-M. Zheng, *Inorganic Chemistry*, 2014, 53, 795-801.
5. A. K. Mondal, S. Goswami and S. Konar, *Dalton Transactions*, 2015, 44, 5086-5094.
6. M. Pinsky and D. Avnir, *Inorganic Chemistry*, 1998, 37, 5575-5582.
7. D. Casanova, J. Cirera, M. Llunell, P. Alemany, D. Avnir and S. Alvarez, *Journal of the American Chemical Society*, 2004, 126, 1755-1763.
8. J. Cirera, E. Ruiz and S. Alvarez, *Chemistry – A European Journal*, 2006, 12, 3162-3167.
9. J. D. Rinehart and J. R. Long, *Chemical Science*, 2011, 2, 2078-2085.
10. C. Benelli and D. Gatteschi, *Chemical Reviews*, 2002, 102, 2369-2388.
11. Y. Yue, J. Sun, P. Yan and G. Li, *Inorganic Chemistry Communications*, 2015, 51, 42-45.
12. Y. Peng, V. Mereacre, A. Baniodeh, Y. Lan, M. Schlageter, G. E. Kostakis and A. K. Powell, *Inorganic Chemistry*, 2016, 55, 68-74.
13. X. Yi, K. Bernot, V. Le Corre, G. Calvez, F. Pointillart, O. Cador, B. Le Guennic, J. Jung, O. Maury, V. Placide, Y. Guyot, T. Roisnel, C. Daiguebonne and O. Guillou, *Chemistry – A European Journal*, 2014, 20, 1569-1576.
14. W.-B. Sun, P.-F. Yan, S.-D. Jiang, B.-W. Wang, Y.-Q. Zhang, H.-F. Li, P. Chen, Z.-M. Wang and S. Gao, *Chemical Science*, 2016, 7, 684-691.
15. J. Jung, X. Yi, G. Huang, G. Calvez, C. Daiguebonne, O. Guillou, O. Cador, A. Caneschi, T. Roisnel, B. Le Guennic and K. Bernot, *Dalton Transactions*, 2015, 44, 18270-18275.
16. S.-D. Jiang and S.-X. Qin, *Inorganic Chemistry Frontiers*, 2015, 2, 613-619.
17. J. Jung, F. Le Natur, O. Cador, F. Pointillart, G. Calvez, C. Daiguebonne, O. Guillou, T. Guizouarn, B. Le Guennic and K. Bernot, *Chemical Communications*, 2014, 50, 13346-13348.
18. N. F. Chilton, D. Collison, E. J. L. McInnes, R. E. P. Winpenny and A. Soncini, *Nature Communications*, 2013, 4, 2551.
19. J. D. Rinehart, M. Fang, W. J. Evans and J. R. Long, *Journal of the American Chemical Society*, 2011, 133, 14236-14239.
20. J. D. Rinehart, M. Fang, W. J. Evans and J. R. Long, *Nat Chem*, 2011, 3, 538-542.
21. A. B. Khelifa, M. S. Belkhiria, G. Huang, S. Freslon, O. Guillou and K. Bernot, *Dalton Transactions*, 2015, 44, 16458-16464.
22. J. J. Le Roy, I. Korobkov, J. E. Kim, E. J. Schelter and M. Murugesu, *Dalton Transactions*, 2014, 43, 2737-2740.
23. A. K. Jassal, N. Aliaga-Alcalde, M. Corbella, D. Aravena, E. Ruiz and G. Hundal, *Dalton Transactions*, 2015, 44, 15774-15778.

24. F. Pointillart, S. Klementieva, V. Kuropatov, Y. Le Gal, S. Golhen, O. Cador, V. Cherkasov and L. Ouahab, *Chemical Communications*, 2012, 48, 714-716.
25. G. Cosquer, F. Pointillart, S. Golhen, O. Cador and L. Ouahab, *Chemistry – A European Journal*, 2013, 19, 7895-7903.
26. F. Pointillart, O. Cador, B. Le Guennic and L. Ouahab, *Coordination Chemistry Reviews*, DOI: <http://dx.doi.org/10.1016/j.ccr.2016.12.017>.
27. H. Wada, S. Ooka, T. Yamamura and T. Kajiwarra, *Inorganic Chemistry*, 2016, DOI: 10.1021/acs.inorgchem.6b01764.
28. S. Hino, M. Maeda, K. Yamashita, Y. Kataoka, M. Nakano, T. Yamamura, H. Nojiri, M. Kofu, O. Yamamuro and T. Kajiwarra, *Dalton Transactions*, 2013, 42, 2683-2686.
29. F. Pointillart, K. Bernot, G. Poneti and R. Sessoli, *Inorganic Chemistry*, 2012, 51, 12218-12229.
30. X. Yi, K. Bernot, O. Cador, J. Luzon, G. Calvez, C. Daiguebonne and O. Guillou, *Dalton Transactions*, 2013, 42, 6728-6731.
31. O. Kahn, *Molecular magnetism*, 1993.
32. T. Kanetomo and T. Ishida, *Inorganic Chemistry*, 2014, 53, 10794-10796.
33. I. Ramade, O. Kahn, Y. Jeannin and F. Robert, *Inorganic Chemistry*, 1997, 36, 930-936.
34. C.-F. Hsu, S.-H. Lin and H.-H. Wei, *Inorganic Chemistry Communications*, 2005, 8, 1128-1132.
35. C. Benelli, A. Caneschi, D. Gatteschi, L. Pardi, P. Rey, D. P. Shum and R. L. Carlin, *Inorganic Chemistry*, 1989, 28, 272-275.
36. C. Benelli, A. Caneschi, D. Gatteschi and L. Pardi, *Inorganic Chemistry*, 1992, 31, 741-746.
37. F.-X. Du, P. Hu, Y.-Y. Gao, F.-P. Xiao and Y.-N. Wu, *Inorganic Chemistry Communications*, 2014, 48, 166-170.
38. T. Ishida, R. Murakami, T. Kanetomo and H. Nojiri, *Polyhedron*, 2013, 66, 183-187.
39. T. Kanetomo and T. Ishida, *Chemical Communications*, 2014, 50, 2529-2531.
40. T. Nakamura and T. Ishida, *Polyhedron*, 2015, 87, 302-306.
41. T. Nakamura and T. Ishida, *AIP Conference Proceedings*, 2016, 1709, 020016.
42. S. Demir, J. M. Zadrozny, M. Nippe and J. R. Long, *Journal of the American Chemical Society*, 2012, 134, 18546-18549.
43. G. Poneti, K. Bernot, L. Bogani, A. Caneschi, R. Sessoli, W. Wernsdorfer and D. Gatteschi, *Chemical Communications*, 2007, DOI: 10.1039/B617898G, 1807-1809.
44. M. L. Kahn, R. Ballou, P. Porcher, O. Kahn† and J.-P. Sutter, *Chemistry – A European Journal*, 2002, 8, 525-531.
45. J.-P. Sutter, M. L. Kahn and O. Kahn, *Advanced Materials*, 1999, 11, 863-865.
46. C. Benelli, A. Caneschi, D. Gatteschi and R. Sessoli, *Journal of Applied Physics*, 1993, 73, 5333-5337.
47. K. Bernot, L. Bogani, R. Sessoli and D. Gatteschi, *Inorganica Chimica Acta*, 2007, 360, 3807-3812.
48. K. Bernot, J. Luzon, L. Bogani, M. Etienne, C. Sangregorio, M. Shanmugam, A. Caneschi, R. Sessoli and D. Gatteschi, *Journal of the American Chemical Society*, 2009, 131, 5573-5579.
49. P.-H. Lin, T. J. Burchell, L. Ungur, L. F. Chibotaru, W. Wernsdorfer and M. Murugesu, *Angewandte Chemie International Edition*, 2009, 48, 9489-9492.
50. Y.-N. Guo, G.-F. Xu, P. Gamez, L. Zhao, S.-Y. Lin, R. Deng, J. Tang and H.-J. Zhang, *Journal of the American Chemical Society*, 2010, 132, 8538-8539.
51. N. Ishikawa, M. Sugita, T. Ishikawa, S.-y. Koshihara and Y. Kaizu, *Journal of the American Chemical Society*, 2003, 125, 8694-8695.
52. N. Ishikawa, *Struct. Bonding (Berlin)*, 2010, 135, 211-228.
53. N. Ishikawa, *Polyhedron*, 2007, 26, 2147-2153.
54. J.-P. Costes, M. Auchel, F. Dahan, V. Peyrou, S. Shova and W. Wernsdorfer, *Inorganic Chemistry*, 2006, 45, 1924-1934.
55. J.-P. Costes, J. M. Clemente-Juan, F. Dahan and J. Milon, *Inorganic Chemistry*, 2004, 43, 8200-8202.

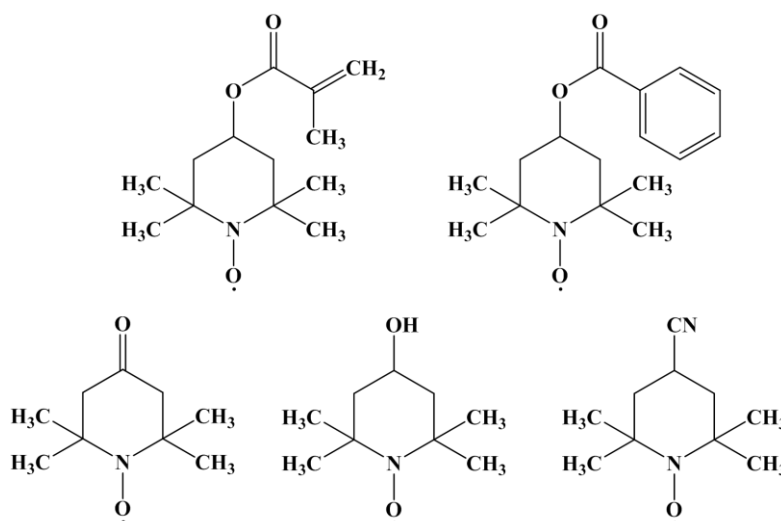
56. S. Osa, T. Kido, N. Matsumoto, N. Re, A. Pochaba and J. Mrozinski, *Journal of the American Chemical Society*, 2004, 126, 420-421.
57. X.-L. Mei, R.-N. Liu, C. Wang, P.-P. Yang, L.-C. Li and D.-Z. Liao, *Dalton Transactions*, 2012, 41, 2904-2909.
58. K. Bernot, L. Bogani, A. Caneschi, D. Gatteschi and R. Sessoli, *Journal of the American Chemical Society*, 2006, 128, 7947-7956.
59. E. Coronado, C. Giménez-Saiz, A. Recuenco, A. Tarazón, F. M. Romero, A. Camón and F. Luis, *Inorganic Chemistry*, 2011, 50, 7370-7372.
60. R. Murakami, T. Ishida, S. Yoshii and H. Nojiri, *Dalton Transactions*, 2013, 42, 13968-13973.
61. A. Lannes, M. Intissar, Y. Suffren, C. Reber and D. Luneau, *Inorganic Chemistry*, 2014, 53, 9548-9560.

3 (TEMPO-R)-4f based multi-dimensional complexes: synthesis and magnetic properties

3.1 Introduction

In the previous chapter, we have employed several TEMPO radicals with almost non-coordinating R groups to construct zero-dimensional complexes. As expected, the different substituents result in totally different molecular edifices and finally different magnetic properties. In this chapter, we have used TEMPO-R radicals with coordinating R groups (scheme 3.1) in order to build extended molecular edifices. The five radicals are.

- R= OCOCH₂CCH₃, as in TEMPO-Methacrylate (abbreviated TEMPO- Methacrylate)
- R= OCOPh, as in 4-Hydroxy-TEMPO benzoate (abbreviated TEMPO- OCOPh)
- R= O, as in 4-Oxo-TEMPO (abbreviated Oxo-TEMPO)
- R= OH, as in 4-Hydroxy-TEMPO (abbreviated TEMPO-OH)
- R= CN, as in 4-Cyano-Tempo (abbreviated Tempo-CN)



Scheme 3.1 Schematic representation of different radicals used in this chapter: TEMPO-Methacrylate (top left), TEMPO-OCOPh (top right), Oxo-TEMPO (bottom left), TEMPO-OH (bottom middle), TEMPO-CN (bottom right).

We have obtained crystalline materials for 12 compounds that range from isolated complexes to 2D networks. Their formulas are:

- [Ln(hfac)₃(TEMPO-methacrylate)]_n (Ln = Dy(**12**)),
- [Ln(hfac)₃(TEMPO-OCOPh)]_n (Ln = Ce(**13**)),
- [Dy(hfac)₃(Oxo-TEMPO)]_n (**14**),
- [(Ce(hfac)₃)₃(Oxo-TEMPO)₄]_n (**15**),
- [Ln(hfac)₃(TEMPO-OH)(H₂O)]_n (Ln = Ce(**16**), Pr(**17**)),
- [Ln(hfac)₃(TEMPO-OH)]_n (Ln = Dy(**18**), Gd(**19**)),

- [Ce(hfac)₃(TEMPO-CN)₂] (**20**),
 -{[Dy(hfac)₃(TEMPO-CN)₂][Dy(hfac)₃(H₂O)₂]₂} (**21**),
 -[Ln(hfac)₃(TEMPO-CN)]_n (Ln = Tb(**22**), Gd(**23**)).

3.2 [Ln(hfac)₃(TEMPO-methacrylate)]_n (**Dy(12)**)

3.2.1 Structural description

Reaction of Ln(hfac)₃·2H₂O with TEMPO-methacrylate has afforded crystalline material only for the Dy^{III} derivative. However, the expected coordination by the substituting R group has been successful in this case.

Single-crystal measurement has been carried out on compound **12** and reveals that it crystallizes in P 2₁2₁2₁ space group. The crystallographic data of compound **12** are given in Table 3.1. The asymmetric unit is made of one Dy(hfac)₃ moiety and one radical (Figure 3.1). One radical connects to the neighboring Dy^{III} in a ‘head to tail’ mode to afford a 1D zig-zag chain. Each Dy^{III} is coordinated by six O_{hfac}, one O_{NO} and one O_{C=O}, to form a square antiprism polyhedron (D_{4d}) with CSM = 0.935.^{1, 2} Selected bond lengths and angles are listed in Table A3.1. The closest intrachain and interchain Dy^{III}-Dy^{III} distances are 10.11 (25) Å and 10.76 (24) Å.

Table 3.1 Main crystallographic parameters for **12**.

Formula	C ₆₂ H ₅₀ Dy ₂ F ₃₆ N ₂ O ₁₈
M[g.mol ⁻¹]	1023.99
Crystal system	orthorhombic
Space group	P 212121
a(Å)	10.618 (5)
b(Å)	18.327 (5)
c(Å)	19.739 (5)
α[°]	90
β[°]	90
γ[°]	90
V[Å ³]	3841 (2)
Z	4
T(K)	150(2)
2θ range	2.03-27.406
Reflns collected	20719
Independent reflns	8284
Observed reflns	6786
Parameters	514
R1/ωR ²	0.0485/0.1393
Goof	1.038

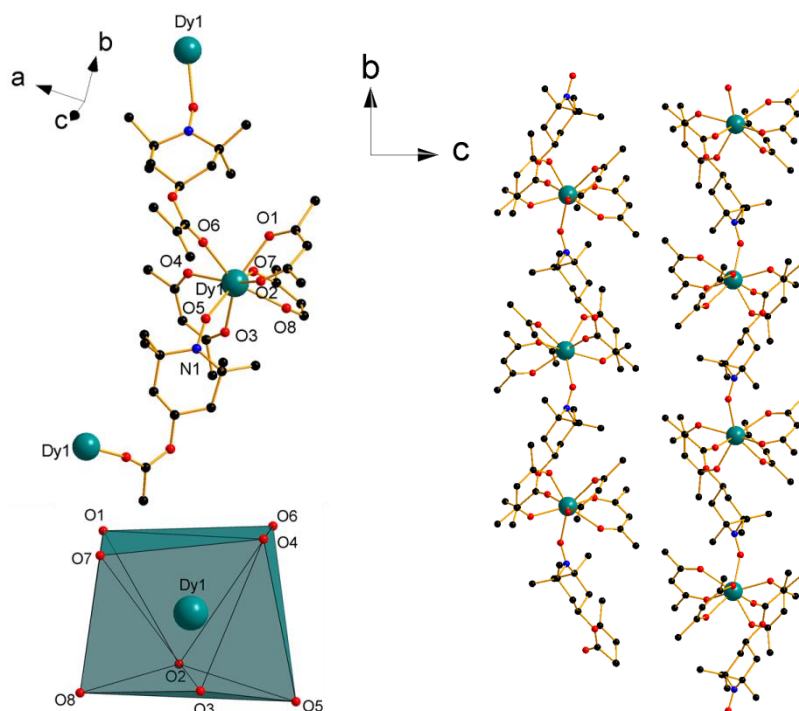


Figure 3.1 Representation of the molecular structure of **12** (left top) and polyhedra of the Dy^{III} ion (left bottom). Packing diagram of 1D linear chain structure along the ‘a’ axis (right). Fluorine and hydrogen atoms are omitted for clarity.

Dynamic magnetic behavior has been investigated on Dy^{III}(**12**) and Tb^{III} derivatives but no magnetic slow relaxation has been detected.

3.3 [Ln(hfac)₃(TEMPO-OCOPh)]_n (Ln = Ce(**13**))

3.3.1 Structural description

As for TEMPO-methacrylate, only one crystalline derivative has been obtained with TEMPO-OCOPh, but similarly coordination by the R substituting group has been possible.

Single-crystal measurement has been performed on compound **13** and reveals that it crystallizes in P 2₁/c space group. The crystallographic data of complex **13** are given in Table 3.2. The asymmetric unit is made of two independent Ce^{III} ions (Figure 3.2). Each chain contains two Ce(hfac)₃ moieties and two radicals connected in a ‘head to tail’ mode to afford a 1D linear chain. Each Ce^{III} is coordinated by six O_{hfac}-, one O_{NO} and one O_{C=O}, to form the square antiprism coordination polyhedron (D_{4d}). However, slight differences are evidenced between Ce1 and Ce2 with CSM = 0.742 and 0.748, respectively. Selected bond lengths and angles are listed in Table A3.2. The closest intrachain and interchain Ce^{III}-Ce^{III} distances are 9.80(23) Å and 10.88(26) Å, respectively.

Table 3.2 Main crystallographic parameters for **13**.

Formula	$C_{62}H_{50}Ce_2F_{36}N_2O_{18}$
$M[g.mol^{-1}]$	2075.28
Crystal system	monoclinic
Space group	P 21/c
$a(\text{\AA})$	17.039 (5)
$b(\text{\AA})$	20.891 (5)
$c(\text{\AA})$	21.736 (5)
$\alpha[^\circ]$	90
$\beta[^\circ]$	90.340 (5)
$\gamma[^\circ]$	90
$V[\text{\AA}^3]$	7737 (3)
Z	4
T(K)	150(2)
2θ range	2.03-27.537
Reflns collected	35065
Independent reflns	17793
Observed reflns	13621
Parameters	1081
$R1/\omega R^2$	0.0576/0.1587
Goof	1.065

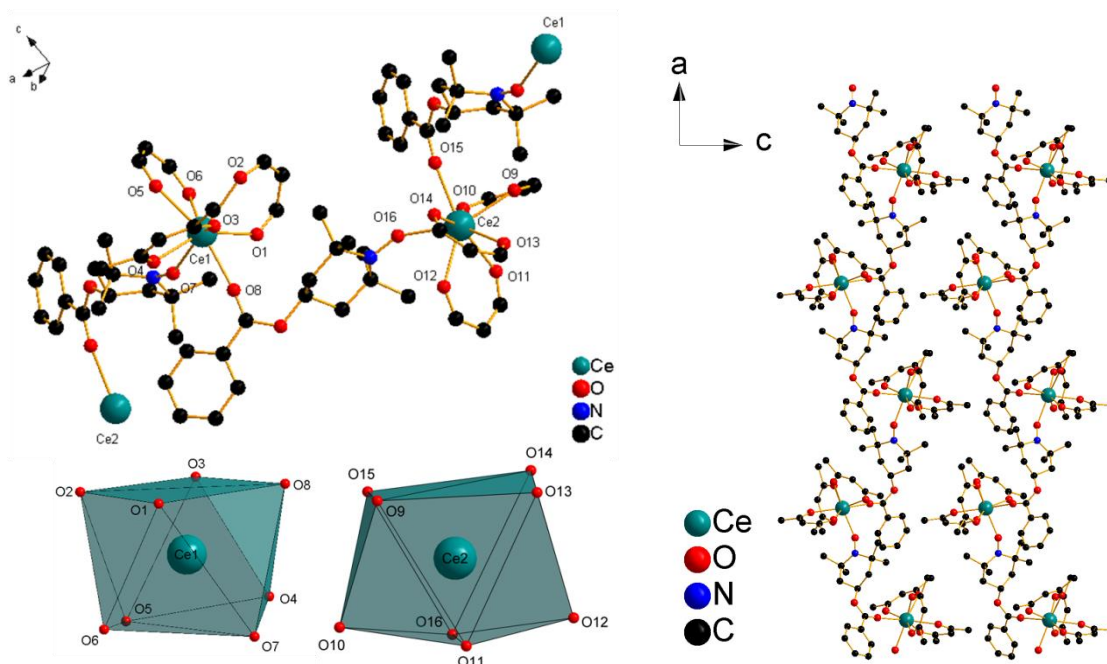


Figure 3.2 Representation of the molecular structure (left top) and polyhedra of the two different Ce^{III} ions (left bottom). Packing diagram of 1D linear chain structure of **13**. Fluorine and hydrogen atoms are omitted for clarity.

As for **12**, dynamic magnetic behavior has been investigated on **13** and other powder derivatives (Tb^{III} and Dy^{III}) but no magnetic slow relaxation either with or without dc field has been observed.

3.4 Structural diversity in combination with Oxo-TEMPO radical

3.4.1.1D zig-zag chain $[\text{Ln}(\text{hfac})_3(\text{Oxo-TEMPO})]_n$ ($\text{Ln} = \text{Dy}(\mathbf{14})$)

3.4.1.1 Structural description

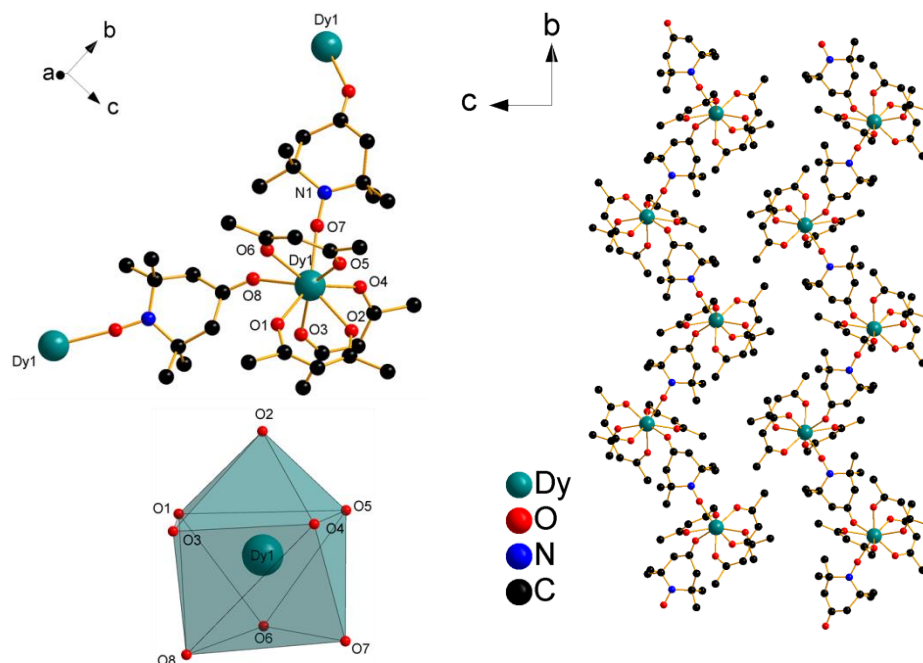


Figure 3.3 (left). Representation of the molecular structure of **14** (left top) and polyhedra of the Dy^{III} ion (left bottom right). Packing diagram of 1D zig-zag chain structure along the ‘a’ axis (right). Fluorine and hydrogen atoms are omitted for clarity.

Oxo-TEMPO radical has also depicted coordination abilities toward the R substituting group. Using Dy^{III} , a 1D compound has been obtained.

Single crystal X-ray diffraction reveals that complex **14** crystallizes in the monoclinic $P2_1/n$ space group. The crystallographic data of complex **14** are given in Table 3.3. The asymmetric unit is made of one $\text{Dy}(\text{hfac})_3$ moiety and one Oxo-TEMPO radical, in which the radical connects the Dy^{III} in a ‘head-to-tail’ mode to form a molecular chain (Figure 3.3). Dy^{III} is surrounded by six oxygen atoms from three hfac^- anions, one monodentate NO moiety and Oxo group. Coordination polyhedron is a square antiprism (D_{4d}) with $\text{CSM} = 0.514$. Selected bond lengths and angles are listed in Table A3.3. The shortest intrachain $\text{Dy}^{\text{III}}-\text{Dy}^{\text{III}}$ distance is 10.86 (27) Å and the shortest interchain $\text{Dy}^{\text{III}}-\text{Dy}^{\text{III}}$ distances is 12.20(26) Å.

Table 3.3 Main crystallographic parameters for **14**.

Formula	C ₂₄ H ₁₉ Dy F ₁₈ N O ₈
M[g.mol ⁻¹]	953.90
Crystal system	monoclinic
Space group	P2 ₁ /n
a(Å)	9.461 (5)
b(Å)	15.063 (5)
c(Å)	23.013 (5)
α[°]	90
β[°]	93.361 (5)
γ[°]	90
V[Å ³]	3274 (2)
Z	4
T(K)	150
2θ range	2.53-27.465
Reflns collected	27997
Independent reflns	7482
Observed reflns	5482
Parameters	479
R1/ωR ²	0.0751/0.2542
Goof	1.083

Unfortunately, as for **12** and **13** no magnetic slow relaxation either with or without dc field has been observed on Dy^{III}(**14**) and other powder derivatives(Sm^{III}, Tb^{III}, Ho^{III}, Er^{III}, Tm^{III} and Yb^{III}).

3.4.2 Two-dimensional 4f-2p network: [(Ce(hfac)₃)₃(Oxo-TEMPO)₄]_n (**15**)

3.4.2.1 Structural description

With Oxo-TEMPO, crystalline material has been obtained not only by using Dy(hfac)₃·2H₂O but also Ce(hfac)₃·2H₂O. In this latter case, a unique and particularly appealing 2D network has been obtained. To the best of our knowledge this is the first time that such a Ce^{III}-TEMPO-R two dimensional network is reported.

Single-crystal X-ray diffraction reveals that complexes **15** crystallizes in the monoclinic P2₁/n space group with a cell volume of 11128.2 (7) Å³. The crystallographic data of complex **15** are given in Table 3.4. The asymmetric unit contains three independent Ce^{III} ions(Figure 3.4). Ce1 is eight coordinated and surrounded by six O_{hfac}- and two O_{NO} of two different radicals. On a magnetic point of view this is expected to create a radical-Ce1-radical unit. The coordination polyhedron of Ce1 is a triangular dodecahedron with D_{2d} site symmetry CSM = 1.100. Ce1-O bond lengths are in the 2.42(4)-2.48(4) Å range.

Contrary to Ce1, Ce2 and Ce3 are nine coordinated. Ce2 is surrounded by six O_{hfac}-, two O_{Oxo} and one O_{NO}. This ninth coordination position of Ce2 implies thus a third radical whose R group further connects Ce3. Ce3 is surrounded by six O_{hfac}-, two O_{NO} and one O_{NO}. Both Ce2 and Ce3 have a spherical capped square antiprism geometry (C_{4v}) but with different CSM values, 0.448 and 0.408, respectively. Ce2-O bond lengths are in the 2.47(3)-2.60(3) Å range

and Ce3-O bond lengths are in the 2.45(4)-2.60(3) Å range. Detailed bond lengths and angles are listed in Table A3.4. Ce1-Ce2 distance is 9.94 (1) Å, Ce2-Ce3 distance is 10.06 (1) Å.

The successive connection of the three different Ce^{III} ions by six different bis-monodentate oxo-TEMPO ligands leads to a 2D network in the ab plane. This network can be described as made of zig-zag chains that are interconnected by Oxo-TEMPO ligands. To the best of our knowledge only one Ce-radical 2D network is reported up to date.³

On a magnetic point of view three different moieties can be identified:

- a three spin radical-Ce1-radical unit.
- a two spin radical-Ce2 unit.
- a two spin radical-Ce3 unit.

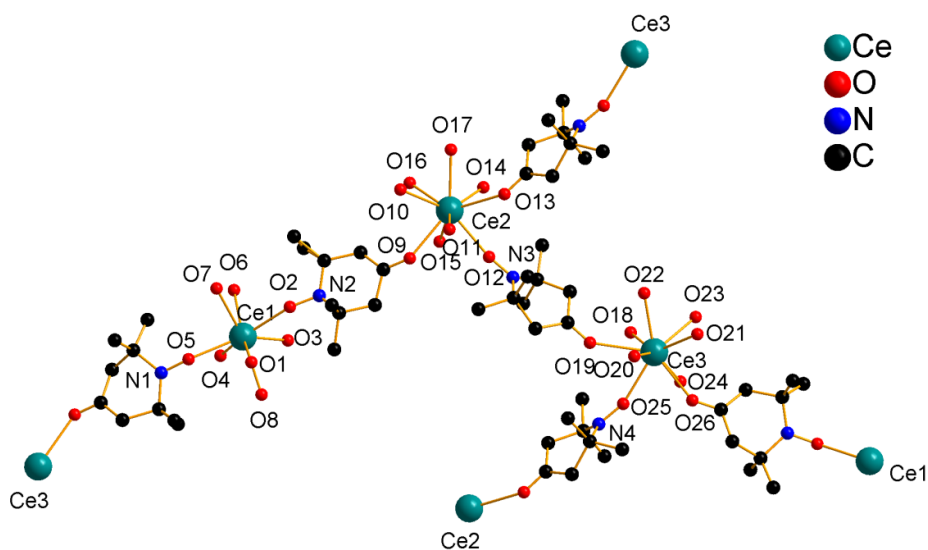


Figure 3.4 Representation of the molecular structure for **15**. Fluorine and hydrogen atoms are omitted for clarity.

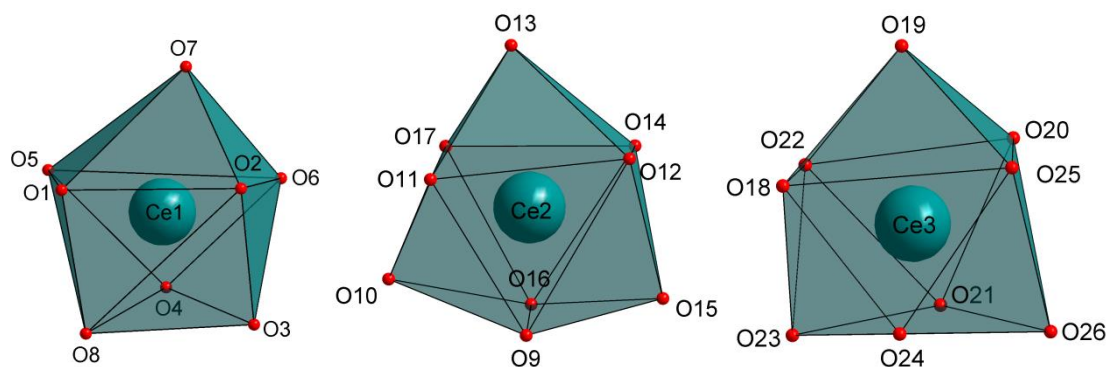
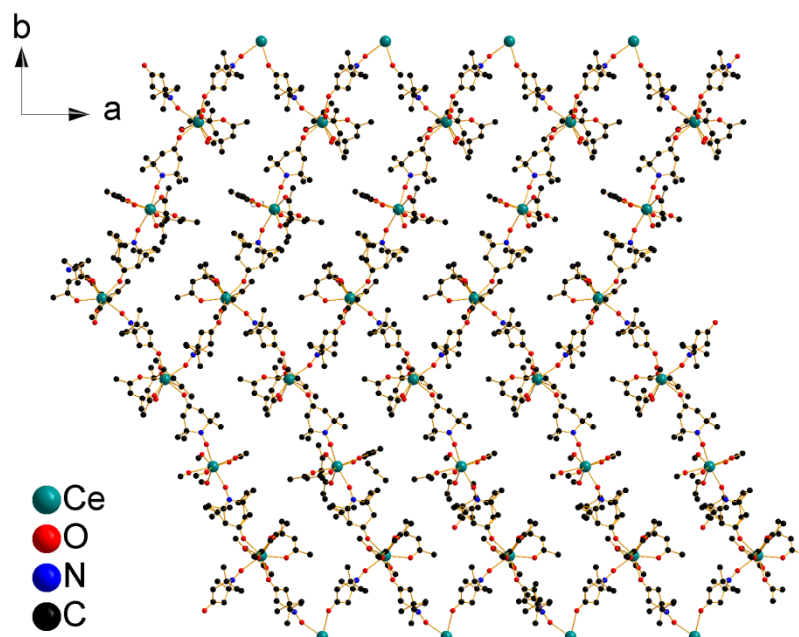


Figure 3.5 Coordination polyhedra of the three crystallographic independent Ce^{III} ions.

Figure 3.6 Packing diagram of the structure along 'c' axis for **15**.Table 3.4 Main crystallographic parameters for **15**.

Formula	C ₈₁ H ₇₂ Ce ₃ F ₅₄ N ₄ O ₂₆
M[g.mol ⁻¹]	2963.79
Crystal system	monoclinic
Space group	P21/n
a(Å)	12.1791 (4)
b(Å)	50.4661 (19)
c(Å)	18.1310 (7)
α[°]	90
β[°]	93.042 (1)
γ[°]	90
V[Å ³]	11128.2 (7)
Z	4
T(K)	200
2θ range	2.53-27.547
Reflns collected	48912
Independent reflns	25569
Observed reflns	13940
Parameters	1645
R1/ωR ²	0.0601/0.1163
Goof	0.971

The presence of three different magnetic units with three different Ce^{III} centers do not allow observing magnetic slow relaxation either with or without dc field on **15** and other derivatives.

3.5 Structural diversity in combination with TEMPO-OH radical

3.5.1 [Ln(hfac)₃(TEMPO-OH)(H₂O)]_n (Ln = Ce(**16**), Pr(**17**))

3.5.1.1 Structural description

The reaction of Ln(hfac)₃·3H₂O (Ln = Ce, Pr) with TEMPO-OH radical affords a one-dimensional compound. To the best of our knowledge this is the first time that Ce^{III} or Pr^{III}-TEMPO chains are obtained.

The single-crystal X-ray diffraction reveals that complex **16** crystallizes in P2₁/n space group (Table 3.5). The asymmetric unit is made of one Ce(hfac)₃·H₂O moiety and one TEMPO-OH radicals (Figure 3.7).

The Ce(hfac)₃·H₂O units are linked by radicals via ‘head to tail’ mode.⁴ Each Ce^{III} ion is nine-coordinated. The coordination polyhedron can be described as a spherical tricapped (O4, O5 and O7) trigonal prism (D_{3h}) with CSM = 0.634. The Ce-O bond lengths are in the 2.460(1)-2.606(1) Å range. Additional bond lengths and angles are listed in Table A3.5. The shortest intrachain Ce-Ce distance is 10.18(22) Å. The shortest interchain Ce-Ce distance is 6.52(13) Å. Hydrogen bond (O7-H1···O3) along this direction of shortest Ce-Ce distance is involved to link the adjacent chains. One may possibly consider this compound as a hydrogen-bonded 2D network. However, in our case we consider that the compound is better described as zig-zag chains.

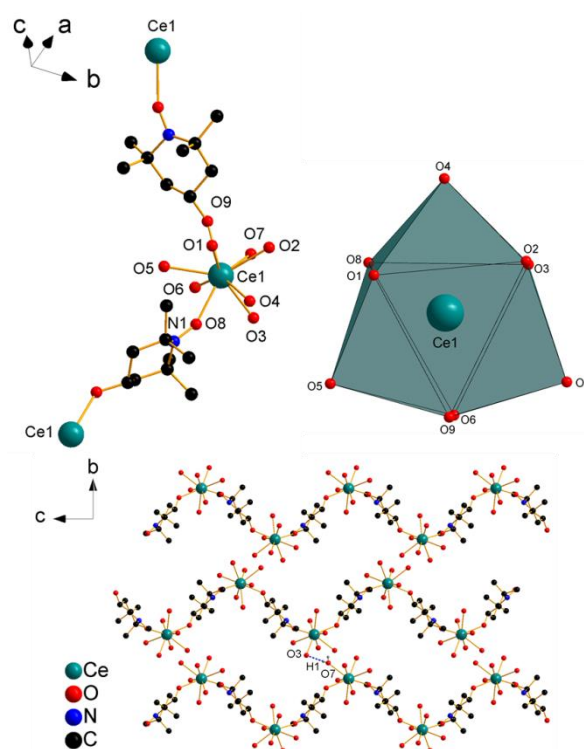


Figure 3.7 Representation of the zig-zag chain structure of **16** (left top) and coordination polyhedra of the Ce^{III} ion (right top). Fluorine, part of hydrogen and carbon (hfac⁻) atoms are omitted for clarity.

Table 3.5 Main crystallographic parameters for **16**.

Formula	C ₂₄ H ₂₂ Ce F ₁₈ N O ₉
M[g.mol ⁻¹]	950.55
Crystal system	monoclinic
Space group	P21/n
a(Å)	12.081(5)
b(Å)	19.185(5)
c(Å)	15.049(5)
α[°]	90
β[°]	100.15(5)
γ[°]	90
V[Å ³]	3433(2)
Z	4
T(K)	150
2θ range	2.53-27.503
Reflns collected	15370
Independent reflns	7884
Observed reflns	6700
Parameters	514
R1/ωR ²	0.0248/0.0555
Goof	1.004

Isostructurality of **16** and **17** has been assessed on the basis of their powder X-ray diffraction patterns (in Figure.A3.1).

3.5.1.2 Static magnetic properties

[Ce(hfac)₃(Tempo-OH)(H₂O)]_n (**16**)

The room temperature value of the $\chi_M T$ product for **16** is 1.07 cm³.K.mol⁻¹ (Figure 3.8). This is somewhat lower than the theoretical value of 1.17 cm³.K.mol⁻¹ expected for one isolated Ce^{III} ion ($J = 5/2$, $g = 6/7$ and $\chi_M T_{300K} = 0.8$ cm³.K.mol⁻¹) and one radical spin center (0.375 cm³.K.mol⁻¹).

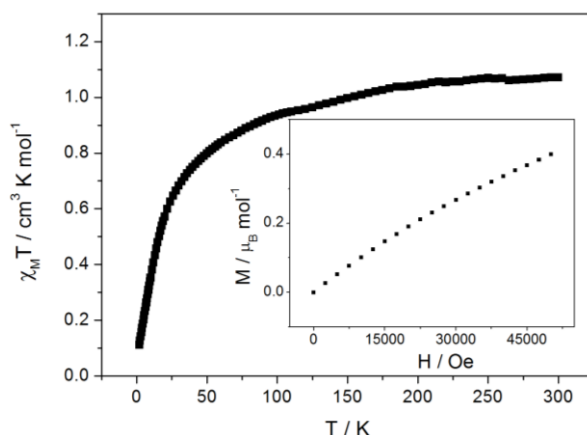


Figure 3.8 Temperature dependence of the $\chi_M T$ of compound **16**. The inset shows the magnetization curve measured at 1.8K.

Upon cooling, the $\chi_M T$ product decreases gradually to reach $0.11 \text{ cm}^3 \cdot \text{K} \cdot \text{mol}^{-1}$ at 2 K due to the progressive depopulation of the Stark sub-levels of the Ce^{III} ions. The magnetization of **16** is shown in the inset, the value of magnetization at 50 kOe is $0.4 \mu_B$.

$[\text{Pr}(\text{hfac})_3(\text{Tempo-OH})(\text{H}_2\text{O})]_n$ (**17**)

The room temperature value of the $\chi_M T$ product for **17** is $1.95 \text{ cm}^3 \cdot \text{K} \cdot \text{mol}^{-1}$ (Figure 3.9). This value well corresponds to the theoretical value of $1.97 \text{ cm}^3 \cdot \text{K} \cdot \text{mol}^{-1}$ expected for one Pr^{III} ion ($J = 4$, $g = 4/5$ and $\chi_M T_{300\text{K}} = 1.6 \text{ cm}^3 \cdot \text{K} \cdot \text{mol}^{-1}$) and one radical spin center ($0.375 \text{ cm}^3 \cdot \text{K} \cdot \text{mol}^{-1}$). Upon cooling, $\chi_M T$ decreases gradually to reach $0.55 \text{ cm}^3 \cdot \text{K} \cdot \text{mol}^{-1}$ at 2K due to the same reason as in **16**. The magnetization of **17** is shown in the inset, the value of magnetization at 50 kOe is $1.35 \mu_B$.

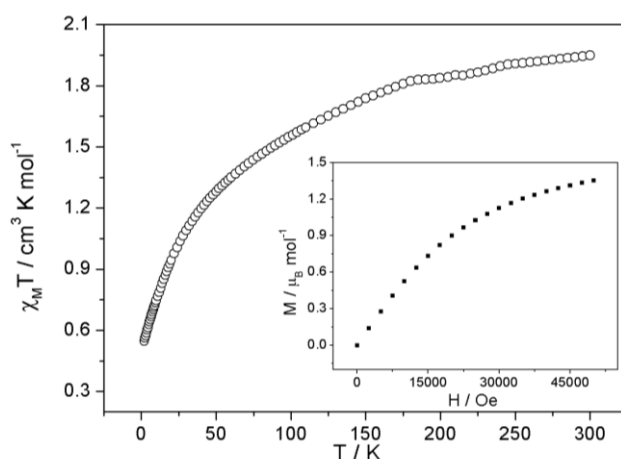


Figure 3.9 Temperature dependence of the $\chi_M T$ product of compound **17**. The inset shows the magnetization curve measured at 1.8 K.

3.5.1.3 Dynamic magnetic properties

The dynamic magnetic susceptibility measurements were performed on both **16** and **17**, while only the **17** exhibits field-induced SMM behavior. This is worth to notice that this is the first example of molecular chain made of Pr^{III} ion that shows SMM behavior.

The extracted relaxation times $\text{Ln}(\tau)$ show a nearly linear dependence on T^{-1} (Figure 3.11), indicating a pure Orbach process, which corresponds to the fifth parameter in equation (1.5).

$$\tau^{-1} = A_1 H^4 T + A_2 H^2 T + \frac{B_1}{1 + B_2 H^2} + C T^n + \tau_0^{-1} \exp(-U_{\text{eff}} / kT) \quad (\text{equ. 1.5})$$

The best fit gives a rather small value of energy barrier, $U_{\text{eff}} = 8.9 \pm 0.5 \text{ K}$ (with $\tau_0 = 9.26 \times 10^{-6} \text{ s}$). This value is comparable to the one observed on **2**, where, as for **17**, Pr^{III} -radical magnetic units are present. One cannot discard that the coupling between the Pr^{III} ion and the radical i) favor the ground state stabilization of the molecule⁵ ii) avoid the degeneracy of the

ground state⁶ and so the relaxation through temperature independent phenomena. These features are common with Tb^{III} derivatives, so a parallel between the behaviors of these two non-Kramer ions toward radical coordination may be drawn. Theoretical insight on that point may be necessary.

The relative high value of τ_0 let suspect the existence of other thermal-dependent regimes. The full fit is not successful except that only the Raman and Orbach processes are included. This provides $C = 2.61 \pm 0.30 \text{ s}^{-1} \text{ K}^{-7}$, $n = 7$, $\tau_0 = 1.27 \pm 0.63 \times 10^{-4} \text{ s}$, $U_{\text{eff}} = 4.32 \pm 0.88 \text{ K}$.

The Cole-Cole plots show the semicircle shape as expected for one relaxation mode, and the moderate value of α (0.22 at 1.8 K) confirms this behavior. The large values of χ_S/χ_T (0.23 at 1.8 K) highlight a sizeable amount of non-relaxing fraction of samples.

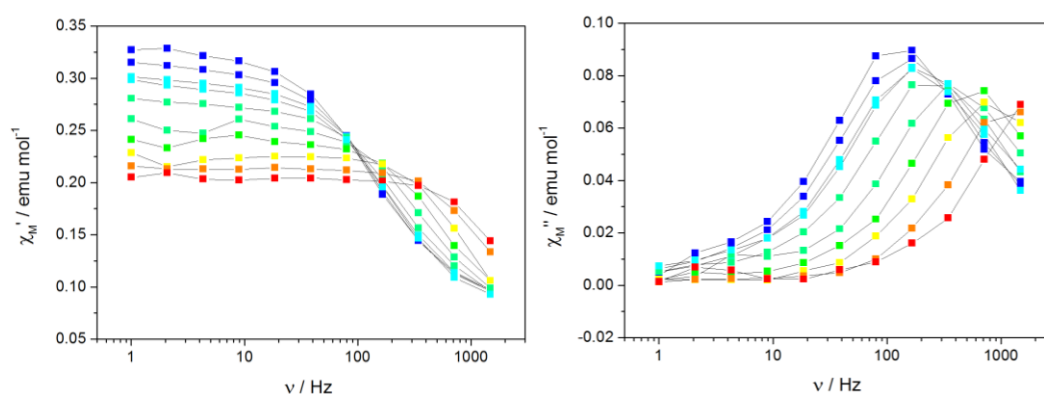


Figure 3.10 Frequency dependence of the in-phase (left) and out-of-phase (right) components of ac susceptibility for **17** under 3600 Oe dc field. Color mapping from 1.8 K to 3.2 K. Temperature plots of these data are available in Figure.A3.3. Lines are guides to the eye.

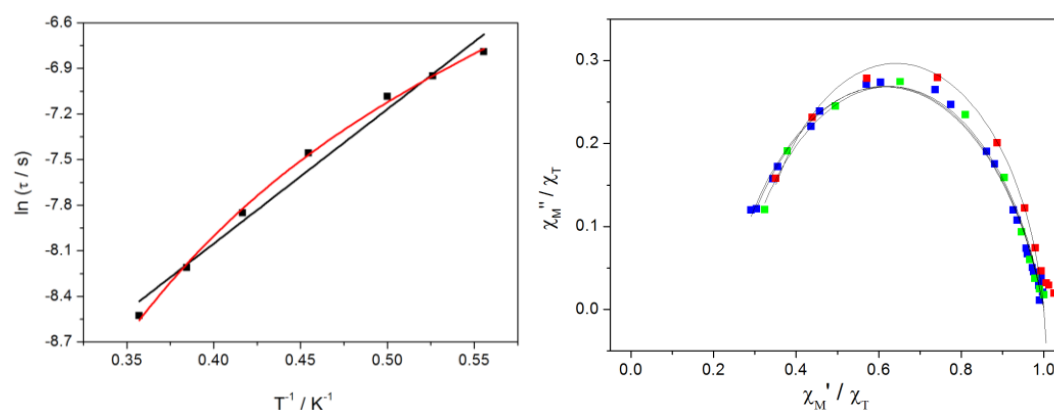


Figure 3.11 Plot of $\ln(\tau)$ versus T^{-1} (left). The black line represents the fit with only orbach process, while the red line represents the fit with Raman and Orbach processes. Normalized Cole-Cole plots for Pr(**17**) under 3600 Oe dc field (right). Color mapping from 1.8 K (blue) to 2.2 K (red). Lines are guides to the eye.

3.5.1.4 Comparison of SMM behaviors of compounds based on Pr^{III}

The chain compound $[\text{Pr}(\text{hfac})_3(\text{Tempo-OH})(\text{H}_2\text{O})]_n$ (**17**) and the zero dimensional compound $\{[(\text{Pr}(\text{hfac})_3)(\text{TEMPO-OMe})(\text{H}_2\text{O})]_2 \cdot \text{TEMPO-OMe}\}$ (**2**) both display SMM behavior. To the best of our knowledge these are the first two examples ever reported.

These two compounds have totally different structures, and both present relatively low symmetry environment but close to two different site symmetries (D_{2d} and D_{3h}). This highlights that the coordination geometry is not the main factor that influences the magnetic behavior. This is further confirmed by the magnetic behavior of their other related oblate derivatives that are not necessarily SMMs. In both cases, the low symmetry environment may cause a small separation between the ground state and the first excited state which finally results in a small energy barrier.

Table 3.6 Summary of the structural and magnetic information of compound **2** and **17**.

Compound	Coordination geometry(Site)	CSM	Energy barrier	τ_0 (s)	α	$(1/\chi_s/\chi_T)$
2 Pr1	Triangular dodecahedron (D_{2d})	0.437	6.3	1.24×10^{-5}	0.27 (1.8 K)	0.23 (1.8 K)
2 Pr2	Triangular dodecahedron (D_{2d})	0.564				
17	trigonal prism (D_{3h})	0.634	8.9	9.26×10^{-6}	0.22 (1.8 K)	0.23 (1.8 K)

Overall both samples display very similar dynamic parameters (energy barrier, characteristic relaxation time, relaxation time distribution and percentage of relaxing fraction). Future rationalization of the Pr^{III} -radical coupling by theoretical approach will be thus necessary to explain the observed behavior.

3.5.2 $[\text{Ln}(\text{hfac})_3(\text{TEMPO-OH})]_n$ (Ln = Dy(**18**) and Gd(**19**))

3.5.2.1 Structural description

When heavy (Ln = Dy(**18**), Gd(**19**)) instead of light lanthanides precursors are reacted with TEMPO-OH radical, the zig-zag chain turn into a linear chain.

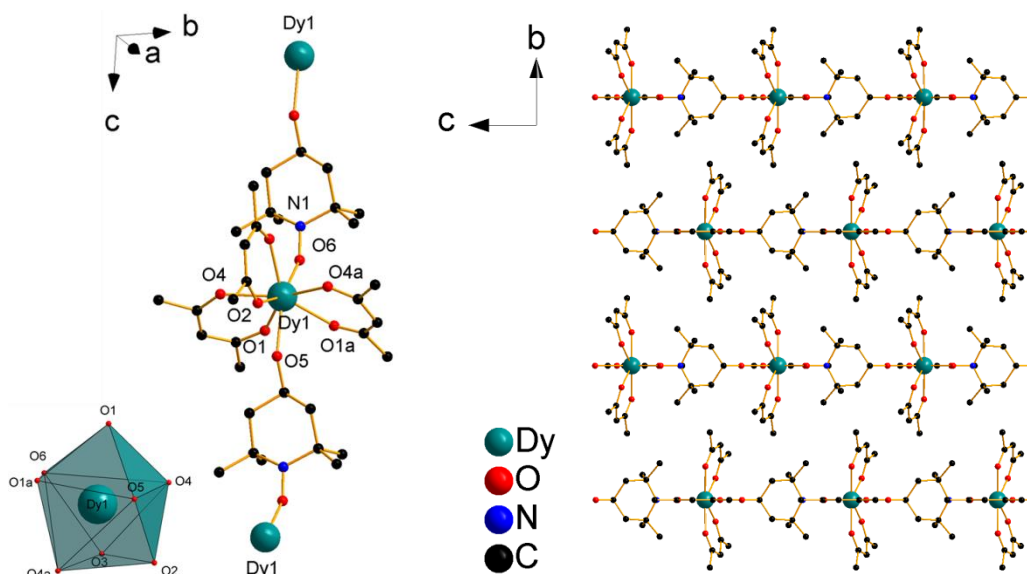


Figure 3.12 Representation of the 1D linear chain structure and polyhedra (left) and packing diagram along axis 'a' in **18** (right). Fluorine and hydrogen atoms are omitted for clarity.

Table 3.7 Main crystallographic parameters for **18**.

Formula	$C_{24}H_{20}DyF_{18}NO_8$
$M[g.mol^{-1}]$	954.91
Crystal system	orthorhombic
Space group	Pnma
$a(\text{\AA})$	20.089 (7)
$b(\text{\AA})$	17.537 (7)
$c(\text{\AA})$	9.534 (3)
$\alpha[^\circ]$	90
$\beta[^\circ]$	90
$\gamma[^\circ]$	90
$V[\text{\AA}^3]$	3359.0 (2)
Z	4
T(K)	150
2θ range	2.53-25.499
Reflns collected	13984
Independent reflns	3239
Observed reflns	2768
Parameters	277
$R1/\omega R^2$	0.0240/0.0529
Goof	1.068

Single-crystal X-ray diffraction reveals that compound **18** is a chain made of $Ln(hfac)_3(TEMPO-OH)$ units. The main structural data is listed in Table 3.7. The asymmetric unit is made of one $Dy(hfac)_3$ moiety and one TEMPO-OH radical (Figure 3.12).

One radical is coordinated to one Dy^{III} ion through O_{NO} and to another Dy^{III} ion through O_{OH} . The coordination polyhedron of Dy^{III} ion is completed by six oxygen atoms arising from three bidentate hfac- anions. The central core DyO_8 forms a severely distorted triangular dodecahedron with $CSM = 5.763$. The Dy-O distances are in the 2.30(2)-2.40(3) Å range. Detailed bond lengths and angles are listed in Table A3.8. The shortest Dy-Dy distance is

9.534 Å. Each chain is well isolated from the other with nearest Dy-Dy interchain distances of 10.62(4) Å. Powder X-Ray diffraction patterns indicate that **18** and **19** are isostructural (see Figure.A3.4).

3.5.2.2 Static magnetic properties

[Dy(hfac)₃(TEMPO-OH)]_n (18)

The dc magnetic susceptibilities were measured for polycrystalline powders of **18**(Figure 3.13). At room temperature, the value of $\chi_M T$ is 14.35 cm³.K.mol⁻¹, in agreement with the expected 14.45 cm³.K.mol⁻¹ for one uncoupled Dy^{III} ion plus one organic spin. Upon cooling, the $\chi_M T$ value keeps almost constant until around 20 K, small maxima is then observed, which suggests a weak ferromagnetic interaction between the Dy^{III} and radical ligand. Below 20 K, the $\chi_M T$ value drops quickly to reach a value of 5.66 cm³.K.mol⁻¹ at 2.0 K. The magnetization of **18** is shown in the inset, the value of magnetization at 50 kOe is 5.95 μ_B .

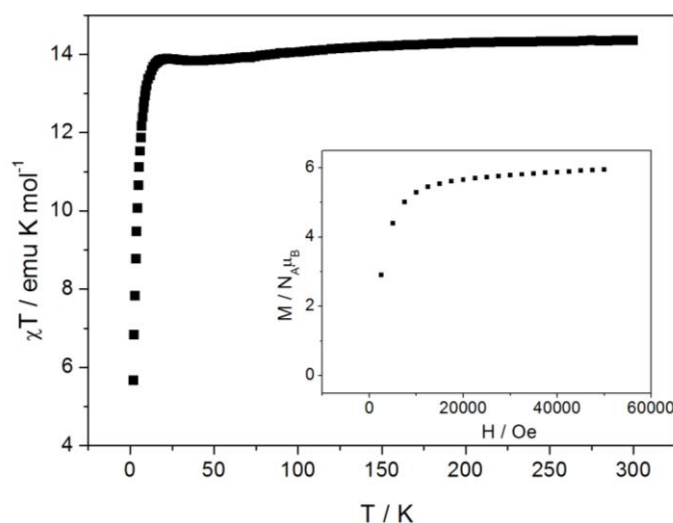


Figure 3.13 Temperature dependence of the $\chi_M T$ product of compound **18**. The inset shows the magnetization curve measured at 1.8 K.

[Gd(hfac)₃(TEMPO-OH)]_n (19)

The $\chi_M T$ product of **19** at 300 K is 8.11 cm³.K.mol⁻¹ (Figure 3.14), slightly lower than the theoretical value of 8.26 cm³.K.mol⁻¹ expected from an isolated Gd^{III} ($\chi_M T=7.88$ cm³.K.mol⁻¹) and one radical spin ($\chi_M T=0.375$ cm³.K.mol⁻¹). Considering these two spin carrier (Gd^{III} $S=7/2$ and radical $S=1/2$). It is commonly observed that at low temperature $\chi_M T$ can reach the limit of 10 or 6.0 cm³.K.mol⁻¹, depending on the ferromagnetic $S_{total} = 4$ state or the antiferromagnetic $S_{total} = 3$ state respectively.^{7,8} For **19**, upon cooling, the $\chi_M T$ product begins to go upwards rapidly to reach 9.85 cm³.K.mol⁻¹ at 2 K, being compatible with the ground ferromagnetic $S_{total} = 4$ state and a strong intramolecular interaction.

The exchange coupling parameter (J) can be determined from the $\chi_M T$ versus T curve simulation. The experimental data of **19** was analyzed with an expression (equ (2.1)) derived from a Heisenberg spin Hamiltonian, $H = -J_{\text{Gd-rad}} S_{\text{Gd}} \cdot S_{\text{rad}}$.⁹

$$\chi_M T = \frac{4N_A g^2 \mu_B^2}{k_B} \frac{7 + 15 \exp(4J_{\text{Gd-rad}} / k_B T)}{7 + 9 \exp(4J_{\text{Gd-rad}} / k_B T)} \frac{T}{T - zJ'} \quad \text{equ (2.1)}$$

The best fit was obtained with $J_{\text{Gd-rad}}/k_B = 14.1 \pm 0.2$ K (9.66 cm⁻¹), $g = 1.93 \pm 0.01$, $zJ' = 0.0084 \pm 0.0003$ K and $R^2 = 0.998$. The ferromagnetic coupling is rather strong (see Table 3.8). The ferromagnetic interchain interaction is small, a common feature observed on Gd-based chain (dipolar interaction).^{10, 11}

Table 3.8 Summary of magnetic exchange coupling constants (K) for Gd complexes.

Compound	$J_{\text{rad-Ln}}$ (K)	$J_{\text{rad-rad}}$ (K)	Ref
{Gd(dca) ₂ (OH)(NIT-p-Py) ₂ } ₂	8.3		12
((Me ₃ Si) ₂ Ng ₂ (THF)Gd) ₂ (μ -N ₂ ³⁻)	-38.8		13
Gd(hfac) ₃ (NITPh) ₂	-1.8	7.4	14
Gd(hfac) ₃ (NIT-o-Py)	-4.4		15
Gd(hfac) ₃ (NITPh-3-Br-4-OH) ₂	4.5	-17.6	16
Gd(hfac) ₃ (2PyNO)(H ₂ O)	-6.9		17
Gd(hfac) ₃ (DTBN)(H ₂ O)	-5.8		18
Gd(hfac) ₃ (6bpyNO)	-5.6		19
Gd(hfac) ₃ (TMIO) ₂	-6.3	-27	20
[Gd(hfac) ₃ (MeOH)(TEMPO)]	-1.8		7
[Gd ₂ (hfac) ₆ (H ₂ O) ₂ (dppnTEMPO)]	3.9		21
Gd(hfac) ₃ (TEMPO) ₂	-6.5/4.0 ¹	49.8 / Y	22
	-10.0/7.5 ¹	15.0 / La	34
[(Cp* ₂ Ln) ₂ (μ -bpym*)] ⁺	-14.4		23
Compound (11)	-10.0		
Compound (19)	14.1		this work

The field dependence of magnetization at 2K is simulated by the Brillouin function with $S_{\text{total}} = 4$ and $g = 2$. The solid line in the inset is slightly higher than the experimental data as 2 K is slightly too high to observe full saturation (see also $\chi_M T$ versus T curve).¹⁷

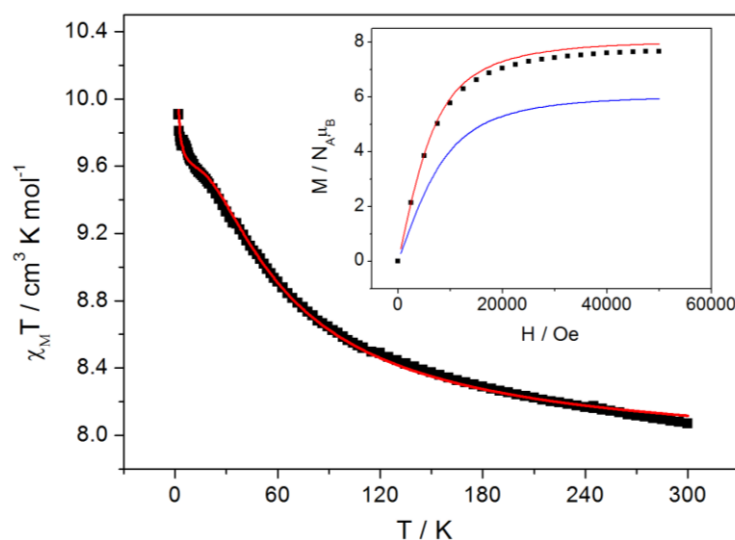


Figure 3.14 Temperature dependence of $\chi_M T$ for complex **19** with the best fit obtained with equ.2.1. In inset, the field variation of magnetization at 2 K is depicted with simulation with Brillouin equation for ferromagnetic Gd^{III}-radical interaction ($S_T=4$) (red curve) or antiferromagnetic Gd^{III}-radical interaction ($S_T=3$) (blue curve).

3.5.2.3 Dynamic magnetic properties

To check if **18** is a SMM, the dynamics of magnetization were investigated from the ac susceptibility measurements at various dc field, as shown in Figure.A3.5. The optimal field of 2400 Oe is selected. Clear frequency dependence of the in phase and out-of-phase components of the magnetization is observed (Figure 3.15). Strikingly at low temperature, two sets of peaks are evidenced in the χ_M'' vs frequency plots indicative of a slow (SR) and fast relaxation (FR) process.

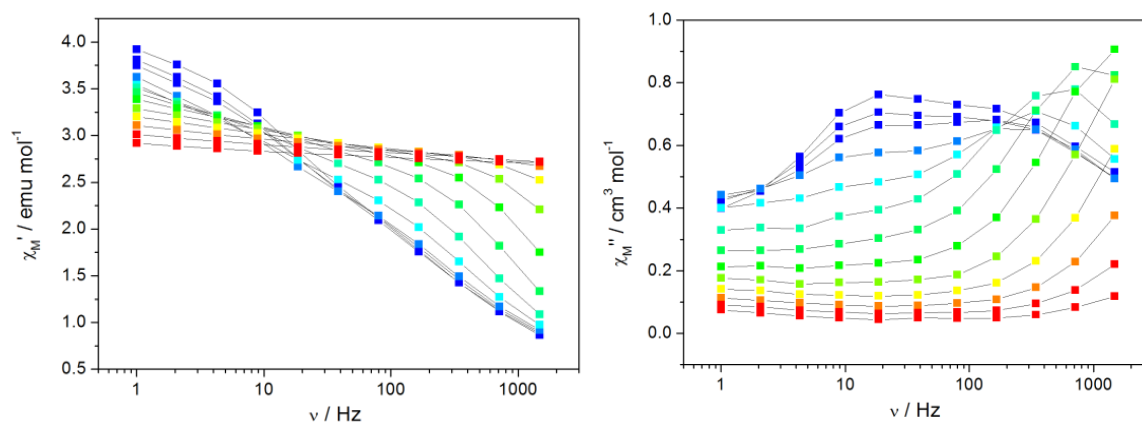


Figure 3.15 Frequency dependence of the in-phase (left) and out-of-phase (right) components of ac susceptibility for **18** under 2400 Oe dc field. Color mapping from 1.8 K to 4 K. Temperature plots of these data are available in Figure.A3.6. Lines are guides to the eye.

For the slow relaxation process (SR), the position of the peaks remains constant as the temperature is increased and this process is probably temperature-independent. As these peaks vanish the fast relaxation process (FR) takes place and the position of the peaks moves towards the higher frequency region. The T^{-1} dependence of $\text{Ln}(\tau)$ follows a thermally

activated behavior (fifth term of equation (1.5)). The energy barrier and the characteristic relaxation time can be determined as: $U_{\text{eff}} = 11.7 \pm 0.9$ K and $\tau_0 = 3.05 \times 10^{-6}$ s. Cole-Cole plots confirm the dual relaxation regimes and only the FR can be fitted (see appendix A3). The non-relaxing part is close to 0.23.

The relative high value of τ_0 let suspect the existence of other thermal-dependent regimes. The full fit is not successful except that only the Raman and Orbach processes are included. This provides $C = 0.40 \pm 0.05$ s⁻¹ K⁻⁹, $n = 9$, $\tau_0 = 1.16 \pm 0.84 \times 10^{-4}$ s, $U_{\text{eff}} = 5.22 \pm 1.34$ K.

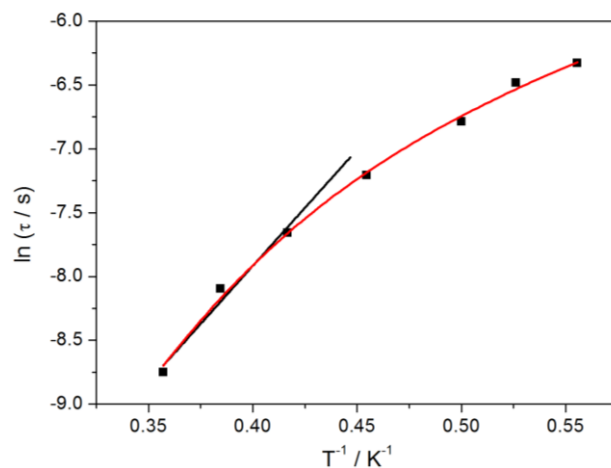


Figure 3.16 Relaxation time ($\ln \tau$) plotted against T^{-1} for Dy(**18**). Plot of $\ln(\tau)$ versus T^{-1} (left). The black line represents the fit with only Orbach process, while the red line represents the fit with Raman and Orbach processes.

3.5.3 Conclusion

In summary, reaction of $\text{Ln}(\text{hfac})_3$ with the TEMPO-OH radical, affords the targeted $(\text{Ln}^{\text{III}}-(\text{TEMPO-R}))_n$ chains. For $\text{Ln}^{\text{III}} = \text{Ce}^{\text{III}}$ (**16**) and Pr^{III} (**17**) a water molecule is bonded to the lanthanide ion and zig-zag chains are obtained. The water molecules allow for the creation of a hydrogen-bond network that connects the chain to form a pseudo-2D network. For $\text{Ln}^{\text{III}} = \text{Dy}^{\text{III}}$ (**18**) and Gd^{III} (**19**) linear chains are obtained.

The radical binds to the Ln^{III} ions in a ‘head to tail’ mode through NO and non-NO groups in both cases, which results in the isolation of the magnetic spin pairs (radical-Ln). Interestingly, only the non-Kramer’s Pr^{III} -based compound displays SMM behavior in the first case, whereas in the latter case it is the Kramer’s Dy^{III} -based compound that displays SMM behavior. We have successfully evaluated the ferromagnetic Gd-radical coupling and the obtained value (14.1 K (9.8 cm⁻¹)) is rather large among the ferromagnetic Gd-radical system.^{9, 24}

3.6 Structural diversity in combination with TEMPO-CN radical

3.6.1 Tri-spin monometallic SMM based on light lanthanide: [Ce(hfac)₃(TEMPO-CN)₂] (20)

3.6.1.1 Structural description

The single-crystal X-Ray diffraction reveals that compound **20** crystallizes in the monoclinic P2₁/c space group. Detailed crystallographic information is listed in Table 3.9.

Table 3.9 Crystallographic parameters for **20**.

Formula	C ₃₅ H ₃₇ Ce F ₁₈ N ₄ O ₈
M[g.mol ⁻¹]	1123.81
Crystal system	monoclinic
Space group	P 21/c
a(Å)	10.3996(4)
b(Å)	16.6323(7)
c(Å)	27.9464(10)
α[°]	90
β[°]	100.269(2)
γ[°]	90
V[Å ³]	4756.4(3)
Z	4
T(K)	150(2)
2θ range	2.03-27.512
Reflns collected	9943
Independent reflns	10915
Observed reflns	8849
Parameters	265
R1/ωR ²	0.0484/0.1269
Goof	1.013

The coordination of light lanthanides with TEMPO-CN does not afford a linear chain. In fact, only the O_{NO} atoms are bound to the lanthanide and the cyanide groups remain uncoordinated.

The asymmetric unit is made of one Ce(hfac)₃ moiety and two TEMPO-CN radicals (Figure 3.17). The Ce^{III} ion is coordinated by eight oxygen atoms, two from O_{NO} from TEMPO-CN radicals and six from three diketonate hfac⁻ groups. The Ln-O_{hfac} bond lengths are in the 2.38(6)-2.53(6) Å range. Additional bond lengths and angles are listed in Table A3.11. The nitroxide oxygen atoms are directly bound to the Ce^{III} ion with bond lengths of 2.405(7) Å, while the nitrogens from the CN groups are free. CSM highlight that Ce^{III} ions do not possess a well-defined symmetry of their surroundings, with CSM = 1.093 for a triangular dodecahedron geometry (D_{2d}) and CSM = 1.488 for a bi-augmented trigonal prism geometry (C_{2v}). The results are listed in Table 3.10. Compared with the only reported tri-spin complex [Ln^{III}(hfac)₃(TEMPO)₂] (Ln = Gd, La, Y)²² and [Dy(hfac)₃(TEMPO-acetamido)₂] (**6**) in

chapter 2, in which the two radical groups are located at “trans” positions with respect to the Ln^{III} center, the present compound **20** is in a rather “cis” configuration.

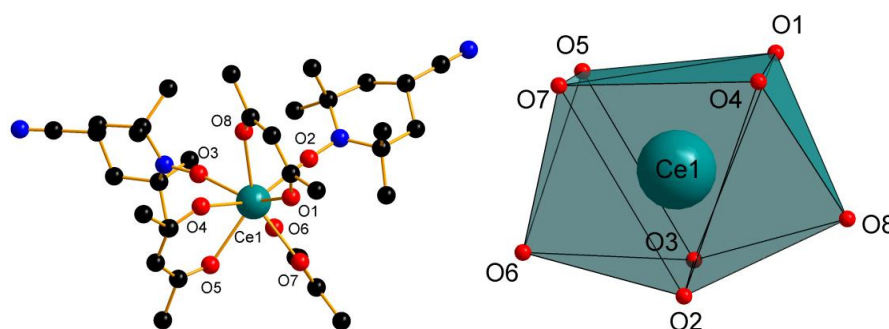


Figure 3.17 Representation of the asymmetric unit (left) and coordination polyhedron (right) for **20**.

3.6.1.2 Static magnetic properties

The room temperature value of the $\chi_{\text{M}}T$ product for **20** is $1.41 \text{ cm}^3 \cdot \text{K} \cdot \text{mol}^{-1}$ (Figure 3.18), which is close to the theoretical value at the non-interacting limit from two radical spin centers and one isolated Ce^{III} ion with $g = 6/7$ ($0.8 \text{ cm}^3 \cdot \text{K} \cdot \text{mol}^{-1}$). The $\chi_{\text{M}}T$ product decreases gradually upon cooling to a minimum of $0.32 \text{ cm}^3 \cdot \text{K} \cdot \text{mol}^{-1}$ at 2 K which is due to the depopulation of low lying excited states. The experimental magnetization is shown in the inset of Figure 3.18, which is recorded up to 5 kOe.

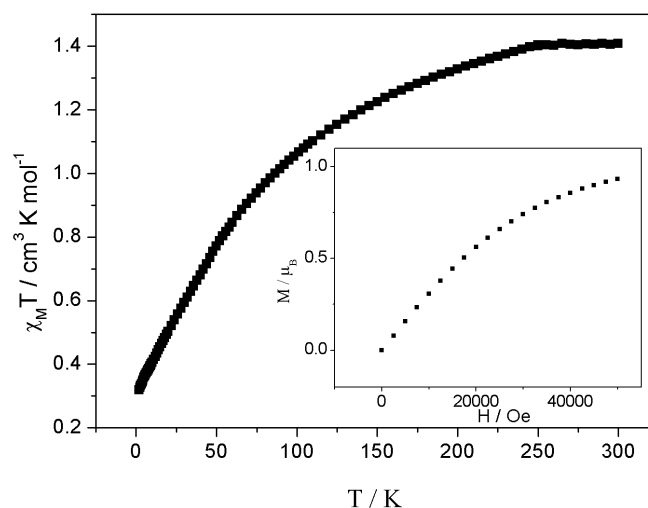


Figure 3.18 Temperature dependence of the $\chi_{\text{M}}T$ product of compound **20**. The inset shows the magnetization curve measured at 1.8 K.

3.6.1.3 Dynamic magnetic properties

The dynamics of magnetization in **20** were investigated from the ac susceptibility measurements at various dc field, as shown in Figure A3.8. Best suited field has been found to be 2800 Oe, resulting in the strong frequency-dependent out-of-phase peaks (Figure 3.19). The Cole-Cole plots of complex **20** can be fitted by the generalized Debye model (Figure 3.20). The values of α are in the range of 0.26-0.30, indicating a moderate distribution of relaxation times.

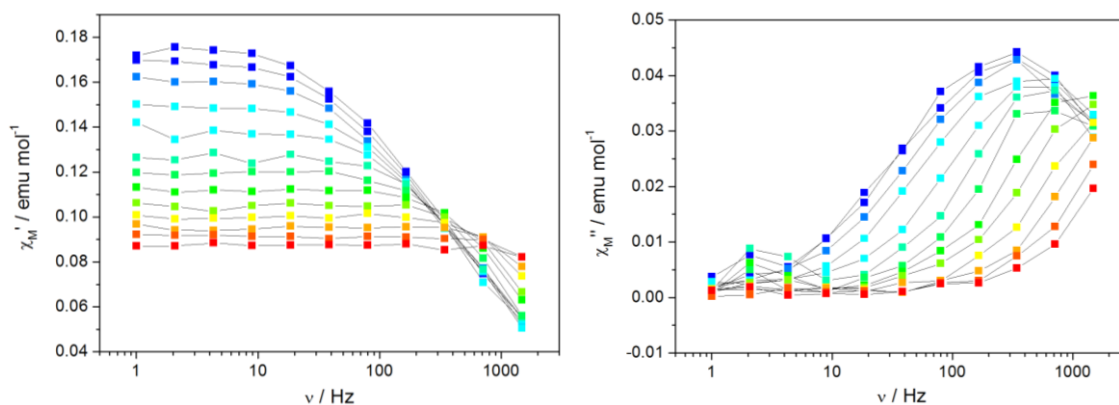


Figure 3.19 Frequency dependence of the in-phase (left) and out-of-phase (right) components of ac susceptibility for compound **20** in 2800 Oe. Color mapping ranges from 1.8 K to 4 K. Temperature plots of these data are available in Figure A3.9. Lines are guides to the eye.

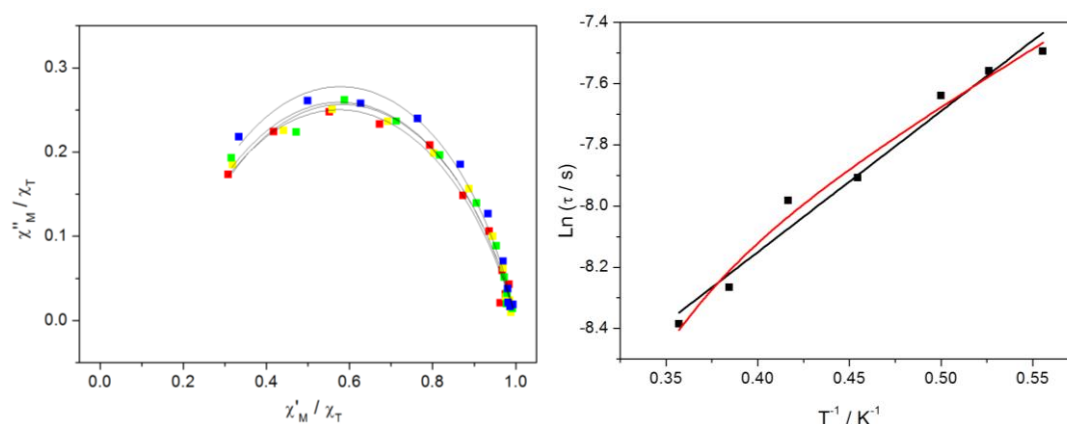


Figure 3.20 Cole-Cole diagrams measured from 1.8 K to 2.2 K for **20** (left). The solid lines represent fitting with an extended Debye model. Lines are guides to the eye. Plot of $\ln(\tau)$ versus (T^{-1}) for **20** (right). The black line represents the fit with only Orbach process, while the red line represents the fit with Raman and Orbach processes.

The $\ln(\tau)$ vs T^{-1} plot shows some kind of linearity in the investigated temperature range. A similar phenomenon is observed on $\{[(\text{Ln}(\text{hfac})_3(\text{TEMPO-OMe})(\text{H}_2\text{O}))_2 \cdot \text{TEMPO-OMe}]\}$ ($\text{Ln} = \text{Ce}(\mathbf{1}), \text{Pr}(\mathbf{2})$) and $[\text{Pr}(\text{hfac})_3(\text{Tempo-OH})(\text{H}_2\text{O})]_n$ (**17**), confirming that the Orbach process is the dominant magnetic pathway in these light-lanthanide-TEMPO based SMMs. Fitting by considering only the fifth term of equation (1.5) gives rise to a quite low energy barrier of 4.6 ± 0.3 K and quite high pre-exponential factor of $\tau_0 = 5.02 \times 10^{-5}$ s.

The relative high value of τ_0 let suspect the existence of other thermal-dependent regimes. The full fit is not successful except if only the Raman and Orbach processes are included. This provides $C = 0.09 \pm 0.05 \text{ s}^{-1} \text{ K}^{-9}$, $n = 9$, $\tau_0 = 7.84 \pm 2.78 \times 10^{-4} \text{ s}$, $U_{\text{eff}} = 3.59 \pm 0.68 \text{ K}$.

3.6.2 Trinuclear compound: $\{[\text{Dy}(\text{hfac})_3(\text{TEMPO-CN})_2] \cdot [\text{Dy}(\text{hfac})_3(\text{H}_2\text{O})_2]_2\}$ (**21**)

3.6.2.1 Structural description

When $\text{Dy}(\text{hfac})_3 \cdot 2\text{H}_2\text{O}$ is used instead of light lanthanide precursors, the tri-spin complex $\text{Dy}(\text{hfac})_3(\text{TEMPO-CN})_2$ is obtained but crystallizes with two uncoordinated $\text{Dy}(\text{hfac})_3 \cdot 2\text{H}_2\text{O}$. This result is obtained whatever the stoichiometry used in the synthesis process.

Compound **21** crystallizes in $C2/c$ space group. The crystallographic data are given in Table 3.10. As shown in Figure 3.21, the asymmetric unit is made of half of a $\text{Dy}(\text{hfac})_3(\text{TEMPO-CN})_2$ molecule and one $\text{Dy}(\text{hfac})_3 \cdot 2\text{H}_2\text{O}$ moieties. In addition, the large void in the structure may imply that certain solvent molecules are contained. However, we have not been able to determine the species of the solvent molecules and this latter have been refined by squeeze method. Dy1 is coordinated by six oxygen atoms from three hfac^- anions and two nitroxide oxygen atoms from two radicals. Dy2 is coordinated by six oxygen atoms from three hfac^- anions and two oxygen atoms from two water molecules. Selected bond lengths and angles are listed in Table A3.14.

Table 3.10 Crystallographic parameters for compound **21**.

Formula	$\text{C}_{65} \text{H}_{51} \text{Dy}_3 \text{F}_{54} \text{N}_4 \text{O}_{24}$
$M[\text{g} \cdot \text{mol}^{-1}]$	2785.6
Crystal system	monoclinic
Space group	$C2/c$
$a(\text{\AA})$	41.918(5)
$b(\text{\AA})$	11.197(5)
$c(\text{\AA})$	23.938(5)
$\alpha[^\circ]$	90
$\beta[^\circ]$	113.924(5)
$\gamma[^\circ]$	90
$V[\text{\AA}^3]$	10270(5)
Z	4
T(K)	150
2θ range	2.63-27.53
Reflns collected	23011
Independent reflns	11821
Observed reflns	11153
Parameters	689
$R1/\omega R^2$	0.0385/0.1313
Goof	1.098

The geometry of Dy1 is either close to a distorted square antiprism (D_{4d}) or triangular dodecahedron (D_{2d}) with $\text{CSM} = 0.947$ and $\text{CSM} = 0.903$, respectively. Dy2 adopts a

triangular dodecahedron geometry (D_{2d}) with the CSM= 0.433. Hydrogen bonds involving O8-H2 \cdots N2 connect the three molecules to form a five spin unit. However, each Dy(hfac) $_3$ ·2H $_2$ O moiety also binds a neighboring one through water supported hydrogen bonding (see Figure 3.23). Overall this pathway is the closest intermolecular Dy^{III}-Dy^{III} distance in **21** (6.06(24) Å).

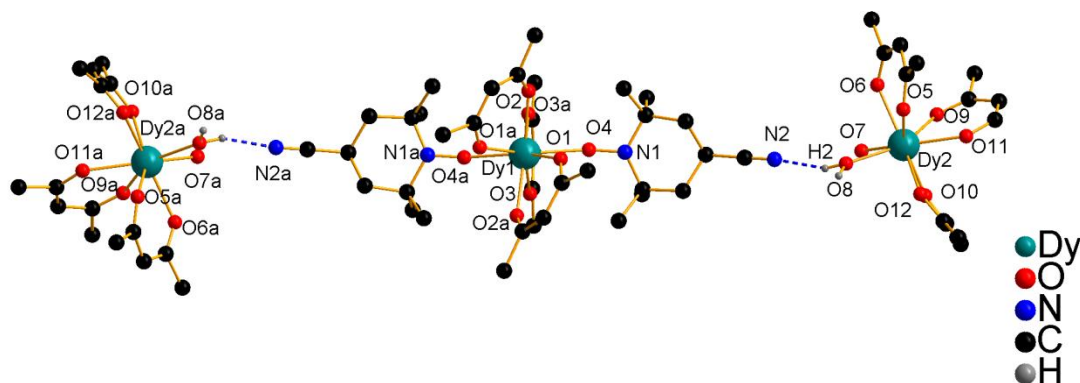


Figure 3.21 Representation of the molecular structure for **21**. The blue dashed lines represent the hydrogen bonds.

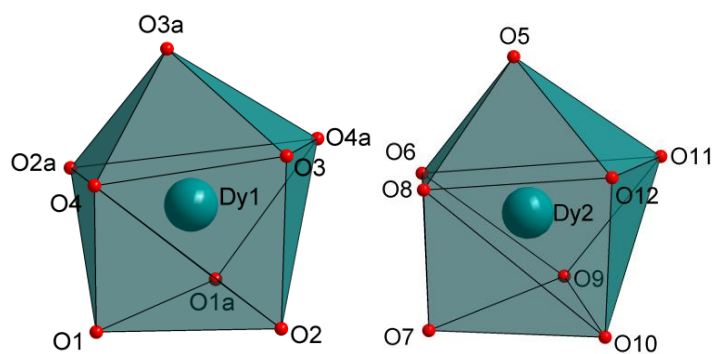


Figure 3.22 Coordination polyhedra of the two crystallographically independent Dy^{III} ions in compound **21**.

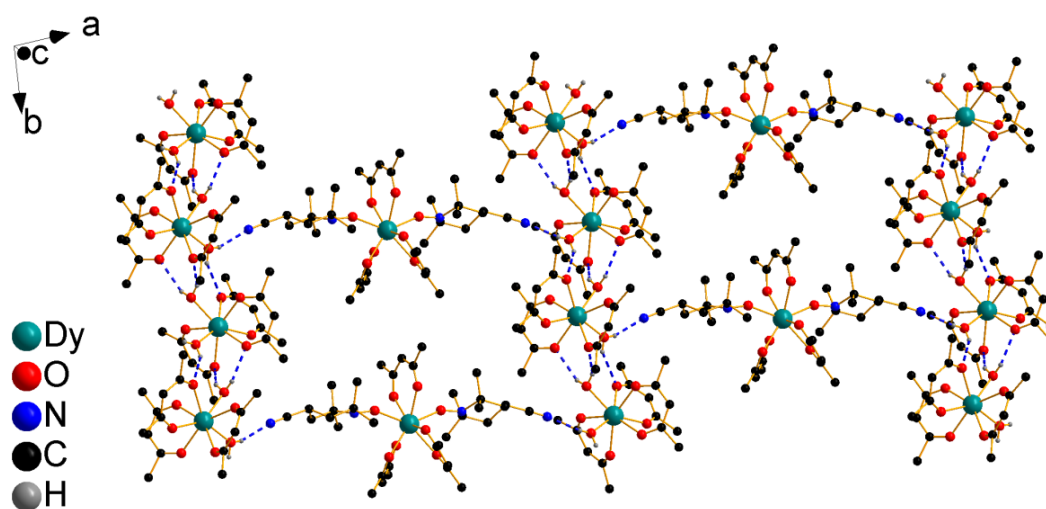


Figure 3.23 Packing diagram in compound **21**. The blue dashed lines represent the main hydrogen bonds in the structure.

3.6.2.2 Static magnetic properties

Static magnetic measurements have been carried out on polycrystalline powders of **21**. The $\chi_M T$ versus T plot is shown in Figure 3.24. The room temperature $\chi_M T$ value is $43.59 \text{ cm}^3 \cdot \text{K} \cdot \text{mol}^{-1}$, slightly larger than the theoretical value of $43.26 \text{ cm}^3 \cdot \text{K} \cdot \text{mol}^{-1}$ for three isolated Dy^{III} ions (${}^6\text{H}_{15/2}$, $g = 4/3$, $C = 14.17 \text{ cm}^3 \cdot \text{K} \cdot \text{mol}^{-1}$) plus two organic spins ($0.75 \text{ cm}^3 \cdot \text{K} \cdot \text{mol}^{-1}$). Upon cooling, the $\chi_M T$ value decreases progressively down to 80 K and drops abruptly to a minimum of $26.03 \text{ cm}^3 \cdot \text{K} \cdot \text{mol}^{-1}$ at 2.0 K, which could be attributed to the depopulation of the Stark sub-levels of $J = 15/2$ multiplet of the Dy^{III} ions. The magnetization is shown in the inset of Figure 3.24.

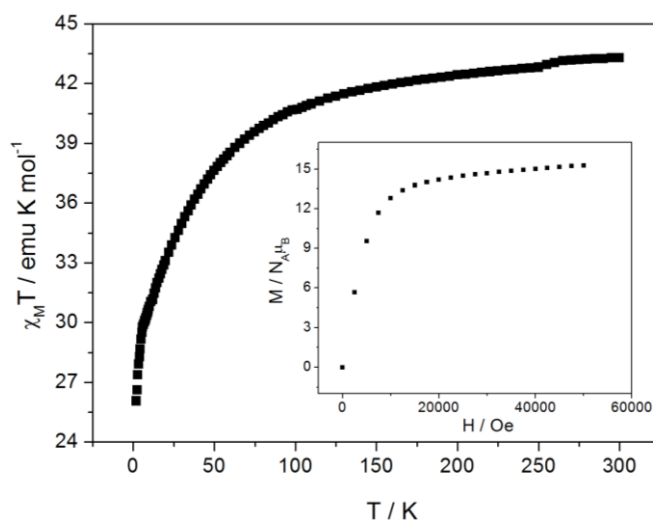


Figure 3.24 Temperature dependence of the $\chi_M T$ product of compound **21**. The inset shows the magnetization curve measured at 1.8 K.

In the absence of crystalline Gd^{III} derivative and given the quite complex spin structure in **21** ($J_{\text{rad-rad}}$, $J_{\text{Dy1-Rad}}$, $J_{\text{Dy2-Dy2}}$) we have not been able to further rationalize its dc magnetic properties.

3.6.2.3 Dynamic magnetic properties

To investigate the magnetization dynamics, alternating current (ac) magnetic susceptibilities have been measured. Under zero dc field, there are no signals of both in-phase and out-of-phase component of the susceptibility. The dynamic response is notably changed when recorded with a static field of 2400 Oe (Figure A3.10). As for **18** two sets of peaks are observed in the χ_M'' vs frequency curves (Figure 3.25).

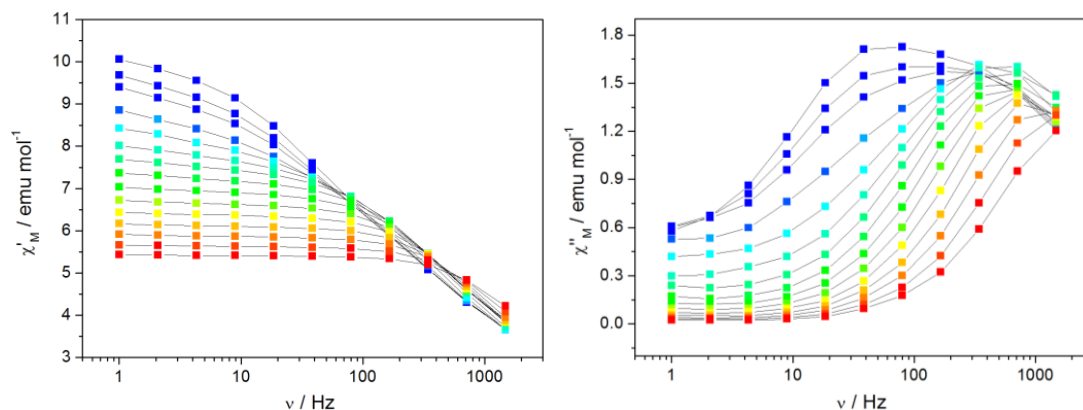


Figure 3.25 Frequency dependence of the in-phase (left) and out-of-phase (right) components of ac susceptibility for **21**. Temperature plots of these data are available in Figure A3.11 Lines are guides to the eye.

In the low temperature region, the broad χ'' maxima shift toward higher frequencies progressively while the temperature is increased, which supports a predominant thermally-assisted Orbach process. This slow relaxing (SR) process vanishes (or merges) around 2.75 K as the other set of peaks becomes visible (fast relaxing process, FR). Contrary to what observed on **18**, where only one Dy^{III} ion is present it seems reasonable to ascribe each set of peak to Dy1 or Dy2.^{25, 26,27} However at this stage of the study we cannot discard the possibility of a double relaxation process on one Dy^{III} center and a silent one on the other.

The relaxation time (τ) is plotted as a function of T^{-1} (see Fig 3.26). Obviously two thermal relaxation regimes take place with a smooth transition between them. The linearity of the SF and FR is described by the fifth term of equation (1.5) individually, yielding: $U_{\text{eff}} = 11.3 \pm 0.7$ K with $\tau_0 = 1.04 \times 10^{-5}$ s for SR and $U_{\text{eff}} = 8.9 \pm 0.5$ K with $\tau_0 = 1.10 \times 10^{-5}$ s for FR, respectively.

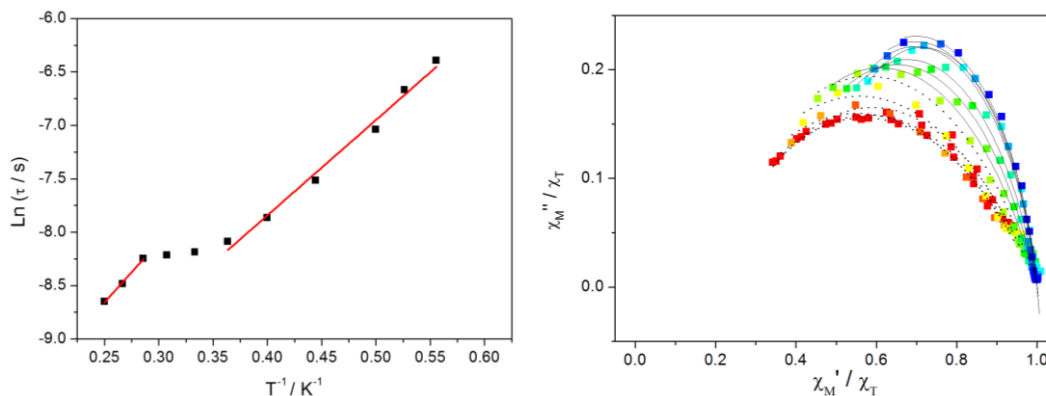


Figure 3.26 Plot of $\ln(\tau)$ versus (T^{-1}) for complex **21**. Normalized Argand plots for **21**. Color mapping from 1.8 K (blue) to 4.5 K (red). Black dotted lines represent the fits of SR process, black full lines stand for the fits of FR process. Lines are guides to the eye.

As expected, the Cole-Cole plot show clearly two sets of semi-circles depending on the considered temperature.²⁸ This results in quite high values of α that are in the range 0.48-0.56 for SR process and 0.27-0.39 for FR process, respectively. The non-relaxing fraction of

magnetization, characterized by the ratio χ_S/χ_T ,²⁹ ranges from 11 to 18% and 22 to 43 % for SR and FR process, respectively.

3.6.3 One dimensional 4f-2p chain, strong interaction and large energy barrier in: $[\text{Ln}(\text{hfac})_3(\text{TEMPO-CN})]_n$ (Ln = Tb(**22**) and Gd(**23**))

3.6.3.1 Structural description

When then Gd^{III} (**23**) and Tb^{III} (**22**) analogues of **21** are synthesized a strictly one dimensional compound is obtained.

Single-crystal X-Ray diffraction reveals that compound **22** crystallizes in the triclinic P-1 space group. The crystallographic data of complex **22** are given in Table 3.11. The asymmetry unit is consist of one Tb(hfac)₃ molecule and one TEMPO-CN molecule (Figure 3.27), where the radicals link the neighboring Tb(hfac)₃ molecules in a ‘‘head to tail’’ mode to form a linear chain. Tb^{III} ions are surrounded by six oxygen atoms from three hfac⁻ anions, one oxygen atom from the NO moiety of one radical and one nitrogen atom from another radical. The TbN₁O₇ core resembles a distorted square antiprism (D_{4d}) with CSM = 0.929. The Ln-O_{hfac} bond lengths are in the 2.33(3)-2.39(3) Å range, while the Ln-O_{Rad} bond length is 2.29 (2) Å, slightly shorter than that of Ln-O_{hfac}.

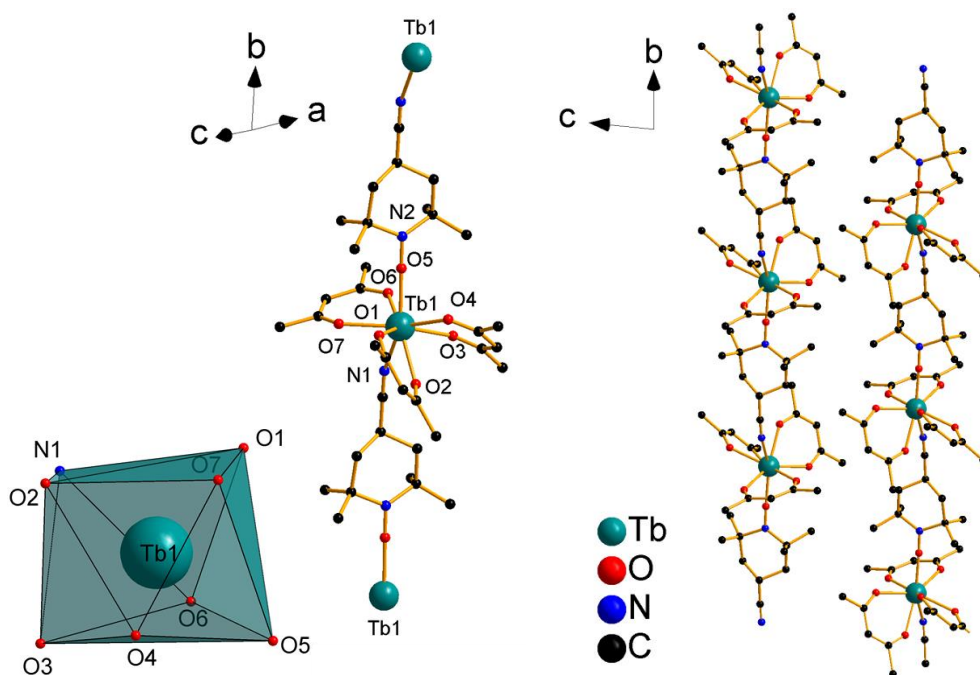


Figure 3.27 Representation of the coordination environment and polyhedra of Tb^{III} ion for Tb(**22**) (left). Packing arrangement of the chains along axis ‘a’ (right). All fluorine and hydrogen atoms are omitted for clarity.

The Ln-N bond lengths are 2.54 (3) Å. Additional bond lengths and angles are listed in Table A3.17. The closest intrachain Tb-Tb distance is 11.12(6) Å, ruling out the possible

trough-chain metal-metal and radical-radical interactions. The shortest interchain Tb-Tb distances are 8.41 (5) Å, suggesting possible dipole-dipole interactions between the chains.³⁰

Table 3.11 Crystallographic information of compound **22**.

Formula	C ₂₅ H ₂₀ F ₁₈ N ₂ O ₇ Tb
M[g.mol ⁻¹]	961.36
Crystal system	P-1
Space group	triclinic
a(Å)	11.0977(6)
b(Å)	11.1157(5)
c(Å)	16.4993(7)
α[°]	77.671(2)
β[°]	74.378(2)
γ[°]	61.352(2)
V[Å ³]	1711.59(14)
Z	2
T(K)	150
2θ range	2.89-27.51
Reflns collected	9967
Independent reflns	7776
Observed reflns	7134
Parameters	506
R1/ωR ²	0.0341/0.0794
Goof	1.067

Table 3.12 Summary of SHAPE factor of coordination geometry of compounds **20**, **21** and **22**.

Compound	Polyhedron	
20	BTPR (C _{2v}) 1.488	TDD (D _{2d}) 1.093
21Dy1	SAP (D _{4d}) 1.171	TDD (D _{2d}) 0.433
21Dy2	SAP (D _{4d}) 0.937	TDD (D _{2d}) 0.911
22	SAP (D _{4d}) 0.929	TDD (D _{2d}) 1.321

3.6.3.2 Static magnetic properties

[Gd(hfac)₃(TEMPO-CN)]_n (23)

The room temperature $\chi_M T$ value is 8.38 cm³.K.mol⁻¹ (Figure 3.28), close to the theoretical value of $\chi_M T_{300K} = 8.26$ cm³.K.mol⁻¹ for an uncoupled system for one Gd^{III} ion (⁸F_{7/2}, g = 2, $\chi_M T = 7.88$ cm³.K.mol⁻¹) plus one radical ($\chi_M T = 0.375$ cm³.K.mol⁻¹). Upon cooling, the $\chi_M T$ value decreases progressively at high temperature but drops quickly below 150 K. Down to 15K, the plot shows a small plateau, approaching 6.06 cm³.K.mol⁻¹, as the system reach a $S_{total} = 3$ ^{7, 18, 19, 31} as observed on compound **11**. The final drop is attributed to relatively weak intermolecular antiferromagnetic coupling.²²

The magnetic data were analyzed by a theoretical expression deduced from the spin Hamiltonian $H = -J_{\text{Rad}}S_{\text{Gd}}$ (equation (2.1), see also compound **11** and **19**) that also introduce a mean field zJ' intermolecular interaction. Best fit is obtained for $J_{\text{Gd-rad}}/k_{\text{B}} = -22.4 \pm 0.2$ K (-15.3 cm⁻¹), $g = 2.01 \pm 0.01$ and $R^2 = 0.999$. To the best of our knowledge this value is among the highest records of Gd-2p compounds ever reported (see Table 3.13).^{12, 17, 21} An additional antiferromagnetic interchain interaction is also considered ($zJ' = -0.04$ K or 0.027 cm⁻¹) as classically observed between 4f-radical-based chains and is expected to be of dipolar origin.^{30, 32, 33}

Table 3.13 Summary of magnetic exchange coupling constants (K) for Gd complexes.

Compound	$J_{\text{rad-Ln}}$ (K)	$J_{\text{rad-rad}}$ (K)	Ref
$\{\text{Gd}(\text{dca})_2(\text{OH})(\text{NIT-p-Py})_2\}_2$	8.3		12
$((\text{Me}_3\text{Si})_2\text{Ng}_2(\text{THF})\text{Gd})_2(\mu\text{-N}_2^{3-})$	-38.8		13
$\text{Gd}(\text{hfac})_3(\text{NITPh})_2$	-1.8	7.4	14
$\text{Gd}(\text{hfac})_3(\text{NIT-o-Py})$	-4.4		15
$\text{Gd}(\text{hfac})_3(\text{NITPh-3-Br-4-OH})_2$	4.5	-17.6	16
$\text{Gd}(\text{hfac})_3(2\text{PyNO})(\text{H}_2\text{O})$	-6.9		17
$\text{Gd}(\text{hfac})_3(\text{DTBN})(\text{H}_2\text{O})$	-5.8		18
$\text{Gd}(\text{hfac})_3(6\text{bpyNO})$	-5.6		19
$\text{Gd}(\text{hfac})_3(\text{TMIO})_2$	-6.3	-27	20
$[\text{Gd}(\text{hfac})_3(\text{MeOH})(\text{TEMPO})]$	-1.8		7
$[\text{Gd}_2(\text{hfac})_6(\text{H}_2\text{O})_2(\text{dppnTEMPO})]$	3.9		21
$\text{Gd}(\text{hfac})_3(\text{TEMPO})_2$	-6.5/4.0 ¹	49.8 / Y	22
	-10.0/7.5 ¹	15.0 / La	34
$[(\text{Cp}^*_2\text{Ln})_2(\mu\text{-bpym}^{\bullet})]^+$	-14.4		23
Compound (11)	-10.0		
Compound (19)	14.1		
Compound (23)	-22.4		this work

The field dependence of magnetization at 2 K is depicted in the inset of Figure 3.28. The saturation magnetization is $6.06 \mu_{\text{B}}$ close to the value expected for a $S_{\text{total}} = 3$ and $g = 2$.

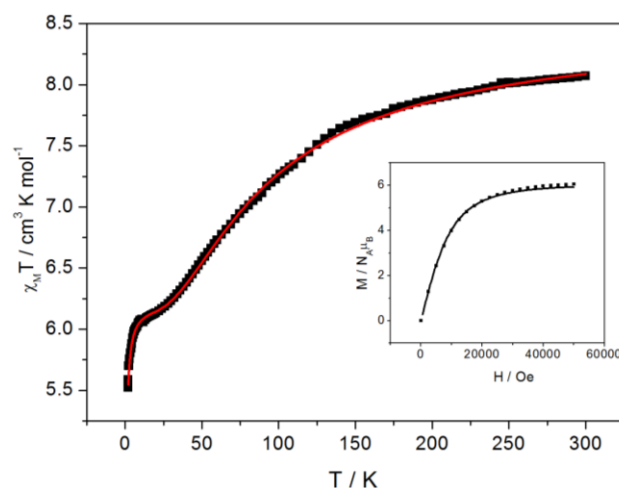


Figure 3.28 Temperature dependence of the $\chi_M T$ product for Gd(**23**) with the best fit of obtained with equ.2.1. The inset shows the field variation of magnetization at 2 K in depicted with best fit with Brillouin equation for $S_{\text{total}} = 3$. For details, see the text.

[Tb(hfac)₃(TEMPO-CN)]_n (22)

The room temperature $\chi_M T$ value is $12.13 \text{ cm}^3 \cdot \text{K} \cdot \text{mol}^{-1}$ (Figure 3.29), close to the expected value of $\chi_M T_{300\text{K}} = 12.20 \text{ cm}^3 \cdot \text{K} \cdot \text{mol}^{-1}$ for an uncoupled system for one Tb^{III} ion (${}^7\text{F}_6$, $g = 3/2$, $\chi_M T = 11.82 \text{ cm}^3 \cdot \text{K} \cdot \text{mol}^{-1}$) plus one radical spin ($\chi_M T = 0.375 \text{ cm}^3 \cdot \text{K} \cdot \text{mol}^{-1}$). Upon cooling, the $\chi_M T$ value decreases progressively and reaches a minimum of $7.28 \text{ cm}^3 \cdot \text{K} \cdot \text{mol}^{-1}$ at 2 K. A slight bump in the low temperature region is visible. The magnetization curve is shown in the inset of Figure 3.29. At 5 T, the magnetization value at 50 kOe is $5.0 \mu_B$, far lower than the expected value of $10 \mu_B$.

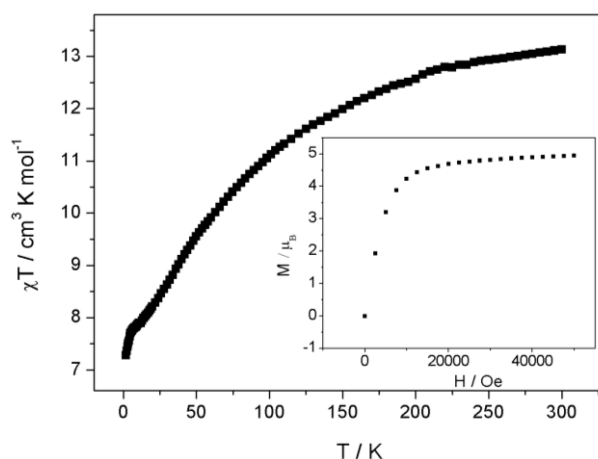


Figure 3.29 Temperature dependence of the $\chi_M T$ product for Tb(**22**).

Low-temperature (0.5 K) hysteresis curve has been recorded and a very small opening of magnetic hysteresis is observed around 2000 Oe.

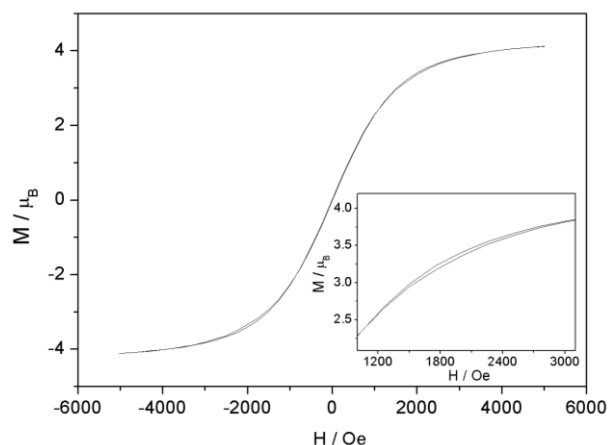


Figure 3.30 Hysteresis curves (M vs H) measured at 0.5 K for Tb(**22**). The inset shows the zoom of the small opening.

3.6.3.3 Dynamic magnetic properties

The dynamic magnetic susceptibility measurement reveals that the powder Dy^{III} derivative do not show any SMM properties as observed on **9**, that can be considered as a monomeric analogue of this chain.

For the Tb^{III} derivative (**22**), an optimum dc field of 2000 Oe has been selected (Figure A3.13) and applied to lift the degeneracy of the ground doublets. A very nice magnetic slow relaxation is observed until 10 K. A low temperature the relaxation is so slow that it shifts outside our investigable frequency range (Figure 3.31).

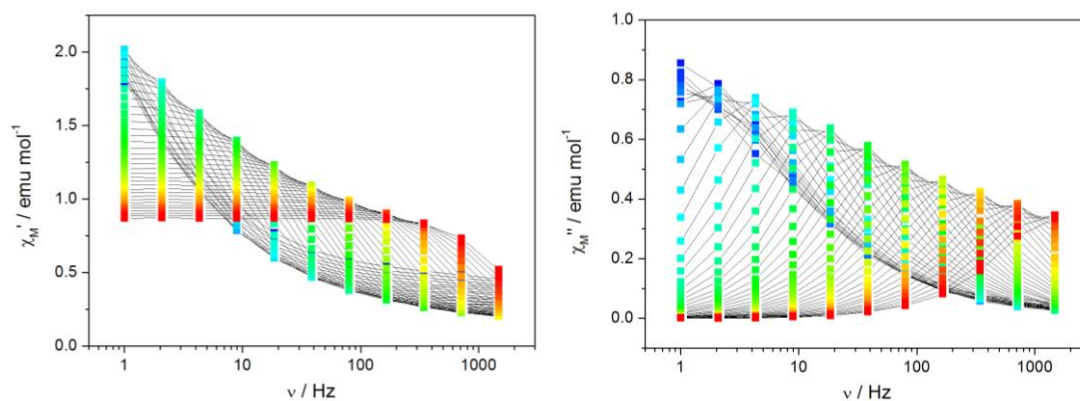


Figure 3.31 Frequency dependence of the in-phase (left) and out-of-phase (right) components of ac susceptibility with 2000 Oe dc field for Tb(**22**). Color mapping ranges from 3.2 (blue) to 9.8 K (red). Lines are guides to the eye.

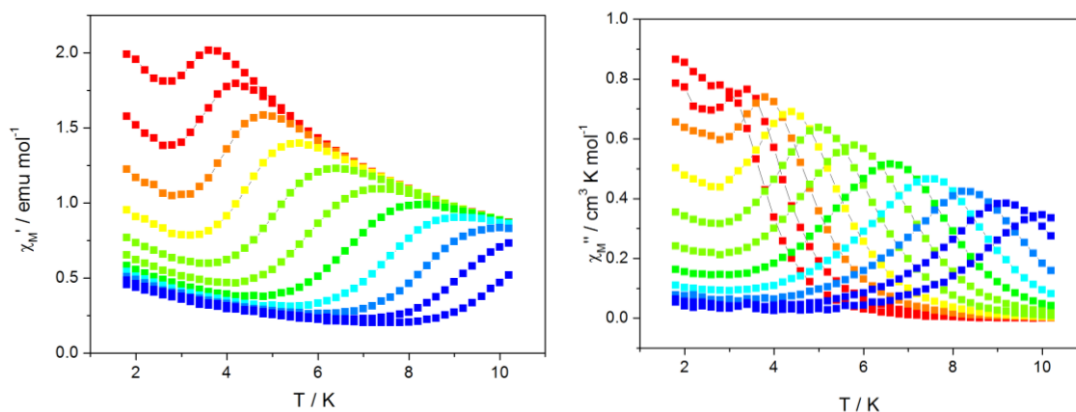


Figure 3.32 Temperature dependence of the in-phase (left top) and out-of-phase (right top) components of ac susceptibility under 2000 Oe dc field for Tb(22). Color mapping from 1 Hz (red) to 1500 Hz (blue). Lines are guides to the eye.

We extracted the relaxation time from the frequency-dependence measurements and plotted against T^{-1} in Fig 3.33. In the high temperature region, the strong linearity suggests an Orbach regime. At intermediate temperatures, the direct or Raman regime visible by the curvature becomes active. Notwithstanding the totally thermal-independent regime (QT) is not reflected in this plot, the tail of the out-of-phase has proved the existence of QT.

As done previously, the overall fit considering all the processes has been tried but was not successful. Only when direct and Orbach processes are involved, a poor fit is obtained with $A2 = 1.26 \pm 0.16 \times 10^{-6} \text{ s}^{-1} \text{ K}^{-1} \text{ Oe}^{-2}$, $\tau_0 = 2.83 \pm 0.69 \times 10^{-6} \text{ s}$, $U_{\text{eff}} = 43.2 \pm 1.75 \text{ K}$. Finally only the Orbach process has been taken into account to fit the linear region of the $\text{Ln}(\tau)$ vs T^{-1} curve, which affords the anisotropy barrier of $65.8 \pm 1.0 \text{ K}$, which is among the highest values reported for a Ln-radical compound.^{4, 23, 27, 34} Pre-exponential factor of τ_0 is $1.93 \times 10^{-7} \text{ s}$. The high effective activation energy is supposed to be associated with exchange bias present at the Tb site created by the magnetic coupling.³⁵

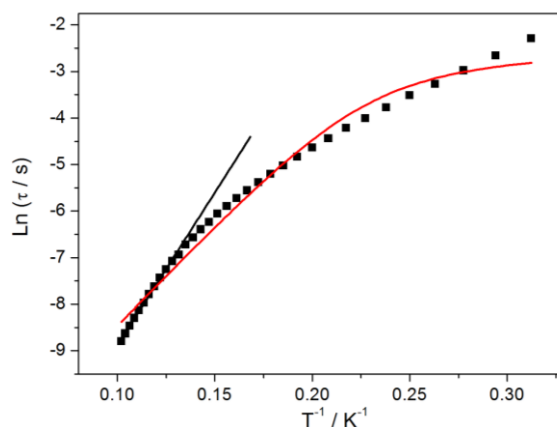


Figure 3.33 Plot of $\ln(\tau)$ versus (T^{-1}) for Tb(22). The black line represents the fit with only Orbach process, while the red line represents the bad agreement obtain from a fit with direct and Orbach processes.

The Cole-Cole plots (in Figure 3.34) display the typical semi-circle profiles. The relaxation times are extracted in the range of 2 K–9 K, giving rise to the maximum α value of 0.44, indicating a relatively wide distribution of the relaxation times, in accordance with the possible existence of multiple processes suggested by the $\ln(\tau)$ versus T^{-1} plot. However a quite important fraction of the sample (89%, $\chi_S/\chi_T = 0.11$) relaxes slowly.

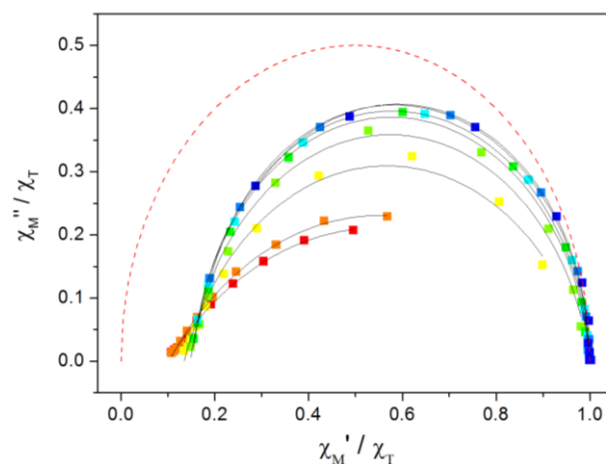


Figure 3.34 normalized Cole-Cole diagram for **22**. The solid lines represent fitting with an extended Debye model. Color mapping ranges from 2.0 (blue) to 9.0 K (red). The dashed line represents ideal single relaxation process ($\alpha = 0$, $\chi_S/\chi_T = 0$). Lines are guides to the eye.

Table 3.14 Main magnetic data extracted from the dynamic properties of **20**, **21** and **22**.

Compound	Energy barrier (K)	τ_0 (s)	α_{\max}	χ_S/χ_T
Ce (20)	4.6	5.02×10^{-5}	0.32 (1.8K)	0.15 (1.8K)
Dy1 (21)	8.9	1.04×10^{-5}	0.51 (1.8K)	0.14 (1.8K)
Dy2 (21)	11.3	1.10×10^{-5}	0.39 (3K)	0.22 (3K)
Tb (22)	65.8	1.93×10^{-7}	0.37 (3K)	0.11 (3K)

This example highlights the feasibility of Ln-based Tempo-R magnetic entities with good SMM properties especially when Tb^{III} ion is used and directly connected to the radical NO group (see also chapter 2). Theoretical insights about the nature of the Tb-radical interaction may be useful to understand the parameters that govern the magnetic slow relaxation in these compounds.

3.6.3.4 Comparison of Gd^{III}-Radical exchange interaction between **11**, **19** and **23**

The combination of TEMPO-R radicals with Gd^{III} has generated strong exchange coupling on $[\text{Gd}(\text{hfac})_3(\text{TEMPO-OCH}_2\text{CCH})(\text{H}_2\text{O})]$ (**11**), $[\text{Gd}(\text{hfac})_3(\text{TEMPO-OH})]_n$ (**19**) and $[\text{Gd}(\text{hfac})_3(\text{TEMPO-CN})]_n$ (**23**) which exceed the one observed on most of Gd-based nitrony nitroxide compounds. However, in all cases the corresponding Dy^{III} derivatives show bad SMM behavior and the Tb^{III} ones can either show optimized or degraded SMM behavior.

These findings highlights, as for compounds obtained in chapter 2 the need for theoretical rationalization of these magnetic couplings.

Table 3.15 Summary of the magnetic exchange interactions on **11**, **19** and **23**.

Compound	$J_{\text{Gd-Rad}}$ (K)	zJ'
11	-9.98	NA
19	14.1	0.0084
23	-22.4	-0.04

NA not available.

3.6.4 Conclusion

In summary, the coordinating R group of TEMPO-CN radical permits the construction of diverse edifices.

Reaction with light-lanthanide based precursor affords a monometallic tri-spin structure (**20**), while the reaction with heavy-lanthanide based precursor gives an unexpected monometallic penta-spin structure (**21**) and the targeted one-dimensional chain (**22**, **23**), respectively.

3.7 Conclusion

In this chapter, we have used five TEMPO radicals with R coordination sites in order to build extended 4f-TEMPO one-dimensional chains.

Table 3.16 Summary of the conditions of the synthesis and measurement.

Ligand	Dimension	Ce	Pr	Nd	Sm	Gd	Tb	Dy	Ho	Er	Tm	Yb
TEMPO-Methacrylate	1D							12				
TEMPO-OCOPh	1D	13										
TEMPO-Oxo	1D							14				
	2D network	15										
TEMPO-OH	1D	16	17			19		18				
TEMPO-CN	0D (tri-spin)	20										
	0D (penta-spin)							21				
	1D					23	22					

Only DC data is available	Non SMM	SMM	Not available	Not pure	Synthese not done
---------------------------	---------	-----	---------------	----------	-------------------

With TEMPO-Methacrylate (section 3.2) and TEMPO-OCOPh (section 3.3) molecular chains with Dy(**12**) and Ce(**13**) have been obtained but without observing any SMM behavior.

With Oxo-TEMPO (section 3.4), a one-dimensional chain Dy(**14**) is obtained as well as an unexpected two-dimensional network Ce(**15**). Unfortunately no ac susceptibility signals have been observed in both cases.

With TEMPO-OH (section 3.5), it appears that different kinds of structures can be obtained depending on the metal ions. Zig-zag chains with light-lanthanide non-Kramer's Pr^{III} (**17**) display SMM behavior whereas based compound rather than the Kramer's Ce^{III} (**16**) don't. Linear chains has been obtained with heavy-lanthanide ions with strong ferromagnetic interaction (14.1 K or 9.66 cm⁻¹) observed on the Gd^{III} (**19**) derivative, but small energy barrier on the Dy^{III} (**18**) derivative.

With TEMPO-CN (section 3.6), a trimeric radical-Ce-radical system (**20**) has been firstly obtained and is identified as a SMM. Then a complex Dy₂-(radical-Dy₁-radical)-Dy₂ system (**21**) which is composed of several magnetic entities is obtained. Additionally, the targeted one-dimensional chain compound has been found to be able to offer excellent magnetic behavior. The extremely strong antiferromagnetic exchange coupling is estimated as high as $J = -22.4$ K (15.3 cm⁻¹) on the Gd(**23**) analogue. A wide slow relaxing temperature range is seen on the Tb(**22**) analogue with rather high energy barrier (65.8 K) which is two times higher than most of nitronyle-nitroxide-based SMMs.³⁶⁻³⁹

In summary, the TEMPO-R radicals when coupled with 4f ions are of great interests for three main reasons:

- when light lanthanide are used, SMM behavior is more likely to be present contrary to what observed with most of diamagnetic ligands and even other radicals
- strong magnetic coupling can be observed with high ferro- or antiferromagnetic coupling observed on Gd^{III} derivatives.
- when Tb^{III} ions are used, excellent magnetic performance can be observed, far superior to the one seen with the corresponding Dy^{III} analogues.

References

1. M. Pinsky and D. Avnir, *Inorganic Chemistry*, 1998, 37, 5575-5582.
2. H. Zabrodsky, S. Peleg and D. Avnir, *Journal of the American Chemical Society*, 1992, 114, 7843-7851.
3. M. Ballesteros-Rivas, H. Zhao, A. Prosvirin, E. W. Reinheimer, R. A. Toscano, J. Valdés-Martínez and K. R. Dunbar, *Angewandte Chemie International Edition*, 2012, 51, 5124-5128.
4. L. Li, S. Liu, H. Li, W. Shi and P. Cheng, *Chemical Communications*, 2015, 51, 10933-10936.
5. H. Wada, S. Ooka, T. Yamamura and T. Kajiwara, *Inorganic Chemistry*, 2016, DOI: 10.1021/acs.inorgchem.6b01764.
6. J. D. Rinehart and J. R. Long, *Chemical Science*, 2011, 2, 2078-2085.
7. T. Nakamura and T. Ishida, *AIP Conference Proceedings*, 2016, 1709, 020016.
8. C. Lescop, D. Luneau, P. Rey, G. Bussière and C. Reber, *Inorganic Chemistry*, 2002, 41, 5566-5574.

9. P. Hu, M. Zhu, X. Mei, H. Tian, Y. Ma, L. Li and D. Liao, *Dalton Transactions*, 2012, 41, 14651-14656.
10. X. Wang, Y. Li, P. Hu, J. Wang and L. Li, *Dalton Transactions*, 2015, 44, 4560-4567.
11. A. C. Cristiano Benelli, Dante Gatteschi, and Roberta Sessoli, *Journal of Applied Physics*, 1993, 73, 5333 (1993).
12. C.-F. Hsu, S.-H. Lin and H.-H. Wei, *Inorganic Chemistry Communications*, 2005, 8, 1128-1132.
13. J. D. Rinehart, M. Fang, W. J. Evans and J. R. Long, *Nat Chem*, 2011, 3, 538-542.
14. C. Benelli, A. Caneschi, D. Gatteschi, L. Pardi, P. Rey, D. P. Shum and R. L. Carlin, *Inorganic Chemistry*, 1989, 28, 272-275.
15. C. Benelli, A. Caneschi, D. Gatteschi and L. Pardi, *Inorganic Chemistry*, 1992, 31, 741-746.
16. F.-X. Du, P. Hu, Y.-Y. Gao, F.-P. Xiao and Y.-N. Wu, *Inorganic Chemistry Communications*, 2014, 48, 166-170.
17. T. Ishida, R. Murakami, T. Kanetomo and H. Nojiri, *Polyhedron*, 2013, 66, 183-187.
18. T. Kanetomo and T. Ishida, *Chemical Communications*, 2014, 50, 2529-2531.
19. T. Kanetomo and T. Ishida, *Inorganic Chemistry*, 2014, 53, 10794-10796.
20. T. Nakamura and T. Ishida, *Polyhedron*, 2015, 87, 302-306.
21. S. G. Reis, M. Briganti, S. Soriano, G. P. Guedes, S. Calancea, C. Tiseanu, M. A. Novak, M. A. del Águila-Sánchez, F. Totti, F. Lopez-Ortiz, M. Andruh and M. G. F. Vaz, *Inorganic Chemistry*, 2016, 55, 11676-11684.
22. R. Murakami, T. Nakamura and T. Ishida, *Dalton Transactions*, 2014, 43, 5893-5898.
23. S. Demir, J. M. Zadrozny, M. Nippe and J. R. Long, *Journal of the American Chemical Society*, 2012, 134, 18546-18549.
24. J. Wang, M. Zhu, C. Li, J. Zhang and L. Li, *European Journal of Inorganic Chemistry*, 2015, 2015, 1368-1375.
25. P.-H. Lin, W.-B. Sun, M.-F. Yu, G.-M. Li, P.-F. Yan and M. Murugesu, *Chemical Communications*, 2011, 47, 10993-10995.
26. P. Bag, C. K. Rastogi, S. Biswas, S. Sivakumar, V. Mereacre and V. Chandrasekhar, *Dalton Transactions*, 2015, 44, 4328-4340.
27. R. Liu, L. Li, X. Wang, P. Yang, C. Wang, D. Liao and J.-P. Sutter, *Chemical Communications*, 2010, 46, 2566-2568.
28. X. Yi, K. Bernot, O. Cador, J. Luzon, G. Calvez, C. Daiguebonne and O. Guillou, *Dalton Transactions*, 2013, 42, 6728-6731.
29. G. Cosquer, F. Pointillart, S. Golhen, O. Cador and L. Ouahab, *Chemistry – A European Journal*, 2013, 19, 7895-7903.
30. P. Hu, X. Wang, Y. Ma, Q. Wang, L. Li and D. Liao, *Dalton Transactions*, 2014, 43, 2234-2243.
31. X. Wang, M. Zhu, J. Wang and L. Li, *Dalton Transactions*, 2015, 44, 13890-13896.
32. L. Bogani, A. Vindigni, R. Sessoli and D. Gatteschi, *Journal of Materials Chemistry*, 2008, 18, 4750-4758.
33. R. Liu, Y. Ma, P. Yang, X. Song, G. Xu, J. Tang, L. Li, D. Liao and S. Yan, *Dalton Transactions*, 2010, 39, 3321-3325.
34. E. M. Fatila, M. Rouzières, M. C. Jennings, A. J. Lough, R. Clérac and K. E. Preuss, *Journal of the American Chemical Society*, 2013, 135, 9596-9599.
35. R. Murakami, T. Ishida, S. Yoshii and H. Nojiri, *Dalton Transactions*, 2013, 42, 13968-13973.
36. F. Pointillart, K. Bernot, G. Poneti and R. Sessoli, *Inorganic Chemistry*, 2012, 51, 12218-12229.
37. J.-X. Xu, Y. Ma, D.-z. Liao, G.-F. Xu, J. Tang, C. Wang, N. Zhou, S.-P. Yan, P. Cheng and L.-C. Li, *Inorganic Chemistry*, 2009, 48, 8890-8896.
38. P. Hu, C. Zhang, Y. Gao, Y. Li, Y. Ma, L. Li and D. Liao, *Inorganica Chimica Acta*, 2013, 398, 136-140.
39. H. Tian, R. Liu, X. Wang, P. Yang, Z. Li, L. Li and D. Liao, *European Journal of Inorganic Chemistry*, 2009, 2009, 4498-4502.

4 Single-Molecule-Magnets based on photo-active ligand: $[\text{Ln}_2(\text{AZO})_6(\text{DMSO})_2(\text{H}_2\text{O})_2] \cdot 4\text{DMSO}$

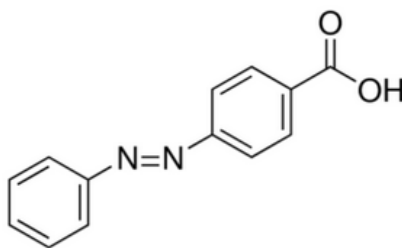
4.1 Introduction

In the previous chapters, we have used the paramagnetic organic radicals as the ligands, then the SMM behaviors are significantly influenced by the contribution of Ln–Rad magnetic coupling and the coordination geometry. From this chapter, we employed the diamagnetic ligands to coordinate the Ln^{III} . In this type of compounds, the ligand field plays important role in the SMM behaviors because the $\text{Ln}^{\text{III}}\text{–Ln}^{\text{III}}$ interaction are expected to be very weak.

It has shown in the literature that a small perturbation of geometry of the metal ions could dramatically influence the dynamic magnetic properties. With this in mind, the modulation of SMM behavior through isomerization is considered because the photo-switchable ligands are widely employed in chemistry. Azobenzene-4-carboxylic Acid (HAZO) is an odd used photo-switchable ligand.¹⁻³ The reverse cis–trans isomerization can be driven by light or occurs thermally in the dark. Thereby it may induce coordination sphere changes in the complex, finally leading to the switching of the SMM behavior.

In this chapter, we aim at synthesizing a new compound with AZO^- salts and try to modulate the SMM behavior by the photo-isomerization process.

Here, we thank Xiaohui YI, a former PhD student of the laboratory, for his contribution in the synthesis and preliminary magnetic measurements.



Scheme 4.1 Schematic representation of the HAZO ligand.

4.2 $[\text{Dy}_2(\text{AZO})_6(\text{DMSO})_2(\text{H}_2\text{O})_2] \cdot 4\text{DMSO}$ (24)

4.2.1 Structural description

The reaction of benzene mono- or polycarboxylate ligands with lanthanide salts in water affords in most cases polycrystalline material by co-precipitation. However in our case, reaction of sodium salt of HAZO ligand with $\text{DyCl}_3 \cdot 6\text{H}_2\text{O}$ provide an amorphous orange powder. We have tried to dissolve this powder in various organic solvent in order to

recrystallize the formed compound. Very large orange prismatic crystals have been obtained by using DMSO as recrystallization solvent.

Single Crystal X-ray diffraction measurement of **24** reveals that the full formula of this compound is $[\text{Dy}_2(\text{AZO})_6(\text{DMSO})_2(\text{H}_2\text{O})_2] \cdot 4\text{DMSO}$. It crystallizes in the triclinic space group P-1. Only one crystallographically independent Dy atom (Dy1) is found in the asymmetric unit. This latter is further composed of three AZO ligands, one H₂O molecule and one DMSO molecule, that all binds the Dy^{III} ion. Finally, two free DMSO molecules complete the asymmetric unit (Figure 4.1).

Table 4.1 Main crystallographic parameters for **24**.

Formula	$\text{C}_{90} \text{H}_{58} \text{Dy}_2 \text{N}_{12} \text{O}_{20} \text{S}_6$
$M[\text{g} \cdot \text{mol}^{-1}]$	2181.13
Crystal system	triclinic
Space group	P-1(N ^o 2)
a(Å)	8.2837(5)
b(Å)	16.9284(11)
c(Å)	18.0074(12)
$\alpha[^\circ]$	73.133(2)
$\beta[^\circ]$	82.367(2)
$\gamma[^\circ]$	86.299(2)
$V[\text{Å}^3]$	2394.2(3)
Z	1
T(K)	298
2 θ range	2.35-27.47
Reflns collected	9949
Independent reflns	10936
Observed reflns	9919
Parameters	594
$R1/\omega R^2$	0.0282/0.0887
Goof	1.054

Each Dy^{III} ion is coordinated by eight oxygen atoms. Four oxygen atoms (O2, O3, O4 and O5) come from two carboxylate clamps of two AZO ligands, thus act as bidentate ligands. Two other oxygen atoms (O1, O6) come from two different AZO ligands that bridges two Dy1 ions. Finally, the coordination polyhedron of Dy1 is completed by one water molecule (O7) and one DMSO molecule (O8). The Dy-O distances are in the 2.27(17) to 2.48(18) Å range (details see Table A4.1). The coordination polyhedron symmetry is determined by Continuous Shape Measurement (CSM) and is evaluated as a distorted bi-augmented trigonal prism (C_{2v}) with CSM = 2.394. The main structural data are reported in Table 4.1.

The shortest intramolecular Dy-Dy distance is 4.61(15) Å and the inversion center located in between the two Dy1 creates a Dy^{III} dimer. Given the short Dy-Dy distance significant dipole-dipole interaction^{4,5} maybe expected in this dimer.

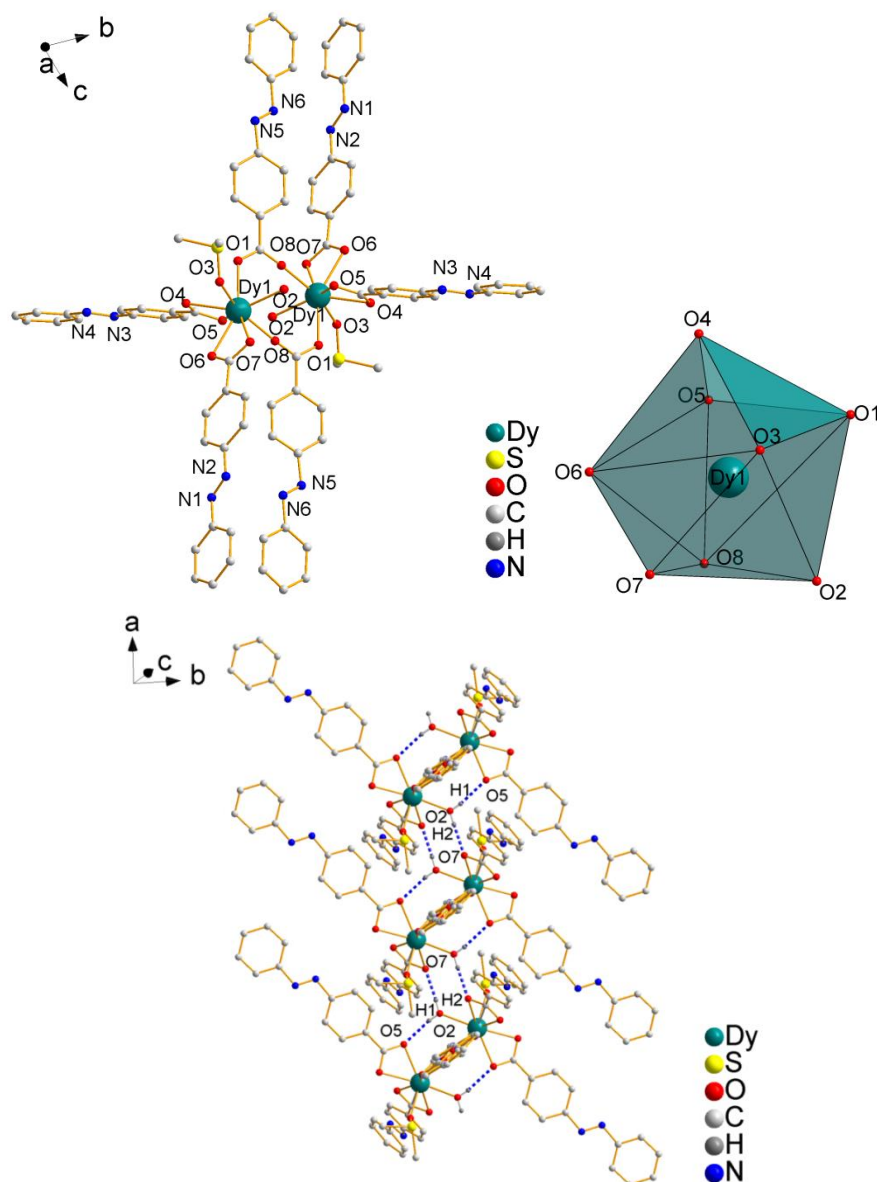


Figure 4.1 Representation of the molecular structure (top left) and polyhedra (top right) for **24**. All hydrogen atoms and free DMSO molecules are omitted for clarity. Intermolecular H-bond is stressed to clarify the pseudo zig-zag chain structure (bottom). Partial hydrogen atoms and all free DMSO molecules are omitted for clarity.

An interesting feature of **24** is that hydrogen atoms of the coordinating water molecule (O7) expand the dimeric structure into a one-dimensional chain edifice through intermolecular interactions. The intermolecular $\text{Dy}^{\text{III}}\text{-Dy}^{\text{III}}$ distance is 6.12(4) Å. Each hydrogen atom bonds two different oxygen atoms (O2-H2---O7 and O2-H1---O5) of two carboxylate clamps. Consequently four different O---H bonds connect the dimers two by two (Figure 4.1). Intermolecular π -stacking between the aromatic parts of the AZO ligands provide further robustness to crystal packing. Finally, two free DMSO molecules are found in between the chains.

In summary, **24** is a supramolecular chain of Dy^{III} -dimers decorated by photo-isomerizable ligands.^{1, 5, 6}

Magnetic measurements will be performed on grinded crystals. In order to check that no solvent-loss could impact the measurement, powder x-ray diffraction (PXRD) of the grinded crystals have been measured. Comparison of PXRD patterns demonstrate that main structural featured are kept when crushing the crystals (Figure A4.1). The yttrium-doped **24@Y** sample is also provided for comparison.

4.2.2 Static magnetic properties

The temperature dependence of the $\chi_{\text{M}}T$ product for **24** is depicted in Figure 4.2. At room temperature, the value of $\chi_{\text{M}}T$ is $27.26 \text{ cm}^3 \cdot \text{K} \cdot \text{mol}^{-1}$, slightly lower than the theoretical value of two non-interacting Dy^{III} ($\chi_{\text{M}}T = 28.34 \text{ cm}^3 \cdot \text{K} \cdot \text{mol}^{-1}$). On cooling, the value of $\chi_{\text{M}}T$ decreases gradually and drops rapidly below 50 K. This behavior is due to the depopulation of the Stark sublevels of $\pm M_{\text{J}}$ states of the Dy^{III} ion, and/or the antiferromagnetic interactions between the Dy^{III} centers.⁷ At 2 K, it reaches $17.21 \text{ cm}^3 \cdot \text{K} \cdot \text{mol}^{-1}$. The maximum value of the magnetization for **24** is $10 \mu_{\text{B}}$, which significantly deviate from the theoretical saturation of $20 \mu_{\text{B}}$, but is a common observation on Ln-based samples.⁸⁻¹¹

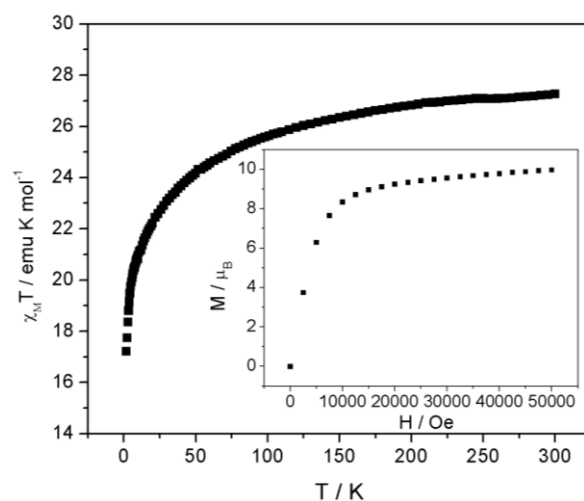


Figure 4.2 Temperature dependence of the $\chi_{\text{M}}T$ product for **24** (left), Inset: Field dependence of the Magnetization.

4.2.3 Dynamic magnetic properties

To investigate the magnetic relaxation behavior of **24**, ac magnetic susceptibility measurements have been carried out in the 2–6 K temperature range under zero dc field at frequencies between 1 and 1000 Hz (Figure 4.3). To explore the influence of the field on the magnetic relaxation, ac susceptibility measurements at various dc field have been investigated. Both the zero field and an optimal 1200Oe field are selected for the investigation. No peaks of χ_{M}'' have been observed, but around 1000 Hz, the tails tend to increase rapidly. It suggests that some peaks may exist in the higher frequency region. This is why we have undertaken an

additional ac measurement in collaboration with Pr Sessoli's group at the University of Florence (Italy) that possesses a high frequency home-made ac device. Zero dc field measurement shows a significant χ_M'' signal with peaks visible in the 10000-70000 Hz region.

The frequency-dependent characteristic of these peaks suggests a zero-field SMM, despite of fast relaxation. Owing to the Kramer's nature of Dy^{III} ions, dipole-dipole and hyperfine interactions should be account for the mixing of the two Kramer's ground states that allows the zero-field fast relaxation.^{7, 12-14}

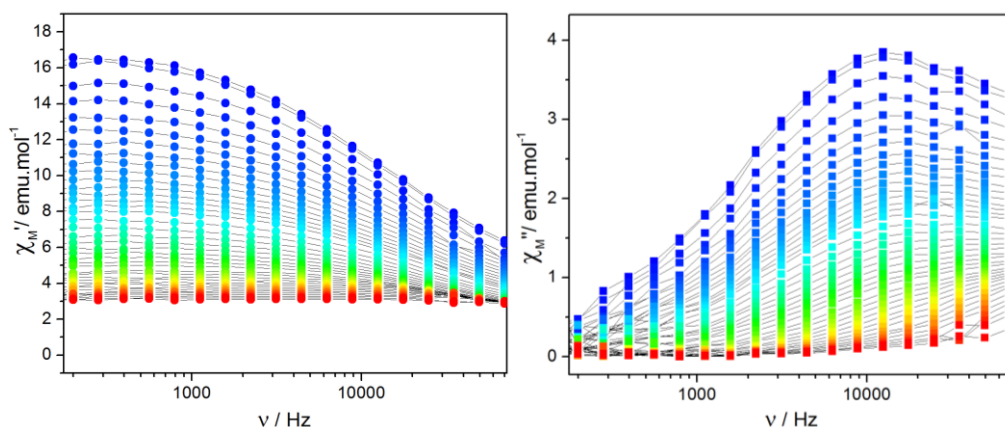


Figure 4.3 Temperature dependence of the in-phase (left) and out-of-phase (right) components of ac susceptibility for **24** under zero dc field. Color mapping ranges from 1.5 to 7.6 K. Temperature plots of these data are available in Figure A4.3. Lines are guides to eye.

The distribution of the relaxation times is relative wide as shown by the normalized Cole-Cole plots (Figure 4.4). The distribution of $(1-\chi_s/\chi_T)$ ranges from 0.64 to 0.83 (Table 4.13), indicative a large relaxing fraction of the sample.

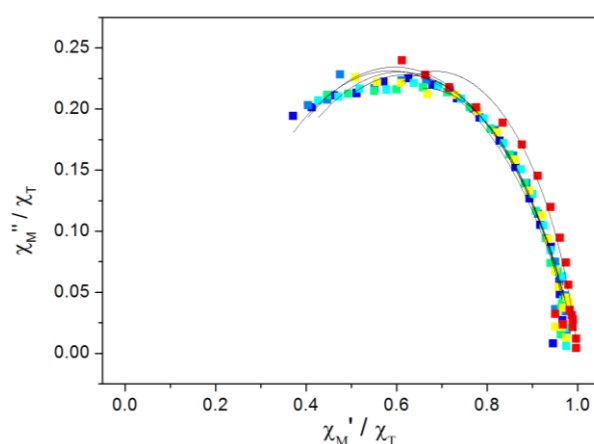


Figure 4.4 Normalized Cole-Cole diagram measured from 1.5 to 5 K for **24** under zero Oe dc field. The solid lines represent fitting with an extended Debye model. Lines are guides to eye.

To shortcut the QT, in most cases the external field is applied.^{15, 16} In this compound, a static dc field of 1200 Oe can slow down the magnetization. Frequency-dependent peaks are

observed to shift into the low frequency region (Figure 4.5). The QT effect is limited to a narrow temperature range because the efficient separation of different admixed $\pm M_J$ energy levels, consequently preventing the spins tunneling from the $+M_J$ state directly to the $-M_J$ state. The energy barrier will be discussed in section 4.3 for comparison with the doping sample.

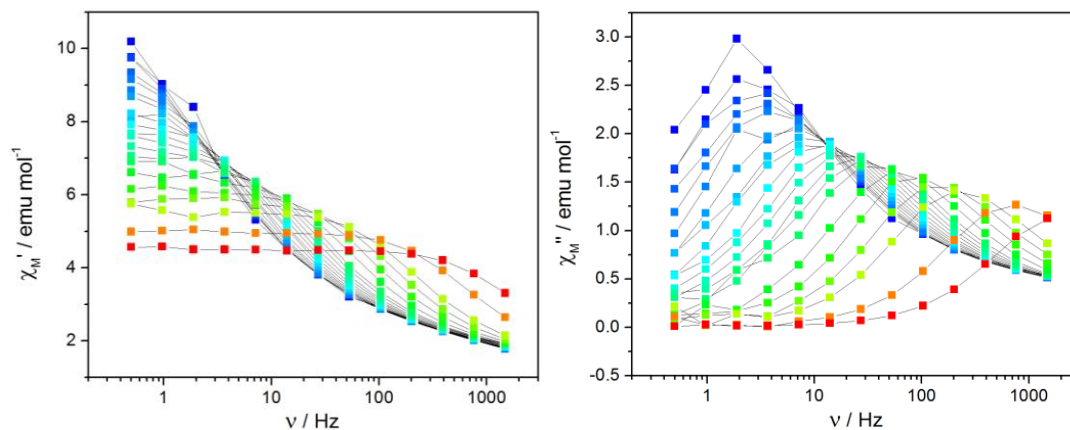


Figure 4.5 Temperature dependence of the in-phase (left) and out-of-phase (right) components of ac susceptibility for **24** under 1200 Oe dc field. Color mapping ranges from 1.8 to 5 K. Temperature plots of these data are available in Figure A4.4. Lines are guides to eye.

The graphic representation of the Cole-Cole plots of χ_M'' versus χ_M' displays the semicircle patterns, which were fitted based on a generalized Debye model (Figure 4.6 and Table A4.5). The fitting results of the data indicate a wide distribution of relaxation times with the maximum value of 0.5 of α , which is compatible with the reported values.^{17, 18} The relaxing fraction $(1 - \chi_s / \chi_T)$ is between 0.70 and 0.89, indicating that most of the sample is relaxing slowly.

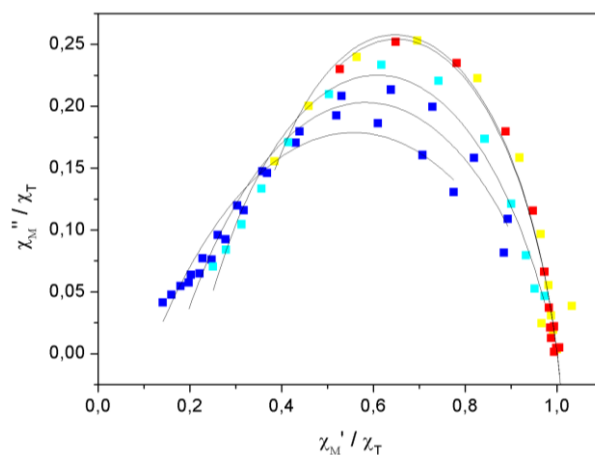


Figure 4.6 Normalized Cole-Cole diagram measured from 2 to 4.5 K for **24** under 1200 Oe dc field. The solid lines represent fitting with an extended Debye model. Lines are guides to eye.

4.3 Influence of magnetic dilution

To minimize the dipole-dipole interactions between the magnetic centers, and to evaluate their influence on the SMM properties of **24**, an Y^{III} doped sample (**24@Y**) has been prepared. Theoretical doping rate is 5% and the effective formula, determined on the basis of EDS measurement is $[\text{Y}_{1.886}\text{Dy}_{0.114}(\text{AZO})_6(\text{DMSO})_2(\text{H}_2\text{O})_2] \cdot 4\text{DMSO}$ (Table A4.6). The temperature dependence of $\chi_M T$ and the magnetization are shown in Figure A4.5.

As for the pure sample, ac susceptibility measurements at various dc field have been investigated for **24@Y** and the same fields are selected (see Figure A4.6). Figure 4.7 shows the alternating-current (ac) susceptibility at various frequencies under zero dc field of compound **24@Y**. Compared to the pure sample in 0Oe, the peaks of out-of-phase are observable in the frequency range of 1-1500Hz. The reason is that the magnetic dilution gives rise to the isolation of the Dy^{III} , reducing the QT deriving from the dipole-dipole interaction, instead of a splitting of degeneracy.^{19, 20}

A set of Cole-Cole diagrams at various temperatures are plotted and the data were well reproduced using generalized Debye models (Figure 4.8). The deviation of the normal semi-circle shape suggests the presence of multiple relaxation processes, confirming by the large distribution of α values ($0.14 < \alpha < 0.60$). The relaxing fraction ($1 - \chi_s / \chi_T$) is remarkably high (between 0.8 and 0.996) when compared with **24** indicating that almost all the sample relaxes slowly.

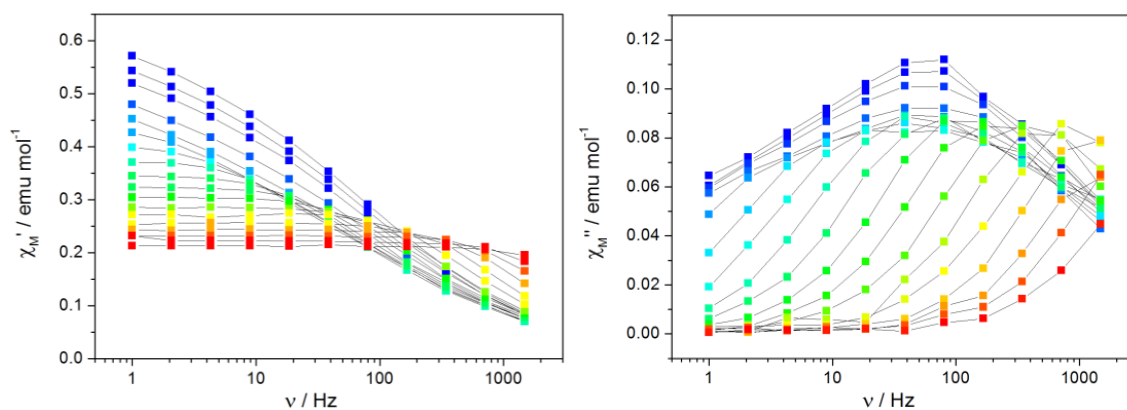


Figure 4.7 Frequency dependence of the in-phase (left) and out-of-phase (right) components of ac susceptibility for **24@Y** under zero dc field. Color mapping ranges from 1.8 (blue) to 5.75 K (red). Temperature plots of these data are available in Figure A4.7. Lines are guides to eye.

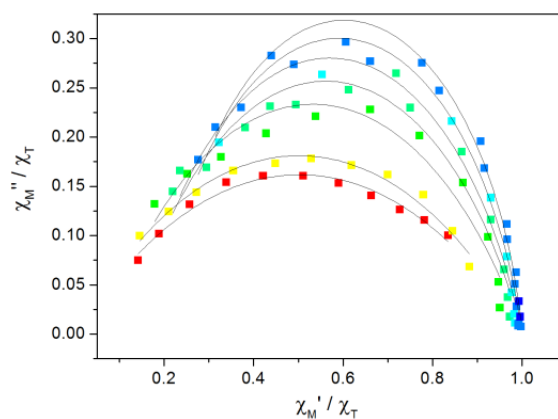


Figure 4.8 Normalized Cole-Cole diagram measured from 1.9 (blue) to 4.2 K (red) for complex **24@Y** under zero dc field. The solid lines represent fitting with an extended Debye model. Lines are guides to eye.

With an external dc field of 1.2 kOe, the χ_M'' maxima further shift toward the lower frequency region. Below 3 K, the complete χ'' maxima are visibly blurred, indicative of a rather slow relaxation of magnetization (Figure 4.9).

The Cole-Cole plots (Figure 4.10) show an almost ideal magnetic relaxation for **24@Y** with extremely low α values (0.10 at 3.2 K) associated with remarkably high relaxing fraction (0.94 at 3.2 K). One can stress that these two dynamic parameters are almost unchanged in all the investigated temperature range as another evidence of the strong robustness of the SMM behavior observed here.

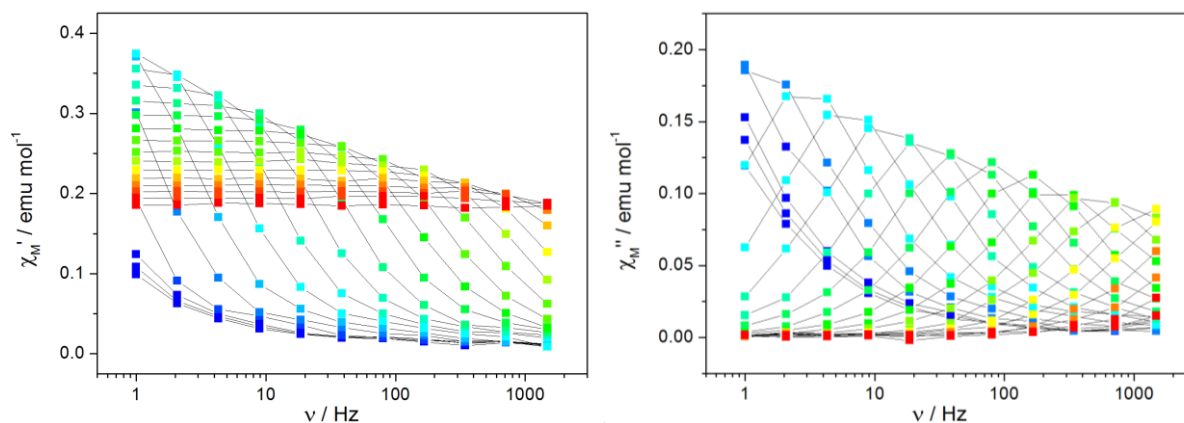


Figure 4.9 Temperature dependence of the in-phase (left) and out-of-phase (right) components of ac susceptibility for **24@Y** under 1200 Oe dc field. Color mapping from 1.8 (blue) to 6.5 K (red). Temperature plots of these data are available in Figure A4.8. Lines are guides to eye.

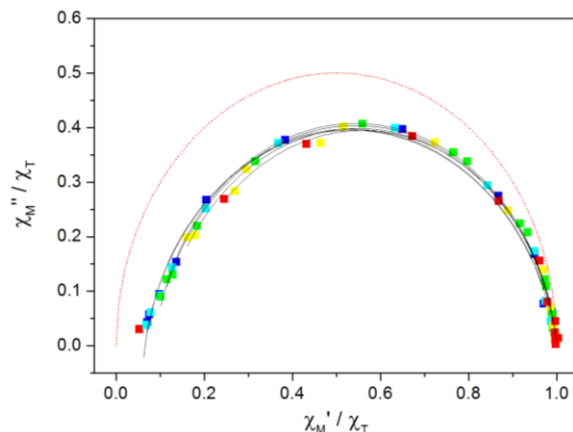


Figure 4.10 Normalized Cole-Cole diagram measured from 1.9 to 4.2 K for **24@Y** under 1200 Oe dc field. The solid lines represent fitting with an extended Debye model. Dotted red line represents the ideal relaxation curve ($\chi_s / \chi_T = 0$, $\alpha = 0$). Color mapping from 3.2 (blue) to 4.7 K (red). Lines are guides to eye.

Relaxation times as a function of T^{-1} for 0 and 1200 Oe dc field are reported in Figure 4.11. Similar procedure as in previous chapters has been used using (1.5):

$$\tau^{-1} = A_1 H^4 T + A_2 H^2 T + \frac{B_1}{1 + B_2 H^2} + CT^n + \tau_0^{-1} \exp(-U_{\text{eff}} / kT) \quad (\text{equ. 1.5})$$

For **24**, under zero dc field, only thermally independent process are operating.

For the in-field measurement, field dependence of τ^{-1} has been estimated considering the first three terms of equation (1.5), however, the data do not match with equation (1.5) with the meaningless negative value of B_1 (Figure A4.9). The failure of the fit may exclude the direct process. So only the last three regimes are considered, in which the third term is merged as τ_{tun}^{-1} for simplification. One should note that for the fourth terms, the parameter of n varies in different occasion. Generally $n = 9$ for Kramer's ions, whereas $n = 5$ in the case of several closely located excited Kramer's pairs. We have analyzed both cases. The fit is seemingly perfect but provides a negative value of τ_0 for the case of $n = 9$. A set of reasonable parameters are obtained $C = 0.50 \pm 0.02 \text{ s}^{-1} \text{ K}^{-5}$, $\tau_0 = 1.47 \times 10^{-9} \text{ s}$, $U_{\text{eff}} = 44.6 \pm 1.1 \text{ K}$ and $\tau_{\text{tun}} = 0.43 \pm 0.11 \text{ s}$ with $R^2 = 0.999$ for the case of $n = 5$. The latter parameters are reasonable for a SMM and were used to describe the SMM behavior.

For the doped compound **24@Y** in the absence of dc field, the relaxation occurs via both thermally-independent and thermally-dependent regimes. Best fit provides: $n = 5$, $C = 0.2 \pm 0.1 \text{ s}^{-1} \text{ K}^{-5}$, $U_{\text{eff}} = 41.6 \pm 4.0 \text{ K}$, $\tau_0 = 3.17 \pm 2.64 \times 10^{-8} \text{ s}$, $\tau_{\text{tun}} = 0.0041 \pm 0.0002 \text{ s}$ with $R^2 = 0.996$; an alternative set of parameters can be found with $n = 9$, $C = 0.00246 \pm 0.00254 \text{ s}^{-1} \text{ K}^{-9}$, $U_{\text{eff}} = 35.4 \pm 5.5 \text{ K}$, $\tau_0 = 1.01 \pm 0.98 \times 10^{-7} \text{ s}$, $\tau_{\text{tun}} = 0.0041 \pm 0.0002 \text{ s}$ with $R^2 = 0.996$.

The in-field measurements of **24@Y** can be fitted using only an Orbach process providing $U_{\text{eff}} = 34.9 \pm 1.3 \text{ K}$, $\tau_0 = 2.51 \times 10^{-7} \text{ s}$ with $R^2 = 0.987$.

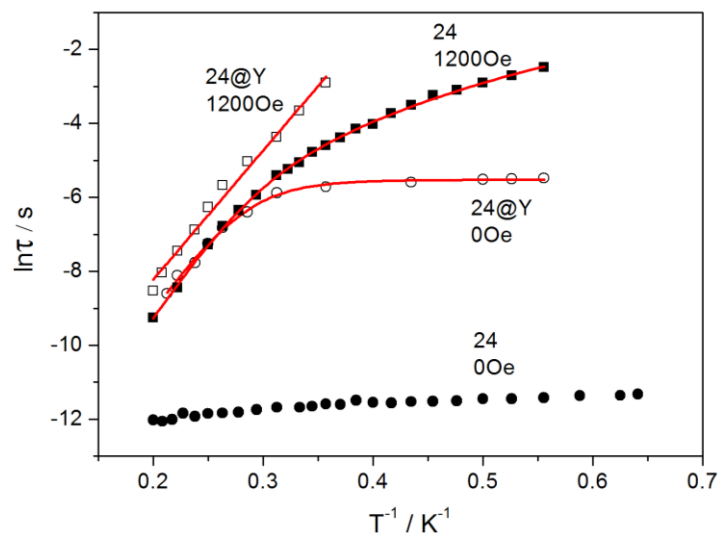


Figure 4.11 Relaxation times ($\ln(\tau)$) plotted against versus (T^{-1}) in 0 Oe (circles) and 1.2 kOe (squares) for **24**(solid) and **24@Y**(open). The red lines represent the best fit.

Hysteresis loops measurements of **24** and **24@Y** have been measured at 0.5 K on the same samples as the one used for ac measurements. Compound **24** does not show any opening of hysteresis, while **24@Y** opens up between 0 and 2000 Oe.

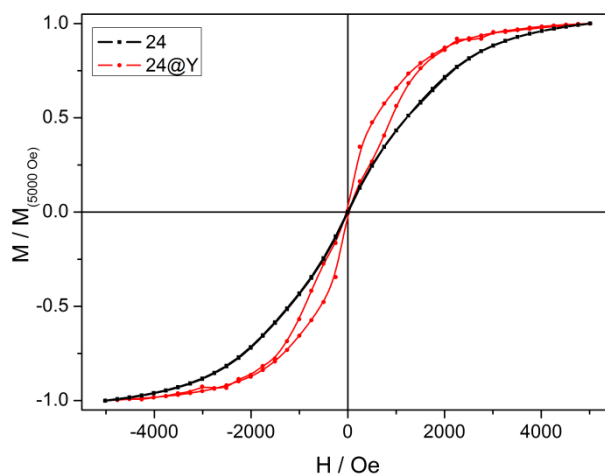


Figure 4.12 Hysteresis curves (M vs H) measured for **24** and **24@Y** at 0.5 K with a ^3He insert with a sweep rate of 15.5 Oe/s.

Table 4.2 Main magnetic data extracted from the dynamic properties.

Compound	Energy barrier (K)	α_{max}	$(1-\chi_S/\chi_T)_{\text{max}}$
Dy (24) (0 Oe)	NA	0.38	0.83
Dy (24) (1200 Oe)	44.6	0.51	0.89
24@Y (0 Oe)	41.6	0.60	0.996
24@Y (1200 Oe)	34.9	0.11	0.94

NA not available.

Overall, the doped compounds exhibits better SMM behavior than the pure sample. This could be related to coupled $\text{Dy}^{\text{III}}\text{-Dy}^{\text{III}}$ interaction which has accelerated both the zero-field and in-field magnetic relaxation, as well as the hysteresis. In addition, the doped derivative has influenced negatively the fraction of non-relaxation samples.

4.4 Influence of isomerization on SMM behavior

Azobenzene (AZO) ligand and their 3d-metal complexes are reported to be able to undergo trans-cis isomerization when irradiated with UV.^{1, 3, 6, 21, 22} Our primary idea to choose HAZO ligand is to control the SMM by the modification of the coordination geometry upon irradiation with UV on the basis of the fact that subtle change of geometry around Ln^{III} ions will affect the ac magnetic properties significantly.

Attempts to test this idea in solid state product have failed. Then we turn to the solution-switch strategy. The UV-vis absorption spectrum of **24** in 1,4-dioxane ($1 \times 10^{-5} \text{ mol L}^{-1}$) was measured. It shows a broad absorption band centered at 330nm and a small absorption band at 440 nm (Figure 4.13). When the solution is irradiated upon UV ($\lambda=365 \text{ nm}$) for various irradiation time, the intensity of the broad band will decrease whereas it increases in the small band until the trans- species transform to the cis- species.

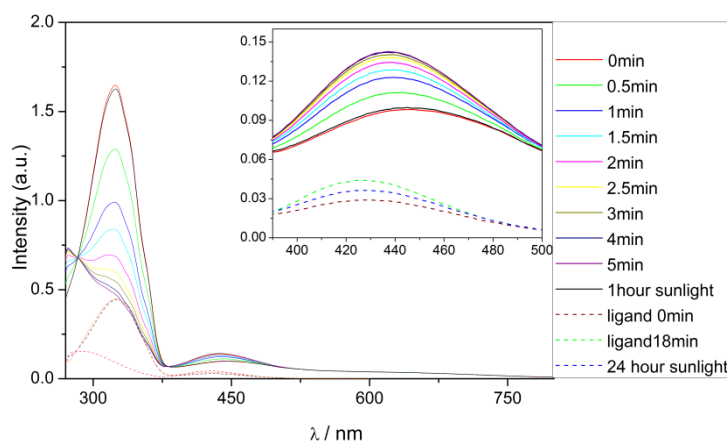


Figure 4.13 UV/Vis absorption spectra of a 1,4-dioxane solution of **24** upon irradiation with UV (365 nm). Arrows indicate an increase/decrease in the absorption bands during the experiment.

According to the above absorption result, we have prepared the non-switched solution and switched solution of **24**. Before measuring the ac magnetic susceptibility, both solutions are concentrated to saturation. The result of the ac magnetic susceptibility of the non-switched solution is shown in Figure 4.14. In the absence of dc field, the peaks of the out-of-phase susceptibility are invisible in the investigated frequency range, which is consistent with the result of the powder derivatives. However, under a 1200 Oe dc field, the position of the peaks keeps unmoved. This indicates that the solution system probably have different relaxing properties than the powder. However this is important to note that the solubilization of the

chain-like compound in polar solvent probably give rise to dimeric compound in solution. Further studies (RMN on the Y-derivative) are currently under progress.

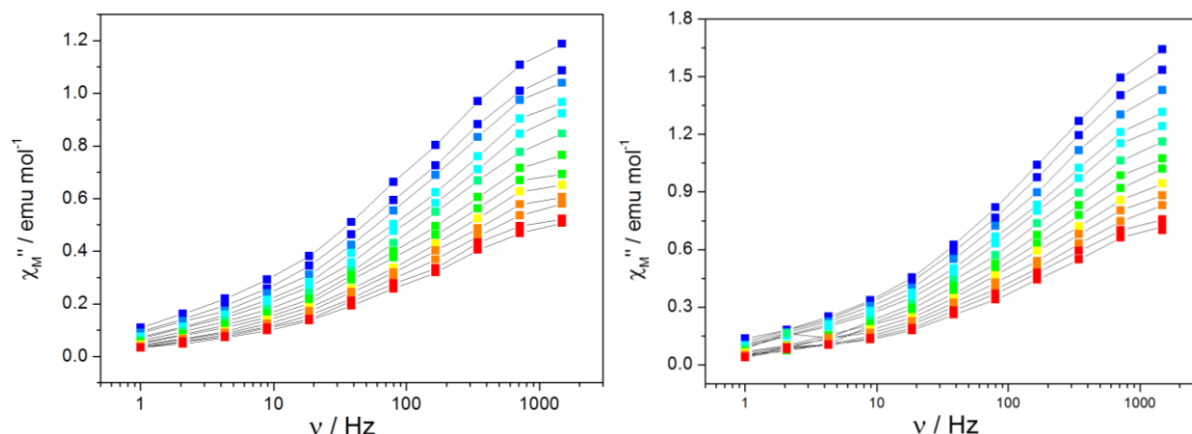


Figure 4.14 Frequency dependence of the out-of-phase components of ac susceptibility for non-switched 1,4-dioxane solution of **24** under zero Oe dc field (left) and 1200 Oe dc field (right). Color mapping ranges from 1.8 (blue) to 3 K (red). Temperature plots of these data are available in Figure A4.12. Lines are guides to eye.

To further check if there is the change in magnetic behavior, the switched solution is measured and the results are also shown in Figure 4.15, but, unfortunately, no significant changes are visible in the available frequency range.

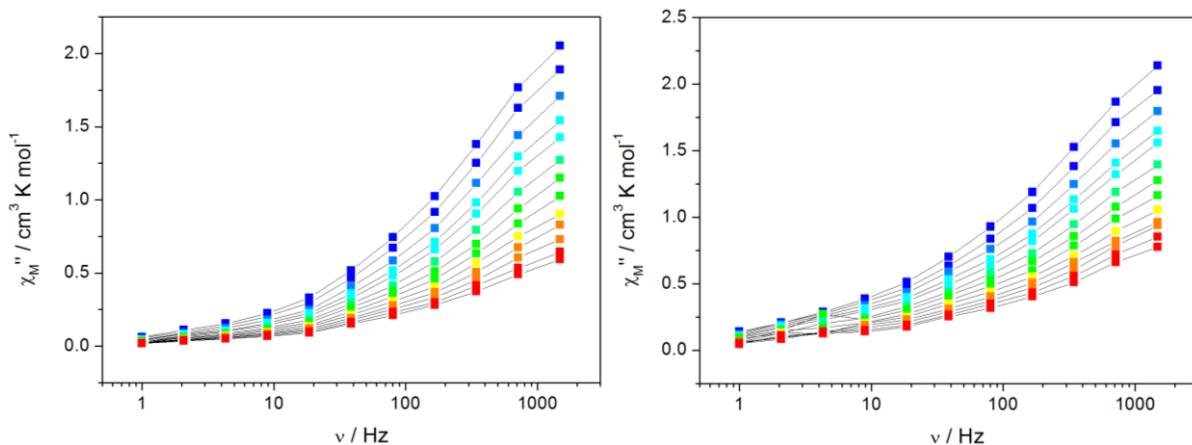


Figure 4.15 Frequency dependence of the out-of-phase components of ac susceptibility for switched 1,4-dioxane solution of **24** under zero Oe dc field (left) and 1200 Oe dc field (right). Color mapping ranges from 1.8 (blue) to 3 K (red). Temperature plots of these data are available in Figure A4.13. Lines are guides to eye.

In order to work in our frequency range, we have performed a similar investigation of the doped sample. A doping rate of 39% in Dy^{III} has been used (the 5% tested on solid is too small to provide reliable magnetic signal on solution) to afford **24@Y_{0.61}**. The ac measurement reveals frequency dependents peaks below 1500Hz that are sensitive to the application of a dc field (Figure 4.16).

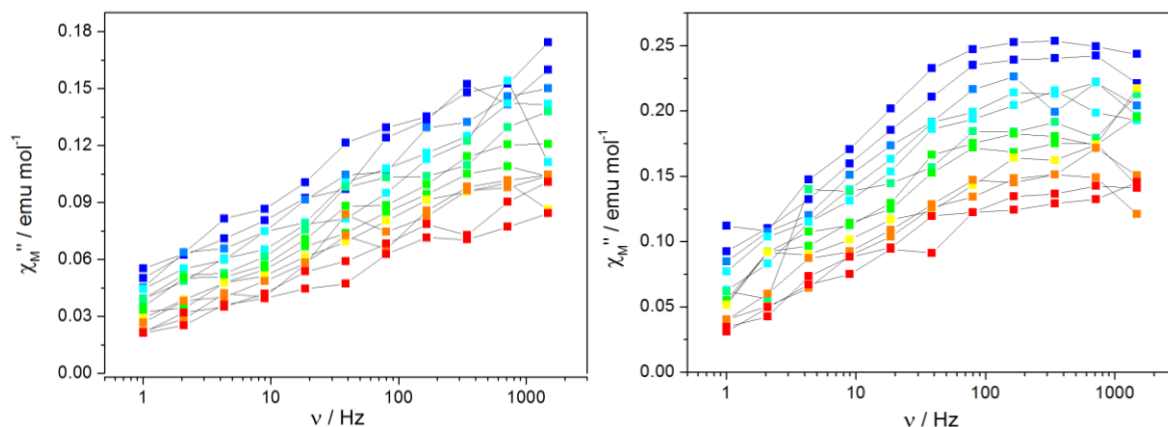


Figure 4.16 Frequency dependence of the out-of-phase components of ac susceptibility for non-switched 1,4-dioxane solution of $\mathbf{24@Y}_{0.61}$ under zero Oe dc field (left) and 800 Oe dc field (right). Color mapping from 1.8 (blue) to 3 K (red). Temperature plots of these data are available in Figure A4.14. Lines are guides to eye.

However, once photo-isomerization is performed on $\mathbf{24@Y}_{0.61}$ no significant change has been observed in the ac behavior of the complex (Figure 4.17). Additional results are shown in appendix A4. This is maybe due to strong deformation of the dimer in solution that compensates the effect of the ligand switching on the geometry of the complex.

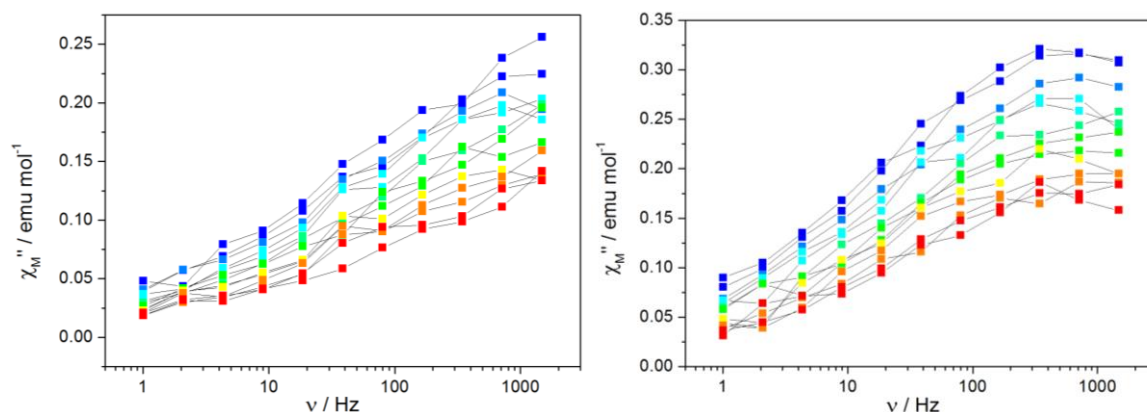


Figure 4.17 Frequency dependence of the out-of-phase components of ac susceptibility for switched 1,4-dioxane solution of $\mathbf{24@Y}_{0.61}$ under zero Oe dc field (left) and 800 Oe dc field (right). Color mapping from 1.8 (blue) to 3 K (red). Temperature plots of these data are available in Figure A4.15. Lines are guides to eye.

4.5 Conclusion

In summary the reaction of the sodium salt of HAZO ligand with Dy^{III} salts with further recrystallization in DMSO provide a pseudo 1D chain. This chain is made of H-bonded dimeric complexes.

Both pure ($\mathbf{24}$) and doped ($\mathbf{24@Y}$) samples show SMM behavior. Remarkable amount of relaxing molecules and small relaxation time distribution is observed on the doped sample in presence of 1200 Oe dc field. Accordingly a significant opening of the hysteresis is observed

on **24@Y**. The doped compound exhibits better SMM behavior than the pure one sample probably because of the suppression of Dy-Dy intramolecular interaction. Further theoretical studies will be necessary to clarify this point.

Additionally, **24** and its doped forms can be solubilized in dioxane affording magnetic slow relaxation in solution that may come from dimeric species. Unfortunately, photo-isomerization of these compounds do not led to modification of their SMM properties.

References

1. H. M. D. Bandara and S. C. Burdette, *Chemical Society Reviews*, 2012, 41, 1809-1825.
2. D. Pinkowicz, M. Ren, L.-M. Zheng, S. Sato, M. Hasegawa, M. Morimoto, M. Irie, B. K. Breedlove, G. Cosquer, K. Katoh and M. Yamashita, *Chemistry – A European Journal*, 2014, 20, 12502-12513.
3. T. K. Prasad, G. Poneti, L. Sorace, M. J. Rodriguez-Douton, A.-L. Barra, P. eugebauer, L. Costantino, R. Sessoli and A. Cornia, *Dalton Transactions*, 2012, 41, 8368-8378.
4. K. Katoh, R. Asano, A. Miura, Y. Horii, T. Morita, B. K. Breedlove and M. Yamashita, *Dalton Transactions*, 2014, 43, 7716-7725.
5. T. Fukuda, K. Matsumura and N. Ishikawa, *The Journal of Physical Chemistry A*, 2013, 117, 10447-10454.
6. J. Hatai and S. Bandyopadhyay, *Chemistry – A European Journal*, 2014, 20, 10020-10026.
7. W.-Y. Zhang, Y.-M. Tian, H.-F. Li, P. Chen, W.-B. Sun, Y.-Q. Zhang and P.-F. Yan, *Dalton Transactions*, 2016, 45, 3863-3873.
8. I. J. Hewitt, J. Tang, N. T. Madhu, C. E. Anson, Y. Lan, J. Luzon, M. Etienne, R. Sessoli and A. K. Powell, *Angewandte Chemie International Edition*, 2010, 49, 6352-6356.
9. S. Zhang, H. Ke, Q. Shi, J. Zhang, Q. Yang, Q. Wei, G. Xie, W. Wang, D. Yang and S. Chen, *Dalton Transactions*, 2016, 45, 5310-5320.
10. D. Hamada, T. Fujinami, S. Yamauchi, N. Matsumoto, N. Mochida, T. Ishida, Y. Sunatsuki, M. Tsuchimoto, C. Coletti and N. Re, *Polyhedron*, 2016, 109, 120-128.
11. S. Zhang, H. Ke, L. Sun, X. Li, Q. Shi, G. Xie, Q. Wei, D. Yang, W. Wang and S. Chen, *Inorganic Chemistry*, 2016, 55, 3865-3871.
12. T. Pugh, N. F. Chilton and R. A. Layfield, *Angewandte Chemie*, 2016, 128, 11248-11251.
13. F. Pointillart, K. Bernot, S. Golhen, B. Le Guennic, T. Guizouarn, L. Ouahab and O. Cador, *Angewandte Chemie International Edition*, 2015, 54, 1504-1507.
14. K. Liu, H. Li, X. Zhang, W. Shi and P. Cheng, *Inorganic Chemistry*, 2015, 54, 10224-10231.
15. S.-D. Jiang, B.-W. Wang, H.-L. Sun, Z.-M. Wang and S. Gao, *Journal of the American Chemical Society*, 2011, 133, 4730-4733.
16. D.-P. Li, T.-W. Wang, C.-H. Li, D.-S. Liu, Y.-Z. Li and X.-Z. You, *Chemical Communications*, 2010, 46, 2929-2931.
17. D. Zeng, M. Ren, S.-S. Bao and L.-M. Zheng, *Inorganic Chemistry*, 2014, 53, 795-801.
18. R. J. Holmberg, M. A. Polovkova, A. G. Martynov, Y. G. Gorbunova and M. Murugesu, *Dalton Transactions*, 2016, 45, 9320-9327.
19. L. Jia, Q. Chen, Y.-S. Meng, H.-L. Sun and S. Gao, *Chemical Communications*, 2014, 50, 6052-6055.
20. F. Habib, P.-H. Lin, J. Long, I. Korobkov, W. Wernsdorfer and M. Murugesu, *Journal of the American Chemical Society*, 2011, 133, 8830-8833.
21. H. A. Wegner, *Angewandte Chemie International Edition*, 2012, 51, 4787-4788.
22. S. Tamesue, Y. Takashima, H. Yamaguchi, S. Shinkai and A. Harada, *Angewandte Chemie International Edition*, 2010, 49, 7461-7464.

5 Slow relaxation and magnetic ordering in a three dimensional metal organic framework

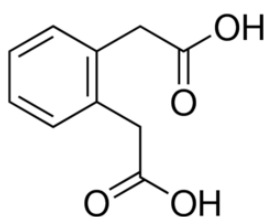
5.1 Introduction

In the previous chapters, the SMMs are 0D or 1D complexes. In this chapter we use of poly-carboxylic acid ligand to target a magnetic metal-organic frameworks (MOFs). MOFs are a kind of porous material and constructed from inorganic nodes and organic linkers. Because their highly porous structures can accommodate a wide variety of different guest molecules, they can exhibit fascinating structural and chemical properties.^{1,2}

An interesting strategy is to create porous MOF-SMM in which the coordination geometry around metal centers is constrained and rigid. Additionally, the tuning of the magnetization dynamics through the influence of different guest molecules within the pores is expected to be realized.^{3,4}

Poly-carboxylic acid can act either in bridging mode or in chelating mode toward the lanthanide, this makes them possible establish a more expanded network. Especially in the presence bridging mode, short metal-metal distance is anticipated to transmit sizable exchange interaction to enable the SMM behavior.

In this chapter, we report the structural and magnetic study of a series of isostructural lanthanide-based MOFs that involves 1,2-Phenylenediacetic Acid (abbreviated as o-PDA). The compound of general formula $\{[\text{Ln}(\text{o-PDA})_3(\text{H}_2\text{O})_2]\cdot 2\text{H}_2\text{O}\}_n$ with Ln= Ce(**25**), Nd(**26**), Gd(**27**) and Dy(**28**)) has been prepared by Insa Badiane, doctor of our group. We thank him for synthesizing all the powders.



Scheme 5.1 Schematic representation of o-PDA ligand.

5.2 Structural description

The crystal structure of the $\{[\text{Dy}(\text{o-PDA})_3(\text{H}_2\text{O})_2]\cdot 2\text{H}_2\text{O}\}_n$ (**28**) derivative has been reported by Wang *et al.*⁵ several years ago and were obtained through hydrothermal synthesis.

We have been able to obtain the same series of compounds by using soft chemistry reaction (see experimental section). The powders were analyzed thanks to Powder X-Ray Diffraction and patterns of all the products are compared to the reported crystal structure of the Dy^{III} (**28**) derivative (CCDC 669663). Superposition of the patterns with the simulated ones is reported in Figure A5.1.

Hereafter we describe the crystal structure of the Dy derivative (**28**) of formula $\{[\text{Dy}(\text{o-PDA})_3(\text{H}_2\text{O})_2] \cdot 2\text{H}_2\text{O}\}_n$. The compound crystallizes in the $C2/c$ space group. The asymmetric unit is made of one and a half o-PDA ligand, one free water molecule, one coordinated water molecule and half Dy^{III} ion. Each Dy^{III} ion is surrounded by nine oxygen atoms, one from a coordinated water molecule (O7) and eight from six different o-PDA ligands. Four oxygen atoms (O1, O2, O4, O6) binds only one Dy^{III} ion (μ_1 mode) and four oxygen atoms (O3, O3a, O5, O5a) bind two Dy^{III} ion (μ_2 mode) (Figure 5.1). On the magnetic point of view this coordination mode is expected to transmit sizeable magnetic interaction between the Dy^{III} ions.⁶⁻⁸ Overall, Dy^{III} chains that spread along the c axis are obtained (Figure 5.2). Each o-PDA ligand connects two parallel chains.

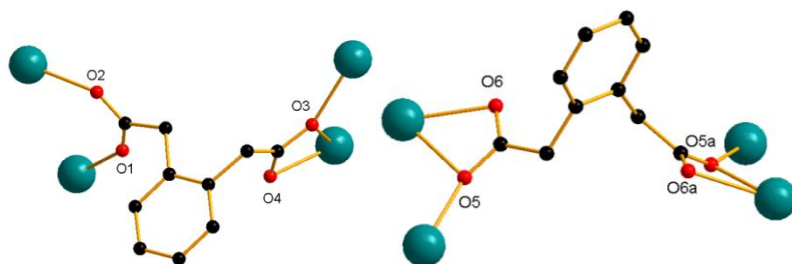


Figure 5.1 Representation of the coordination modes of the o-PDA ligand in $\text{Dy}(\mathbf{28})$.⁵

The coordination polyhedron of the Dy^{III} ion is also depicted in Figure 5.3 and is a distorted spherical capped square-antiprism (C_{4v}) (the quantitative result of the continuous shape measurement (CSM) is 2.870, as shown in Table A5.1). The oxygen atom of the water molecule occupies the capping position whereas other oxygen atoms come from the organic ligand. The two square planes of the polyhedron are not strictly parallel and have a dihedral angle of 11.0° . The Dy-O distances are in the 2.28(18) Å-2.49(19) Å range, the O-Dy-O angles are in the $52.15(6)$ - $151.40(7)^\circ$ range (details are listed in Table A5.2).

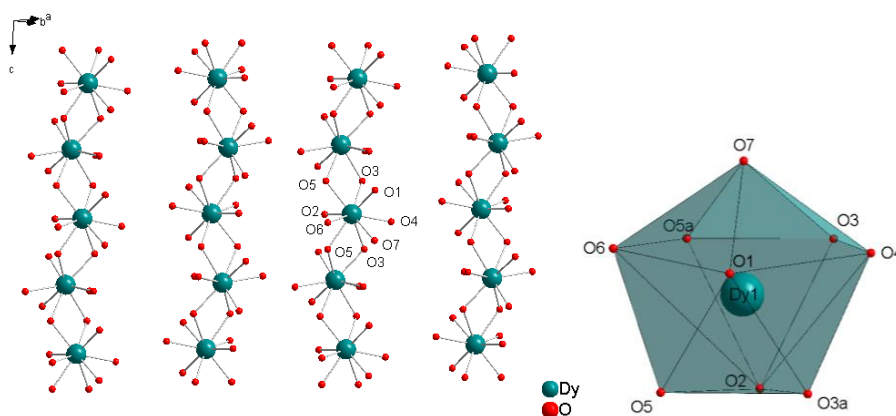


Figure 5.2 View of the chain structure formed by the Dy^{III} ions (left) and the corresponding coordination polyhedron (right). Carbon and hydrogen atoms are omitted for clarity.

Within a chain, the shortest Dy-Dy distance is 4.01(1) Å. The interchain Dy-Dy distances are 7.82(2) Å, 9.42(3) Å and 9.36(3) Å depending of the considered neighboring chain. The network can be described as a (6, 3) topologic structure with a honeycomb-like core (Figure 5.3).

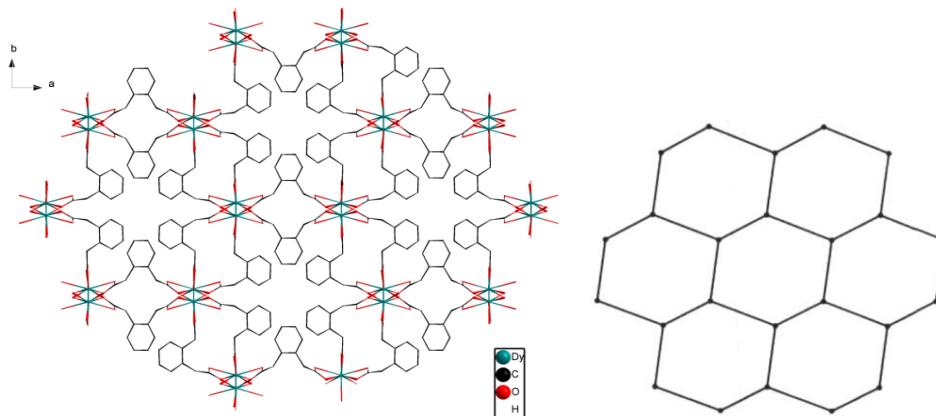


Figure 5.3 Packing diagram (left) and topology (right) viewed along 'c' axis of Dy(28).⁵

5.3 Static magnetic properties

5.3.1 $\{[\text{Nd}(\text{o-PDA})_3(\text{H}_2\text{O})_2] \cdot 2\text{H}_2\text{O}\}_n$ (26)

At room temperature, the value of $\chi_M T$ product is $1.63 \text{ cm}^3 \cdot \text{K} \cdot \text{mol}^{-1}$ (Figure 5.4), which is in good agreement with the expected value of one isolated Nd^{III} ion ($\chi_M T = 1.64 \text{ cm}^3 \cdot \text{K} \cdot \text{mol}^{-1}$). Upon cooling, $\chi_M T$ decreases gradually to $0.65 \text{ cm}^3 \cdot \text{K} \cdot \text{mol}^{-1}$ at 2 K due to the progressive depopulation of the levels of the $J = 9/2$ multiplet of the Nd^{III} . The magnetization value of Nd(26) reaches $1.21 \mu_B$ at 5 Tesla significantly lower than the theoretical saturation value. There is no evidence of long-range ordering.

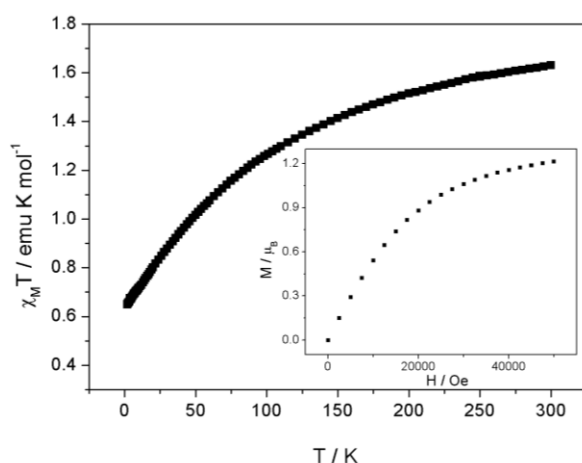


Figure 5.4 Temperature dependence of the $\chi_M T$ product for Nd(26). Inset: Field dependence of the Magnetization at 2.0 K.

5.3.2 {[Gd₂(o-PDA)₃(H₂O)₂].2H₂O}_n (**27**)

The room temperature value of the $\chi_M T$ product of Gd(**27**) is $7.96 \text{ cm}^3 \cdot \text{K} \cdot \text{mol}^{-1}$ (Figure 5.5), which is in good agreement with the expected value of one isolated Gd^{III} ion ($7.88 \text{ cm}^3 \cdot \text{K} \cdot \text{mol}^{-1}$). Upon cooling, the value of $\chi_M T$ product decreases slowly until 30 K, to reach a minimum of $7.64 \text{ cm}^3 \cdot \text{K} \cdot \text{mol}^{-1}$. Upon further cooling, the value of $\chi_M T$ product increases abruptly until $9.15 \text{ cm}^3 \cdot \text{K} \cdot \text{mol}^{-1}$ at 2 K, indicative of strong ferromagnetic coupling between the adjacent Gd^{III} ions.

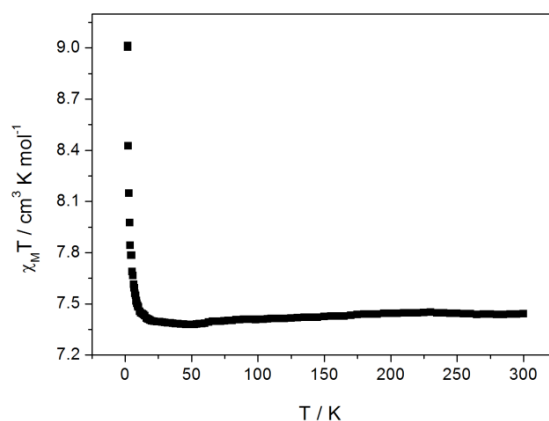


Figure 5.5 Temperature dependence of the $\chi_M T$ product for Gd(**27**).

5.3.3 {[Dy(o-PDA)₃(H₂O)₂].2H₂O}_n (**28**)

The room temperature value of $\chi_M T$ product of Dy(**28**) is $13.64 \text{ cm}^3 \cdot \text{K} \cdot \text{mol}^{-1}$ (Figure 5.6), which is in good agreement with the expected value of one isolated Dy^{III} ($\chi_M T = 14.17 \text{ cm}^3 \cdot \text{K} \cdot \text{mol}^{-1}$). Upon cooling, the value of $\chi_M T$ product decreases progressively down to 15 K to reach $12.58 \text{ cm}^3 \cdot \text{K} \cdot \text{mol}^{-1}$. Upon further cooling, $\chi_M T$ increases to reach $30.6 \text{ cm}^3 \cdot \text{K} \cdot \text{mol}^{-1}$ at 2.0 K. This indicates that a significant ferromagnetic coupling is active in the low-temperature region.⁹ Such behavior have also been observed on the previously mentioned Dy(Stilbene) derivative¹⁰ (chapter 2) and is expected to be a consequence of the μ_2 mode of the oxygen ions (O3 and O5) that binds neighboring Dy^{III}. This is also in agreement with previously observed results on similar compounds which should be attributed to intramolecular interactions.^{11, 12} The field dependent magnetization has been determined at 2 K in the 0-50 kOe field range. The magnetization value increases up to $5.07 \mu_B$ at 50 kOe without reaching saturation.

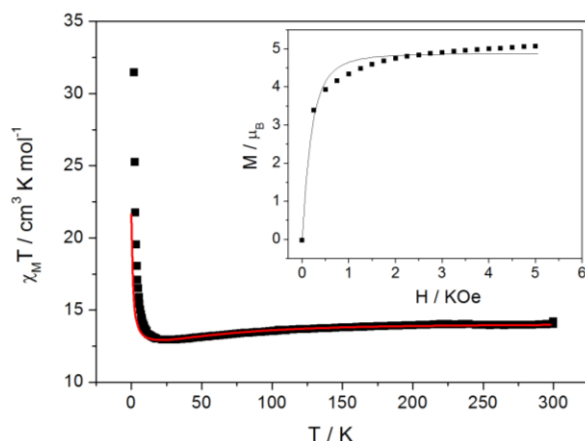


Figure 5.6 Experimental (black squares) and calculated (red line) $\chi_M T$ vs T curve for Dy(**28**). Inset: Experimental (black squares) and calculated (black line) M vs H curve.

Given the strong intramolecular ferromagnetic interaction observed here, and the relatively high distances observed between the chains, one may expect a single-chain magnet (SCM) behavior for Dy(**28**).¹²⁻¹⁵ Such behavior is seen when magnetic slow relaxation of a chain-based compound is confined in the chain. The compound consequently behaves as a one-dimensional molecular magnet that adopts an Ising-spin chain dynamics.¹⁶⁻¹⁸

On a static magnetic point of view, this implies the creation of magnetic domains within the chain that all relax collectively. These coherent domains create a “correlation length” that is observed when the magnetic interaction along the chain (J_{intra}) is strong enough when compared to the temperature and possible weak interchain interactions (J_{inter}).¹⁸⁻²⁰ The growth of “correlation length” induces an exponential variation of $\chi_M T$:

$$\chi_M T \propto \exp(2J_{\text{intra}}/k_B T) \quad (\text{equ. 5.1}).^{21-24}$$

where J is the coupling constant between the Dy^{III} ions. Plotting the logarithm of $\chi_M T$ versus the inverse of the temperature should afford a straight line (Figure 5.7), and the slope directly provides the exchange energy between the Dy^{III} ions.^{25, 26} In the 2-10 K temperature range the plot shows a clear linearity and fitting of this region with equ. (5.1) gives a slope of 2.08 ± 0.02 K and a J_{intra} value of 1.04 K (i.e. 0.71 cm^{-1}). This is a quite low value for J_{intra} and this may compete with small J_{inter} mainly with dipolar origin that can exist in between the chains.²⁷

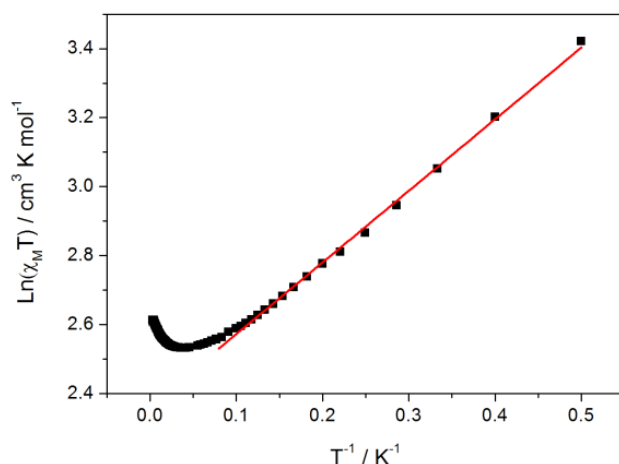


Figure 5.7 Plot of $\ln(\chi_M T)$ vs T^{-1} for Dy(**28**). The red line represents the scaling of the data using an Ising temperature dependence of the susceptibility.

5.4 Theoretical calculation

Ab initio calculations for Dy(**28**) were carried out using the structure obtained from the experimental single-crystal X-ray diffraction analysis. The simulated curve of $\chi_M T$ vs T is well superposed with the experimental data, as shown in Figure 5.6. The exchange interaction (J_{exch}) and dipolar coupling (J_{dip}) interaction are calculated as 0.01 and 0.05 cm^{-1} , respectively. The total magnetic interaction is estimated as $J = 0.06 \text{ cm}^{-1}$ (0.09 K), with $J = J_{\text{exch}} + J_{\text{dip}}$.¹⁰ The contribution of dipolar coupling interaction of intermolecular-nature is much larger than the exchange interaction of intramolecular-nature, this may explain the occurrence of the 3D ordering.²⁸⁻³¹ We can state here the ratio of intra/inter interaction does not enable the single-chain-magnet behavior. Thereby this compound can be well called a SMM. The sign of exchange interaction and dipolar coupling interaction confirms the ferromagnetic interaction originates from both the two coupling interactions. Moreover, the calculated magnetization is also consistent with the experimental result.

5.5 Dynamic magnetic properties

5.5.1 $\{[\text{Nd}(\text{o-PDA})_3(\text{H}_2\text{O})_2] \cdot 2\text{H}_2\text{O}\}_n$ (**26**)

Ac magnetic susceptibilities measurements are performed for Nd(**26**) under an optimum field of 2000 Oe, where temperature independent magnetic slow relaxation is minimized (Figure A5.4). Ac measurements reveal a full frequency dependent peak below 4 K between 1 and 1499 Hz (Figure 5.8) indicative of field-induced SMM behavior and relaxation time as a function of T^{-1} is reported in Figure 5.9. This plot is almost linear over the entire temperature range, confirming the efficiency of the external static field to provide a probably pure thermally activated regime. Analysis of the linearity gives a calculated relaxation barrier of $U_{\text{eff}} = 2.8 \pm 0.2 \text{ K}$ and a τ_0 value of $6.07 \times 10^{-5} \text{ s}$ for the thermally activated regime. The value of

energy barrier is less spectacular. However, the high value of τ_0 may highlight the presence of other thermal-dependent regimes. Attempt to fit the plot is successful only when the Raman and Orbach processes are considered. The superposition gives $C = 0.06 \pm 0.01 \text{ s}^{-1} \text{ K}^{-9}$, $n = 9$, $\tau_0 = 8.74 \pm 0.69 \times 10^{-5} \text{ s}$, $U_{\text{eff}} = 2.1 \pm 0.2 \text{ K}$ and $R^2 = 0.995$.

Cole-Cole plots show a narrow distribution of relaxation times with $\alpha_{\text{max}} = 0.18$ at 3.0 K. The non-relaxing fraction of the magnetization varies between 0.15 (1.8 K) and to 0.28 (3.0 K).

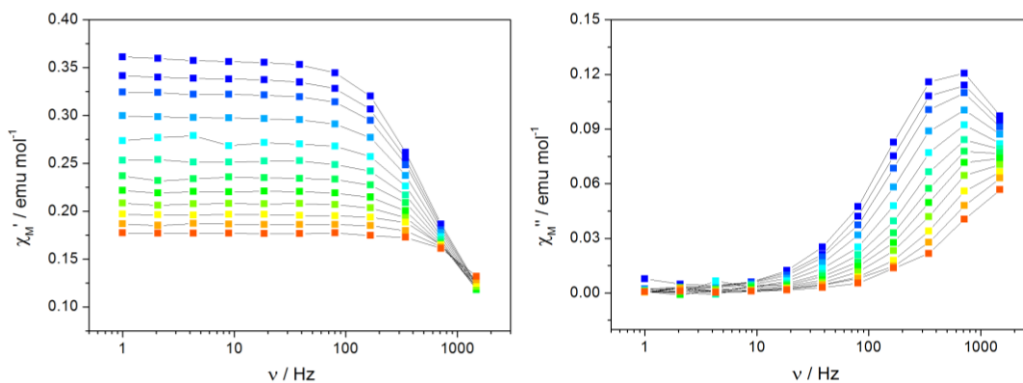


Figure 5.8 Frequency dependence of the in-phase (left) and out-of-phase (right) components of ac susceptibility with 2000 Oe dc field for Nd(26). Color mapping from 1.8 K (blue) to 3.8 K (red). Temperature plots of these data are available in Figure A5.5. Lines are guides to the eye.

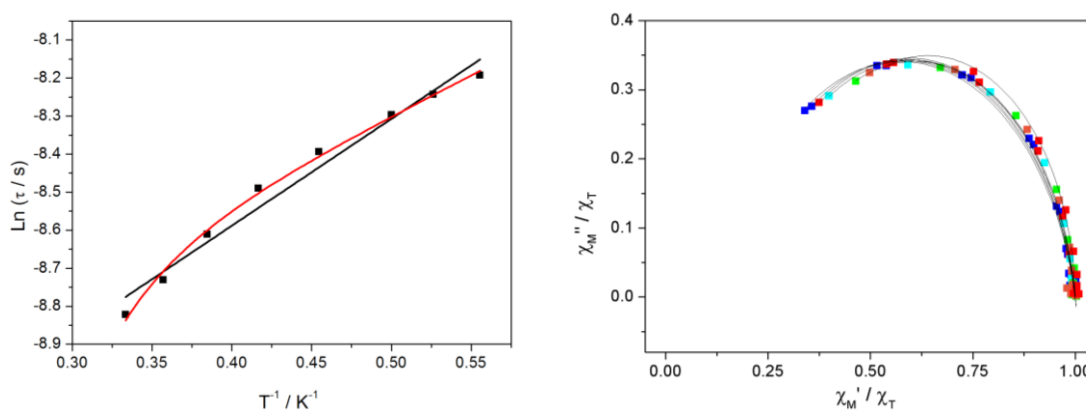


Figure 5.9 Relaxation time $\ln(\tau)$ in dependence of (T^{-1}) under 2000 Oe dc field. The black line represents the fit with only orbach process, while the red line represents the fit with Raman and Orbach processes. Normalized Cole-Cole plots for Nd(26) under 2000 Oe dc field (right). Color mapping from 1.8 K (blue) to 3.0 K (red). Lines are guides to the eye.

Other Ln^{III} analogues, such as Pr^{III} and Sm^{III} do not display any SMM behaviors except Ce^{III} (25), which presents a fast relaxation even in the presence of external field. One can see the data in the Figure A5.6.

5.5.2 $\{[\text{Dy}(\text{o-PDA})_3(\text{H}_2\text{O})_2] \cdot 2\text{H}_2\text{O}\}_n$ (28)

In order to investigate the magnetic relaxation behavior of Dy(28), ac magnetic susceptibility measurements with various frequencies (1-1500 Hz) in the 1.8-5 K temperature range have been carried out within zero applied field. Maxima of out-of-phase signals have

been observed (Figure 5.10) and relaxation times (τ) are extracted and plotted versus T^{-1} . In the investigated temperature range, the relaxation time τ shows a thermal dependence that is not affected by temperature independent phenomenon. This is a rare feature for nine-coordinated Dy^{III} ions.³² The Cole-Cole plots (Figure 5.11) show a moderate distribution of relaxation times ($\alpha=0.27$ at 1.8 K) and the non-relaxing fraction of magnetization χ_s/χ_T is very low (0.07 at 1.8 K). The details are shown in Table 5.1. In other words most of the sample relaxes slowly with a sizeable distribution of its relaxation times. Discussion about the variation of the dynamic parameters over the different dc field and compounds will be presented at the end of this chapter.

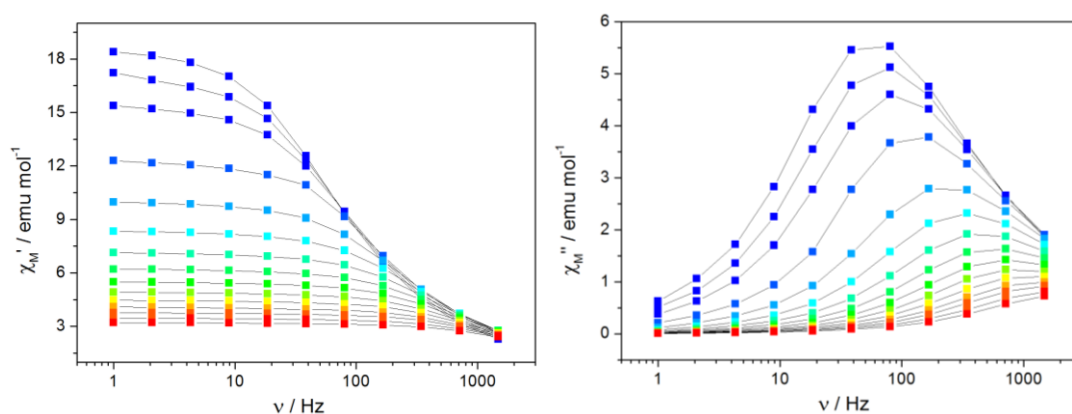


Figure 5.10 Frequency dependence of the in-phase (left) and out-of-phase (right) components of ac susceptibility for Dy(28) under zero dc field. Color mapping from 1.8 K (blue) to 5 K (red). Temperature plots of these data are available in Figure A5.8. Lines are guides to the eye.

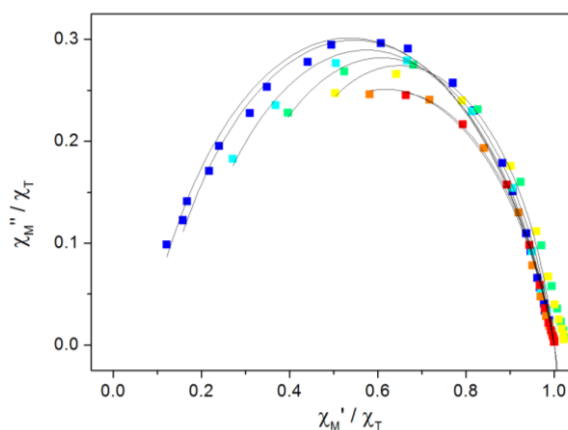


Figure 5.11 Normalized Cole-Cole plot Dy(28) under zero dc field. Color mapping from 1.8 K (blue) to 4.5 K (red). Lines are guides to the eye.

A field scan at 2 K has been performed in order to check if in-field relaxation processes are observed in Dy(28). As the field is applied the relaxation times are lowered with an optimum dc field obtained at 1200 Oe (Figure A5.7). Indeed, ac measurement under an applied field of 1200 Oe have been carried-out and as expected, the positions of χ_M'' maxima have been shifted to a lower frequency region (Figure 5.12).

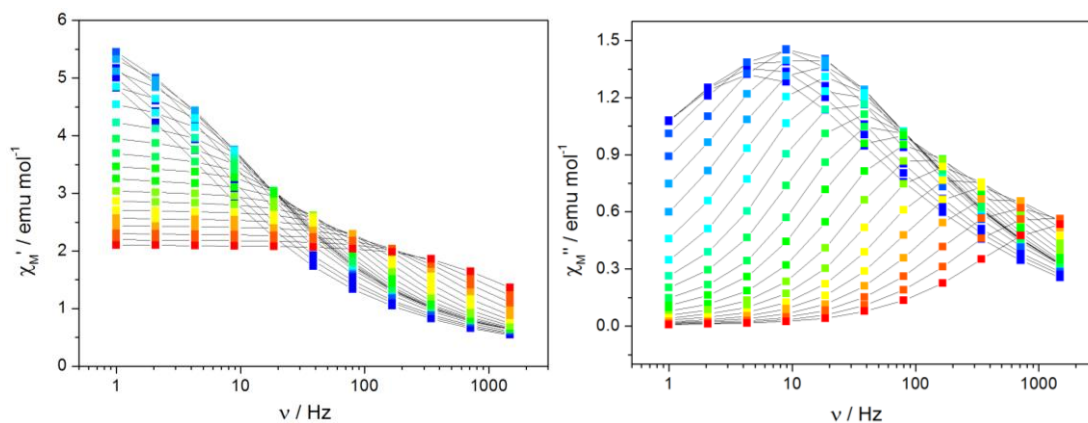


Figure 5.12 Frequency dependence of the in-phase (left) and out-of-phase (right) components of ac susceptibility for Dy(**28**) under 1200 dc field. Color mapping from 1.8 K (blue) to 7 K (red). Temperature plots of these data are available in Figure A5.9. Lines are guides to the eye.

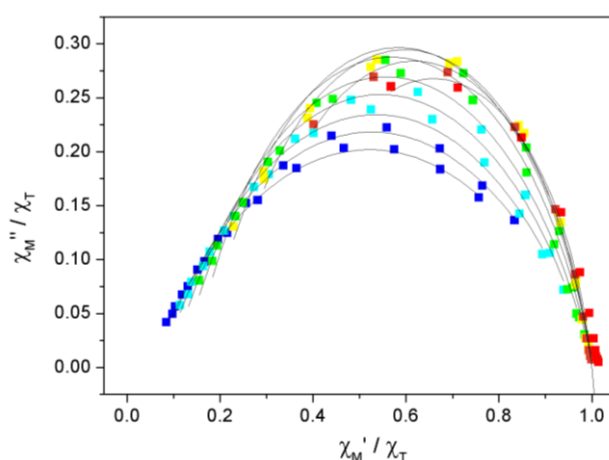


Figure 5.13 Normalized Cole-Cole plot for Dy(**28**) under 1200 Oe dc field. Color mapping from 1.8 K (blue) to 6.5 K (red). Lines are guides to the eye.

As evidenced by the Cole-Cole plots (Figure 5.13) the distribution of the relaxation time is higher under 1200 Oe dc field ($\alpha = 0.50$ at 1.9 K) but with a very low χ_s/χ_T value (0.04).^{10, 33, 34} This may indicate that the entire sample is relaxing but with different competing relaxation modes.

5.5.3 $\{[\text{Dy}_{0.08}\text{Y}_{0.92}(\text{o-PDA})_3(\text{H}_2\text{O})_2] \cdot 2\text{H}_2\text{O}\}_n$ (**28@Y**)

Magnetic dilution is a standard technique used to investigate the magnetic property of a given SMM without the influence of its neighbors.³⁵⁻⁴⁷ Once crystallized in an isomorphous diamagnetic matrix, the SMM behavior is generally optimized as intermolecular interactions that are likely to create additional, and damaging, pathways for the magnetic relaxation are suppressed.^{38, 40}

In the particular case of Dy(**28**) the magnetic dilution can be interesting for two reasons: -it's an easy way to investigate on the influence of the magnetic interactions (either J_{intra} or J_{inter}) on the relaxing properties of the isolated Dy^{III} ion.

-it can be a definitive proof of the existence/absence of SCM behavior, as the magnetic dilution avoid the creation of coherent magnetic domains within a chain a so the creation of correlation lengths.

On an experimental point of view, magnetic dilution can be easily performed by synthesizing heteronuclear Dy/Y adducts with a very small content in Dy^{III} ion. Here, we have mixed the DyCl₃ and YCl₃ in a 1: 9 ratio (10% of Dy^{III}) to synthesize the diluted sample. The magnetization value at 50 kOe is compared with the pure compound, thus the real ratio of the doping sample is estimated to be 1:11.5 magnetically(8% of Dy^{III}). The EDS result is shown in Table A5.9, and confirms these results (5.5% of Dy^{III}).

Dc magnetic measurement of **28@Y** shows no increase of $\chi_M T$ at low temperature (Figure A5.11). This doping rate is thus appropriate to study the magnetic behavior of the isolated Dy^{III} ion.

The ac magnetic measurements were first carried out in zero field(Figure 5.14). The out-of-phase peaks are broader when compared with Dy(**28**) and their position temperature independent below 4 K indicating the presence of at least two relaxation regimes.

The appearance of QT arise a question, why the QT effect shrinks in the pure Dy compound, but expands in the doping one at zero dc field? In the pure sample, one Dy^{III} ion can interact with two neighboring Dy^{III} ions within short distances to create strong intrachain ferromagnetic interaction, thus the QT can be suppressed to some extent, as is generally accepted that ferromagnetic interaction can slowdown the magnetic relaxation.⁴⁸ This is the reason why QT is less pronounced in Dy(**28**). In **28@Y** this interaction vanishes because Dy^{III} ions are well isolated in the Y matrix, thereby QT is released again at low temperature.

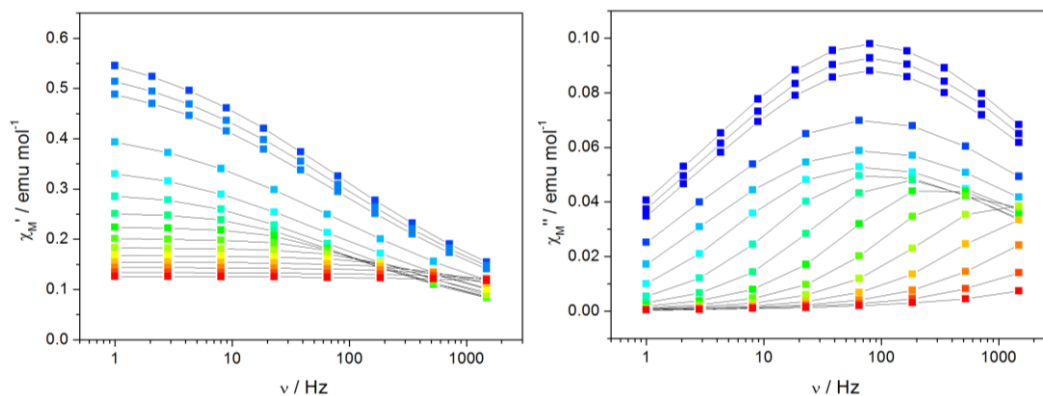


Figure 5.14 Frequency dependence of the in-phase (left) and out-of-phase (right) components of ac susceptibility for **28@Y** under zero dc field. Color mapping from 1.8 K (blue) to 8.0 K (red). Temperature plots of these data are available in Figure A5. 13. Lines are guides to the eye.

Comparison of the Cole-Cole plot (Figure 5.15) is also interesting as a similar fraction of the sample is able to relax slowly ($\chi_s/\chi_T = 0.06$ for Dy(**28**) while $\chi_s/\chi_T = 0.07$ for **28@Y** at 2 K.) but the distribution of the relaxation time is severely damaged ($\alpha=0.27$ for Dy(**28**) while $\alpha=0.58$ for **28@Y** at 1.8 K). This is in agreement with a sample that is experiencing several relaxation modes.⁴⁹⁻⁵¹

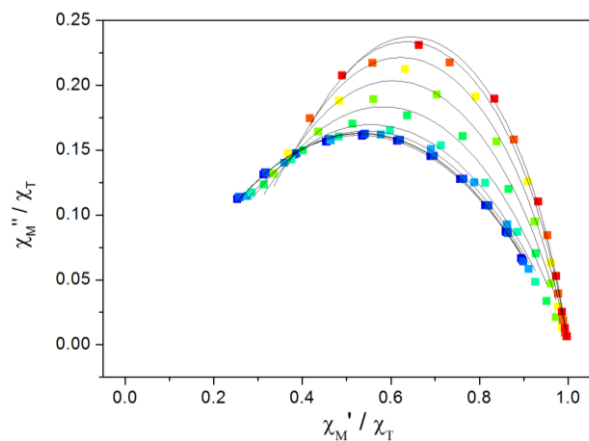


Figure 5.15 Normalized Cole-Cole plots for complex **28@Y** under 0 Oe dc field (right). Color mapping from 1.8 K (blue) to 5.5 K (red). Lines are guides to the eye.

However, by applying an optimum dc field of 1200 Oe the magnetic relaxation of **28@Y** is severely enhanced with relaxation times out of our investigable frequency range at low temperature (Figure 5.16).

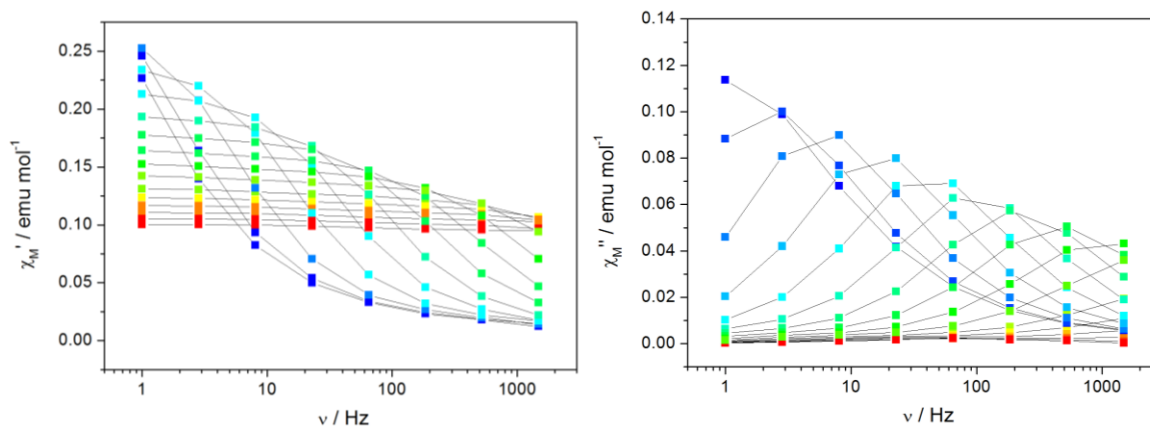


Figure 5.16 Frequency dependence of the in-phase (left) and out-of-phase (right) components of ac susceptibility for **28@Y** under 1200 dc field. Color mapping from 2.5 K to 10 K. Temperature plots of these data are available in Figure A5.14. Lines are guides to the eye.

We obtained a distribution of α in the 0.28-0.34 range from the Cole-Cole plot (Figure 5.17), revealing a moderate distribution of relaxation times. The values of χ_S/χ_T remain stable between 0.04 and 0.06.

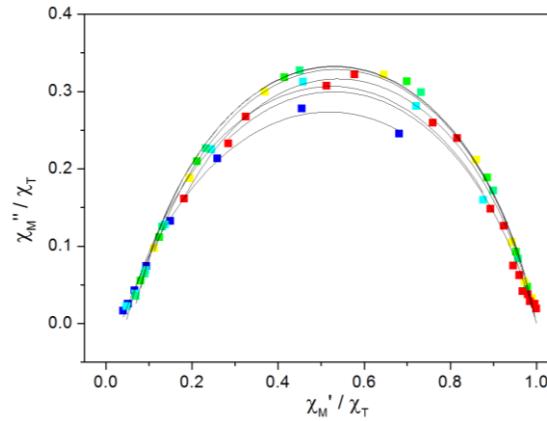


Figure 5.17 Normalized Cole-Cole plots for complex **28@Y** under 1200 Oe dc field (right). Color mapping from 3.0 K (blue) to 6.0 K (red). Lines are guides to the eye.

Relaxation times as a function of T^{-1} for 0 and 1200 Oe dc field are reported in Figure 5.18 for direct comparison. We recall here, that relaxation can occur because of different relaxation phenomena, according to equation (1.5):

$$\tau^{-1} = A_1 H^4 T + A_2 H^2 T + \frac{B_1}{1 + B_2 H^2} + C T^n + \tau_0^{-1} \exp(-U_{\text{eff}} / kT) \quad (\text{equ. 1.5})$$

Where the first term represents quantum tunneling, the second and three represent the direct process, the fourth the Raman process and the fifth the Orbach process.

However global fitting of the τ^{-1} vs T^{-1} curves is likely to lead to over-parametrization. This is the reason why each parameter has to be determined as independently as possible (see also chapter 2).

For the 0 dc field measurement the straight line observed when plotting the relaxation times may be a consequence of the occurrence of a thermally activated relaxation process (*i.e.* an Orbach process). This relaxation process is the fifth parameter in equation (1.5). Considering a pure Orbach relaxation the anisotropy barrier is estimated to be $U_{\text{eff}} = 9.2 \pm 0.1$ K with $\tau_0 = 1.5 \times 10^{-5}$ s ($R^2 = 0.997$). This value is relatively small compared to Dy-based SMMs.^{52, 53} The high value of τ_0 let suspect the existence of Raman process. The superposition realized with Raman and Orbach regimes provides $C = 2.37 \pm 0.61$ s⁻¹ K⁻⁹, $n = 9$, $\tau_0 = 1.78 \pm 0.11 \times 10^{-5}$ s, $U_{\text{eff}} = 8.8 \pm 0.1$ K with $R^2 = 0.999$.

For the in-field measurement, the situation is trickier. Field dependence of τ^{-1} has been estimated on the basis of data of Figure 5.15 considering the first three terms of equation (1.5). Best fit provides: $A_1 = (3.5 \pm 0.7) \times 10^{-13}$ s⁻¹ K⁻¹ Oe⁻⁴, $A_2 = (2.4 \pm 0.4) \times 10^{-6}$ s⁻¹ K⁻¹ Oe⁻⁴, $B_1 = (679.0 \pm 1.4) \text{s}^{-1}$, $B_2 = (1.6 \pm 0.02) \times 10^{-5}$ Oe⁻² with $R^2 = 0.999$. The extremely small value of A_1 is consistent with what observed Lucaccini *et al.*⁵⁴ on similar compound. One should note that the acceleration of the relaxation in higher field is driven by direct process.⁵⁵

The next step is to determine the parameters of the last two terms with the first three terms fixed to the above values. However, the fit is not successful. So only the high-temperature

region is fitted by the Orbach process, which provides $U_{\text{eff}} = 41.6 \pm 1.8$ K, $\tau_0 = 3.06 \times 10^{-7}$ s ($R^2 = 0.989$).

For **28@Y** under 0 dc field, the curvature at the intermediate temperature implies the existence of Raman or direct process. Unfortunately, the attempt to fit this plot is not successful. Linear fit considering the fifth term of equation (1.5) gives $U_{\text{eff}} = 23.4 \pm 1.4$ K and $\tau_0 = 4.12 \times 10^{-6}$ s ($R^2 = 0.989$). The tunneling rate is determined as $\tau_{\text{tun}} = 0.0018$ s.

For the in-field measurement, estimation of the first three terms of equation (1.5) is not successful as τ^{-1} is constant (0.01s) whatever the field is. Hence, only the fourth and fifth terms are considered. Best fit (Figure 5.18) provides: $C = 0.06 \pm 0.01$ s $^{-1}$ K $^{-5}$, $n = 5$, $\tau_0 = 5.00 \pm 3.27 \times 10^{-8}$ s, $U_{\text{eff}} = 53.5 \pm 3.75$ K with $R^2 = 0.996$.

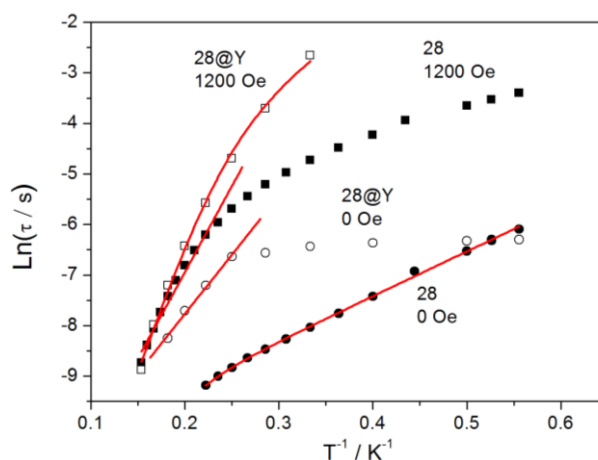


Figure 5.18 Plot of $\ln(\tau)$ versus (T^{-1}) at 0 Oe (circles) and 1.2 kOe (squares) for Dy(**28**) (solid) and **28@Y**(open). The solid lines represent the best fits.

Table 5.1 Main magnetic data extracted from the dynamic properties of Nd(**26**), Dy(**28**) and **28@Y**.

Compound	Energy barrier (K)	α (1.8K)	χ_S/χ_T (1.8K)
Nd (26) (2000 Oe)	2.8 ± 0.2	0.14	0.15
Dy (28) (0 Oe)	9.2 ± 0.1	0.27	0.07
Dy (28) (1200 Oe)	45.8 ± 1.6	0.51	0.04
28@Y (0 Oe)	23.4 ± 1.4 K	0.58	0.06
28@Y (1200 Oe)	98.9 ± 12.9 K	0.34	0.04

5.6 Characterization of magnetic hysteresis

Hysteresis curve have been recorded for **28** and **28@Y** in the ^3He region. Compound **28** shows an opening of hysteresis between ± 5000 Oe with a coercitive field of 250 Oe and a remnant magnetization of $1.2 \mu_B$ in zero field. While for the doped **28@Y**, the hysteresis is closed.

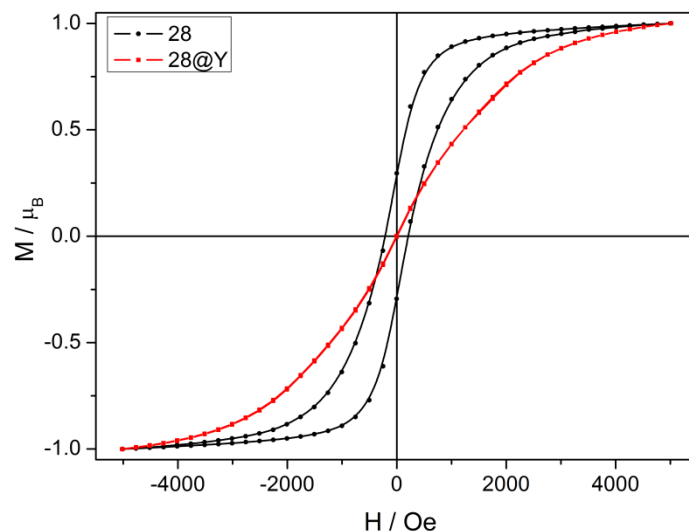


Figure 5.19 Hysteresis curves (M vs H) measured for **28** and **28@Y** at 0.5K with a ^3He insert with a sweep rate of 15.5 Oe/s.

The discrepancies between the ac behavior of the pure and doped sample are a proof of a collective magnetic behavior in Dy(**28**) (possible 3D ordering) as the diluted sample does not show any such behavior. This signifies that magnetic interactions in Dy(**28**) have a positive impact on the magnetic slow relaxation in zero-field. One can postulate that ferromagnetic J_{inter} induce an exchange biased interaction between the Dy^{III} ions that suppress thermally independent relaxation pathways. Such behavior has been observed in the past on antiferromagnetic interacting Mn_4 clusters,^{56, 57} ferromagnetic Fe_4 supramolecular chains,⁵⁸ ferromagnetic cyanide-based SMM,⁵⁹ and ferromagnetically connected Dy-radical based tetramers.⁶⁰

5.7 Conclusion

In conclusion, the reaction of the deprotonated o-PDA ligand with Ln^{III} lead to a series of isostructural MOFs.

-A rare Nd analogue has exhibited single-molecule-magnet behavior, as well as the Ce analogue, which displays a fast relaxation even in external field. To design a light lanthanide SMM is always a hard job. The key difficulty is how to modulate the appropriate ligand field to maintain the Ising anisotropy of the ions considering their complicated coordination environment. Moreover, other strategies should also be proposed to enhance the energy barriers, because up to now, the largest energy barrier among them is 74 K,⁶¹ much smaller than the heavier ones.^{7, 62-64}

-The Gd analogue has also displayed ferromagnetic interaction.

-For the Dy analogue, the single-chain-magnet behavior is excluded by the employment of scaling procedure which gives a low correlation length. In addition, the theoretical calculation also confirms that the dipolar coupling ($J=0.05 \text{ cm}^{-1}$) is the main contribution to the total

coupling ($J_{\text{exchange}}=0.01 \text{ cm}^{-1}$), which results in a small ratio of $J_{\text{intra}}/J_{\text{inter}}$, confirming the above result.

The dynamics of the magnetization has been investigated in zero field and external field. Compound Dy(**28**) can be taken as a good example of SMM showing weak QT in zero field due to the presence of the ferromagnetic interaction. Thanks to the method of magnetic dilution, we have been able to study the influence of the magnetic interaction. The diluted sample has afforded rich information. The QT is re-activated in zero-field as the ferromagnetic interaction does not govern the relaxation any longer in the doped sample. This may be an example of exchange-biased SMM behavior. Additionally, an hysteretic behavior is observed at 0.5 K for **28**, that may be due to collective magnetic behavior at low temperature (3D ordering).

Finally, MOFs-SMM strategy appears to be feasible in designing the multifunctional SMM. The ability to tune the spatial arrangement allows a better control of the multi-dimensional organization of the magnetic centres. In addition, guest molecules can tune the properties of SMM-MOFs in an easy manner.

References

1. X. Zhang, V. Vieru, X. Feng, J.-L. Liu, Z. Zhang, B. Na, W. Shi, B.-W. Wang, A. K. Powell, L. F. Chibotaru, S. Gao, P. Cheng and J. R. Long, *Angewandte Chemie International Edition*, 2015, 54, 9861-9865.
2. P. Cheng, *Springer-Verlag*, Berlin, Heidelberg, Germany 2015.
3. X. Gu, R. Clérac, A. Hourri and D. Xue, *Inorganica Chimica Acta*, 2008, 361, 3873-3876.
4. J.-B. Peng, Y.-P. Ren, X.-J. Kong, L.-S. Long, R.-B. Huang and L.-S. Zheng, *CrystEngComm*, 2011, 13, 2084-2090.
5. X. S. W. C. Y. Wang, X. Li, , *Wuji Huaxue Xuebao*, 2008, , 24, 781-783.
6. X. Yi, K. Bernot, F. Pointillart, G. Poneti, G. Calvez, C. Daiguebonne, O. Guillou and R. Sessoli, *Chemistry – A European Journal*, 2012, 18, 11379-11387.
7. P.-H. Lin, T. J. Burchell, R. Clérac and M. Murugesu, *Angewandte Chemie*, 2008, 120, 8980-8983.
8. S. Biswas, S. Das, G. Rogez and V. Chandrasekhar, *European Journal of Inorganic Chemistry*, 2016, DOI: 10.1002/ejic.201600335, n/a-n/a.
9. J.-D. Leng, J.-L. Liu, W.-Q. Lin, S. Gomez-Coca, D. Aravena, E. Ruiz and M.-L. Tong, *Chemical Communications*, 2013, 49, 9341-9343.
10. X. Yi, K. Bernot, O. Cador, J. Luzon, G. Calvez, C. Daiguebonne and O. Guillou, *Dalton Transactions*, 2013, 42, 6728-6731.
11. C.-M. Liu, D.-Q. Zhang and D.-B. Zhu, *Chemical Communications*, 2016, 52, 4804-4807.
12. Y.-d. Luo, G.-m. Sun, D.-m. Li and F. Luo, *Inorganic Chemistry Communications*, 2011, 14, 778-780.
13. L. Su, W.-C. Song, J.-P. Zhao and F.-C. Liu, *Chemical Communications*, 2016, 52, 8722-8725.
14. P. C. Arosio, M.; Mariani, M.; Orsini, F.; Bogani, L.; Caneschi, A.; Lago, J.; Lascialfari, A., *J. Appl. Phys.* , 2015,, 117, 17B310.
15. Y.-C. Hui, Y.-S. Meng, Z. Li, Q. Chen, H.-L. Sun, Y.-Q. Zhang and S. Gao, *CrystEngComm*, 2015, 17, 5620-5624.
16. M. G. F. Vaz, R. A. A. Cassaro, H. Akpınar, J. A. Schlueter, P. M. Lahti and M. A. Novak, *Chemistry – A European Journal*, 2014, 20, 5460-5467.
17. K. Bernot, L. Bogani, R. Sessoli and D. Gatteschi, *Inorganica Chimica Acta*, 2007, 360, 3807-3812.

18. L. Bogani, C. Sangregorio, R. Sessoli and D. Gatteschi, *Angewandte Chemie*, 2005, 117, 5967-5971.
19. O. V. P. Billoni, V.; Pescia, D.; Vindigni, A.: , *Phys. Rev. B* 2011,, 84.
20. Y.-Z. Zheng, Y. Lan, W. Wernsdorfer, C. E. Anson and A. K. Powell, *Chemistry – A European Journal*, 2009, 15, 12566-12570.
21. E. Bartolome, J. Bartolome, A. Arauzo, J. Luzon, L. Badia, R. Cases, F. Luis, S. Melnic, D. Prodius, S. Shova and C. Turta, *Journal of Materials Chemistry C*, 2016, 4, 5038-5050.
22. E. Bartolome, J. Bartolome, S. Melnic, D. Prodius, S. Shova, A. Arauzo, J. Luzon, L. Badia-Romano, F. Luis and C. Turta, *Dalton Transactions*, 2014, 43, 10999-11013.
23. E. Bartolome, J. Bartolome, S. Melnic, D. Prodius, S. Shova, A. Arauzo, J. Luzon, F. Luis and C. Turta, *Dalton Transactions*, 2013, 42, 10153-10171.
24. K. Bernot, L. Bogani, A. Caneschi, D. Gatteschi and R. Sessoli, *Journal of the American Chemical Society*, 2006, 128, 7947-7956.
25. P. Hu, X. Wang, Y. Ma, Q. Wang, L. Li and D. Liao, *Dalton Transactions*, 2014, 43, 2234-2243.
26. D. S. Gatteschi, R.; Caneschi, A.; Bogani, L.; Vindigni, A.: , *In 225th National Meeting of the American-Chemical-Society: New Orleans, Louisiana, 2003*; , pp U147-U147.
27. L. C. Bogani, A.; Fedi, M.; Gatteschi, D.; Massi, M.; Novak, M. A.; Pini, M. G.; Rettori, A.; Sessoli, R.; Vindigni, A.: , *Phys. Rev. Lett.*, 2004, , 92.
28. Z. Wang, B. Zhang, H. Fujiwara, H. Kobayashi and M. Kurmoo, *Chemical Communications*, 2004, DOI: 10.1039/B314221C, 416-417.
29. F. Prins, E. Pasca, L. J. de Jongh, H. Kooijman, A. L. Spek and S. Tanase, *Angewandte Chemie International Edition*, 2007, 46, 6081-6084.
30. E.-Q. Gao, P.-P. Liu, Y.-Q. Wang, Q. Yue and Q.-L. Wang, *Chemistry – A European Journal*, 2009, 15, 1217-1226.
31. C. M. Kareis, J.-H. Her, P. W. Stephens, J. G. Moore and J. S. Miller, *Chemistry – A European Journal*, 2012, 18, 9281-9288.
32. D. N. Woodruff, R. E. P. Winpenny and R. A. Layfield, *Chemical Reviews*, 2013, 113, 5110-5148.
33. G. Cosquer, F. Pointillart, S. Golhen, O. Cador and L. Ouahab, *Chemistry – A European Journal*, 2013, 19, 7895-7903.
34. M. Kavala, R. Boča, L. Dlhán, V. Brezová, M. Breza, J. Kožíšek, M. Fronc, P. Herich, L. Švorc and P. Szolcsányi, *The Journal of Organic Chemistry*, 2013, 78, 6558-6569.
35. A. Amjad, A. M. Madalan, M. Andruh, A. Caneschi and L. Sorace, *Chemistry – A European Journal*, 2016, 22, 12849-12858.
36. A. H. Biltmo, P.: , *Phys. Rev. B*, 2008, , 78.
37. C. M. S. S. Gannarelli, D. M.; Rosenbaum, T. F.; Aeppli, G.; Fisher, A. J.: , *Phys. Rev. B*, 2012,, 86.
38. F. Habib, P.-H. Lin, J. Long, I. Korobkov, W. Wernsdorfer and M. Murugesu, *Journal of the American Chemical Society*, 2011, 133, 8830-8833.
39. J. Liu, Y.-C. Chen, J.-J. Lai, Z.-H. Wu, L.-F. Wang, Q.-W. Li, G.-Z. Huang, J.-H. Jia and M.-L. Tong, *Inorganic Chemistry*, 2016, 55, 3145-3150.
40. K. R. Meihaus, J. D. Rinehart and J. R. Long, *Inorganic Chemistry*, 2011, 50, 8484-8489.
41. F. Moro, D. Kaminski, F. Tuna, G. F. S. Whitehead, G. A. Timco, D. Collison, R. E. P. Winpenny, A. Ardavan and E. J. L. McInnes, *Chemical Communications*, 2014, 50, 91-93.
42. M. N. C. Popova, E. P.; Malkin, B. Z.; Saikin, S. K.: , *Phys. Rev. B* 2000, , 61, 7421-7427.
43. J. A. M. Quilliam, S.; Kycia, J. B., *Phys. Rev. B* 2012, , 85.
44. J. A. Rodriguez, A. A.; Carlo, J. P.; Dunsiger, S. R.; MacDougall, G. J.; Russo, P. L.; Savici, A. T.; Uemura, Y. J.; Wiebe, C. R.; Luke, G. M.: , *Phys. Rev. Lett.*, 2010, , 105.
45. C. Schlegel, E. Burzurí, F. Luis, F. Moro, M. Manoli, E. K. Brechin, M. Murrie and J. van Slageren, *Chemistry – A European Journal*, 2010, 16, 10178-10185.
46. J. van Slageren, S. Dengler, J. Gómez-Segura, D. Ruiz-Molina and M. Dressel, *Inorganica Chimica Acta*, 2008, 361, 3714-3717.

47. L. Vergnani, A.-L. Barra, P. Neugebauer, M. J. Rodriguez-Douton, R. Sessoli, L. Sorace, W. Wernsdorfer and A. Cornia, *Chemistry – A European Journal*, 2012, 18, 3390-3398.
48. L. Jia, Q. Chen, Y.-S. Meng, H.-L. Sun and S. Gao, *Chemical Communications*, 2014, 50, 6052-6055.
49. D. Zhang, Y.-M. Tian, W.-B. Sun, H.-F. Li, P. Chen, Y.-Q. Zhang and P.-F. Yan, *Dalton Transactions*, 2016, 45, 2674-2680.
50. Y.-S. Meng, Y.-S. Qiao, Y.-Q. Zhang, S.-D. Jiang, Z.-S. Meng, B.-W. Wang, Z.-M. Wang and S. Gao, *Chemistry – A European Journal*, 2016, 22, 4704-4708.
51. A. J. Calahorra, I. Oyarzabal, B. Fernandez, J. M. Seco, T. Tian, D. Fairen-Jimenez, E. Colacio and A. Rodriguez-Dieguez, *Dalton Transactions*, 2016, 45, 591-598.
52. W.-Y. Zhang, Y.-M. Tian, H.-F. Li, P. Chen, W.-B. Sun, Y.-Q. Zhang and P.-F. Yan, *Dalton Transactions*, 2016, 45, 3863-3873.
53. D. Pinkowicz, M. Ren, L.-M. Zheng, S. Sato, M. Hasegawa, M. Morimoto, M. Irie, B. K. Breedlove, G. Cosquer, K. Katoh and M. Yamashita, *Chemistry – A European Journal*, 2014, 20, 12502-12513.
54. E. Lucaccini, L. Sorace, M. Perfetti, J.-P. Costes and R. Sessoli, *Chemical Communications*, 2014, 50, 1648-1651.
55. P. L. Then, C. Takehara, Y. Kataoka, M. Nakano, T. Yamamura and T. Kajiwara, *Dalton Transactions*, 2015, 44, 18038-18048.
56. W. Wernsdorfer, N. Aliaga-Alcalde, D. N. Hendrickson and G. Christou, *Nature*, 2002, 416, 406-409.
57. T. N. Nguyen, W. Wernsdorfer, M. Shiddiq, K. A. Abboud, S. Hill and G. Christou, *Chemical Science*, 2016, 7, 1156-1173.
58. A. Nava, L. Rigamonti, E. Zangrando, R. Sessoli, W. Wernsdorfer and A. Cornia, *Angewandte Chemie International Edition*, 2015, 54, 8777-8782.
59. D. Pinkowicz, H. I. Southerland, C. Avendaño, A. Prosvirin, C. Sanders, W. Wernsdorfer, K. S. Pedersen, J. Dreiser, R. Clérac, J. Nehr Korn, G. G. Simeoni, A. Schnegg, K. Holldack and K. R. Dunbar, *Journal of the American Chemical Society*, 2015, 137, 14406-14422.
60. G. Poneti, K. Bernot, L. Bogani, A. Caneschi, R. Sessoli, W. Wernsdorfer and D. Gatteschi, *Chemical Communications*, 2007, DOI: 10.1039/B617898G, 1807-1809.
61. J. J. Baldoví, J. M. Clemente-Juan, E. Coronado, Y. Duan, A. Gaita-Ariño and C. Giménez-Saiz, *Inorganic Chemistry*, 2014, 53, 9976-9980.
62. N. Ishikawa, M. Sugita, T. Okubo, N. Tanaka, T. Iino and Y. Kaizu, *Inorganic Chemistry*, 2003, 42, 2440-2446.
63. M. T. Gamer, Y. Lan, P. W. Roesky, A. K. Powell and R. Clérac, *Inorganic Chemistry*, 2008, 47, 6581-6583.
64. K. S. Gavrilenko, O. Cador, K. Bernot, P. Rosa, R. Sessoli, S. Golhen, V. V. Pavlishchuk and L. Ouahab, *Chemistry – A European Journal*, 2008, 14, 2034-2043.

General conclusion

In this thesis, we focus on the structural and magnetic characterization of a series of lanthanide-based TEMPO radical containing compounds and two diamagnetic carboxylic acids containing compounds.

We have conducted the tests to assembly the targeted dimensions by choosing the appropriate radical ligands. At the beginning, we hope to design 0D compound by using the ligands with non-coordinating substituents, and 1D compound with the coordinating substituents. The results are generally in agreement with our expectation. This strategy is also feasible on the carboxylic ligands.

Before studying the Ln^{III}-(TEMPO-R) system, we have two main goals, strong Ln^{III}-radical exchange coupling and high dynamic performance.

In chapter 2, our design of 0D compounds begins with TEMPO-OMe, which affords a penta-spin system $\{[(\text{Ln}(\text{hfac})_3)(\text{TEMPO-OCH}_3)(\text{H}_2\text{O})]_2 \cdot \text{TEMPO-OCH}_3\}$. Surprisingly SMM behaviors with modest activation energies have been found for the Ce^{III} (**1**), Nd^{III} (**2**) and Pr^{III} (**3**) derivatives (independent of the Kramer or non-Kramer ion character) whereas the Dy^{III} one (**5**) remains silent. We can claim here it is the first time that a Pr^{III}-based has been reported. In these SMMs, the coordination geometry is not main factor that governs the SMM behavior, but the electrostatic environment which plays an important role in the slow relaxation. The work going with TEMPO-NH₂ and TEMPO-Acetamido either give very modest performance or non-SMM behavior. Our first goal has been realized by the combination of Ln^{III} with TEMPO-OCH₂CCH because a strong Ln-TEMPO AF interaction (-10.38K or 7.11cm⁻¹) on [Gd(hfac)₃(TEMPO-OCH₂CCH)(H₂O)] (**11**) is obtained. This strong interaction permits to observe the SMM behavior on both Dy^{III} and Tb^{III} derivatives.

In chapter 3, we have successfully synthesized the expected 1D chains firstly by three radicals, TEMPO-Methacrylate, TEMPO-OCOPh and Oxo-TEMPO. Combination of Oxo-TEMPO with Ce^{III} even gives a 2D network. The first 1D SMM is realized by [Pr(hfac)₃(TEMPO-OH)(H₂O)]_n (**17**) with a modest activation energy. The Dy^{III} derivative [Dy(hfac)₃(TEMPO-OH)]_n (**18**) also displays a modest SMM behavior. Moreover, strong ferromagnetic interaction (14.1 K or 9.66 cm⁻¹) has been observed on the Gd^{III} (**19**) derivative.

In the subsequent work on TEMPO-CN, we have various type of compounds. Again a Ce^{III} based SMM [Ce(hfac)₃(TEMPO-CN)₂] (**20**) with a small energy barrier is obtained. Then a complex Dy₂-(radical-Dy₁-radical)-Dy₂ system (**21**) which is composed of several magnetic entities is obtained. Finally a 1D chain on Gd^{III} derivative, [Gd(hfac)₃(TEMPO-CN)]_n (**23**) displays the strongest exchange coupling in this thesis. This strong exchange coupling (J = -22.4 K or 15.3 cm⁻¹) permits us to expect an excellent dynamic properties on the Tb^{III} (**22**) derivative with a rather high energy barrier of 65.8 K.

At the moment, hundreds of SMM are reported, in terms of the quantity, light-lanthanide based SMMs are far less than the heavy ones based SMMs. This is because the structural-

magneto relationship is not very clear for light-lanthanides. We have successfully synthesized several light-lanthanide based SMMs. especially on the basis of TEMPO radicals, they are found to be very suitable for the design of SMM. Even though we do not propose any declaration concerning the structural-magneto relationship, the accumulation of quantity may promote the comprehension in future work.

In this thesis, we have stressed that The TEMPO-R radicals can serve to dramatically increase the exchange coupling.

In the future work, the synthesis of other TEMPO-R radicals or other aliphatic nitroxide radicals (TEMPO-R radicals belong to aliphatic nitroxide radicals) should be put in agenda.

In the second part, we have selected one photo-switchable acid ligand and one dicarboxylic acid ligand to construct the building blocks. In chapter 4, we are able to obtain a chain-like arrangement of dinuclear complexes chain $[\text{Dy}_2(\text{AZO})_6(\text{DMSO})_2(\text{H}_2\text{O})_2] \cdot 4\text{DMSO}$ (**24**) with remarkable SMM behavior. The diamagnetic doping method offers a possibility to understand that the $\text{Dy}^{\text{III}}\text{-Dy}^{\text{III}}$ interaction can serve to accelerate the relaxation. We also hope that we can be able to modify the environment of Ln^{III} ions by the photo-isomerization transformation. Unfortunately this test is not successful.

A series of isostructural MOFs with chain-like structure are obtained by using o-PDA ligand. The last light lanthanide based SMM, $\{[\text{Nd}_2(\text{o-PDA})_3(\text{H}_2\text{O})_2] \cdot 2\text{H}_2\text{O}\}_n$ (**25**) is obtained with a small activation barrier. The Dy analogue exhibits an excellent SMM behavior. Through the theoretical calculation, dipolar coupling ($J=0.05 \text{ cm}^{-1}$) is identified as the main contribution to the total coupling ($J_{\text{exchange}}=0.01 \text{ cm}^{-1}$), which results in a small ratio of $J_{\text{intra}}/J_{\text{inter}}$, precluding the single-chain-magnet behavior. Thanks to the method of magnetic dilution, we have been able to confirm that (**28**) is a good example of exchange-biased SMM.

The future work will continue, on the basis of the results in this thesis, to achieve three main realistic objectives: 1) to further slow down the magnetic relaxation and increase the anisotropy barrier; 2) to seek for the new and more powerful 4f-2p system to augment the magnetic coupling; 3) to explore more SMMs based on the light-lanthanides and understand their unique structural-magneto relationship.

Appendix A1. Synthesis Information

All the ligands are purchased either from TCI Chemicals or Aldrich and used without further purification.

Synthesis of precursor A: $\text{Ln}(\text{hfac})_3 \cdot 2\text{H}_2\text{O}$ (Ln= Gd, Eu, Tb, Dy, Ho, Er, Tm, Yb, Y)

A modified method on the basis of ref [1] was used to prepare $\text{Ln}(\text{hfac})_3 \cdot 2\text{H}_2\text{O}$. 24 mmol (3.39 mL) of Hhfac is poured into 100 mL of cold Et_2O . 1.78 mL of aqueous ammoniac solution is added dropwise, giving abundant production of white smokes. Once they disappear, a 10 mL aqueous $\text{LnCl}_3 \cdot n\text{H}_2\text{O}$ (Ln= Gd, Eu, Tb, Dy, Ho, Er, Tm, Yb, Y) (8 mmol) is added in two portions. After each addition, the organic phase is washed by water and the aqueous phase is discarded. The organic phase is then dried on Na_2SO_4 , filtered, and concentrated under reduced pressure. The yellow oil is extracted with heptane and is left in freezer at 2°C to crystallize. The compound then crystallizes after several days.

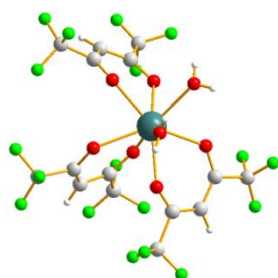


Figure A1.1 $\text{Ln}(\text{hfac})_3 \cdot 2\text{H}_2\text{O}$.

Synthesis of precursor B: $\text{Ln}(\text{hfac})_3 \cdot 2\text{H}_2\text{O}$ (Ln=Ce, Pr, Nd)

The method of synthesis of $\text{Ln}(\text{hfac})_3 \cdot 2\text{H}_2\text{O}$ (Ln=Ce, Pr, Nd) is further modified. The key point to crystallize $\text{Hhfac} \cdot 2\text{H}_2\text{O}$ is to work in strict stoichiometry and avoid an excess of hfac^- in the mixture. Firstly a solution of $\text{LnCl}_3 \cdot n\text{H}_2\text{O}$ (1.42 mmol) in 1.2 mL of water, is prepared in a test tube. We thus synthesize $\text{Hhfac} \cdot 2\text{H}_2\text{O}$ by adding 1 mL of Hhfac ($d = 1.47, 7.07$ mmol) to 5 mL of water. The mixture is stirred for 2 hours; the obtained white solid is then washed with cool water and dried. It has to be stored in the dark. The solid is then dissolved in 12 mL of Et_2O . 0.78 mL of a 25 % aqueous ammoniac ($d=0.91$) solution is added to form NH_4hfac . This solution is then added dropwise gently in the test tube containing the $\text{LnCl}_3 \cdot n\text{H}_2\text{O}$ solution. A very strong shaking of the tube allow for efficient extraction of $\text{LnCl}_3 \cdot n\text{H}_2\text{O}$ by NH_4hfac (very few gases are emitted for such small quantities). The organic phase is washed with 1.2 mL of water dried on Na_2SO_4 . After filtration the mixture is concentrated. The yellowish oil is mixed with n-heptane and is held in the refrigerator for several days to crystallize.

Chapter 2: Synthesis of $\{[(Ln(hfac)_3)(TEMPO-OCH_3)(H_2O)]_2 \cdot TEMPO-OCH_3\}$ (Ln=Ce(1), Pr(2), Nd(3), Dy(4), Gd(5))

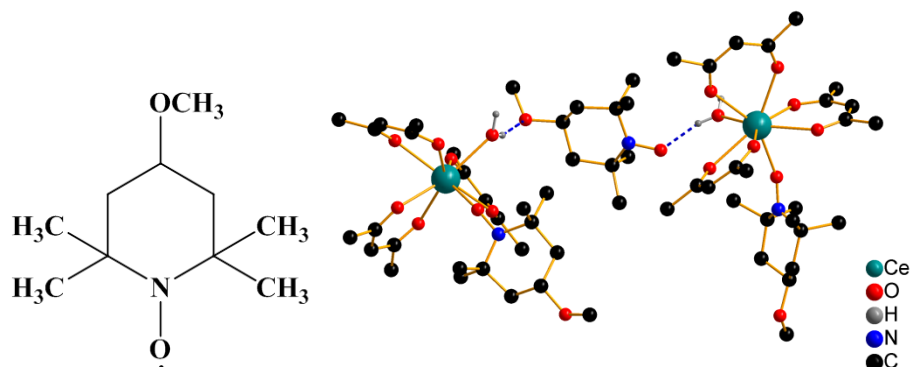


Figure A1.2 TEMPO-OMe (left) and $\{[(Ce(hfac)_3)(TEMPO-OCH_3)(H_2O)]_2 \cdot TEMPO-OCH_3\}$ (1) (right).

A suspension containing 0.1 mmol $[Ce(hfac)_3(H_2O)_2]$ hydrate in 20 mL of n-heptane was boiled until dissolution. Then 0.15 mmol of TEMPO- OCH_3 dissolved in 2 mL of $CHCl_3$ was added while hot. After being stirring for 10 min, the solution was filtered and was kept at around 4°C. Several days later dark-violet plat crystals of **1** were obtained. Complexes **2**, **3**, **4** and **5** were synthesized in the similar procedure, but obtained as powders instead of crystals.

Synthesis of $\{[Ln(hfac)_3H_2O]_2(TEMPO-NH_2)_2\}$ (Ln=Dy(5), Gd(6))

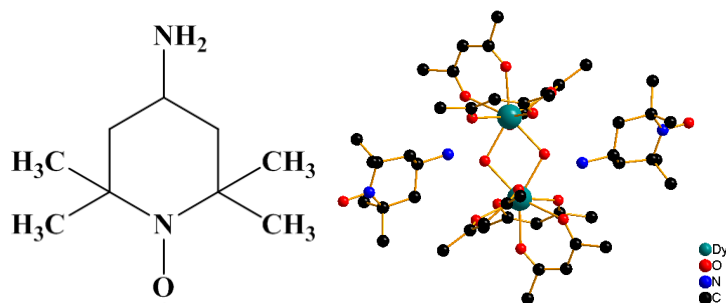


Figure A1.3 TEMPO-NH₂ (left) and $[Ln(hfac)_3H_2O]_2(TEMPO-NH_2)_2$ (6) (right).

A suspension containing 0.1 mmol $[Dy(hfac)_3(H_2O)_2]$ hydrate in 20 mL of n-heptane was boiled until dissolution. Then the solution was cooled to 70°C, next 0.1 mmol of TEMPO-NH₂ dissolved in 2 mL of $CHCl_3$ was added. The solution was kept at around 4°C, and after several days dark-orange block crystals of **6** were obtained. Complex **7** was synthesized in the similar procedure, but obtained as powders instead of crystals.

Synthesis of $[\text{Ln}(\text{hfac})_3(\text{TEMPO-Acetamido})_2]$ ($\text{Ln}=\text{Dy}$ (**8**))

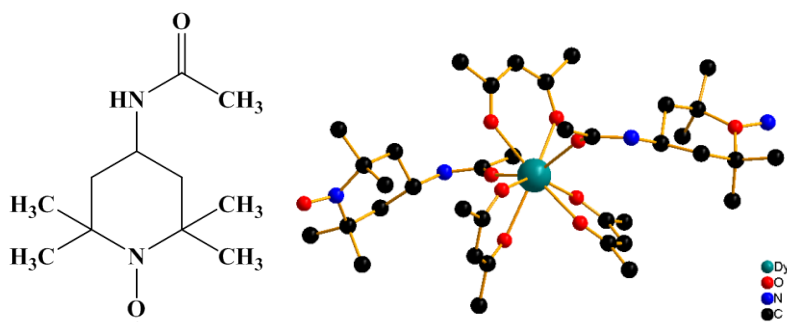


Figure A1.4 TEMPO-Acetamido (left) and $[\text{Ln}(\text{hfac})_3(\text{Tempo-Acetamido})_2]$ (**8**) (right).

$[\text{Dy}(\text{hfac})_3(\text{H}_2\text{O})_2]$ (0.1 mmol) was suspended in 20 ml boiling n-heptane for 20 min, then the suspension was cooled to 70 °C. TEMPO-Acetamido (0.1 mmol) in CH_2Cl_2 (5 ml) was added to this suspension. After stirring for 10 min, the solution was left undisturbed in the refrigerator to evaporate slowly to afford the pale yellow prism crystals of **8**.

Synthesis of $[\text{Ln}(\text{hfac})_3(\text{TEMPO-OCH}_2\text{CCH})(\text{H}_2\text{O})]$ ($\text{Ln}=\text{Dy}$ (**9**), **Tb**(**10**), **Gd**(**11**))

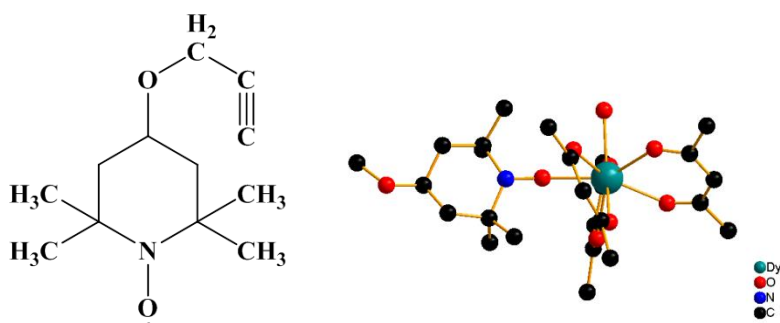


Figure A1.5 TEMPO-OCH₂CCH (left) and $[\text{Ln}(\text{hfac})_3(\text{TEMPO-OCH}_2\text{CCH})(\text{H}_2\text{O})]$ (**9**) (right).

A starting material $[\text{Dy}(\text{hfac})_3(\text{H}_2\text{O})_2]$ (0.1 mmol) was dissolved in n-heptane (20 mL). After being boiled and concentrated to a volume of ca. 10 mL, the solution was allowed to stand to be cooled. A dichloromethane solution (4 mL) containing 0.1 mmol of TEMPO-OCH₂CCH was added to the above n-heptane solution. The combined solution was stirred and filtered, and the filtrate was kept in a refrigerator. The yellow-prism crystals were collected. Complexes **10** and **11** were synthesized in the similar procedure, but obtained as powders instead of crystals.

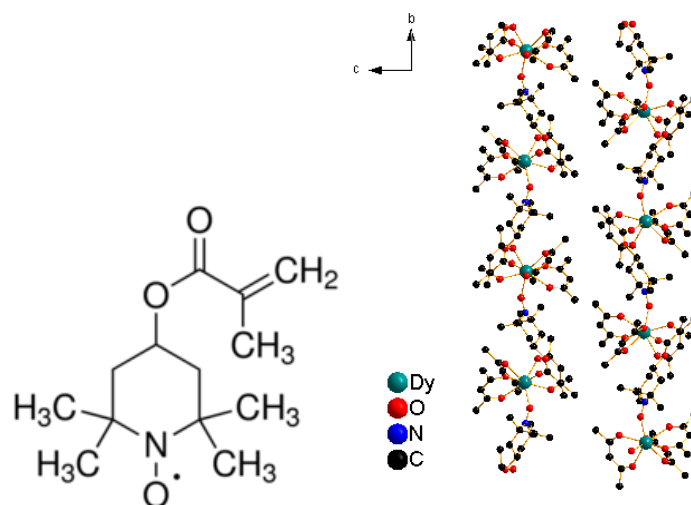
Chapter 3: Synthesis of $[\text{Ln}(\text{hfac})_3(\text{TEMPO-Methacrylate})]_n$ ($\text{Ln}=\text{Dy}$ (12))

Figure A1.6 TEMPO- Methacrylate (left) and $[\text{Ce}(\text{hfac})_3(\text{TEMPO-Methacrylate})]_n$ (**12**) (right).

0.1 mmol $[\text{Dy}(\text{hfac})_3(\text{H}_2\text{O})_2]$ was suspended in 20 ml boiling n-heptane for 20 min, then the suspension was cooled to 70 °C. 0.1 mmol TEMPO-Methacrylate in 5 ml CH_2Cl_2 was added to this suspension. After stirring for 10 min, the solution was left undisturbed in the refrigerator to evaporate slowly to afford orange-prism crystals of **12** was obtained.

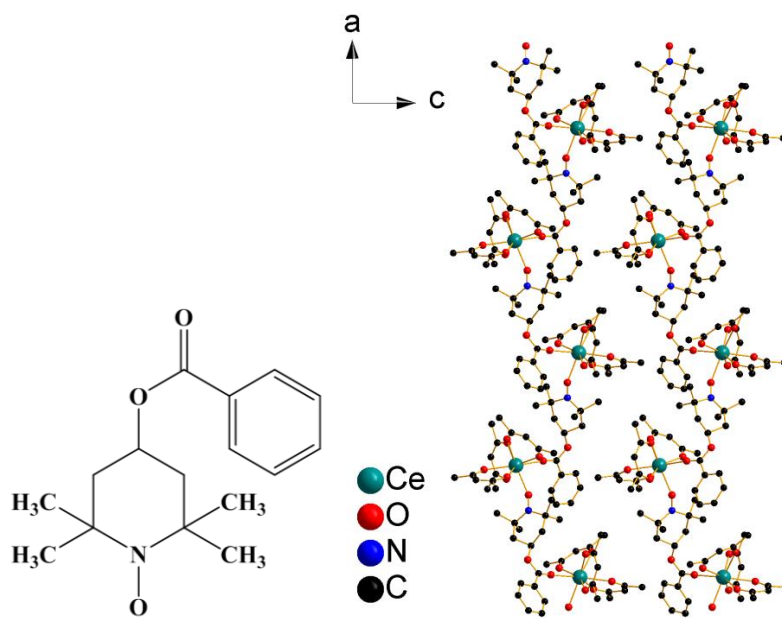
Synthesis of $[\text{Ln}(\text{hfac})_3(\text{TEMPO-OCOPh})]_n$ ($\text{Ln}=\text{Ce}$ (13))

Figure A1.7 TEMPO-OCOPh (left) and $[\text{Ce}(\text{hfac})_3(\text{TEMPO-OCOPh})]_n$ (**13**) (right).

0.1 mmol of $[\text{Ce}(\text{hfac})_3(\text{H}_2\text{O})_2]$ was added to n-heptane (20 mL), and this solution was boiled for 20 min. The solution was subsequently cooled to 70 °C, 0.2 mmol of TEMPO-OCOPh) in CH_2Cl_2 (5 mL) was added, and the mixture was stirred for 10 min at this temperature. Then, the solution was cooled to room temperature and filtered, then the filtrate was left at around 4 °C for several days to give dark-violet crystals of **13** suitable for X-ray analysis.

Synthesis of $[\text{Ln}(\text{hfac})_3(\text{Oxo-TEMPO})]_n$ (Ln=Dy(**14**))

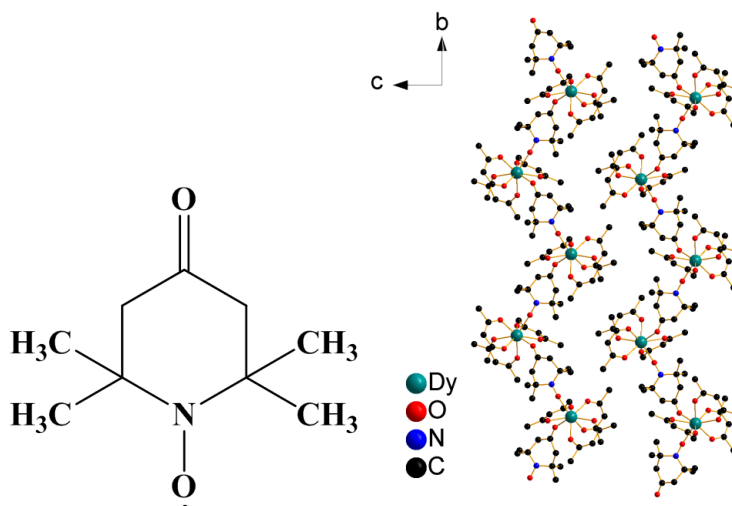


Figure A1.8 Oxo-TEMPO (left) and $[\text{Dy}(\text{hfac})_3(\text{Oxo-TEMPO})]_n$ (**14**) (right).

A solution of $[\text{Dy}(\text{hfac})_3(\text{H}_2\text{O})_2]$ (0.1 mmol) in 30 mL dry boiling heptane was kept for 20min. Then the solution was cooled to 70 °C, and a solution of Oxo-TEMPO (0.1 mmol) in 3 mL CH_2Cl_2 was added. The resulting solution was stirred for 10 min and then cooled to room temperature. The filtrate was allowed to stand at around 4°C for slow evaporation. After several days, orange-needle crystals of **14** were collected.

Synthesis of $[(\text{Ln}(\text{hfac})_3)_3(\text{Oxo-Tempo})_4]_n$ (Ln=Ce(**15**))

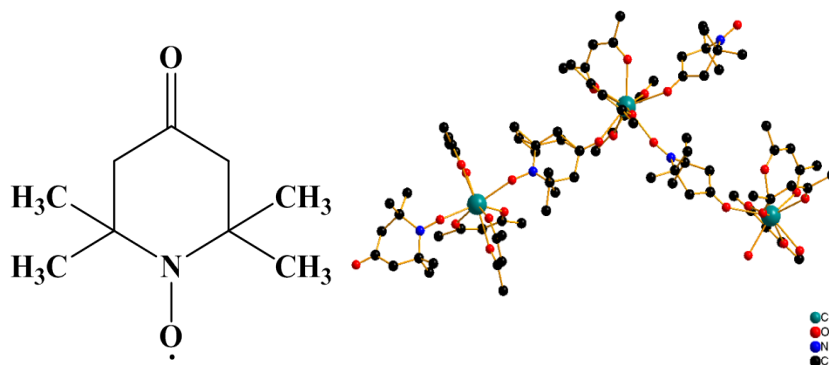


Figure A1.9 Oxo-TEMPO (left) and $[(\text{Ce}(\text{hfac})_3)_3(\text{Oxo-Tempo})_4]_n$ (**15**) (right).

A solution of $[\text{Ce}(\text{hfac})_3(\text{H}_2\text{O})_3]$ (0.1 mmol) in 30 mL dry boiling heptane was kept for 20 min. Then the solution was cooled to 70 °C, and a solution of Oxo-TEMPO (0.1 mmol) in 3 mL of CH_2Cl_2 was added. The resulting solution was stirred for 10 min and then cooled to room temperature. The filtrate was allowed to stand at around 4°C for slow evaporation. After several days, orange-needle crystals of **15** were collected.

Synthesis of $[\text{Ln}(\text{hfac})_3\text{H}_2\text{O}(\text{TEMPO-OH})]_n$ (Ln=Ce(**16**) and Pr(**17**))

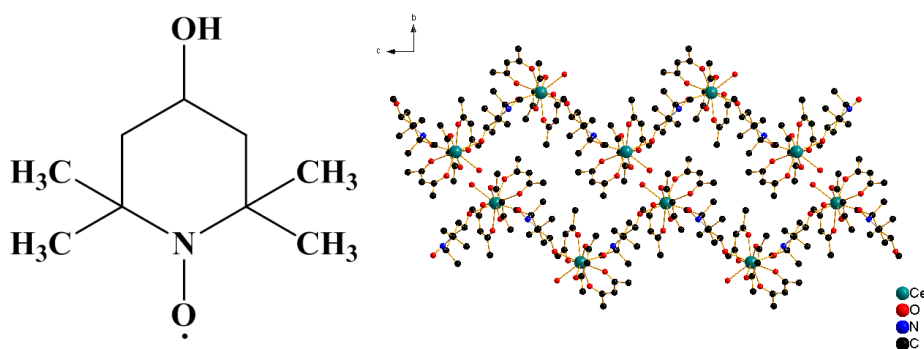


Figure A1.10 TEMPO-OH (left) and $[\text{Ln}(\text{hfac})_3\text{H}_2\text{O}(\text{TEMPO-OH})]_n$ (**16**) (right).

Dissolving 0.05 mmol $\text{Ce}(\text{hfac})_3(\text{H}_2\text{O})_3$ in boiling n-heptane (20 mL). After being stirred for 20 min, the solution was cooled to 70 °C, to which 0.05 mmol TEMPO-OH in CH_2Cl_2 (5 mL) was added. The resulting solution was stirred for 5 min and then cooled to around 4 K. Slowly evaporation of the final solution for about several days violet-plat crystals of **16** suitable for single-crystal X-ray analysis. Complex **17** were synthesized in the similar procedure, but obtained as powders instead of crystals.

Synthesis of $[\text{Ln}(\text{hfac})_3(\text{TEMPO-OH})]_n$ (Ln=Dy(**18**) and Gd(**19**))

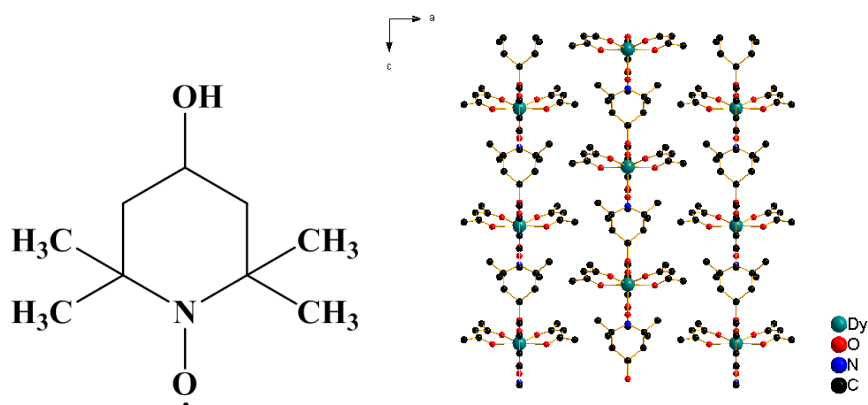


Figure A1.11 TEMPO-OH (left) and $[\text{Dy}(\text{hfac})_3(\text{TEMPO-OH})]_n$ (**18**) (right).

Dissolving 0.05 mmol $\text{Dy}(\text{hfac})_3(\text{H}_2\text{O})_2$ in boiling n-heptane (20 mL). After being stirred for 20 min, the solution was cooled to 70 °C, to which 0.05 mmol TEMPO-OH in CH_2Cl_2 (5 mL) was added. The resulting solution was stirred for 5 min and then cooled to around 4 K. Slowly evaporation of the final solution for about several days yield yellow-prism crystals of **15** suitable for single-crystal X-ray analysis. Complex **19** were synthesized in the similar procedure, but obtained as powders instead of crystals.

Synthesis of $[\text{Ce}(\text{hfac})_3(\text{TEMPO-CN})_2]$ (**20**)

A starting material $[\text{Ce}(\text{hfac})_3(\text{H}_2\text{O})_2]$ (0.10 mmol) was dissolved in 15 ml of n-heptane. After being boiled for 5 minutes, the solution was cooled and kept at 70°C. A 4 mL dichloromethane solution containing 0.20 mmol of TEMPO-CN was added to the above n-heptane solution. The combined solution was stirred and filtered, and the filtrate was kept in a refrigerator. The violet prism-shaped crystals of **20** were obtained suitable for X-ray diffraction after several days.

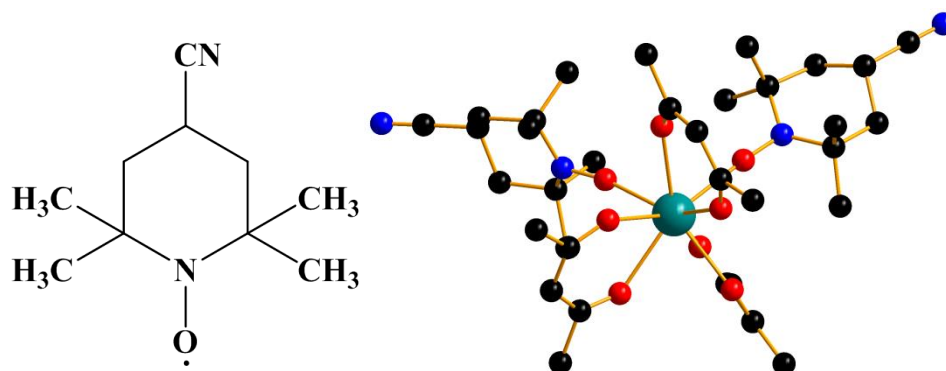


Figure A1.12 TEMPO-CN (left) and $[\text{Ce}(\text{hfac})_3(\text{TEMPO-CN})_2]$ (**20**) (right).

Synthesis of $\{[\text{Dy}(\text{hfac})_3(\text{TEMPO-CN})_2][\text{Dy}(\text{hfac})_3(\text{H}_2\text{O})_2]_2\}$ (**21**)

A starting material $\text{Dy}(\text{hfac})_3(\text{H}_2\text{O})_2$ (0.10 mmol) was dissolved in 15 ml of n-heptane. After being boiled for 5 minutes, the solution was cooled and kept at 70°C. A 4 mL dichloromethane solution containing 0.10 mmol of TEMPO-CN was added to the above n-heptane solution. The combined solution was stirred and filtered, and the filtrate was kept in a refrigerator. The pale yellow prism polycrystalline crystals of **21** were obtained after several days.

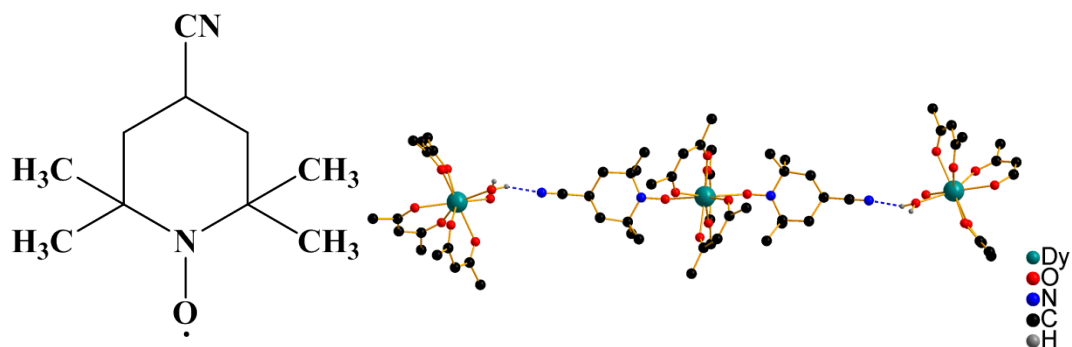


Figure A1.13 TEMPO-CN (left) and $\{[\text{Dy}(\text{hfac})_3(\text{TEMPO-CN})_2][\text{Dy}(\text{hfac})_3(\text{H}_2\text{O})_2]_2\}$ (**21**) (right).

Synthesis of $[\text{Ln}(\text{hfac})_3(\text{TEMPO-CN})]_n$ (**Tb (22)** and **Gd (23)**)

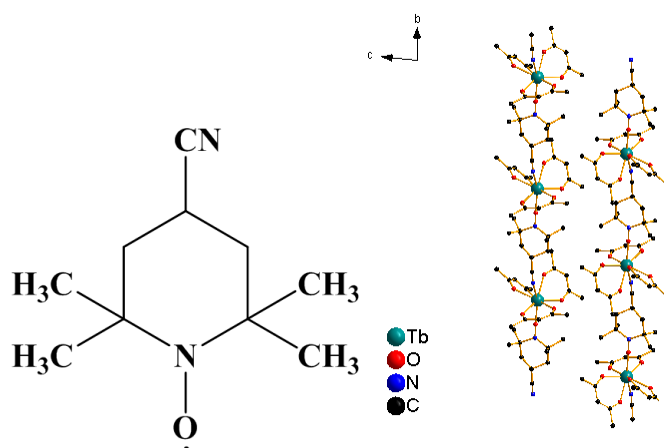


Figure A1.14 TEMPO-CN (left) and $[\text{Dy}(\text{hfac})_3(\text{TEMPO-CN})]_n$ (**22**) (right).

A starting material $\text{Tb}(\text{hfac})_3(\text{H}_2\text{O})_2$ (0.10 mmol) was dissolved in 15 ml of n-heptane. After being boiled for 5 minutes, the solution was cooled and kept at 70°C . A 4 mL dichloromethane solution containing 0.10 mmol of TEMPO-CN was added to the above n-heptane solution. The combined solution was stirred and filtered, and the filtrate was kept in a refrigerator. The pale yellow needle-shaped polycrystalline crystals of **22** were obtained. Complex **23** was synthesized in the similar procedure, but obtained as powders instead of crystals.

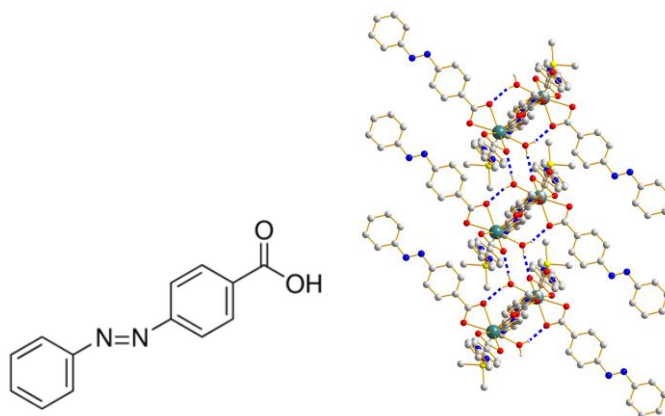
Chapter 4: Synthesis of $[\text{Dy}_2(\text{AZO})_6(\text{DMSO})_2(\text{H}_2\text{O})_2] \cdot 4\text{DMSO}$ (24**)**

Figure A1.15 HAZO (left) and $[\text{Dy}_2(\text{AZO})_6(\text{DMSO})_2(\text{H}_2\text{O})_2] \cdot 4\text{DMSO}$ (**24**) (right).

0.3 mmol Azobenzene-4-carboxylic acid was deprotonated by equivalent NaOH. Then 0.1 mmol $\text{DyCl}_3 \cdot 6\text{H}_2\text{O}$ salt was added to the solution, precipitation of an orange amorphous powder immediately appears. The precipitates were filtered and dried by ether. In a second step we have dissolved the dry precipitate into Dimethylsulfoxide (DMSO). After ten days, orange needle-shaped crystals of **24** were obtained. The doping sample **24@Y** was synthesized in the same procedure but with a starting salt of $\text{DyCl}_3 \cdot 6\text{H}_2\text{O}$ and $\text{YCl}_3 \cdot 6\text{H}_2\text{O}$ in a molar ratio of 19:1.

Chapter 5: Synthesis of $\{[\text{Ln}_2(\text{o-PDA})_3(\text{H}_2\text{O})_2] \cdot 2\text{H}_2\text{O}\}_n$ (Ln= Ce(25), Nd(26), Gd(27) and Dy(28))

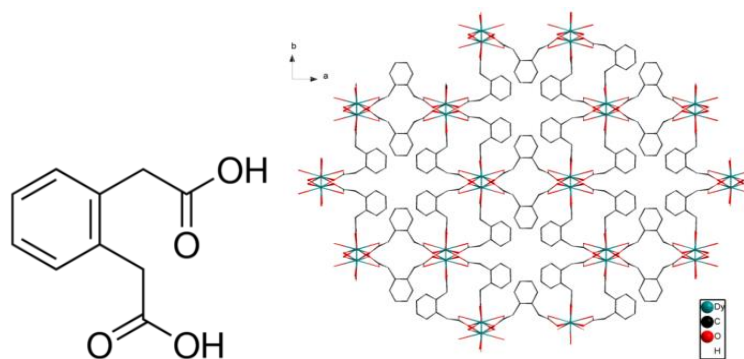


Figure A1.16 H₂-o-PDA (left) and $\{[\text{Dy}_2(\text{o-PDA})_3(\text{H}_2\text{O})_2] \cdot 2\text{H}_2\text{O}\}_n$ (28) (right).

1.5mmol 1,2-Phenylenediacetic Acid was deprotonated by equivalent NaOH in 20 ml H₂O. This solution is added directly into a stirred LnCl₃·6H₂O (1.5mmol) aqueous solution to produce white precipitates, then the precipitates were filtered and washed by distilled water, finally dried in the air. Complexes **25**, **26**, **27** and **28@Y** (DyCl₃·6H₂O and YCl₃·6H₂O in a molar ratio of 9:1) were synthesized in the similar procedure and obtained as powders.

Reference

1. M. F. Richardson, W. F. Wagner and D. E. Sands, *Journal of Inorganic and Nuclear Chemistry*, 1968, 30, 1275-1289.

Appendix A2. Supplementary information for Chapter 2

Table A2.1 Selected bond distances and angles for Ce(1).

	Bond lengths (Å)		Angles (°)
Ce1-O1	2.474(5)	Ce1-O8-N1	151.1(5)
Ce1-O2	2.472(5)	Ce2-O17-N2	156.2(5)
Ce1-O3	2.477(5)	O1-Ce1-O8	88.4(2)
Ce1-O4	2.475(5)	O10-Ce2-O17	87.3(2)
Ce1-O5	2.470(5)	O8-N1-C5	116.0(6)
Ce1-O6	2.468(5)	O8-N1-C2	114.7(6)
Ce1-O7	2.461(5)	O17-N2-C3	115.9(6)
Ce1-O8	2.417(5)	O17-N2-C1	115.1(6)
Ce2-O10	2.442(5)	O11-Ce2-O17	74.3(2)
Ce2-O11	2.490(5)	O14-Ce2-O17	101.6(2)
Ce2-O12	2.471(5)	O16-Ce2-O17	74.29(19)
Ce2-O13	2.481(5)	O15-Ce2-O17	77.4(2)
Ce2-O14	2.454(5)	O5-Ce1-O8	80.4(2)
Ce2-O15	2.440(5)	O3-Ce1-O8	75.08(19)
Ce2-O16	2.456(5)	O2-Ce1-O8	72.86(19)
Ce2-O17	2.427(5)	O6-Ce1-O8	105.9(2)

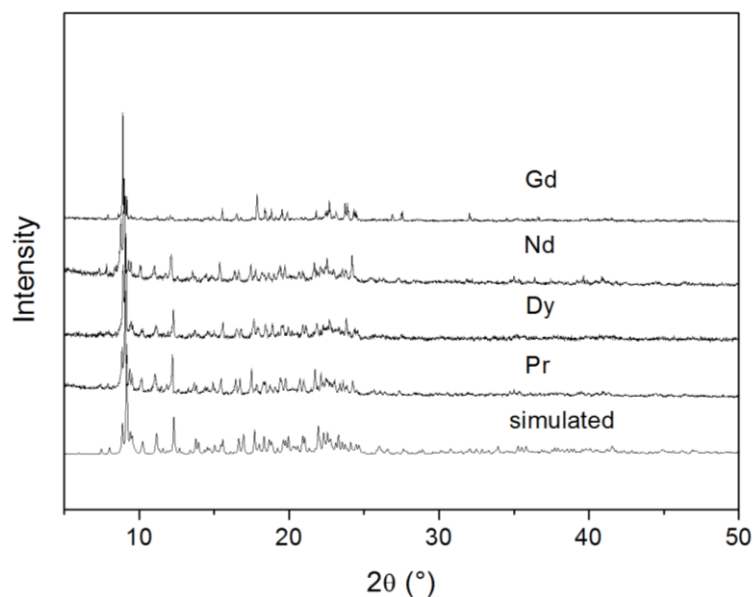


Figure A2.1 PXRD patterns of the microcrystalline powders of Pr(2), Nd(3), Gd(4), Dy(5) and comparison with to the simulated pattern from structural data file of Ce(1).

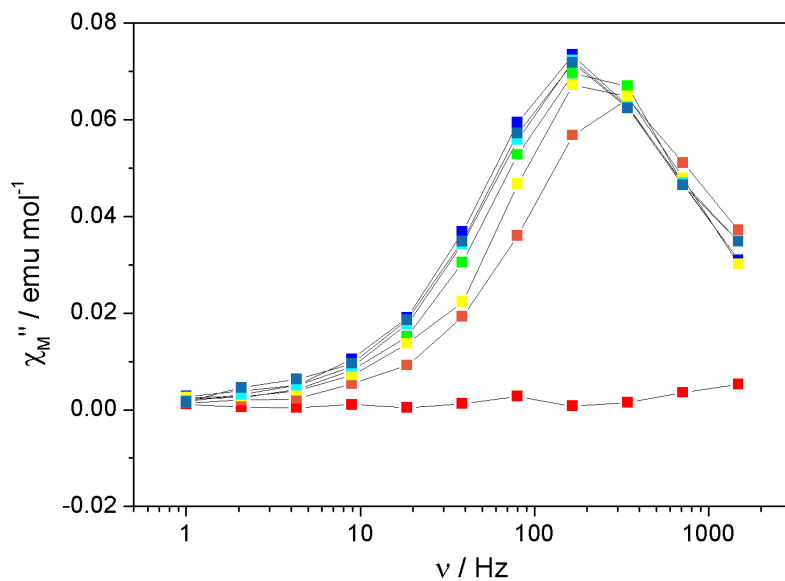


Figure A2.2 Frequency dependence of the out-of-phase components of the magnetization for various dc fields for Ce(1). Color mapping from 0 Oe (red) to 2000 Oe (blue), 200 Oe step.

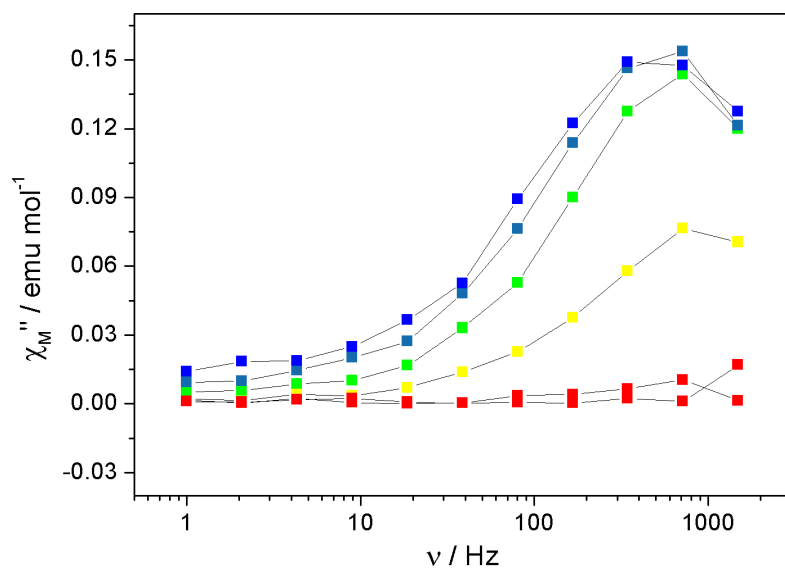


Figure A2.3 Frequency dependence of the out-of-phase components of the magnetization for various dc fields for Pr(2). Color mapping ranges from 0 Oe (red) to 4800 Oe (blue).

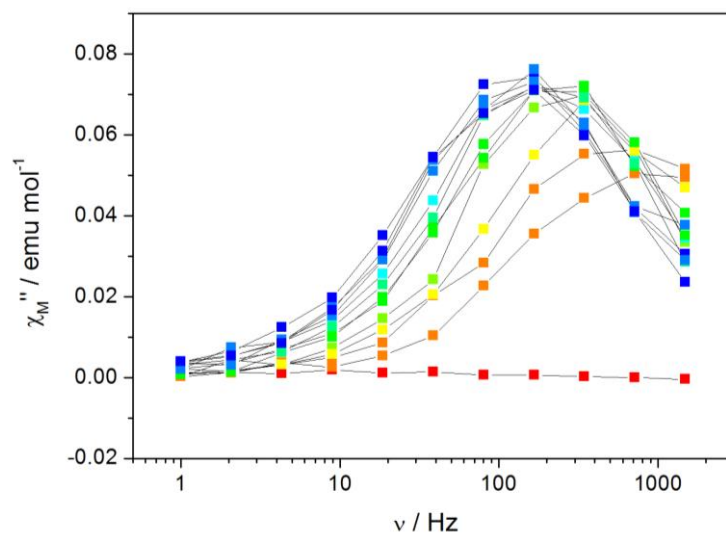


Figure A2.4 Frequency dependence of the out-of-phase components of the magnetization for various dc fields for Nd(3). Color mapping ranges from 0 Oe (red) to 3600 Oe (blue).

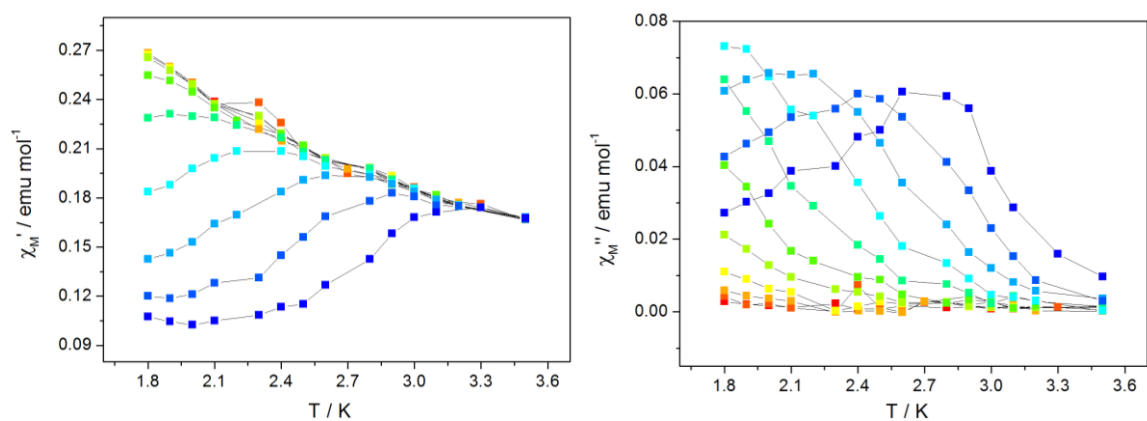


Figure A2.5 Temperature dependence of the in-phase (left) and out-of-phase (right) components of ac susceptibility under 800 Oe dc field for Ce(1). Color mapping ranges from 1 Hz (red) to 1500 Hz (blue).

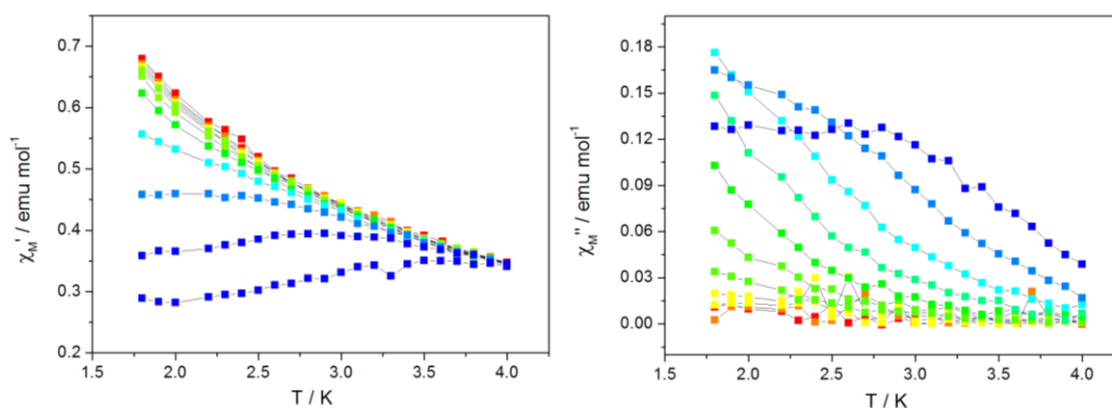


Figure A2.6 Temperature dependence of the in-phase (left) and out-of-phase (right) components of ac susceptibility under 3600 Oe dc field for Pr(2). Color mapping from 1 Hz (red) to 1500 Hz (blue).

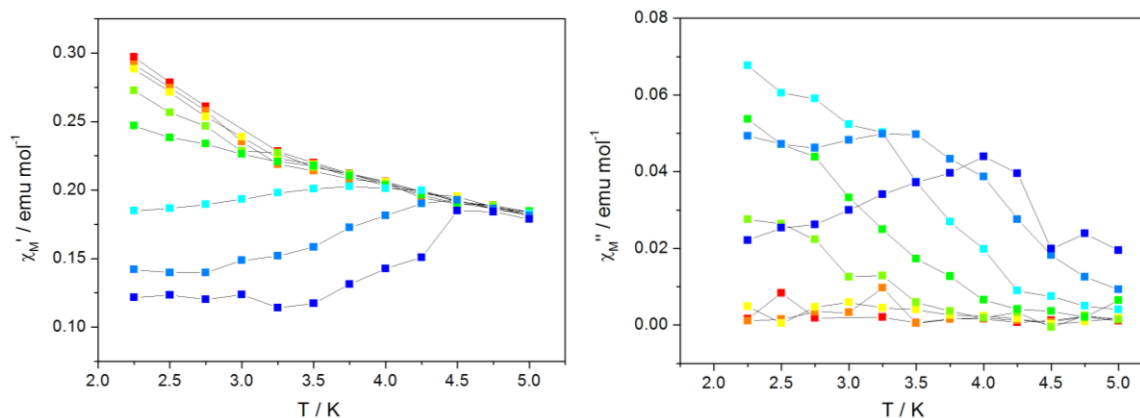


Figure A2.7 Temperature dependence of the in-phase (left) and out-of-phase (right) components of ac susceptibility under 3600 Oe dc field for Nd(3). Color mapping from 1 Hz (red) to 1500 Hz (blue).

Table A2.2 Relaxation times extracted from the fitting of χ'' vs frequency curves of Ce(1) under 800 Oe dc field.

T (K)	τ (μ s)	T (K)	τ (μ s)
1.8	927.08	2.25	402.48
1.9	762.8	2.43	253.26
2.0	603.93	2.5	203.74
2.13	443.45		

Table A2.3 Values extracted from the Argand plot of Ce(1) under 800 Oe dc field.

T (K)	χ_s	χ_T	α	R^2
1.8	0.10063	0.26917	0.07397	0.989
1.9	0.09681	0.26036	0.06185	0.98887
2.0	0.09142	0.25047	0.08813	0.97241
2.1	0.08987	0.23831	0.07347	0.97728

Table A2.4 Relaxation times extracted from the fitting of χ'' vs frequency curves of Pr(2) under 3600 Oe dc field.

T (K)	τ (μ s)	T (K)	τ (μ s)
1.8	376.86	2.3	201.83
1.9	330.1	2.4	184.68
2.0	275.22	2.5	151.1
2.2	233.86	2.6	114.35

Table A2.5 Values extracted from the Argand plot of Pr(2) under 3600 Oe dc field.

T (K)	χ_s	χ_T	α	R
1.8	0.1925	0.67837	0.20123	0.98559
1.9	0.1672	0.64995	0.24801	0.9833
2.0	0.1461	0.62129	0.26786	0.98247
2.2	0.19499	0.57069	0.15483	0.97209

Table A2.6 Relaxation times extracted from the fitting of χ'' vs frequency curves of Nd(3) under 3600 Oe dc field.

T (K)	τ (μ s)	T (K)	τ (μ s)
1.8	1486.45	2.75	780.42
1.9	1370.1	3.0	554.61
2.0	1222.86	3.25	443.03
2.25	927.88	3.5	300.34
2.5	831.94	3.75	210.32

Table A2.7 Values extracted from the Argand plot of Nd(3) under 3600 Oe dc field.

T (K)	χ_s	χ_T	α	R
1.8	0.10732	0.32925	0.20134	0.94881
1.9	0.11336	0.31687	0.15675	0.95456
2.0	0.11317	0.30704	0.16675	0.97623
2.25	0.10418	0.29448	0.2621	0.94514
2.75	0.11085	0.25449	0.09968	0.98997

Table A2.8 Selected bond distance and angles for Dy(6).

	Bond lengths (\AA)		Angles ($^\circ$)
Dy1-O1	2.302(3)	Dy1-O1-Dy2	107.76(12)
Dy1-O2	2.315(3)	Dy1-O2-Dy2	107.59(12)
Dy1-O3	2.374(3)	O8-Dy1-O6	73.67(12)
Dy1-O4	2.366(4)	O1-Dy2-O2	72.45(11)
Dy1-O5	2.350(4)	O4-Dy1-O2	77.53(12)
Dy1-O6	2.434(3)	O4-Dy1-O7	87.33(12)
Dy1-O7	2.354(3)	O2-Dy2-O13	110.83(12)
Dy1-O8	2.374(3)	O2-Dy2-O10	85.26(11)
Dy2-O1	2.303(3)	O4-Dy1-O6	108.60(12)
Dy2-O2	2.296(3)	O8-Dy1-O7	72.27(11)
Dy2-O9	2.330(4)	O3-Dy1-O6	69.44(12)
Dy2-O10	2.449(3)	O6-Dy1-O4	108.60(12)
Dy2-O11	2.383(4)	O9-Dy2-O10	71.24(11)
Dy2-O12	2.375(3)	O1-Dy2-O9	148.39(12)
Dy2-O13	2.353(3)	O12-Dy2-O14	133.25(12)
Dy2-O14	2.382(4)	O2-Dy2-O13	110.83(12)

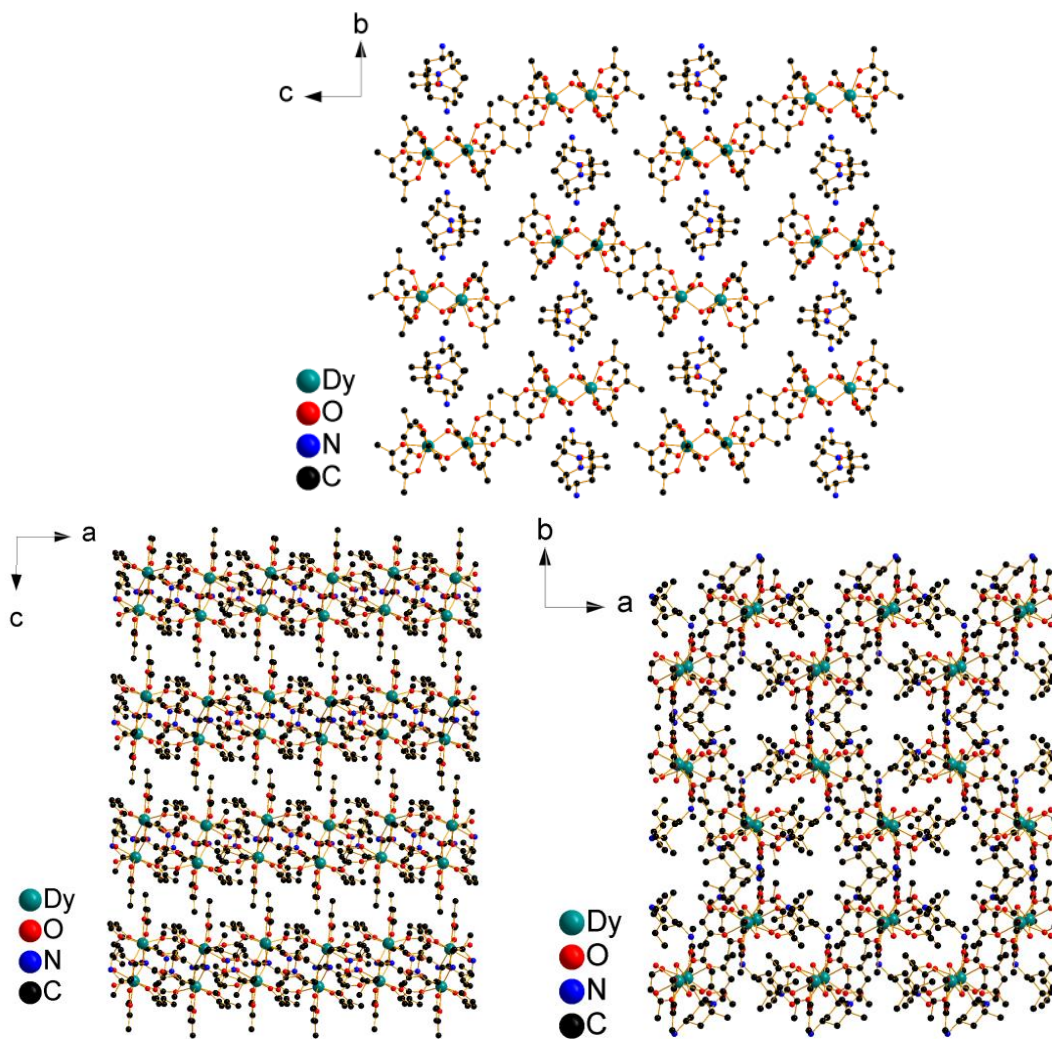


Figure A2.8 Packing diagram of Dy(6) along 'a' axis (top), 'b' axis (bottom left) and 'c' axis (bottom right).

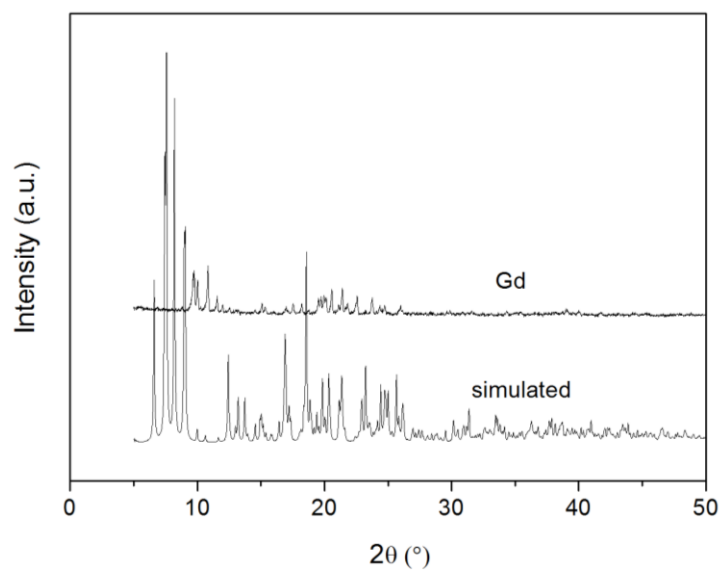


Figure A2.9 PXRD patterns of the microcrystalline powders of Gd(7) and comparison with the simulated pattern from structural data file of Dy(6).

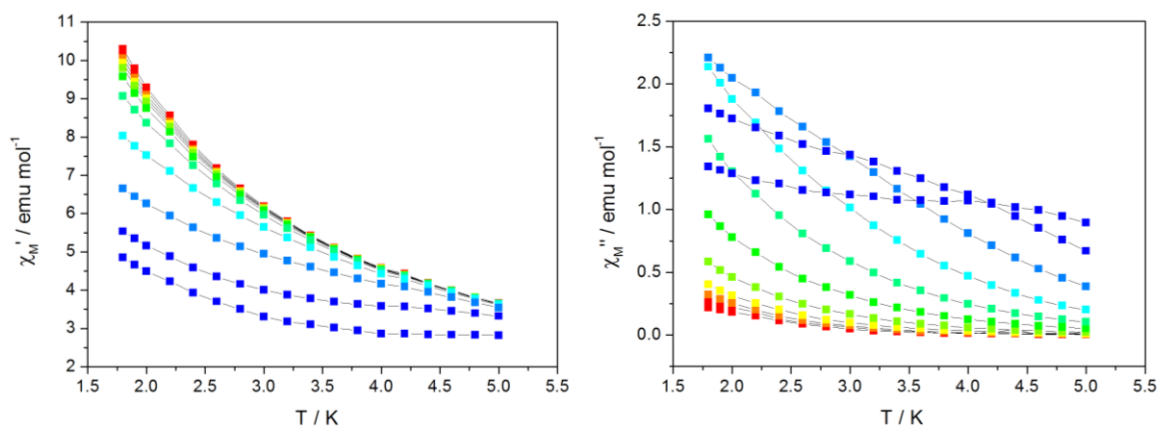


Figure A2.10 Temperature dependence of the in-phase (left) and out-of-phase (right) components of ac susceptibility under 800 Oe dc field for Dy(6). Color mapping from 1 Hz (red) to 1500 Hz (blue). Lines are guides to eye.

Table A2.9 Relaxation times extracted from the fitting of χ'' vs frequency curves of Dy(6) under 800 Oe dc field.

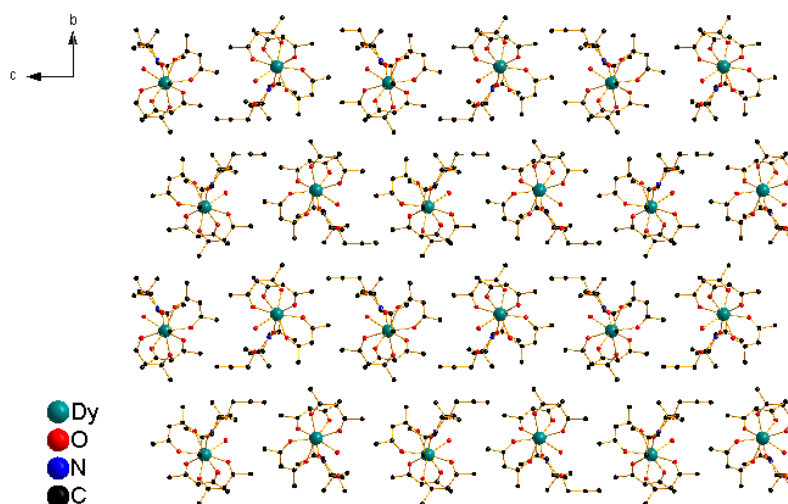
T (K)	τ (μ s)	T (K)	τ (μ s)
1.8	547.99	3.0	295.2
1.9	518.17	3.2	265.54
2.0	481.99	3.4	240.33
2.2	442.64	3.6	214.22
2.4	393.68	3.8	190.07
2.6	361.6	4.0	168.5
2.8	326.17		

Table A2.10 Values extracted from the Argand plot of Dy(6) under 800 Oe dc field.

T (K)	χ_s	χ_T	α	R
1.8	4.0690	10.149	0.1920	0.94467
1.9	3.47567	9.76836	0.2754	0.94837
2.0	3.60033	9.1416	0.20146	0.94384
2.2	3.5739	8.3939	0.13932	0.97114
2.4	3.15045	7.71435	0.16465	0.9744
2.6	2.92782	7.11614	0.15728	0.97751
2.8	2.79432	6.6108	0.12887	0.99107
3.0	2.65944	6.15106	0.0969	0.99552
3.2	2.52528	5.76007	0.08683	0.9961
3.4	2.48119	5.40085	0.05878	0.99786
3.6	2.2983	5.09703	0.07306	0.99445
3.8	2.21004	4.81158	0.05771	0.99864
4.0	2.0319	4.55787	0.06042	0.99834
4.2	1.97583	4.39424	0.05903	0.99878
4.4	1.97757	4.17754	0.0432	0.99904

Table A2.11 Selected bond distances and angles for **8**.

	Bond lengths (Å)		Angles (°)
Dy1-O1	2.361(4)	O4-Dy1-O8	101.94(13)
Dy1-O2	2.380(4)	O3-Dy1-O8	78.68(13)
Dy1-O3	2.302(3)	O3-Dy1-O1	113.39(13)
Dy1-O4	2.309(3)	O1-Dy1-O2	71.22(13)
Dy1-O5	2.355(4)	O4-Dy1-O5	82.72(13)
Dy1-O6	2.388(3)	O8-Dy1-O6	72.09(12)
Dy1-O7	2.397(4)	O1-Dy1-O6	138.72(12)
Dy1-O8	2.328(4)	O2-Dy1-O7	71.92(14)
		O5-Dy1-O6	72.92(12)
		O8-Dy1-O7	71.94(13)
		O3-Dy1-O7	135.17(13)
		O3-Dy1-O4	148.60(13)
		O5-Dy1-O7	142.94(13)

Figure A2.11 Packing diagram for Dy(**9**) along 'a' axis.Table A2.12 Selected bond distances and angles for Dy(**9**).

	Bond lengths (Å)		Angles (°)
Dy1-O1	2.371(3)	O3-Dy1-O8	72.12(9)
Dy1-O2	2.328(3)	O1-Dy1-O2	70.94(9)
Dy1-O3	2.370(2)	O6-Dy1-O7	79.51(10)
Dy1-O4	2.333(3)	O3-Dy1-O5	129.02(10)
Dy1-O5	2.354(3)	O2-Dy1-O5	134.45(9)
Dy1-O6	2.332(3)	O8-Dy1-O1	111.77(10)
Dy1-O7	2.362(3)	O8-Dy1-O6	84.72(10)
Dy1-O8	2.326(3)	O1-Dy1-O7	72.54(10)
		O3-Dy1-O6	76.16(9)
		O8-Dy1-O2	78.06(10)
		O4-Dy1-O7	145.81(9)
		O5-Dy1-O4	74.63(10)
		O2-Dy1-O7	117.78(10)

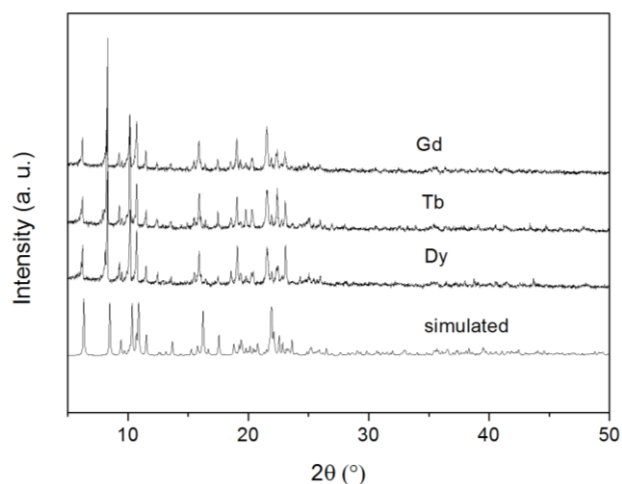


Figure A2.12 PXRD patterns of the microcrystalline powders of Dy(**9**), Tb(**10**) and Gd(**11**) and comparison with to the simulated pattern from structural data file of **9**.

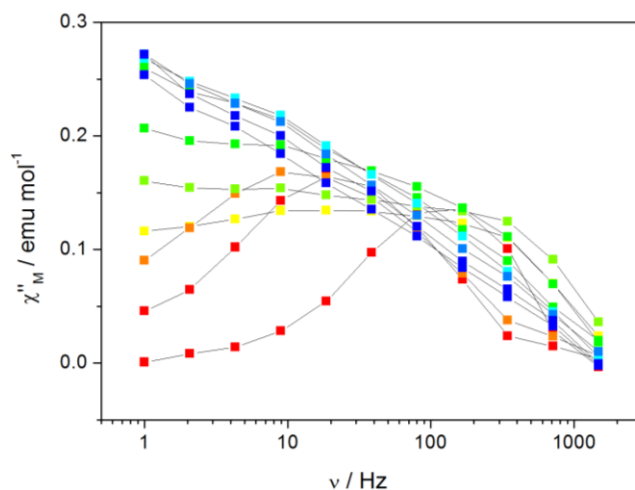


Figure A2.13 Out-of-phase components in dependence of scanning field of Dy(**9**). Color mapping from 0 Oe (red) to 4000 Oe (blue), 400 Oe step.

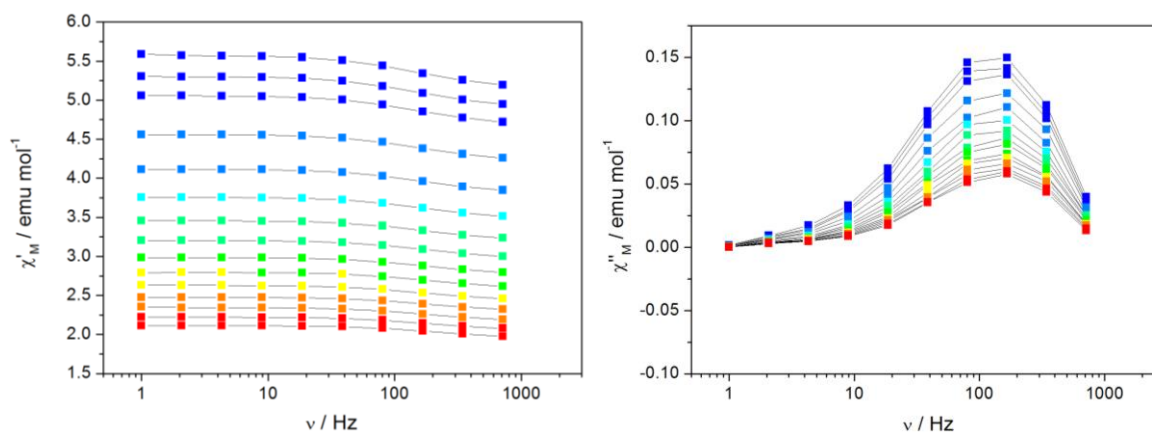


Figure A2.14 Frequency dependence of the in-phase (left) and out-of-phase (right) components of ac susceptibility under zero dc field for Dy(**9**). Color mapping from 1.8 K (blue) to 5 K (red).

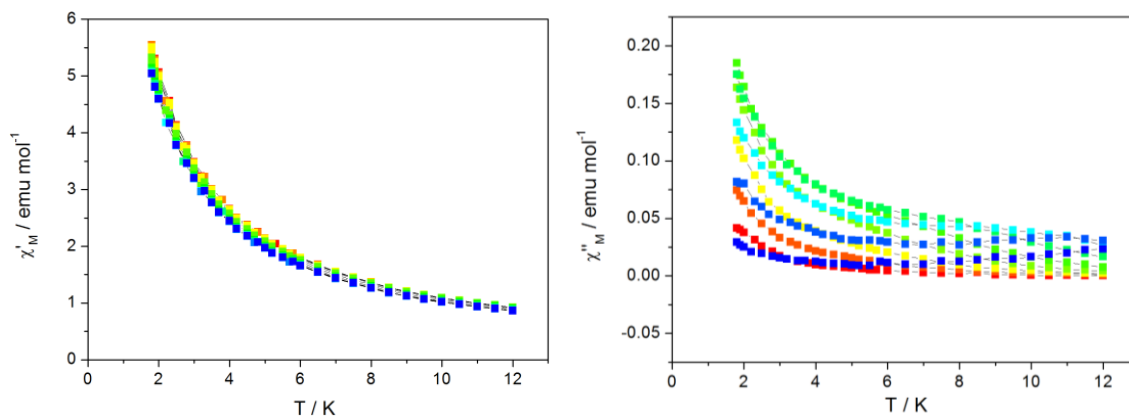


Figure A2.15 Temperature dependence of the in-phase (left) and out-of-phase (right) components of ac susceptibility under 400 Oe dc field for Dy(9). Color mapping from 1 Hz (red) to 1500 Hz (blue).

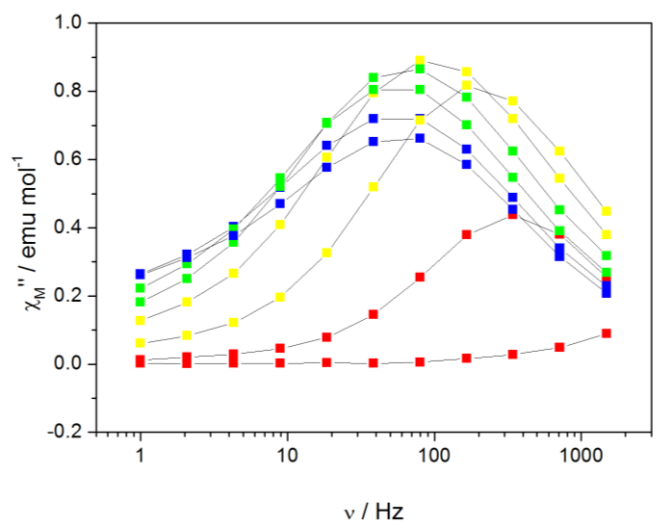


Figure A2.16 Frequency dependence of out-of-phase components for various dc fields for Tb(10). Color mapping ranges from 0 Oe (red) to 2800 Oe (blue), 400 Oe step.

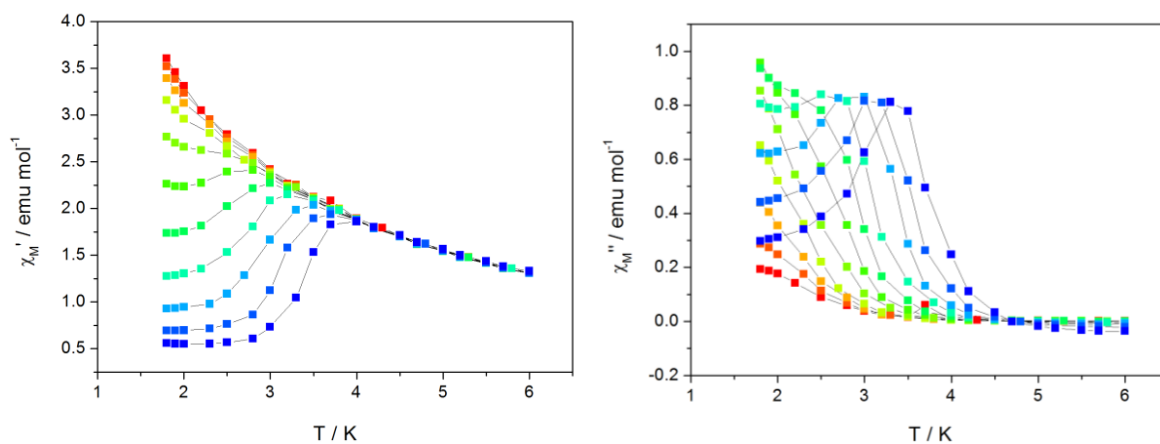


Figure A2.17 Temperature dependence of the in-phase (left) and out-of-phase (right) components of ac susceptibility under 1600 Oe dc field for Tb(10). Color mapping from 1 Hz (red) to 1500 Hz (blue).

Table A2.13 Relaxation times extracted from the fitting of χ'' vs frequency curves of Dy(9) in 400Oe.

T (K)	τ (μ s)	T (K)	τ (μ s)
1.8	7636.76	6.0	4948.93
1.9	7915.24	6.5	4568.13
2.0	7691.26	7.0	4181.27
2.5	7194.91	7.5	3619.46
3.0	6679.1	8.0	3353.79
3.5	6391.36	8.5	2815.15
4.0	6121.22	9.0	2421.93
4.5	5966.6	9.5	2247.61
5.0	5747.17	10.0	1884.86
5.5	5363.65	10.5	1648.27

Table A2.14 Values extracted from the Argand plot of Dy(9) in 400Oe.

T (K)	χ_s	χ_T	α	R
2.0	4.58913	5.08304	0.24522	0.96825
2.5	3.7761	4.14479	0.20621	0.99786
3.0	3.195	3.49036	0.18438	0.99687
3.5	2.76697	3.01577	0.16794	0.98982
4.0	2.4385	2.66097	0.19049	0.99221
4.5	2.17957	2.38294	0.20366	0.98895
5.0	1.9718	2.14455	0.14858	0.99096
5.5	1.80164	1.95561	0.12153	0.98652
6.0	1.65828	1.7995	0.11151	0.98443
6.5	1.53663	1.67259	0.14276	0.99022

Table A2.15 Relaxation times extracted from the fitting of χ'' vs frequency curves of Tb(10) in 1600Oe.

T (K)	τ (μ s)	T (K)	τ (μ s)
1.8	2986.35	2.5	977.42
1.9	2712.15	2.75	574.23
2.0	2333.19	3.0	307.78
2.25	1604.84	3.25	152.74

Table A2.16 Values extracted from the Argand plot of Tb(10) in 1600Oe.

T (K)	χ_s	χ_T	α	R ²
1.8	0.34871	3.73565	0.33496	0.9971
1.9	0.3273	3.58929	0.34323	0.99843
2.0	0.31254	3.4207	0.3433	0.99866
2.25	0.3026	3.0942	0.3141	0.98064
2.5	0.32219	2.81024	0.24981	0.98773
2.75	0.36512	2.55921	0.15747	0.97049
3.0	0.40217	2.38045	0.08335	0.99252
3.25	0.36878	2.23234	0.05782	0.99549

Appendix A3. Supplementary information for Chapter 3

Table A3.1 Selected bond distances and angles for **12**.

	Bond lengths (Å)		Angles (°)
Dy1-O1	2.357(7)	O1-Dy1-O8	80.1(3)
Dy1-O2	2.363(7)	O6-Dy1-O2	79.2(3)
Dy1-O3	2.366(7)	O3-Dy1-O2	124.5(3)
Dy1-O4	2.358(7)	O1-Dy1-O4	110.4(3)
Dy1-O5	2.358(7)	O6-Dy1-O5	82.9(2)
Dy1-O7	2.381(8)	O7-Dy1-O6	116.8(3)
Dy1-O8	2.319(6)	O1-Dy1-O7	70.7(3)
Dy1-O6	2.352(7)	O8-Dy1-O4	137.9(3)

Table A3.2 Selected bond distances and angles for **13**.

	Bond lengths (Å)		Angles (°)
Ce1-O1	2.472(3)	O1-Ce1-O2	69.31(10)
Ce1-O2	2.457(3)	O2-Ce1-O7	146.78(10)
Ce1-O3	2.430(3)	O6-Ce1-O5	68.88(10)
Ce1-O4	2.470(3)	O3-Ce1-O7	140.53(11)
Ce1-O5	2.448(3)	O1-Ce1-O5	135.38(10)
Ce1-O6	2.463(3)	O4-Ce1-O2	134.74(10)
Ce1-O7	2.447(3)	O2-Ce1-O6	75.78(11)
Ce1-O8	2.484(3)	O8-Ce1-O5	149.65(11)
Ce2-O9	2.417(3)	O16-Ce2-O12	74.74(11)
Ce2-O16	2.436(3)	O10-Ce2-O15	75.74(10)
Ce2-O12	2.436(3)	O15-Ce2-O9	78.37(11)
Ce2-O11	2.455(3)	O16-Ce2-O13	143.50(11)
Ce2-O14	2.461(3)	O9-Ce2-O13	74.11(11)
Ce2-O13	2.463(3)	O11-Ce2-O12	69.56(10)
Ce2-O15	2.487(3)	O14-Ce2-O10	149.76(10)
Ce2-O10	2.485(3)	O12-Ce2-O14	77.15(10)

Table A3.3 Selected bond distances and angles for **14**.

	Bond lengths (Å)		Angles (°)
Dy1-O1	2.314(8)	O3-Dy1-O4	72.4(3)
Dy1-O2	2.372(7)	O1-Dy1-O2	72.6(3)
Dy1-O3	2.334(7)	O6-Dy1-O5	72.0(3)
Dy1-O4	2.330(6)	O3-Dy1-O5	147.1(2)
Dy1-O5	2.321(7)	O2-Dy1-O5	71.1(3)
Dy1-O6	2.387(9)	O6-Dy1-O1	71.2(3)
Dy1-O7	2.324(7)	O8-Dy1-O5	140.7(2)
Dy1-O8	2.415(7)	O3-Dy1-O7	121.2(3)
		O3-Dy1-O2	76.1(3)
		O8-Dy1-O2	141.1(3)
		O4-Dy1-O6	148.9(3)
		O5-Dy1-O4	99.1(2)
		O5-Dy1-O7	84.8(2)

Table A3.4 Selected bond distances and angles for **15**.

	Bond lengths (Å)		Angles (°)
Ce1-O1	2.472(4)	O1-Ce1-O2	76.44(14)
Ce1-O2	2.419(4)	O8-Ce1-O1	67.93(13)
Ce1-O3	2.457(5)	O4-Ce1-O3	70.67(17)
Ce1-O4	2.446(4)	O3-Ce1-O5	140.84(16)
Ce1-O5	2.424(4)	O4-Ce1-O5	73.30(14)
Ce1-O6	2.481(4)	O4-Ce1-O6	68.22(13)
Ce1-O7	2.477(4)	O2-Ce1-O7	77.46(16)
Ce1-O8	2.469(4)	O7-Ce1-O5	79.68(13)
Ce2-O9	2.538(4)	O11-Ce2-O10	67.75(11)
Ce2-O10	2.501(4)	O14-Ce2-O10	133.43(11)
Ce2-O11	2.490(3)	O13-Ce2-O17	70.62(11)
Ce2-O12	2.467(3)	O15-Ce2-O13	130.87(11)
Ce2-O13	2.597(3)	O9-Ce2-O13	133.59(12)
Ce2-O14	2.484(4)	O16-Ce2-O14	74.68(11)
Ce2-O15	2.541(4)	O17-Ce2-O14	74.07(12)
Ce2-O16	2.471(3)	O12-Ce2-O15	71.90(12)
Ce2-O17	2.472(3)	O17-Ce2-O12	138.45(11)
Ce3-O18	2.478(4)	O25-Ce3-O18	88.03(12)
Ce3-O19	2.647(3)	O18-Ce3-O19	70.93(12)
Ce3-O20	2.448(4)	O22-Ce3-O19	70.97(11)
Ce3-O21	2.499(4)	O18-Ce3-O21	137.82(13)
Ce3-O22	2.481(4)	O20-Ce3-O21	68.48(13)
Ce3-O23	2.455(3)	O22-Ce3-O25	139.55(11)
Ce3-O24	2.521(4)	O24-Ce3-O20	146.84(12)
Ce3-O25	2.455(3)	O21-Ce3-O24	110.59(12)
Ce3-O26	2.600(3)	O23-Ce3-O26	99.51(12)

Table A3.5 Selected bond distances and angles for Ce(**16**).

	Bond lengths (Å)		Angles (°)
Ce1-O1	2.4605(16)	O3-Ce1-O4	69.88(5)
Ce1-O2	2.5160(17)	O2-Ce1-O7	67.28(6)
Ce1-O3	2.4948(16)	O6-Ce1-O5	68.60(5)
Ce1-O4	2.5049(17)	O3-Ce1-O7	72.49(6)
Ce1-O5	2.5109(18)	O1-Ce1-O5	73.40(6)
Ce1-O6	2.4862(17)	O4-Ce1-O2	66.83(5)
Ce1-O7	2.6066(18)	O2-Ce1-O6	134.86(5)
Ce1-O8	2.4764(16)	O4-Ce1-O5	121.32(6)
Ce1-O9	2.5503(17)	O8-Ce1-O2	135.16(6)
		O6-Ce1-O9	80.20(6)
		O8-Ce1-O9	140.82(6)
		O6-Ce1-O7	67.58(6)
		O9-Ce1-O3	135.13(5)
		O8-Ce1-O5	71.91(6)

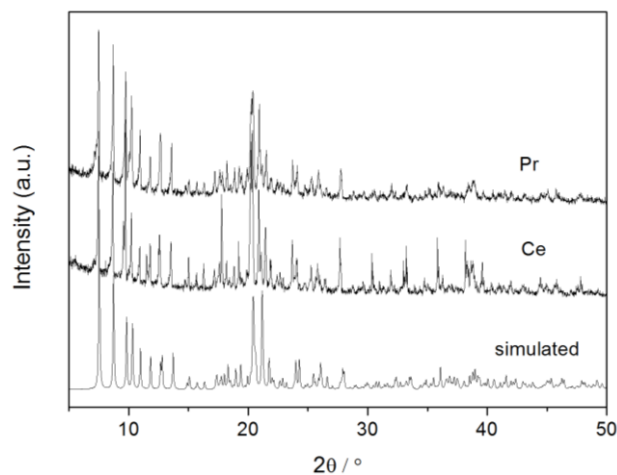


Figure A3.1 PXRD patterns of the microcrystalline powders of Ce(**16**) and Pr(**17**) and comparison with the simulated pattern of **16**.

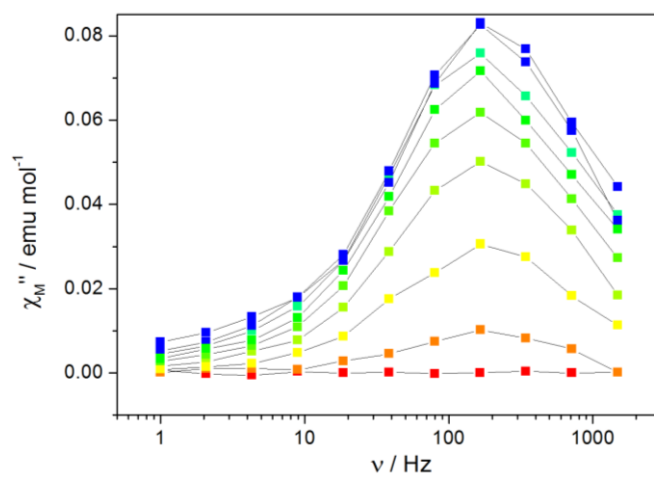


Figure A3.2 Frequency dependence of the out-of-phase components of the magnetization for various dc fields for Pr(**17**). Color mapping from 0 Oe (red) to 2400 Oe (blue). Lines are guides to the eye.

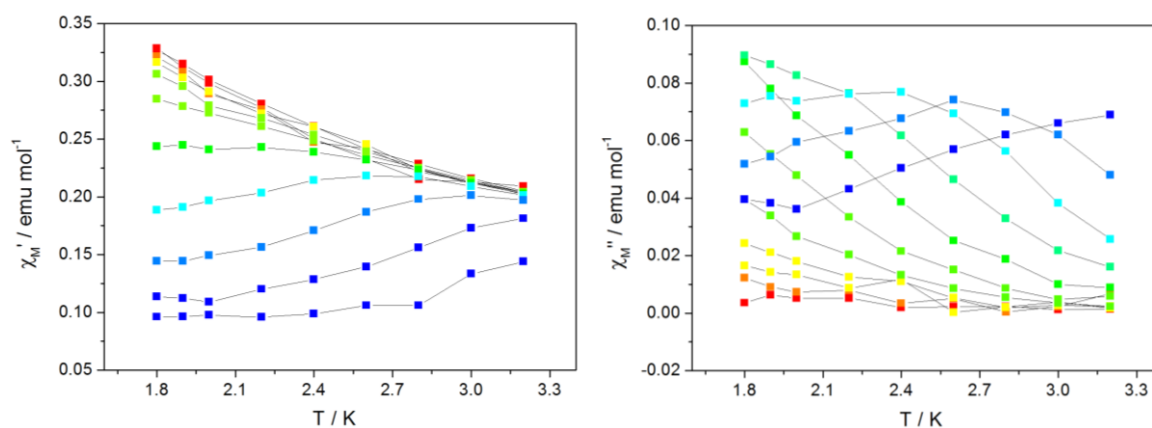


Figure A3.3 Temperature dependence of the in-phase (left) and out-of-phase (right) components of ac susceptibility for under 3600 Oe dc field for complex **17**. Color mapping from 1 Hz (red) to 1500 Hz (blue). Lines are guides to the eye.

Table A3.6 Values extracted from the fitting of χ_M'' vs frequency curves for Pr(17).

T(K)	τ (μ s)	T(K)	τ (μ s)
1.8	1124.58	2.4	388.89
1.9	958.61	2.6	271.25
2.0	837.90	2.8	198.02
2.2	577.25		

Table A3.7 Values extracted from the Argand plot under 3600 Oe dc field for Pr(17).

T (K)	χ_s	χ_T	α	R ²
1.8	0.07529	0.33047	0.22663	0.97836
1.9	0.0739	0.31577	0.22016	0.98937
2	0.07597	0.30124	0.20674	0.98287
2.2	0.07782	0.27361	0.11876	0.96614

Table A3.8 Selected bond distances and angles for Dy(18).

	Bond lengths (\AA)		Angles ($^\circ$)
Dy1-O1	2.349(2)	O3-Dy1-O2	73.34(9)
Dy1-O2	2.377(3)	O1-Dy1-O4	144.76(7)
Dy1-O3	2.346(2)	O6-Dy1-O2	149.18(9)
Dy1-O4	2.328(2)	O3-Dy1-O5	136.89(9)
Dy1-O5	2.396(3)	O2-Dy1-O5	63.55(9)
Dy1-O6	2.303(2)	O4-Dy1-O2	71.85(6)
Dy1-O1a	2.349(2)	O5-Dy1-O6	147.26(9)
Dy1-O4a	2.328(2)	O2-Dy1-O4a	71.85(6)
		Dy1-N1-O6	138.3(2)
		O1a-Dy1-O2	124.43(6)

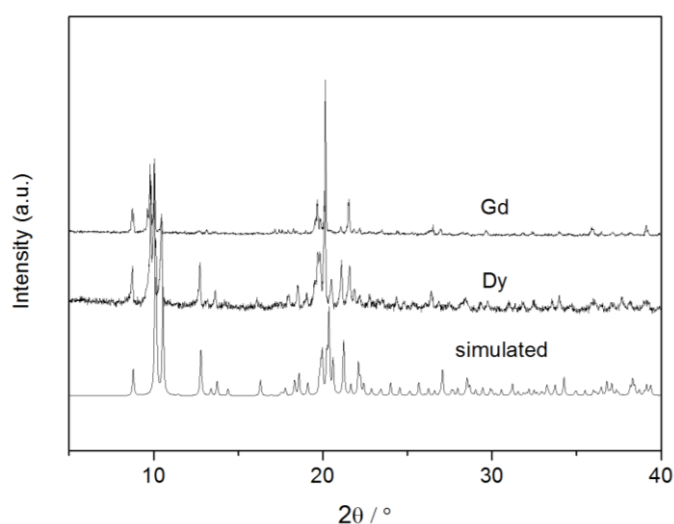


Figure A3.4 PXRD patterns of the microcrystalline powders of Dy(18) and Gd(19) and comparison with the simulated pattern of 18.

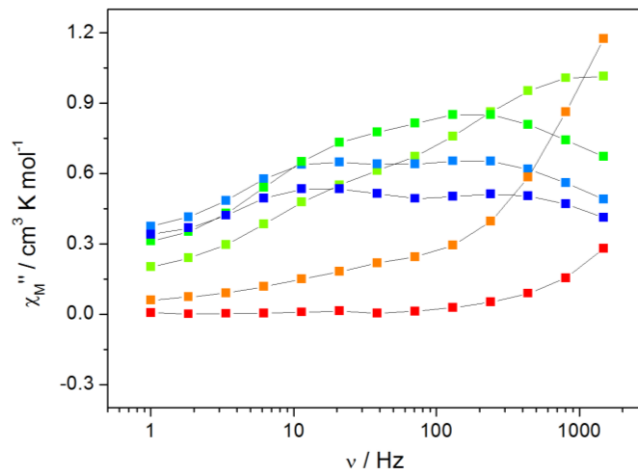


Figure A3.5 Frequency dependence of the out-of-phase components of the magnetization for various dc fields for Dy(18). Color mapping from 0 Oe (red) to 3000 Oe (blue), 600 Oe step. Lines are guides to the eye.

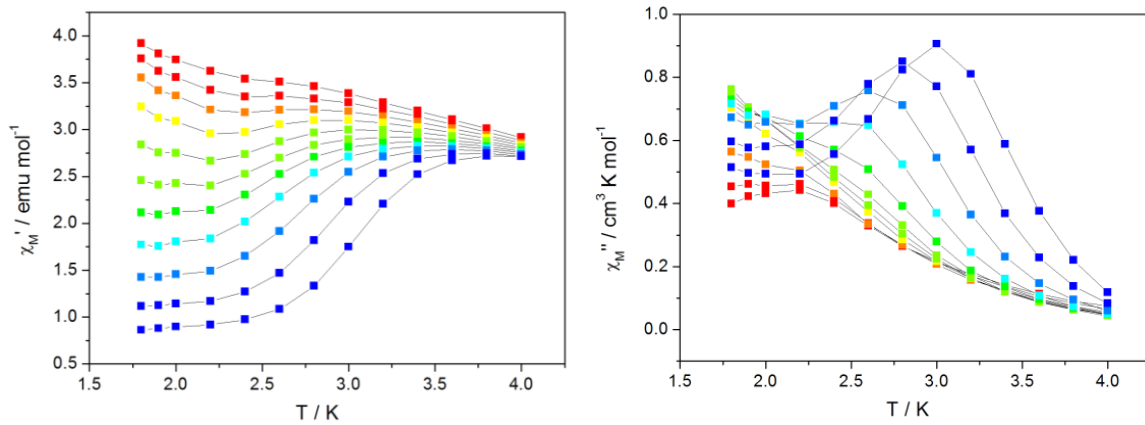
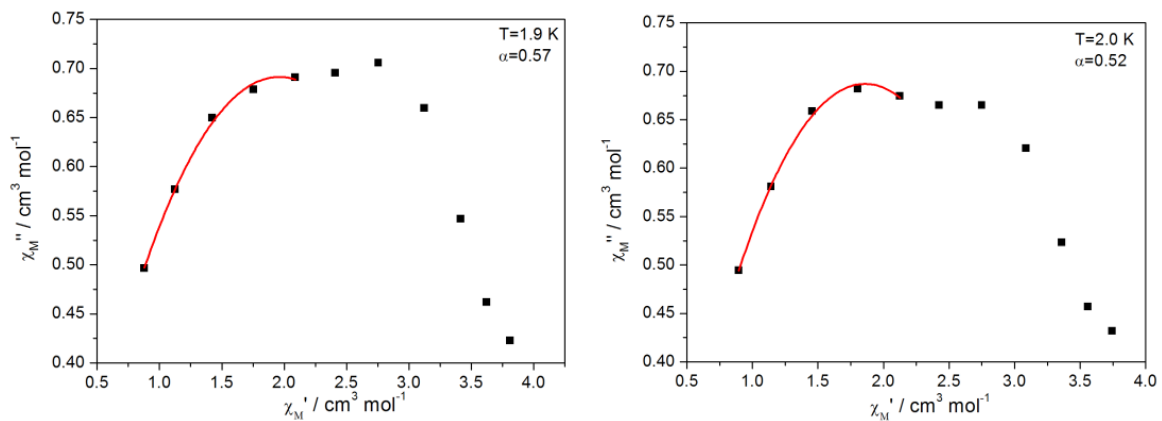


Figure A3.6 Temperature dependence of the in-phase (left) and out-of-phase (right) components of ac susceptibility for under 2400 Oe dc field for Dy(18). Color mapping from 1 Hz (red) to 1500 Hz (blue). Lines are guides to the eye.



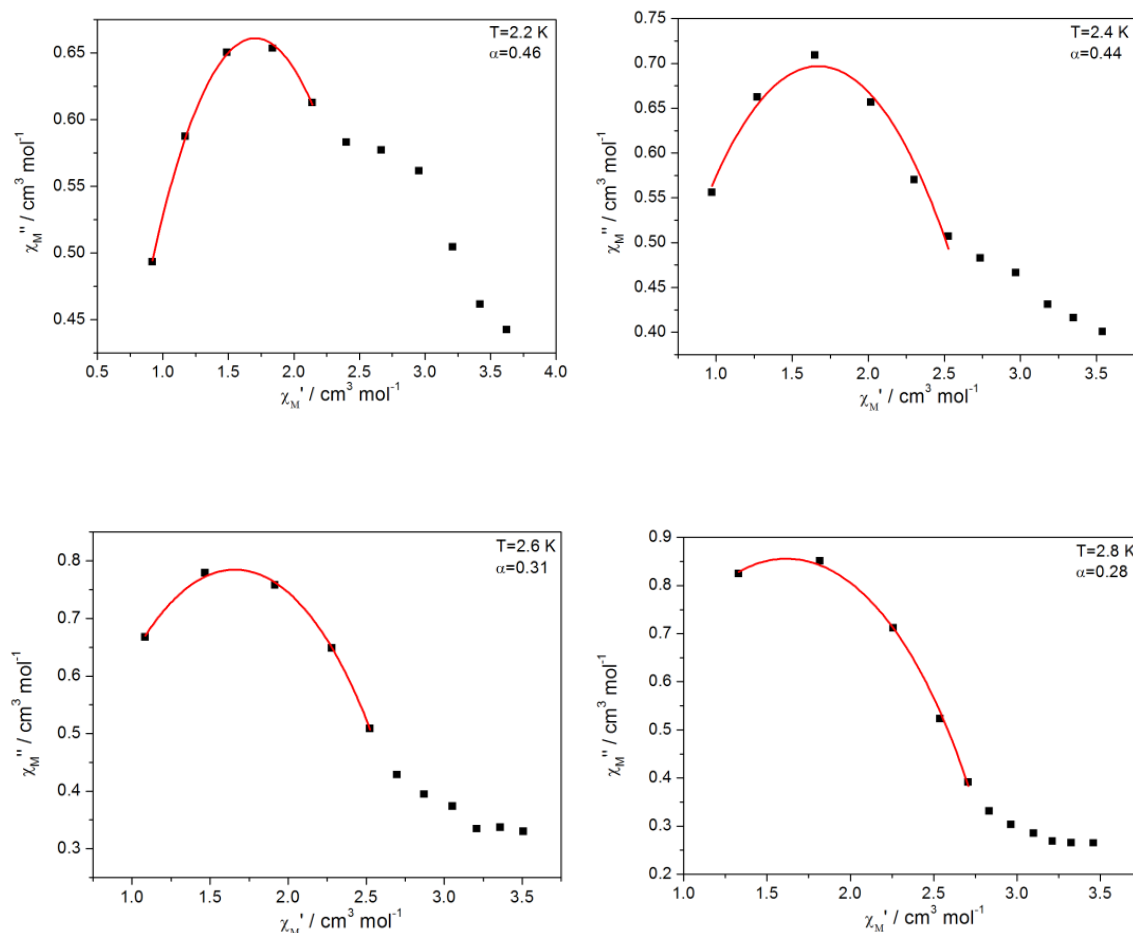


Figure A3.7 Double peaked Cole-Cole plot measured Dy(**18**) under a 2400 Oe dc field, solid lines correspond to the best fits.

Table A3.9 Values extracted from the fitting of χ_M'' vs frequency curves of complex Dy(**18**) in 2400Oe.

T (K)	τ (μ s)	T (K)	τ (μ s)
1.8	1785.9	2.4	471.9
1.9	1528.8	2.6	304.8
2.0	1126.0	2.8	158.6
2.2	741.4		

Table A3.10 Values extracted from the Argand plot of complex Dy(**18**) in 2400Oe.

T (K)	χ_s	χ_T	α	R^2
1.9	0.00978	3.90934	0.56607	0.99505
2.0	0.13847	3.57909	0.51622	0.99619
2.2	0.25032	3.15758	0.45651	0.99804
2.4	0.20223	3.14041	0.436	0.9509
2.6	0.34453	2.97234	0.31404	0.99701
2.8	0.26368	2.96813	0.28153	0.9957

Table A3.11 Selected bond distances and angles for **20**.

	Bond lengths (Å)		Angles (°)
Ce1-O1	2.445(6)	O1-Ce1-O8	68.89(19)
Ce1-O2	2.405(7)	O6-Ce1-O7	68.9(2)
Ce1-O3	2.384(6)	O4-Ce1-O5	68.6(2)
Ce1-O4	2.460(6)	O3-Ce1-O7	142.4(2)
Ce1-O5	2.476(6)	O1-Ce1-O5	114.7(2)
Ce1-O6	2.476(6)	O4-Ce1-O2	142.1(2)
Ce1-O7	2.455(6)	O2-Ce1-O6	72.1(2)
Ce1-O8	2.527(6)	O8-Ce1-O5	135.42(19)
		O7-Ce1-O4	108.6(2)
		O4-Ce1-O8	70.57(19)
		O3-Ce1-O1	145.5(2)
		O6-Ce1-O3	79.9(2)
		N2-O3-Ce1	168.1(5)
		N1-O2-Ce1	175.5(5)

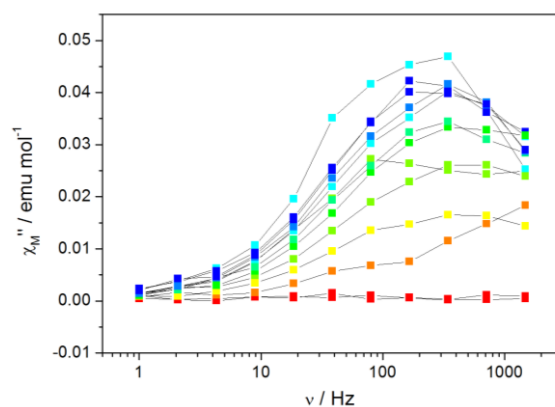
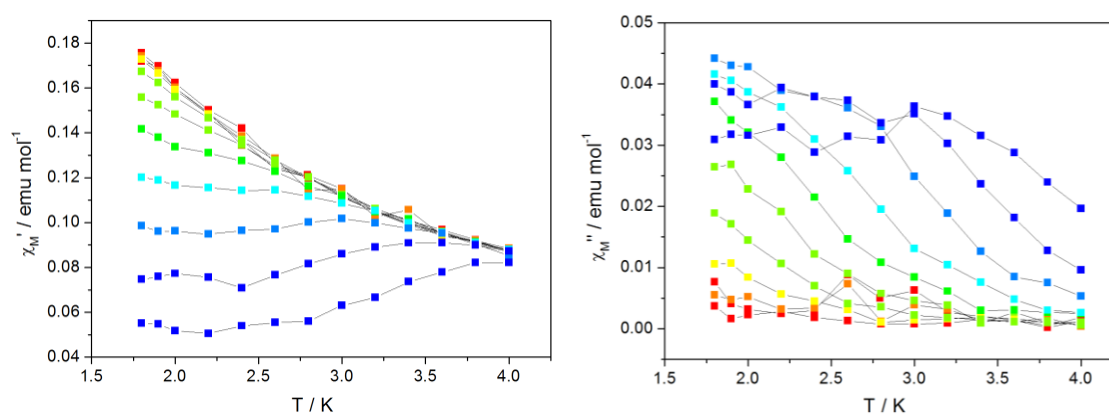
Figure A3.8 Frequency dependence of the out-of-phase components of the magnetization for various dc fields for **20**. Color mapping range from 0 Oe (red) to 3600 Oe (blue), 400 Oe step. Lines are guides to the eye.Figure A3.9 Temperature dependence of the in-phase (left) and out-of-phase (right) components of ac susceptibility for under 2800 Oe dc field for complex **20**. Color mapping from 1 Hz (red) to 1500 Hz (blue). Lines are guides to the eye.

Table A3.12 Values extracted from the fitting of χ_M'' vs frequency curves of complex **20** in 2800 Oe.

T (K)	τ (μ s)	T (K)	τ (μ s)
1.8	555.67	2.4	341.56
1.9	521.21	2.6	257.28
2.0	481.05	2.8	228.25
2.2	367.79		

Table A3.13 Values extracted from the Argand plot of complex **20** in 2800Oe.

T (K)	χ_s	χ_T	α	R
1.8	0.02648	0.17845	0.32356	0.96402
1.9	0.02824	0.17163	0.29861	0.98353
2.0	0.02524	0.16356	0.29985	0.97892
2.2	0.02355	0.15107	0.25911	0.98246

Table A3.14 Selected bond distances and angles for **21**.

	Bond lengths (\AA)		Angles ($^\circ$)
Dy1-O2	2.337(2)	O3-Dy1-O1	124.90(9)
Dy1-O4	2.342(2)	O7-Dy2-O5	134.47(8)
Dy1-O3	2.345(2)	O6-Dy2-O10	136.96(9)
Dy1-O1	2.347(2)	O11-Dy2-O6	107.75(10)
Dy1-O2a	2.337(2)	O1-Dy1-O1a	75.92(14)
Dy1-O4a	2.342(2)	O4a-Dy1-O1	146.2(1)
Dy1-O3a	2.345(2)	O2a-Dy1-O3a	146.33(8)
Dy1-O1a	2.347(2)	O4a-DY1-O3a	75.82(9)
Dy2-O11	2.304(2)	O8-Dy2-O7	75.00(9)
Dy2-O10	2.306(2)	O11-Dy2-O9	71.50(9)
Dy2-O6	2.339(2)	O9-Dy2-O12	133.47(8)
Dy2-O8	2.339(2)	O5-Dy2-O9	114.77(9)
Dy2-O7	2.360(2)	O10-Dy2-O7	73.70(9)
Dy2-O12	2.377(2)	O8-Dy2-O12	75.53(9)
Dy2-O5	2.394(2)	O4-Dy1-O3	75.82(9)
Dy2-O9	2.413(2)	O11-Dy2-O10	86.32(10)
		N1-O4-Dy1	154.7(2)

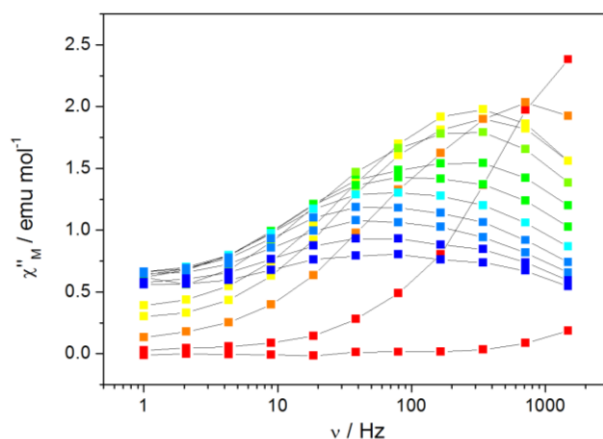


Figure A3.10 Frequency dependence of the out-of-phase components of the magnetization for various dc fields for **21**. Color mapping from 0 Oe (red) to 4800 Oe (blue), 400 Oe step. Lines are guides to the eye.

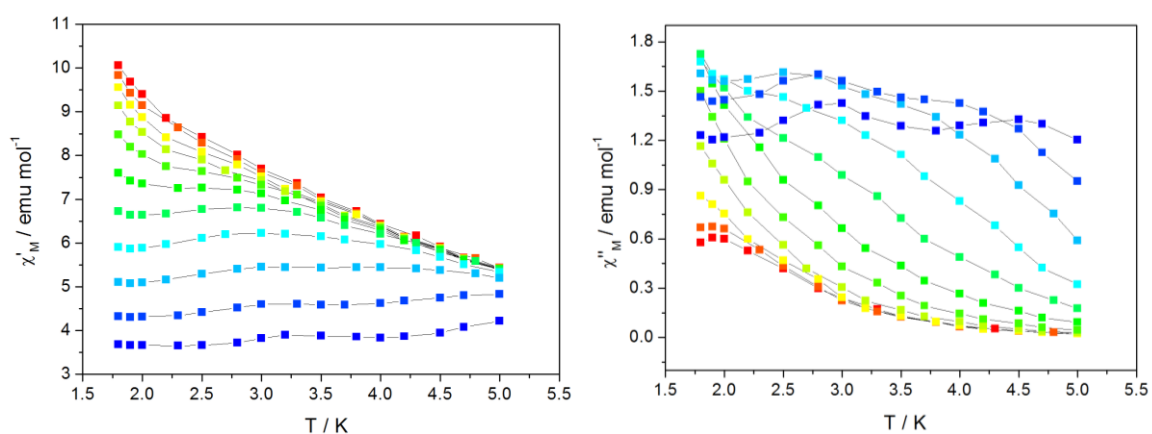


Figure A3.11 Temperature dependence of the in-phase (left) and out-of-phase (right) components of ac susceptibility for under 2400 Oe dc field for complex **21**. Color mapping from 1 Hz (red) to 1500 Hz (blue). Lines are guides to the eye.

Table A3.15 Values extracted from the fitting of χ''_M vs frequency curves of **21** under 2400 Oe dc field.

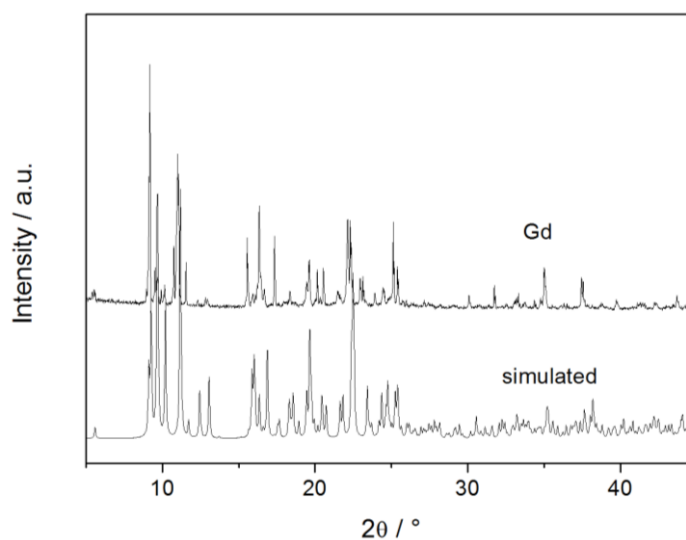
T (K)	τ (μs)	T (K)	τ (μs)
1.8	1672.61	3.25	270.34
1.9	1269.84	3.5	262.23
2	875.38	3.75	242.63
2.25	544.39	4	206.75
2.5	383.36	4.25	175.21
2.75	307.26	4.5	141.99
3	278.09		

Table A3.16 Values extracted from the Argand plot of **21** under 2400 Oe dc field.

T (K)	χ_s	χ_T	α	R^2
1.8	1.94319	10.74131	0.51179	0.9776
1.9	1.67131	10.41287	0.54124	0.98668
2	1.4045	10.12312	0.55793	0.98683
2.25	1.01796	9.39797	0.56181	0.96987
2.5	1.01086	8.74733	0.51877	0.96286
2.75	1.32187	8.1649	0.44802	0.97983
3	1.72343	7.76307	0.39074	0.97979
3.25	2.23199	7.38398	0.32443	0.98082
3.5	2.49995	7.03281	0.2665	0.98404
3.75	2.84457	6.65394	0.16425	0.97569
4	2.53945	6.42348	0.19555	0.98616
4.25	2.42863	6.15	0.18383	0.98468
4.5	2.34907	5.89827	0.16669	0.98759

Table A3.17 Selected bond distances and angles for Tb(**22**).

	Bond lengths (Å)		Angles (°)
Tb1-O1	2.346(2)	O1-Tb1-O2	72.64(9)
Tb1-O2	2.347(2)	O6-Tb1-O7	73.35(8)
Tb1-O3	2.330(3)	O4-Tb1-O3	71.9(1)
Tb1-O4	2.386(3)	O3-Tb1-O7	144.85(9)
Tb1-O5	2.291(2)	O1-Tb1-O5	83.93(9)
Tb1-O6	2.376(2)	O5-Tb1-O2	145.05(10)
Tb1-O7	2.336(2)	O2-Tb1-O6	140.03(9)
Tb1-N1	2.540(3)	O7-Tb1-O5	89.81(9)
		O7-Tb1-N1	74.62(10)
		O4-Tb1-O6	128.24(9)
		O3-Tb1-N1	75.45(11)
		N2-O5-Tb1	176.6(2)

Figure A3.12 PXR D patterns of the microcrystalline powders of Gd(**23**) and comparison with the simulated pattern from structural data file of Tb(**22**).

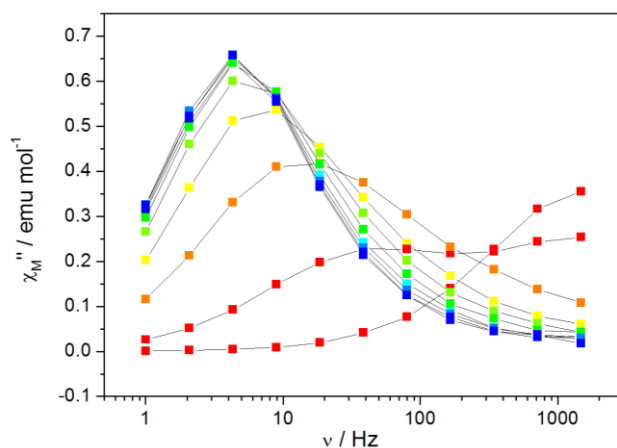


Figure A3.13 Frequency dependence of the out-of-phase components of the magnetization for various dc fields for Tb(22). Color mapping from 0 Oe (red) to 3600 Oe (blue), 400 Oe step. Lines are guides to the eye.

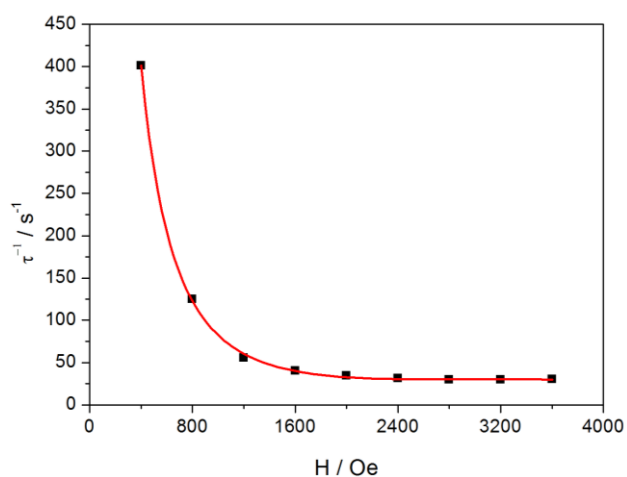


Figure A3.14 Field dependence of τ^{-1} for Tb(22). The best fit gives negative value of A1.

Table A3.18 Values extracted from the fitting of χ_M'' vs frequency curves of Tb(22) in 2000 Oe.

T (K)	τ (μ s)	T (K)	τ (μ s)
3.2	100512.2	6.6	2334.4
3.4	69606.7	6.8	1958.8
3.6	50727.9	7	1666.7
3.8	37960.8	7.2	1402
4	29618.1	7.4	1197
4.2	22846.7	7.6	966.7
4.4	18195.8	7.8	842.6
4.6	14728.1	8	706.6
4.8	11787.1	8.2	589
5	9676.4	8.4	490.8
5.2	7962.6	8.6	414.2
5.4	6585.4	8.8	345.7
5.6	5483.1	9	292.5
5.8	4583.5	9.2	248.2
6	3851.4	9.4	210.8
6.2	3254.7	9.6	177.8
6.4	2741.2	9.8	150.8

Table A3.19 Values extracted from the Argand plot of Tb(22) in 2000 Oe.

T (K)	χ_s	χ_T	α	R^2
2	0.36148	3.61205	0.44133	0.99841
3	0.30059	2.94347	0.39575	0.999
4	0.26492	1.97194	0.20997	0.98741
5	0.22804	1.54456	0.10952	0.98476
6	0.1968	1.29024	0.05868	0.99128
7	0.17513	1.11593	0.0396	0.99582
8	0.16315	0.98424	0.01743	0.99503
9	0.15747	0.87827	0.00532	0.98851

Appendix A4. Supplementary information for Chapter 4

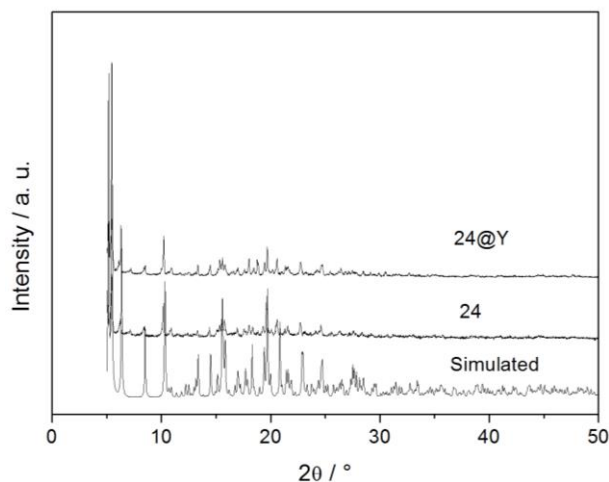


Fig A4.1 PXRD patterns of the microcrystalline powders of Dy(**24**) and **24@Y** with comparison to the structural data file of the Dy^{III} derivative (**24**).

Table A 4.1 Selected bond lengths and angle for **24**.

Bond	Distance(Å)	Atoms	Angle(°)
Dy1-O1	2.3413(18)	O2-Dy1-O6	53.79(6)
Dy1-O2	2.4782(18)	O5-Dy1-O7	53.30(5)
Dy1-O3	2.3580(19)	O1-Dy1-O4	77.49(7)
Dy1-O4	2.2800(19)	O3-Dy1-O2	149.80(6)
Dy1-O5	2.4090(18)	O8-Dy1-O3	77.58(7)
Dy1-O6	2.381(2)	O1-Dy1-O7	145.43(6)
Dy1-O7	2.4842(19)	O2-Dy1-O7	123.55(6)
Dy1-O8	2.2731(18)	O8-Dy1-O6	73.39(6)

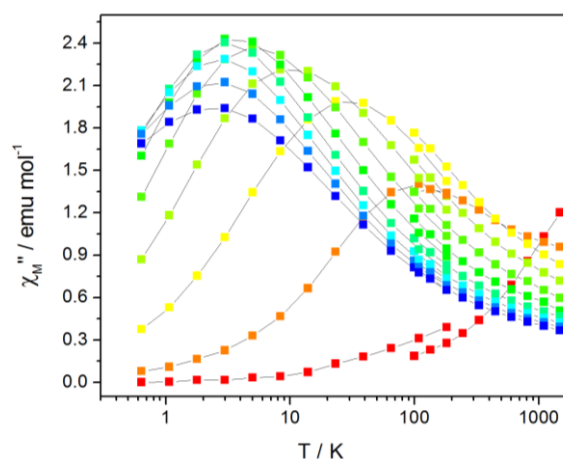


Figure A4.2 Frequency dependence of the out-of-phase components of the magnetization for various dc fields for **24**. Color mapping ranges from 0 Oe (red) to 1800 Oe (blue), 200Oe step at 2 K. Lines are guides to eye.

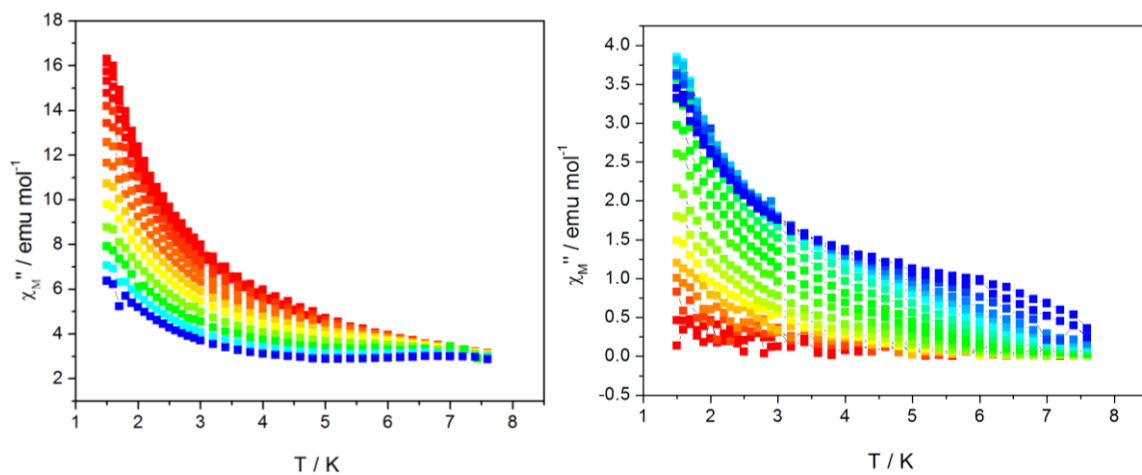


Figure A4.3 Temperature dependence of the in-phase (left) and out-of-phase components (right) of ac susceptibility under zero dc field for **24**. Color mapping from 1.6 Hz (red) to 70000 Hz (blue). Lines are guides to eye.

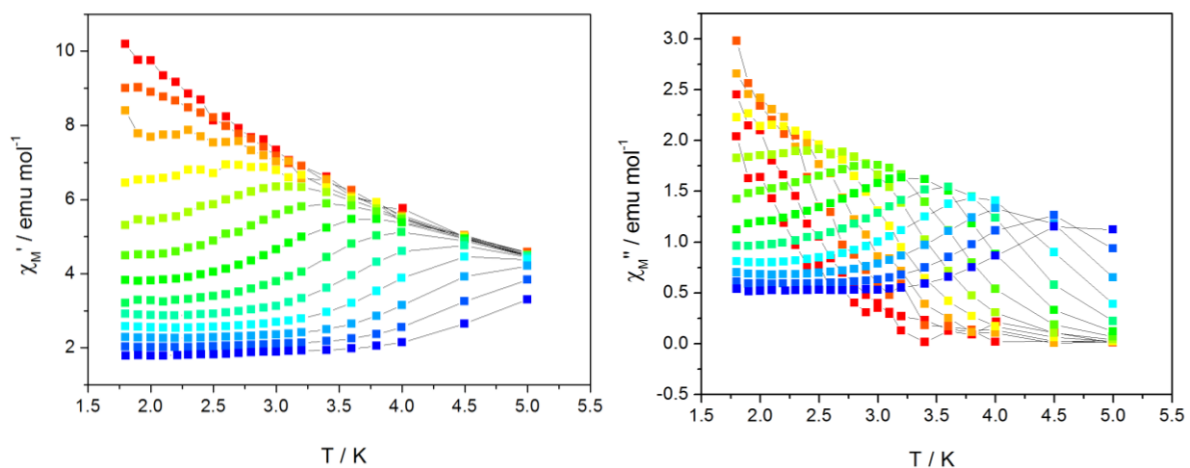


Figure A4.4 Temperature dependence of the in-phase (left) and out-of-phase components (right) of ac susceptibility under 1200 Oe dc field for **24**. Color mapping from 1 Hz (red) to 1500 Hz (blue). Lines are guides to eye.

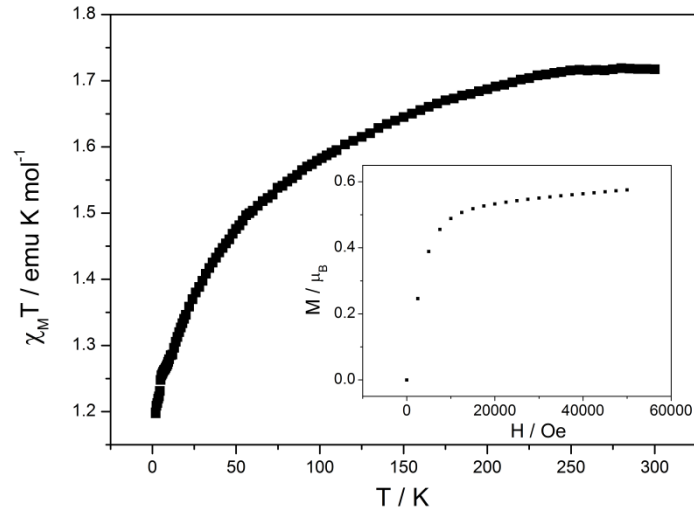


Figure A4.5 Temperature dependence of the $\chi_M T$ for **24@Y**. In inset, field dependence of the magnetization.

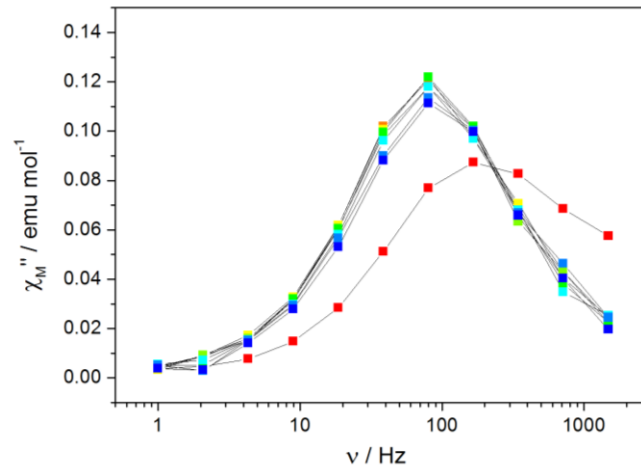


Figure A4.6 Frequency dependence of the out-of-phase components of the magnetization for various dc fields for **24@Y** at 4 K. Color mapping ranges from 0 Oe (red) to 2400 Oe (blue). Lines are guides to eye.

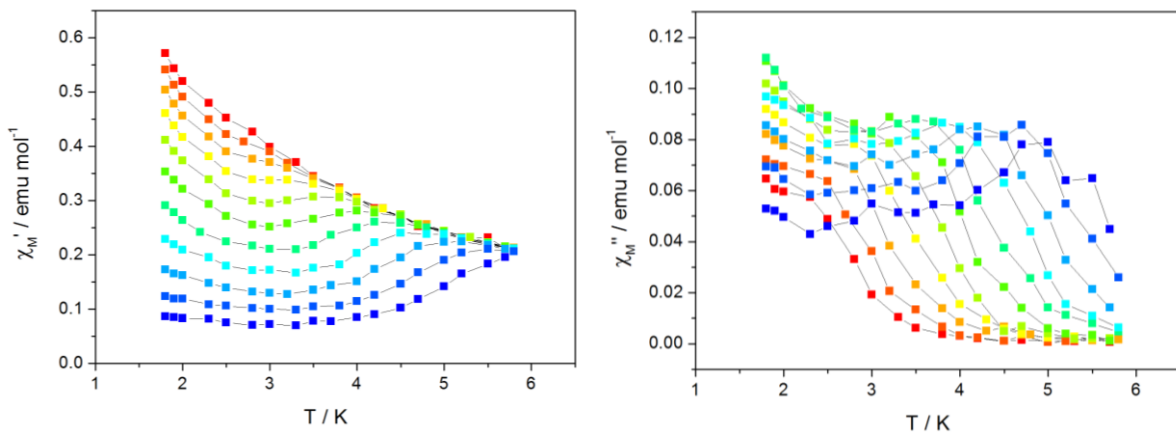


Figure A4.7 Temperature dependence of the in-phase (left) and out-of-phase components (right) of ac susceptibility under zero dc field for **24@Y**. Color mapping from 1 Hz (red) to 1500 Hz (blue). Lines are guides to eye.

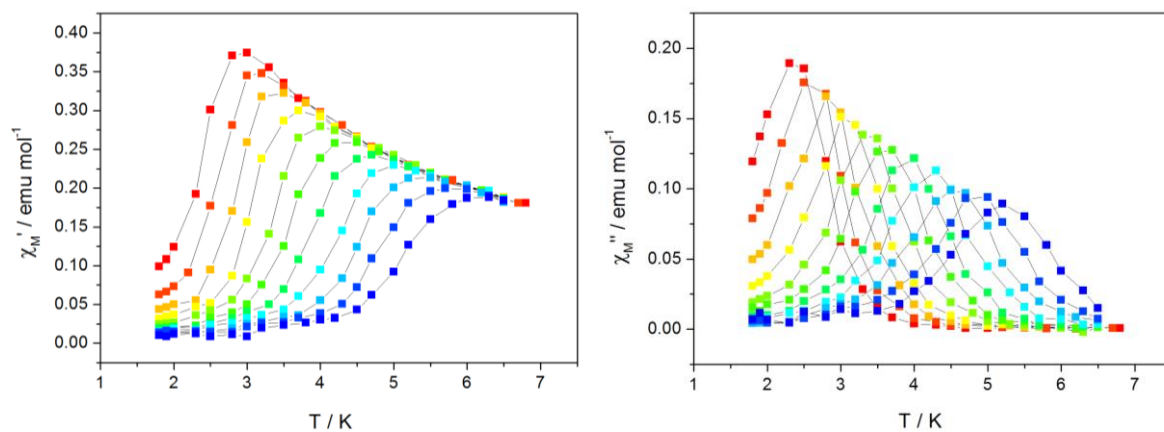


Figure A4.8 Temperature dependence of the in-phase (left) and out-of-phase components (right) of ac susceptibility under 1200 Oe dc field for **24@Y**. Color mapping from 1 Hz (red) to 1500 Hz (blue). Lines are guides to eye.

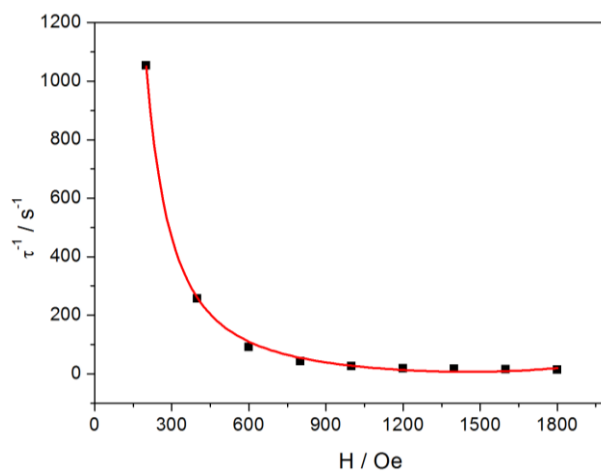


Figure A4.9 Plot of τ^{-1} in dependence of T^{-1} under 1200 Oe for **24**. The solid line is the fit which gives negative value of A_2 .

Table A4.2 Values extracted from the fitting of out-of-phase vs frequency curves of **24** under zero dc field.

T(K)	τ (μ s)	T(K)	τ (μ s)
1.56	12.08	3.6	7.412
1.6	11.705	3.8	7.268
1.7	11.649	4	7.1436
1.8	10.99	4.2	6.63
1.9	10.62	4.4	7.217
2	10.67	4.6	6.08
2.1	10.05	4.8	5.793
2.2	9.94	5	5.732
2.3	9.87	5.2	2.138
2.4	9.52	5.4	5.22
2.5	9.7	5.6	2.0715
2.6	10.265	5.8	5.227
2.7	9.148	6	1.173
2.8	9.233	6.2	4.707
2.9	8.7	6.4	5.074
3	8.49	6.6	1.342
3.2	8.496	6.8	4.852
3.4	7.983	7	1.514

Table A4.3 Values extracted from the Argand plot of **24** under zero dc field.

T (K)	χ_s	χ_T	α	R^2
1.5	2.97887	17.1248	0.35023	0.98496
1.6	2.76175	16.92522	0.36368	0.99045
1.7	1.98566	15.80747	0.3841	0.98711
1.8	2.46957	14.75472	0.36527	0.99275
1.9	2.71247	13.61281	0.32931	0.98594
2.0	2.46109	12.84982	0.33114	0.98665
2.1	2.13122	12.36549	0.36532	0.99242
2.2	2.43879	11.51997	0.3225	0.98119
2.3	3.42929	10.92201	0.26632	0.99683
2.4	2.13977	10.54856	0.33853	0.98952
2.5	2.14465	10.0131	0.32491	0.97908
2.6	1.89476	9.69353	0.35001	0.99271
2.7	1.93798	9.2637	0.33633	0.99245
2.8	1.78645	8.93077	0.34482	0.99044
2.9	1.84095	8.56643	0.32611	0.99287
3.0	1.74682	8.28565	0.33595	0.98729
3.2	2.53213	7.64486	0.28939	0.99952
3.4	1.64625	7.22024	0.31998	0.98957
3.6	1.61581	6.78323	0.31043	0.99004
3.8	1.52133	6.4259	0.31333	0.9888
4.0	1.43809	6.1105	0.331554	0.98681
4.2	1.43421	5.82133	0.31236	0.98936
4.4	1.43286	5.53894	0.30004	0.99128
4.6	1.52287	5.28741	0.27961	0.98913
4.8	1.53401	5.04815	0.25926	0.98551
5.0	1.76116	4.71337	0.19133	0.98515
5.2	1.63099	4.58884	0.28264	0.98738
5.4	1.63191	4.39093	0.19114	0.98804
5.6	1.467	4.10212	0.18484	0.9922
5.8	1.34801	3.98032	0.19953	0.9867

Table A4.4 Values extracted from the fitting of out-of-phase vs frequency curves of **24** under 1200 Oe dc field.

T(K)	τ (μ s)	T(K)	τ (μ s)
1.8	82900	2.9	8411
1.9	66270	3	6375
2	54698	3.1	5299
2.1	44993	3.2	4486
2.2	39117	3.4	2620
2.3	30000	3.6	1737
2.4	24115	3.8	1140
2.5	17903	4	691
2.6	15830	4.5	215
2.7	12475	5	95.7
2.8	10127		

Table A4.5 Values extracted from the Argand plot of **24** under 1200 Oe dc field.

T (K)	χ_s	χ_T	α	R^2
2.0	1.42171	12.57671	0.5122	0.96459
2.5	1.53526	9.19159	0.42241	0.92064
3.0	1.60097	7.53005	0.33573	0.95907
4.0	1.63916	5.56922	0.19686	0.93946
4.5	1.49957	5.01535	0.20111	0.98069

Table A4.6 The EDS results of **24@Y**.

Element	Atomic percentage (%)				Avarage atomic percentage (%)
	Y	90.6	96.1	97.2	94.6
Dy	9.4	3.9	2.8	5.4	5.5

Table A4.7 Values extracted from the fitting of out-of-phase vs frequency curves of **24@Y** under zero dc field.

T(K)	τ (μ s)	T(K)	τ (μ s)
1.8	4191.421	3.5	1674.72
1.9	4076.277	3.8	1089.669
2	4027.789	4	709.177
2.3	3730.481	4.2	423.671
2.8	3301.701	4.5	299.427
3.2	2808.886	4.7	184.701

Table A4.8 Values extracted from the Argand plot of **24@Y** under zero dc field.

T (K)	χ_s	χ_T	α	R^2
2.3	0.00235	0.5744	0.59994	0.95736
2.8	0.00136	0.48337	0.55637	0.9578
3.2	0.02532	0.38969	0.4105	0.90375
3.5	0.04341	0.35462	0.32584	0.93394
3.8	0.04618	0.32865	0.2641	0.94235
4.0	0.05593	0.30694	0.19347	0.97783
4.2	0.05808	0.28657	0.14215	0.98118

Table A4.9 Values extracted from the fitting of out-of-phase vs frequency curves of **24@Y** under 1200 Oe dc field.

T(K)	τ (μ s)	T(K)	τ (μ s)
2.8	54438.363	4	1895.207
3	25684.195	4.2	1023.252
3.2	12615.411	4.5	578.088
3.5	6529.945	4.8	323.155
3.8	3427.98	5	197.047

Table A4.10 Values extracted from the Argand plot of **24@Y** under 1200 Oe dc field.

T (K)	χ_s	χ_T	α	R^2
3.5	0.02208	0.33981	0.10651	0.9798
4.0	0.02599	0.29893	0.07206	0.99007
4.2	0.02483	0.28148	0.07726	0.99159
4.5	0.02579	0.2666	0.07955	0.98812
4.7	0.02941	0.25228	0.07187	0.99157

Table A4.11 EDS results of **24@Y_{0.69}**.

Element	Atomic percentage (%)					Avarage atomic percentage (%)
	73.3	75	65.5	67.8	64.6	
Y						69
Dy	26.7	25	34.5	32.2	35.4	31

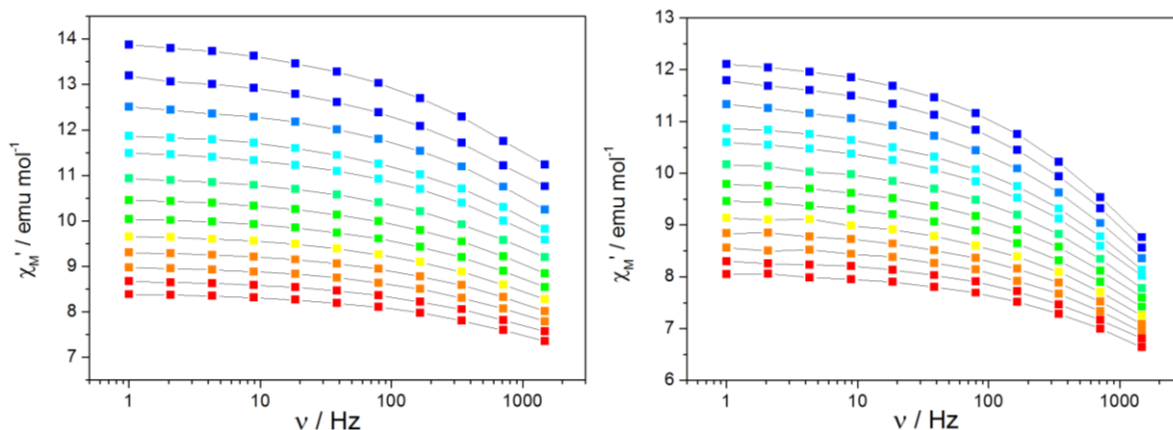


Figure A4.10 Frequency dependence of the in-phase components of ac susceptibility for non-switched 1,4-dioxane solution of **24** under zero Oe dc field (left) and 800 Oe dc field (right). Color mapping from 1.8 (blue) to 3 K (red). Lines are guides to eye.

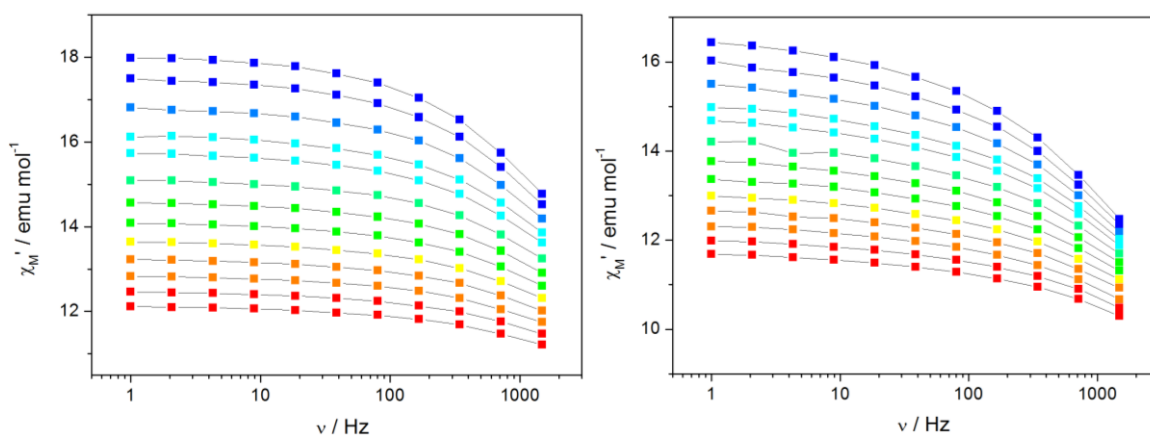


Figure A4.11 Frequency dependence of the in-phase components of ac susceptibility for switched 1,4-dioxane solution of **24** under zero Oe dc field (left) and 800 Oe dc field (right). Color mapping from 1.8 (blue) to 3 K (red). Lines are guides to eye.

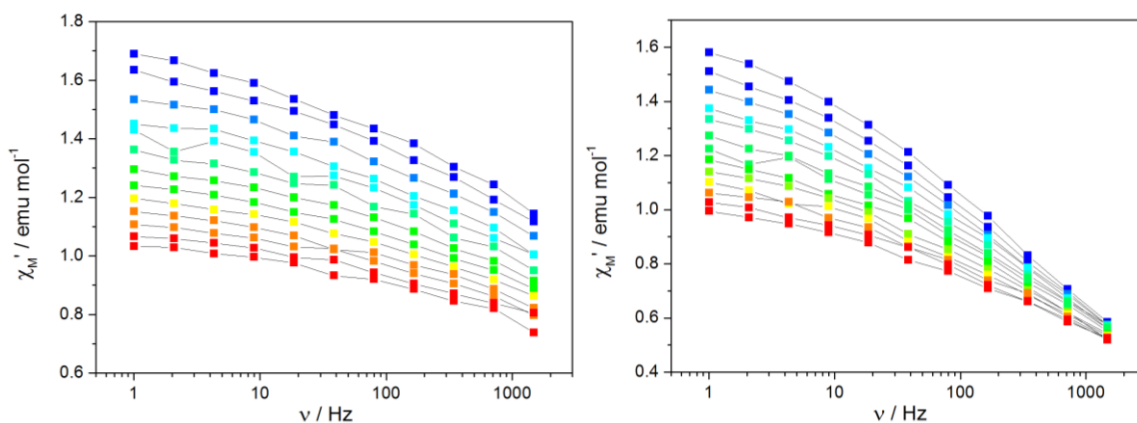


Figure A4.12 Frequency dependence of the in-phase components of ac susceptibility for non-switched 1,4-dioxane solution of **24@Y_{0.61}** under zero Oe dc field (left) and 800 Oe dc field (right). Color mapping from 1.8 (blue) to 3 K (red). Lines are guides to eye.

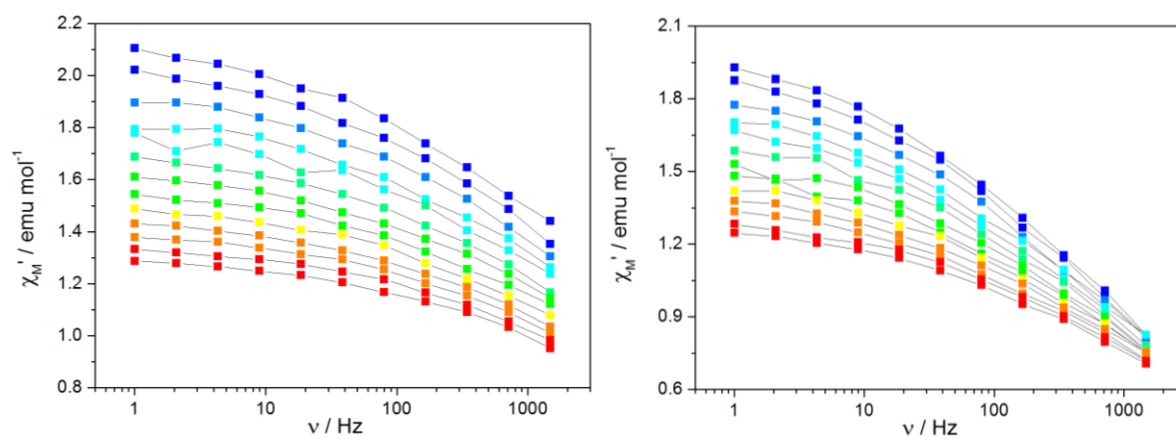


Figure A4.13 Frequency dependence of the in-phase components of ac susceptibility for switched 1,4-dioxane solution of **24**@**Y**_{0.61} under zero Oe dc field (left) and 800 Oe dc field (right). Color mapping from 1.8 (blue) to 3 K (red). Lines are guides to eye.

Appendix A5. Supplementary information for Chapter 5

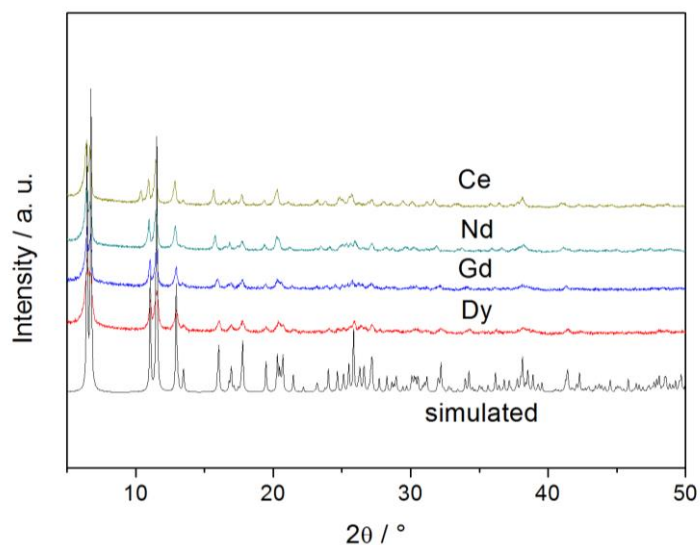


Figure A5.1 PXR D patterns of the microcrystalline powders of Ce(**25**), Nd (**26**), Gd(**27**) and Dy(**28**) and comparison with the simulated pattern from the structural data file of the Dy^{III} derivative (CCDC 669663).

Table A5.1 Summary of SHAPE factor of coordination geometry of Dy(**28**).

Coordination geometry(site symmetry)	Spherical capped square antiprism	Spherical tricapped trigonal prism
SHAPE factors	2.870	3.234

Table A5.2 Selected bond lengths and angles of Dy(**28**).

Bond	Distance(Å)	Atoms	Angle(°)
Dy1-O5b	2.450(2)	O5-Dy1-O3a	68.64(6)
Dy1-O4c	2.495(2)	O2b-Dy1-O7	141.22(6)
Dy1-O1	2.281(2)	O5-Dy1-O7	135.45(7)
Dy1-O3a	2.397(2)	O1-Dy1-O5	78.73(7)
Dy1-O6b	2.493(2)	O1-Dy1-O6b	87.55(8)
Dy1-O5	2.385(2)	O3c-Dy1-O6b	115.16(6)
Dy1-O2b	2.408(2)	O4c-Dy1-O5b	115.50(6)
Dy1-O7	2.423(2)	O1-Dy1-O5b	133.55(7)
Dy1-O3c	2.465(2)	O3a-Dy1-O7	133.42(7)
		O6b-Dy1-O5b	52.45(6)
		O4c-Dy1-O2b	103.72(7)
		O1-Dy1-O2b	144.26(6)

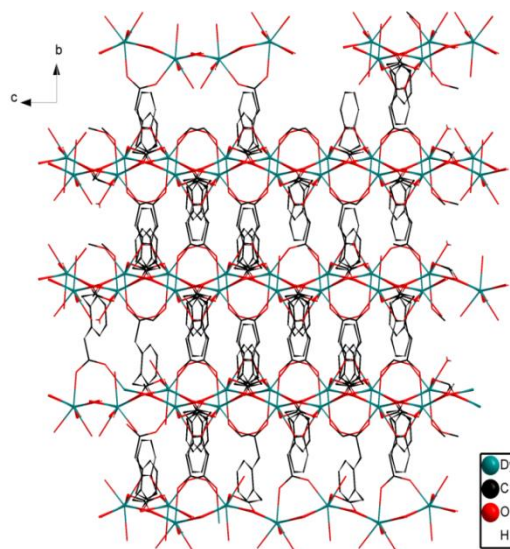


Figure A5.2 Packing diagram of Dy(28) along 'a' axis.

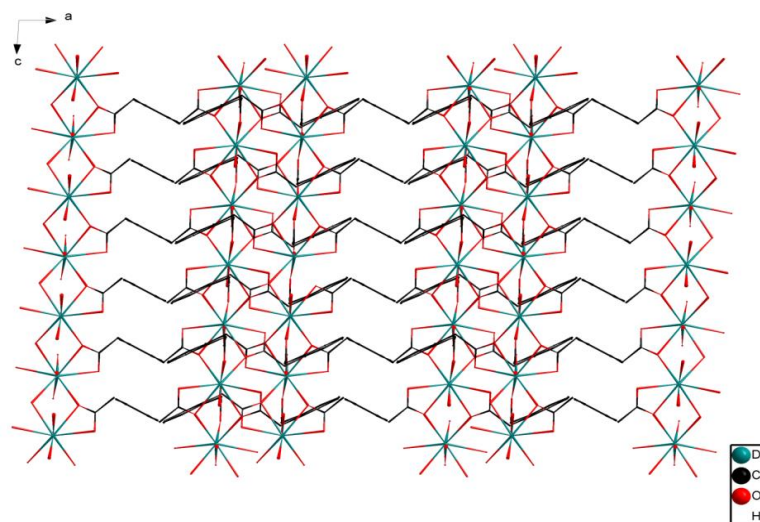


Figure A5.3 Packing diagram of Dy(28) along 'b' axis.

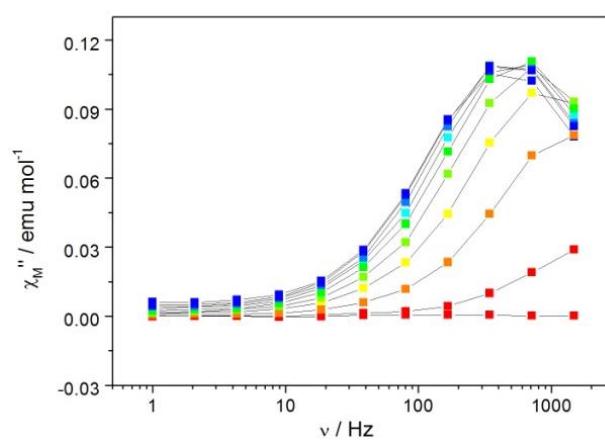


Figure A5.4 Frequency dependence of the out-of-phase components of the magnetization for various dc fields for Nd(26). Color mapping from 0 Oe (red) to 3200 Oe (blue), 400 Oe step. Lines are guides to the eye.

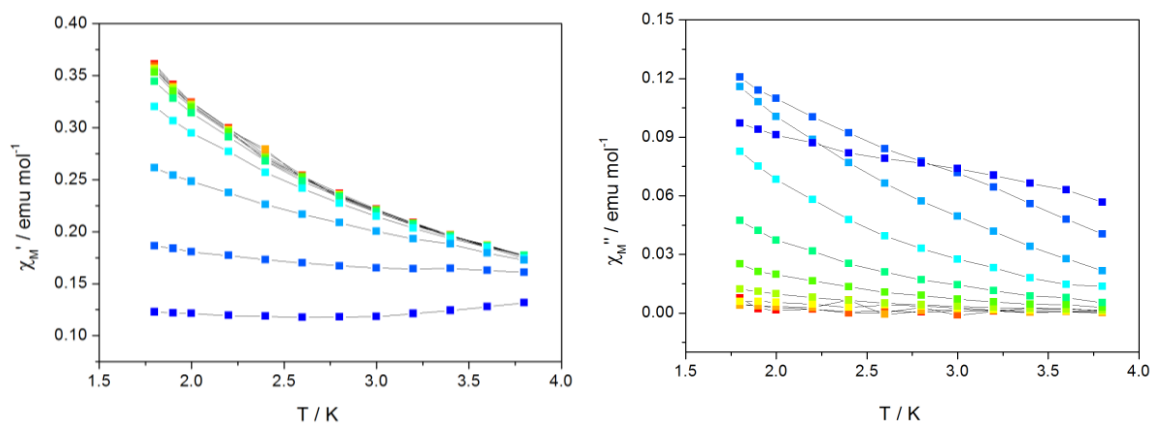


Figure A5.5 Temperature dependence of the in-phase (left) and out-of-phase (right) components of ac susceptibility for under 2000 Oe dc field for Nd(**26**). Color mapping from 1 Hz (red) to 1500 Hz (blue). Lines are guides to the eye.

Table A5.3 Values extracted from the fitting of χ'' vs frequency curves of Nd(**26**) under 2000 Oe dc field.

T (K)	τ (μ s)	T (K)	τ (μ s)
1.8	276.51872	2.4	205.51935
1.9	263.039	2.6	182.02881
2.0	249.32607	2.8	161.41737
2.2	226.14	3.0	147.47077

Table A5.4 Values extracted from the Argand plot of Nd(**26**) under 2000 Oe dc field.

T (K)	χ_s	χ_T	α	R
1.8	0.05368	0.36071	0.14002	0.97752
1.9	0.0588	0.34071	0.11702	0.98964
2.0	0.06217	0.32394	0.09886	0.99154
2.2	0.0593	0.2991	0.0991	0.99106
2.6	0.05548	0.25307	0.08583	0.97305
2.8	0.03918	0.23622	0.12557	0.95091
3.0	0.06177	0.2196	0.01803	0.96983

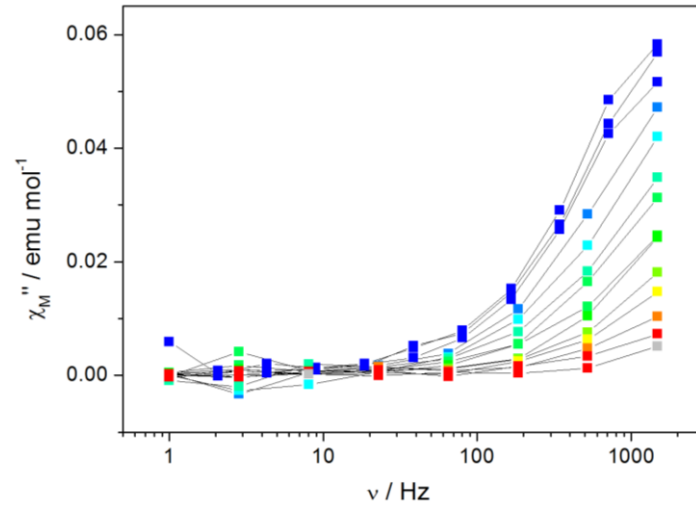


Figure A5.6 Frequency dependence of the out-of-phase components of ac susceptibility for Ce(**25**) under 1800 Oe dc field. Color mapping from 1.8 K (blue) to 4.75 K (red). Lines are guides to the eye.

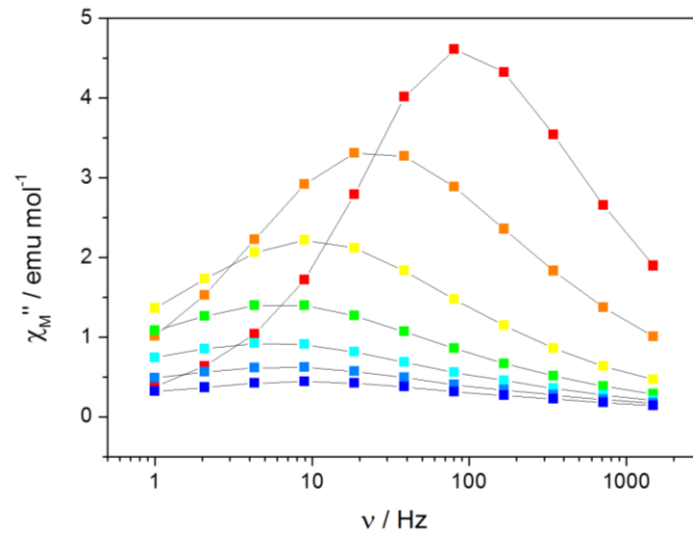


Figure A5.7 Frequency dependence of the out-of-phase components of the magnetization for various dc fields for Dy(**28**). Color mapping from 0 Oe (red) to 2400 Oe (blue). 400 Oe step. Lines are guided for eyes.

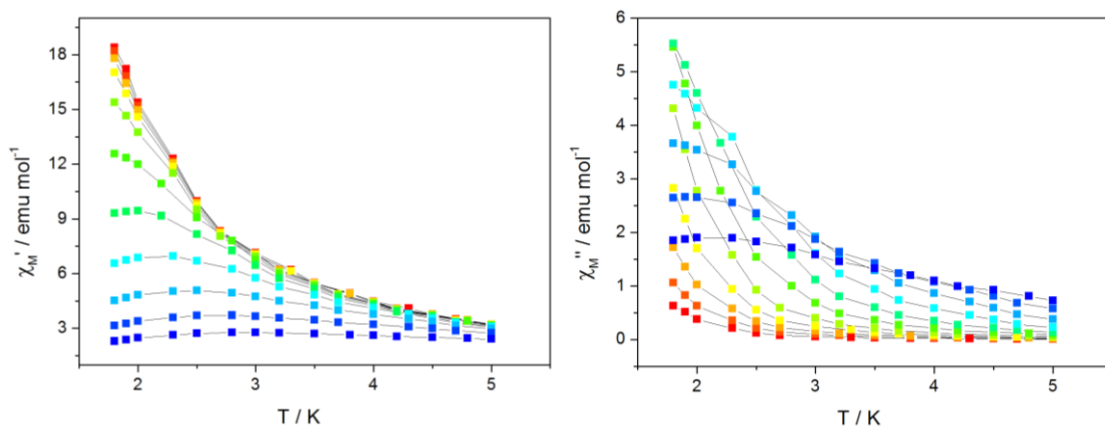


Figure A5.8 Temperature dependence of the in-phase (left) and out-of-phase (right) components of ac susceptibility for under zero Oe dc field for Dy(**28**). Color mapping from 1 Hz (red) to 1500 Hz (blue). Lines are guides to the eye.

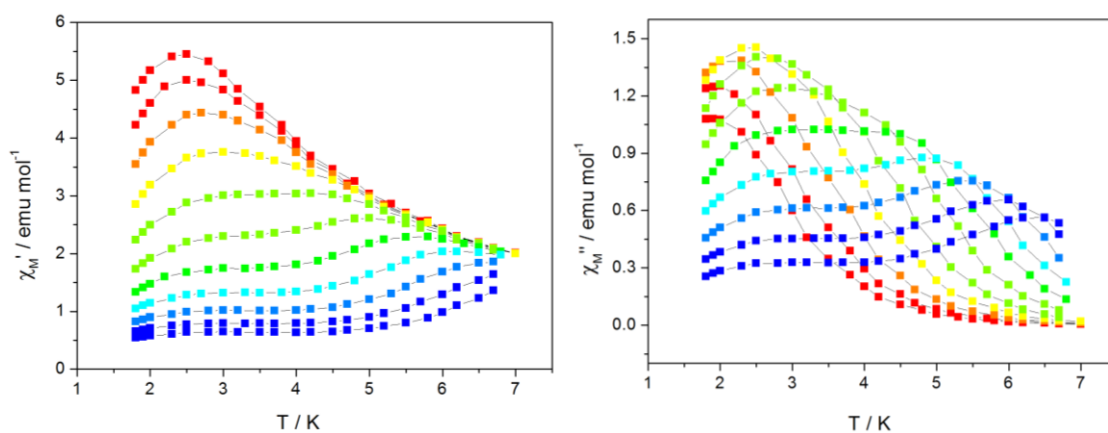


Figure A5.9 Temperature dependence of the in-phase (left) and out-of-phase (right) components of ac susceptibility for under 1200 Oe dc field for Dy(**28**). Color mapping from 1 Hz (red) to 1500 Hz (blue). Lines are guides to the eye.

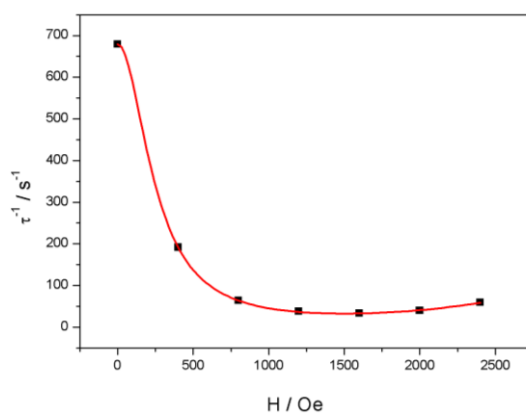


Figure A5.10 Field dependence of the relaxation time τ (left) and plot of τ^{-1} in dependence of T^{-1} under 1200 Oe (square) for Dy(**28**). The solid line is the best fit.

Table A5.5 Values extracted from the fitting of χ'' vs frequency curves of Dy(**28**) in 0Oe.

T (K)	τ (μ s)	T (K)	τ (μ s)
1.8	2254	3.25	257
1.9	1842	3.5	210
2.0	1462	3.75	177
2.25	984	4.0	146
2.5	596	4.25	123
2.75	427	1.5	103
3.0	324		

Table A5.6 Values extracted from the Argand plot of Dy(28) in 0Oe.

T (K)	χ_s	χ_T	α	R
1.8	1.36832	18.781	0.26624	0.98752
1.9	1.29069	17.38694	0.28065	0.98729
2.0	1.43309	15.55076	0.25815	0.99001
2.25	1.74364	12.32842	0.19157	0.96817
2.5	1.47307	10.01096	0.24099	0.99673
2.75	1.44099	0.35901	0.23854	0.99812
3.0	1.39978	7.13994	0.23638	0.84397
3.25	1.6332	6.10743	0.1752	0.92603
3.5	1.63161	5.37	0.15097	0.9572
3.75	1.50745	4.80478	0.16442	0.94361
4.0	1.0412	0.4649	0.2621	0.99373
4.25	1.38768	3.99652	0.17763	0.95321
4.5	0.97507	3.75562	0.24562	0.99648

Table A5.7 Values extracted from the fitting of χ'' vs frequency curves of Dy(28) in 1200Oe.

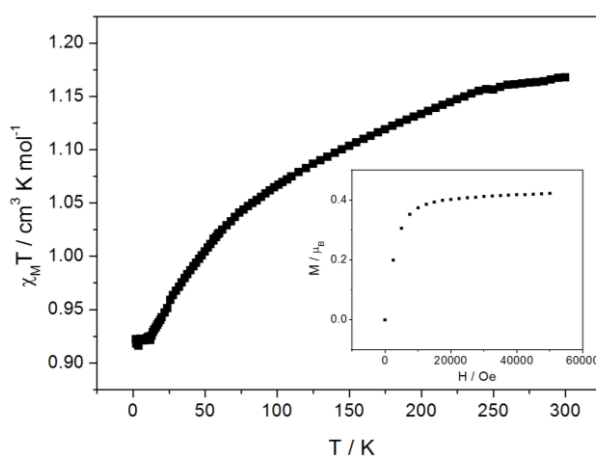
T (K)	τ (μ s)	T (K)	τ (μ s)
1.8	33344	4.25	2575
1.9	29234	4.5	2009
2.0	25837	4.75	1481
2.25	19405	5.0	1105
2.5	14550	5.25	817
2.75	11288	5.5	598
3.0	8837	5.75	437
3.25	6941	6.0	314
3.5	5471	6.25	227
3.75	4302	6.5	161
4.0	3369		

Table A5.8 Values extracted from the Argand plot of Dy(**28**) in 1200Oe.

T (K)	χ_s	χ_T	α	R
1.8	0.27392	6.65083	0.50624	0.99834
1.9	0.28278	0.75013	0.49961	0.99796
2.0	0.29521	6.82897	0.49147	0.99805
2.25	0.31738	6.80634	0.47345	0.99766
2.5	0.35421	6.539	0.44963	0.99659
2.75	0.37551	6.15706	0.43	0.99422
3.0	0.40744	5.71796	0.40481	0.98989
3.25	0.42156	5.27362	0.38073	0.98421
3.5	0.44258	4.83277	0.35305	0.98033
3.75	0.4588	4.42301	0.3255	0.97557
4.0	0.46471	4.08167	0.30436	0.97815
4.25	0.47395	3.77153	0.279	0.98015
4.5	0.48832	3.51733	0.24993	0.98046
4.75	0.49242	3.2749	0.23512	0.98593
5.0	0.50871	3.05634	0.21282	0.98915
5.25	0.51891	2.87523	0.20242	0.99298
5.5	0.53126	2.71295	0.19496	0.99511
5.75	0.56121	2.56804	0.18395	0.99641
6.0	0.57209	2.43776	0.18773	0.99836
6.25	0.71423	2.27172	0.12617	0.96573
6.5	0.68551	2.16187	0.15337	0.91785
6.75	0.60624	2.09618	0.2087	0.9994

Table A5.9 The EDS results of **28**@Y.

Element	Atomic percentage (%)						Average atomic percentage (%)
	94.6	94.0	95.2	96.4	92.8	93.9	
Y	94.6	94.0	95.2	96.4	92.8	93.9	94.5
Dy	5.4	6.0	4.8	3.6	7.2	6.1	5.5

Figure A5.11 Temperature dependence of dc susceptibilities of **28**@Y. Inset: the magnetization dependence of field.

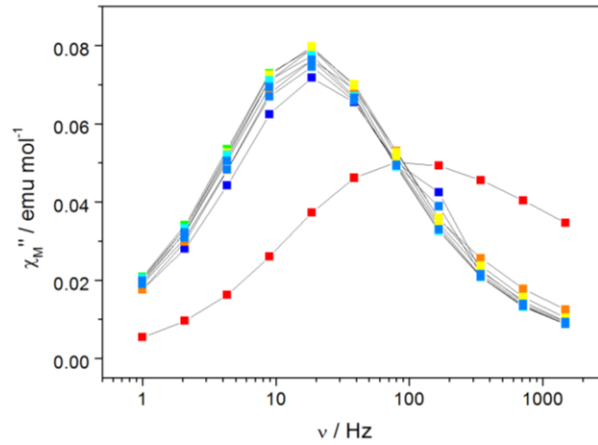


Figure A5.12 Frequency dependence of the out-of-phase components of the magnetization for various dc fields for **28@Y**. Color mapping from 0 Oe (red) to 2000 Oe (blue), 400 Oe step. Lines are guides to the eye.

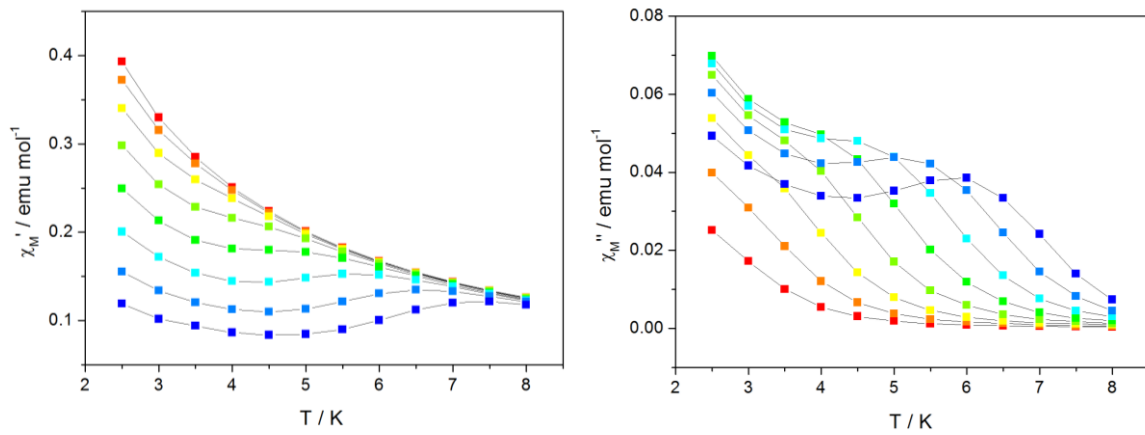


Figure A5.13 Temperature dependence of the in-phase (left) and out-of-phase (right) components of ac susceptibility for under zero Oe dc field for **28@Y**. Color mapping from 1 Hz (red) to 1500 Hz (blue). Lines are guides to the eye.

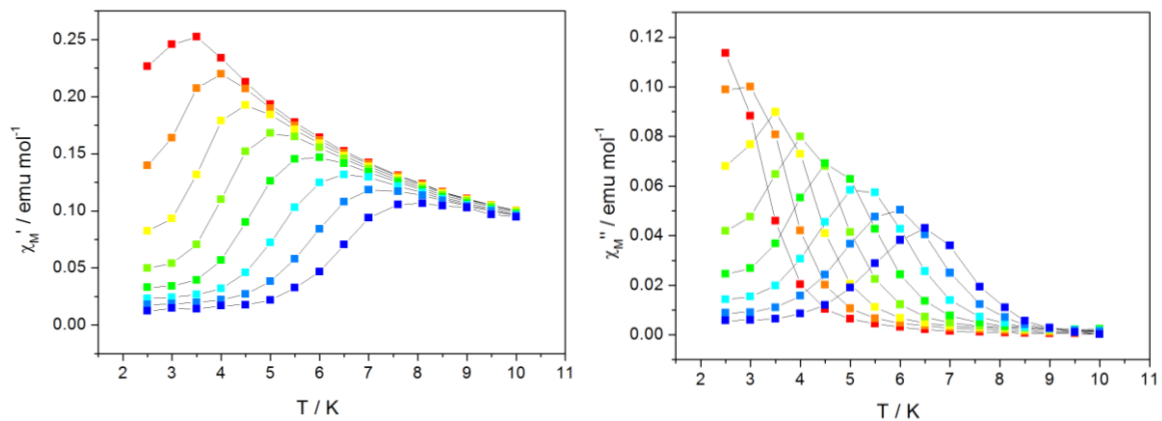


Figure A5.14 Temperature dependence of the in-phase (left) and out-of-phase (right) components of ac susceptibility under 1200 Oe dc field for **28@Y**. Color mapping from 1 Hz (red) to 1500 Hz (blue). Lines are guides to the eye.

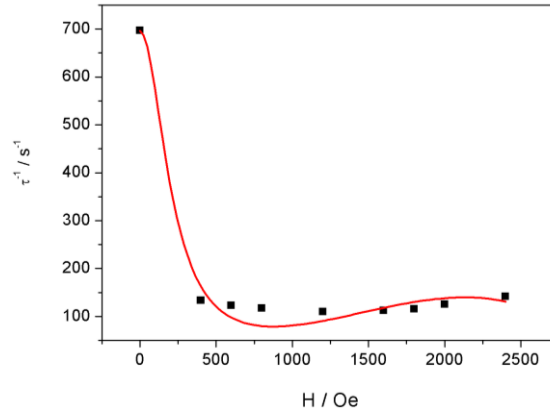


Figure A5.15 Plot of τ^{-1} in dependence of T^{-1} under 1200 Oe for Dy(**28**). The solid line is the fit.

Table A5.10 Values extracted from the fitting of χ'' vs frequency curves of **28@Y** under zero dc field.

T (K)	τ (μs)	T (K)	τ (μs)
1.8	1840.4422	3.5	1416.0258
1.9	1796.35353	4.0	1310.70463
2.0	1785.903	4.5	744.1353
2.5	1720.14773	5.0	450.1479
3.0	1605.87412	5.5	261.36

Table A5.11 Values extracted from the Argand plot of **28@Y** under zero dc field.

T (K)	X_S	X_T	α	R
1.8	0.03396	0.60882	0.58047	0.99854
1.9	0.03415	0.57271	0.57594	0.99749
2.0	0.03431	0.54287	0.57351	0.99684
2.5	0.03816	0.43112	0.55853	0.99072
3.0	0.03938	0.35583	0.53621	0.97299
3.5	0.04919	0.29941	0.47328	0.95658
4.0	0.05391	0.25746	0.39506	0.95998
4.5	0.05546	0.22661	0.32509	0.98093
5.0	0.05489	0.20209	0.27438	0.99333
5.5	0.05298	0.18288	0.25031	0.99849

Table A5.12 Values extracted from the fitting of χ'' vs frequency curves of **28@Y** under 1200 Oe dc field.

T (K)	τ (μs)	T (K)	τ (μs)
3.0	70406.77946	5.0	1622.50456
3.5	24492.89183	5.5	741.74789
4.0	9151.09973	6.0	341.77203
4.5	3780.54332	6.5	139.55733

Table A5.13 Values extracted from the Argand plot of **28@Y** under 1200 Oe dc field.

T (K)	X_S	X_T	α	R
3.0	0.01279	0.36028	0.3432	0.99582
3.5	0.0132	0.28768	0.27272	0.9849
4.0	0.01457	0.24415	0.21742	0.9937
4.5	0.01343	0.21711	0.21441	0.99311
5.0	0.01313	0.19518	0.21873	0.99459
5.5	0.01398	0.17814	0.23413	0.98751
6.0	0.00946	0.16416	0.27875	0.98258

Appendix A6. Experimental set-up

1. Crystal Structure Determination

Single crystal was mounted on a APEXII AXS-Bruker diffractometer equipped with a CCD camera and a graphite-monochromated MoK α radiation source ($\lambda=0.71073 \text{ \AA}$), from the Centre de Diffraction (CDFIX), Université de Rennes 1, France. Data were collected at 150K. Structure was solved with a direct method using the SIR-97 program and refined with a full-matrix least-squares method using the SHELXL-97 program and WinGx interface.

2. X-ray Powder Diffraction

Diagrams have been collected using a Panalytical X'Pert Pro diffractometer with an X'Celerator detector. The typical recording conditions were 45kV, 40mA for Cu-K α ($\lambda=1.542\text{\AA}$), the diagrams were recorded in θ - θ mode in 60 min between 5° and 75° (8378 measurements) with a step size of 0.0084° and a scan time of 50s. The calculated patterns were produced using the Powdercell and WinPLOTR software programs.

3. UV-visible Absorption Measurements

UV-vis absorption spectra have been done on a Perkin-Elmer lambda 650 spectrometer. Liquid state measurements have been performed for evaluating molar absorption coefficients of the ligand.

4. Energy dispersive spectropgy

All EDS measurements were carried out with a Hitachi TM-1000, Tabletop microscope version 02.11(Hitachi High-technologies, Corporation Tokyo Japan) with an EDS analysis system (SwiftED-TM, Oxford Instruments Link INCA). The detector is a silicon drift one, with an energy resolution of 165 ev which allows us to detect the elements from Na to U. With SwiftED-TM software, quantitative analysis can be performed. All samples were observed by means of an electron beam accelerated at 15 Kv, under high vacuum. Samples were assembled on carbon discs, stuck on an aluminium stub fixed at 7 nm from the EDX beam, with an angle of measurement of 22° . Reproducibility of the elemental analysis was carefully checked by reproducing several times the measurements on different takings for each sample.

5. Magnetic dc and ac Measurements

Samples were measured on a Quantum Design MPMS magnetometer on polycrystalline sample embedded in grease to avoid in-field orientation of the crystallites. Measurements were corrected for the diamagnetic contribution, as calculated with Pascal's constants, and for the diamagnetism of the sample holder, as independently determined. In an ideal paramagnetic substance the $\chi_M T$ vs T curve should be constant, since the energy should be degenerate with respect to M_J , projection of the angular momentum J. However, in molecular complexes containing lanthanide ions, the presence of the CF lifts the degeneracy and mixes

the M_J states so that, for low temperatures, a decrease in the $\chi_M T$ vs T is observed. The fitting of the χT vs T curve can then give some information on the low lying levels of the complex. Magnetization curves were measured with an Oxford VSM system at various sweeping rates (from $0.4 \text{ T}\cdot\text{min}^{-1}$ to $1.2 \text{ T}\cdot\text{min}^{-1}$).

The dynamic properties can be detected through a susceptometer. When the sample is placed in an oscillating magnetic field $H(t)$, It is therefore useful to determine the dynamic or differential susceptibility $\delta M/\delta H$ by applying a small oscillating magnetic field.

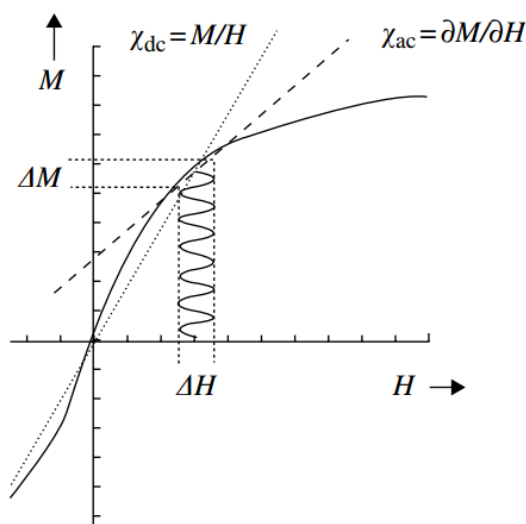


Figure A6.1 Reproduction of a schematic magnetization curve where the differences between M/H and dM/dH are highlighted. The amplitude of the oscillating field is enlarged for clarity.

$$H(t) = H_0 + h \exp(i\omega t) \quad (\text{equ. A6.1})$$

H_0 is the static field, ranging from zero to a certain constant, ω is the angular frequency, the corresponding magnetization $M(t)$ is expressed as:

$$M(t) = M_0 + m(\omega) \exp(i\omega t) \quad (\text{equ. A6.2})$$

The differentiable susceptibility $\chi_M(\omega) = m(\omega)/h$, then we have

$$\chi_M(\omega) = \chi'(\omega) - i\chi''(\omega) \quad (\text{equ. A6.3})$$

$\chi'(\omega)$ is called imaginary component and $\chi''(\omega)$ is the real component. The relationship between $\chi'(\omega)$ or $\chi''(\omega)$ and frequency is illustrated in Figure A6.2.

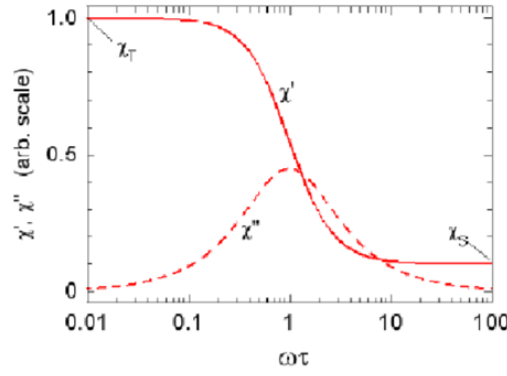


Figure A6.2 Scheme of the theoretical frequency dependence of the real and imaginary component of the susceptibility in a semi-log scale.

When the frequency is extremely low, namely $\omega\tau \ll 1$, the experimental susceptibility is equal to the static susceptibility under low frequency field, this susceptibility is termed as isothermal susceptibility χ_T . When the frequency is high, namely $\omega\tau \gg 1$, the spins will redistribute and become uncoupled with the lattice, the experimental susceptibility is termed as adiabatic susceptibility χ_S .

The susceptibility can be expressed as

$$\chi(\omega) = \frac{\chi_T - \chi_S}{1 + (i\omega\tau)^{1-\alpha}} + \chi_S \quad (\text{equ. A6.4})$$

$$\chi_M'(\omega) = \frac{\chi_T - \chi_S}{1 + \omega^2\tau^2} + \chi_S \quad (\text{equ. A6.5})$$

$$\chi_M''(\omega) = \frac{\omega\tau(\chi_T - \chi_S)}{1 + \omega^2\tau^2} \quad (\text{equ. A6.6})$$

When $\omega\tau=1$, we will get the maximum of the χ_M'' , then the relaxation time τ will be calculated by the corresponding frequency ($\tau=1/2\pi\nu$).

Under different frequency, we can get a series of relaxation time τ at each temperature which could describe the orbach process. The main factor that governs the intrinsic relaxation barrier for such species is considered to be symmetry-related single-ion anisotropy.

$$\tau_{\text{Orbach}} = \tau_0 \exp\left(\frac{U_{\text{eff}}}{K_B T}\right) \quad (\text{equ. A6.7})$$

U_{eff} is the amount of energy required for reversal of the magnetization and τ_0 represents the average relaxation time in response to thermal fluctuations.

As we have mentioned in Chapter 1, the total relaxation time can be determined by the ac susceptibility measurement. The contribution to relaxation time by other relaxation process can be determined by equation (1.5).

Plotting the χ' and χ'' susceptibility at the given temperatures by varying the field frequency, we can obtain the Cole-Cole plots, or the Argand plots. The Cole-Cole plots generally show the typical semi-circle pattern when a rigorous single relaxation process is present. The susceptibility is defined as:

$$\chi(\omega) = \frac{\chi_T - \chi_S}{1 + (i\omega\tau)^{(1-\alpha)}} + \chi_S \quad (\text{equ. A6.7})$$

α is a constant, which donates the distribioin of relaxation time of the total spins, when $\alpha=0$, there is a single relaxation process, while $\alpha=1$ represents the case of spin class. Normally, the value of α is very small for SMM. Then the in-phase and out-of-phase component are extracted as following. Practically, the relaxation time of each spin distributes in a wide temperature range, that is to say, there are other relaxation process.

These two parameters χ_T and χ_S can be extracted as the two intercepts of the semicircle with the χ' axis, being obviously constrained such that $\chi_T > \chi_S$, by fitting the experimental curve with the following expression:

$$\chi'' = \frac{1}{2}(\chi_s - \chi_T) \tan\left(\frac{\pi}{2}\alpha\right) + \frac{1}{2} \sqrt{[(\chi_T - \chi_S) \tan\left(\frac{\pi}{2}\alpha\right)]^2 - 4[\chi'^2 - \chi'(\chi_T + \chi_S) + \frac{1}{4}(\chi_T + \chi_S)^2 - \frac{(\chi_T - \chi_S)^2}{4(\sin(\pi/2)(1-\alpha))^2} + \frac{1}{4}(\chi_T - \chi_S)^2 (\tan\left(\frac{\pi}{2}\alpha\right))^2]}$$

(equ. A6.8)

Appendix A7. Additional structural information

$\{[(\text{Ce}(\text{hfac})_3)(\text{TEMPO-OCH}_3)(\text{H}_2\text{O})]_2 \cdot \text{TEMPO-OCH}_3\}$ (1)

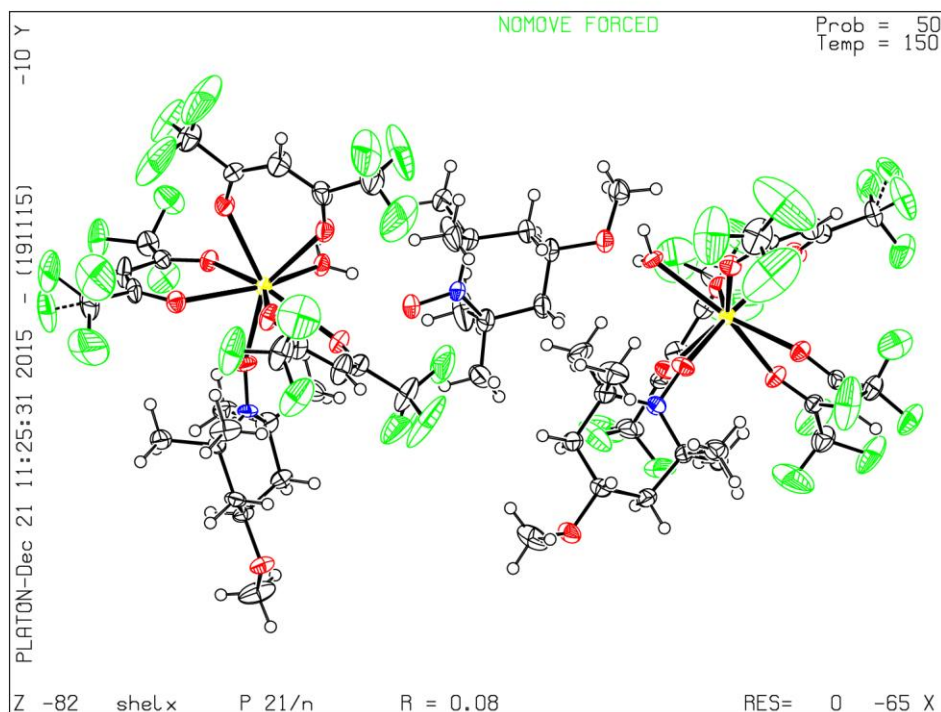


Table A7.1 Atomic parameters for 1.

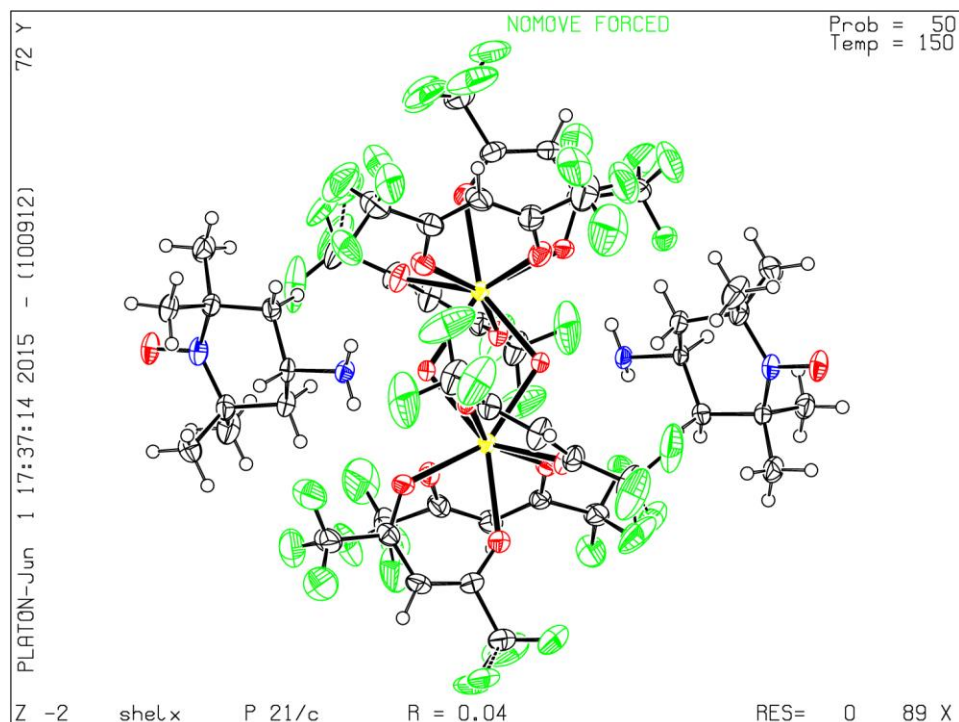
Atom	x/a	y/b	z/c	Atom	x/a	y/b	z/c
C015	0.6660(8)	0.25585(17)	0.8644(4)	F1	0.4353(7)	0.2513(2)	0.5611(4)
C01P	0.4525(8)	0.43628(18)	0.0756(4)	F10	1.1104(15)	0.4092(3)	0.9429(9)
C020	0.4128(10)	0.3679(2)	0.8491(5)	F11	0.9098(19)	0.4061(2)	0.9352(8)
C021	0.0126(11)	0.4114(2)	0.6454(7)	F12	0.9620(16)	0.41983(19)	0.8545(5)
C022	0.3038(11)	0.4931(2)	0.3499(4)	F13	0.6534(10)	0.20676(14)	0.8158(4)
C025	1.0055(10)	0.3677(2)	0.8814(4)	F14	0.4610(8)	0.22816(19)	0.8200(6)
C026	0.8385(9)	0.25243(18)	0.6820(4)	F15	0.5957(10)	0.20937(15)	0.9088(4)
C027	0.447(1)	0.2685(2)	0.6147(5)	F16	0.6570(12)	0.33817(18)	1.0005(4)
C028	0.7702(11)	0.5066(2)	0.3015(5)	F17	0.8610(9)	0.3195(2)	1.0380(3)
C029	0.3248(10)	0.48248(19)	0.0895(4)	F18	0.6827(8)	0.29497(15)	1.0490(3)
C02D	0.7606(12)	0.5251(2)	0.1844(5)	F2	0.3872(7)	0.29455(19)	0.5929(4)
C02F	0.4944(10)	0.4131(2)	0.0272(4)	F20	0.7288(16)	0.4838(3)	0.4625(4)

A7 Additional structural information

C02O	0.1300(9)	0.3640(2)	0.1219(5)	F21	0.9144(14)	0.4693(2)	0.4363(5)
C02Q	0.7298(11)	0.3132(2)	1.0074(4)	F22	0.8643(12)	0.5167(2)	0.4367(4)
C02R	0.3763(12)	0.4619(2)	0.0499(4)	F24	0.6627(15)	0.5439(2)	0.1605(7)
C02Y	0.2566(16)	0.5260(3)	0.3625(6)	F25	0.7954(11)	0.51203(16)	0.1356(4)
C030	0.2930(15)	0.4179(2)	0.4396(5)	F26	0.1486(10)	0.52646(16)	0.3943(4)
C032	0.9368(11)	0.2271(2)	0.6691(6)	F27	0.3595(12)	0.54145(18)	0.3975(5)
C033	0.3234(12)	0.3407(2)	0.1795(6)	F28	0.2155(12)	0.54084(17)	0.3058(4)
C036	1.0048(17)	0.4011(3)	0.9013(6)	F3	0.3711(7)	0.2569(2)	0.6546(4)
C037	0.8134(16)	0.4900(3)	0.4221(6)	F30	0.2215(14)	0.3945(2)	0.4106(5)
C038	1.2052(12)	0.2976(3)	0.9577(5)	F31	0.4087(11)	0.4050(3)	0.4724(5)
C039	0.2476(15)	0.5107(3)	0.0567(6)	F32	0.2308(14)	0.42813(19)	0.4844(5)
C1	0.1255(9)	0.37312(17)	0.1946(4)	F33	0.3058(13)	0.53558(18)	0.0869(6)
C10	0.7347(10)	0.4862(2)	0.3484(4)	F34	0.1238(11)	0.5139(2)	0.0679(7)
C11	0.7132(9)	0.50304(18)	0.2334(4)	F35A	0.293(3)	0.5196(4)	0.0011(8)
C12	1.1026(9)	0.3174(2)	0.9073(4)	F35B	0.191(3)	0.5072(6)	-0.0073(8)
C13	1.0937(10)	0.3479(2)	0.9232(4)	F36	0.4280(8)	0.38704(14)	0.0297(3)
C14	0.6977(9)	0.25012(19)	0.6485(4)	F37	0.4654(8)	0.42223(16)	-0.0361(3)
C15	0.5999(8)	0.27268(19)	0.6535(4)	F38	0.6312(7)	0.40737(17)	0.0437(3)
C16	0.3233(9)	0.44108(19)	0.3887(4)	F4	0.9544(13)	0.2289(3)	0.6058(5)
C166	-0.1405(8)	0.37842(18)	0.1838(4)	F49	0.8642(18)	0.5418(3)	0.2126(5)
C167	-0.1227(8)	0.41158(18)	0.2043(4)	F5	1.0665(9)	0.2306(2)	0.7013(6)
C168	0.035(1)	0.45631(18)	0.2234(6)	F6	0.8896(11)	0.20098(17)	0.6717(8)
C17	0.2845(12)	0.4709(2)	0.3957(5)	F7	1.2806(9)	0.2800(2)	0.9280(4)
C18	1.060(1)	0.2982(2)	0.5830(5)	F8A	1.263(3)	0.3126(4)	1.0135(10)
C19	0.8427(9)	0.31555(18)	0.5134(4)	F8B	1.325(2)	0.3125(5)	0.9882(14)
C2	0.4699(9)	0.38457(18)	0.6939(5)	F9	1.1357(10)	0.2790(2)	0.9874(5)
C20	0.6892(10)	0.3082(2)	0.5041(4)	N1	0.4888(7)	0.35914(15)	0.7437(3)
C21	0.4454(12)	0.3199(4)	0.4403(8)	N2	0.1274(6)	0.40696(14)	0.1997(3)
C22	0.6205(18)	0.2978(3)	0.3786(6)	N3	0.6414(7)	0.35023(16)	0.4215(3)
C23	0.8706(11)	0.3573(3)	0.3890(5)	O00F	0.0677(6)	0.38226(13)	0.6672(3)
C24	0.8576(10)	0.3500(2)	0.5106(4)	O1	0.8882(6)	0.33805(12)	0.6876(3)

A7 Additional structural information

C25	0.7689(14)	0.3972(2)	0.4510(6)	O10	0.5807(6)	0.40164(13)	0.2729(3)
C27	-0.0079(9)	0.36120(18)	0.2145(4)	O11	0.3757(7)	0.42963(13)	0.3433(3)
C28	0.3139(9)	0.3861(2)	0.6576(5)	O12	0.6479(7)	0.46492(14)	0.3374(3)
C29	0.2131(8)	0.38340(18)	0.7049(4)	O13	0.6268(6)	0.48371(14)	0.2060(3)
C3	0.0018(8)	0.42736(16)	0.1834(4)	O14	0.3583(7)	0.49062(13)	0.3006(3)
C30	0.4089(9)	0.3155(2)	0.8004(4)	O15	0.3292(6)	0.48079(12)	0.1514(3)
C31	0.5607(11)	0.3785(3)	0.6428(6)	O16	0.4898(6)	0.42849(12)	0.1364(3)
C32	0.5165(11)	0.4141(2)	0.7327(6)	O17	0.2467(6)	0.41943(13)	0.1993(3)
C33	0.7295(8)	0.29901(18)	0.9382(4)	O19	0.9146(6)	0.30411(13)	0.5782(3)
C34	0.6763(9)	0.26920(18)	0.9271(4)	O2	0.6206(5)	0.29712(12)	0.6855(3)
C35	0.5932(12)	0.2247(2)	0.8524(5)	O3	0.9229(6)	0.36181(13)	0.8270(3)
C36	-0.0309(9)	0.4341(2)	0.1076(5)	O31	-0.2579(6)	0.36758(13)	0.2101(3)
C37	0.2557(9)	0.3608(2)	0.2430(5)	O4	1.0355(6)	0.30307(14)	0.8576(3)
C4	0.6004(10)	0.3191(2)	0.4361(5)	O5	0.7689(6)	0.31624(12)	0.8979(3)
C5	0.3863(8)	0.34929(18)	0.7833(4)	O6	0.7037(6)	0.26639(12)	0.8144(3)
C6	0.2361(9)	0.35344(18)	0.7422(4)	O7	0.8957(6)	0.27275(12)	0.7209(3)
C7	0.7847(10)	0.3633(2)	0.4425(5)	O8	0.6184(6)	0.35119(13)	0.7669(3)
Ce01	0.80570(4)	0.31394(2)	0.78182(2)	O9	0.5583(7)	0.36245(16)	0.3706(3)
Ce02	0.45558(4)	0.44945(2)	0.24335(2)				

{[Dy(hfac)₃(H₂O)]₂(TEMPO-NH₂)₂} (6)Table A7.2 Atomic parameters for **6**.

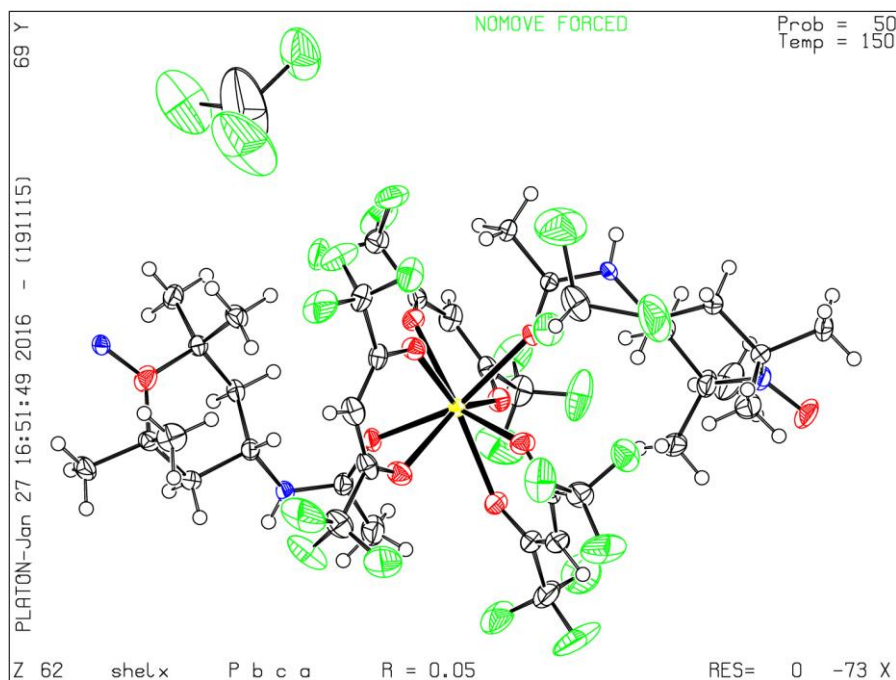
Atom	x/a	y/b	z/c	Atom	x/a	y/b	z/c
C064	0.0385(4)	0.11797(19)	0.2108(2)	F026	-0.0256(4)	0.00258(17)	0.0675(2)
C066	0.5458(5)	0.1310(2)	0.1437(2)	F028	0.7265(3)	0.01928(19)	0.2266(2)
C068	0.3816(4)	0.25888(18)	0.2736(2)	F029	0.3816(5)	0.08690(15)	0.03098(19)
C069	0.0672(5)	0.2168(2)	0.0850(2)	F031	0.2200(4)	0.08897(15)	0.0677(2)
C070	0.1800(5)	0.19987(19)	0.4017(2)	F032	0.1957(5)	0.1075(2)	-0.0445(2)
C071	0.3188(4)	0.01293(19)	0.0765(2)	F033	0.3618(5)	0.08993(14)	0.12064(17)
C072	0.0157(5)	0.1254(2)	0.0830(2)	F034	0.3280(6)	0.04096(17)	0.4308(2)
C076	0.4524(5)	0.3290(2)	0.1221(2)	F035	0.2654(5)	0.27462(15)	0.4338(2)
C077	0.3243(5)	0.37941(19)	0.1835(2)	F036	0.0855(5)	0.27132(16)	0.43501(19)
C078	0.4176(5)	0.3417(2)	0.3222(2)	F037	0.3676(4)	0.12803(16)	0.03688(16)
C079	-0.0487(5)	0.0567(2)	0.3340(2)	F038	0.4952(4)	0.19828(18)	0.4162(2)
C080	0.0252(5)	0.0769(2)	0.1019(2)	F10A	0.309(2)	0.0893(11)	0.5254(7)
C081	-0.0785(5)	-0.1000(2)	0.1905(3)	F10B	0.2325(9)	0.0565(3)	0.5138(3)
C082	-0.1195(5)	0.1766(2)	0.2546(3)	F11	-0.2226(4)	0.02925(19)	0.3737(2)

A7 Additional structural information

C083	0.0812(5)	-0.1594(2)	0.1714(2)	F12A	-0.084(2)	0.0224(10)	0.4234(10)
C084	0.3043(5)	0.0642(2)	0.0238(2)	F12B	-0.0631(7)	-0.0028(4)	0.4057(4)
C085	0.2998(8)	0.0900(2)	-0.0345(3)	F13	-0.1253(5)	0.02424(17)	0.3299(3)
C087	0.4011(5)	0.0299(2)	0.3841(2)	F1A	0.375(2)	0.0605(9)	-0.0716(9)
C088	0.3253(6)	-0.0699(2)	0.0737(2)	F1B	0.3071(12)	0.0590(4)	-0.0776(3)
C089	0.6166(5)	0.0147(3)	0.2309(3)	F2	-0.1267(4)	0.0271(2)	0.1299(2)
C090	0.0519(5)	-0.1323(2)	0.3706(2)	F20	0.6205(5)	0.21178(17)	0.1492(3)
C091	0.5478(5)	0.0552(2)	0.1996(2)	F21	0.7217(4)	0.15924(19)	0.1053(2)
C092	0.3185(5)	0.0127(2)	0.0258(2)	F22	0.5874(5)	0.02964(17)	0.2107(3)
C093	0.1852(5)	0.1223(2)	0.4528(2)	F23	0.5927(4)	0.0133(2)	0.2834(2)
C094	0.5787(5)	0.2849(2)	0.3011(3)	F24	-0.0797(4)	0.21978(15)	0.2728(3)
C095	0.4220(7)	-0.0230(2)	0.4064(3)	F30A	0.557(3)	0.1993(11)	0.0805(13)
C096	0.1846(5)	0.1738(2)	0.4517(2)	F30B	0.5702(12)	0.1828(5)	0.0639(5)
C097	-0.1072(5)	0.0978(2)	0.3117(3)	F3A	0.1636(18)	0.0604(9)	0.0679(9)
C098	0.1741(6)	0.2568(2)	0.4072(2)	F3B	0.1268(11)	0.0542(4)	0.0404(5)
C1	0.1205(4)	0.07332(18)	0.2117(2)	F4	-0.1094(4)	0.1768(2)	0.19990(19)
C10	-0.0499(4)	0.13380(18)	0.2810(2)	F6	0.6213(5)	0.1635(2)	0.3700(3)
C100	-0.0678(6)	0.0397(2)	0.0852(3)	F7A	0.626(2)	0.1349(10)	0.4351(12)
C101	0.4593(5)	0.1156(2)	0.3858(2)	F7B	0.5842(12)	0.1440(4)	0.4598(4)
C102	0.6058(5)	0.0917(2)	0.1703(3)	F8A	0.537(2)	-0.0248(11)	0.4275(13)
C104	0.4646(5)	0.0677(2)	0.4074(2)	F8B	0.4919(12)	-0.0276(4)	0.4482(5)
C105	0.6150(6)	0.1720(3)	0.1158(3)	F9	0.0713(6)	0.0753(2)	0.5136(2)
C106	-0.1182(6)	0.0162(3)	0.3623(3)	N1	0.4776(3)	0.32837(14)	0.22467(17)
C107	0.5435(7)	0.1551(3)	0.4086(4)	N2	0.0260(4)	0.13879(15)	0.26843(19)
C109	0.1774(8)	0.0949(3)	0.5094(3)	N3	0.1899(4)	0.23271(15)	0.24090(17)
C11	0.0887(4)	0.16241(18)	0.10327(19)	N4	0.3122(4)	0.04440(16)	0.24150(17)
C2	0.2259(4)	0.08532(16)	0.2457(2)	O1	0.2051(3)	0.04684(11)	0.23783(13)
C3	0.1935(4)	0.09244(18)	0.3066(2)	O10	0.1814(3)	0.18298(12)	0.35229(13)
C4	0.1145(4)	0.13729(17)	0.3141(2)	O11	0.0540(3)	0.04772(13)	0.33131(16)
C5	0.1813(5)	0.18621(18)	0.3136(2)	O12	0.0536(3)	0.13640(12)	0.27074(14)
C6	0.2761(4)	0.27380(17)	0.24060(19)	O13	0.1704(3)	0.15808(12)	0.13754(13)
C7	0.3095(4)	0.28551(18)	0.18070(19)	O14	0.0998(3)	0.05881(13)	0.13387(14)

A7 Additional structural information

C8	0.3905(4)	0.33077(17)	0.1780(2)	O15	0.5544(3)	0.36193(13)	0.22352(17)
C9	0.4627(4)	0.30342(19)	0.2806(2)	O16	-0.0512(3)	0.17252(14)	0.27344(17)
Dy01	0.28175(2)	0.08835(2)	0.16238(2)	O2	0.2974(3)	0.13977(11)	0.24051(13)
Dy02	0.21501(2)	0.09922(2)	0.31472(2)	O3	0.4433(3)	0.05063(13)	0.20549(15)
F008	-0.0182(3)	0.22200(13)	0.04869(16)	O4	0.4429(3)	0.13726(13)	0.14129(15)
F014	0.1694(3)	0.27944(11)	0.35737(13)	O5	0.2922(4)	0.09334(13)	0.06368(15)
F015	0.0465(3)	0.24498(12)	0.12968(14)	O6	0.3103(3)	0.00464(13)	0.12539(13)
F021	0.1581(3)	0.23602(13)	0.06140(15)	O7	0.3912(3)	0.13162(13)	0.34898(15)
F022	-0.2279(3)	0.17506(17)	0.2652(2)	O8	0.3277(3)	0.03155(13)	0.34493(14)
F024	0.1765(4)	0.12567(18)	0.55298(15)	O9	0.1890(4)	0.09338(13)	0.41169(16)
F025	0.4419(4)	0.05446(13)	0.36536(17)	F026	-0.0256(4)	0.00258(17)	0.0675(2)

[Dy(hfac)₃(TEMPO-acetamido)₂ (8)Table A7.3 Atomic parameters for **8**.

Atom	x/a	y/b	z/c	Atom	x/a	y/b	z/c
C043	0.3677(3)	0.2044(2)	0.19491(19)	Cl1	0.55337(17)	0.23347(14)	-0.02289(9)
C044	0.0871(3)	0.2281(2)	0.3327(2)	Cl2	0.44770(9)	0.21647(7)	0.05733(7)
C045	0.3509(3)	0.1230(2)	0.11959(19)	Cl3	0.5028(2)	0.32531(11)	0.03658(15)
C046	0.1605(3)	0.1965(2)	0.32492(18)	Cl4	0.1792(3)	0.3821(3)	0.2590(2)
C047	0.2484(3)	0.2646(2)	0.0615(2)	Cl5	0.0250(2)	0.3925(2)	0.29091(17)
C048	0.3265(3)	-0.0123(2)	0.0938(2)	Cl6	0.0700(2)	0.42565(19)	0.19183(12)
C049	0.2516(3)	0.1416(2)	0.3859(2)	Dy01	0.26487(2)	0.11267(2)	0.13021(2)
C052	0.1430(3)	0.1415(2)	0.29960(18)	F011	0.0871(3)	0.27649(15)	0.13926(17)
C053	0.0890(3)	0.0954(2)	0.08597(19)	F014	0.3156(2)	0.29260(15)	0.20808(18)
C055	0.2099(3)	0.1012(2)	0.30116(18)	F015	-0.0172(2)	0.23166(18)	0.14521(19)
C056	0.2858(3)	0.1602(2)	0.04163(18)	F018	0.4128(3)	0.28710(16)	0.16000(15)
C057	0.2475(4)	0.1279(2)	0.4420(2)	F019	0.5015(2)	0.09630(18)	0.01720(15)
C058	0.0566(3)	0.2300(2)	0.1559(2)	F024	0.4259(3)	0.27921(17)	0.23904(17)
C059	0.3979(3)	0.1120(2)	0.2217(2)	F025	0.4001(3)	0.0437(2)	0.28398(18)

A7 Additional structural information

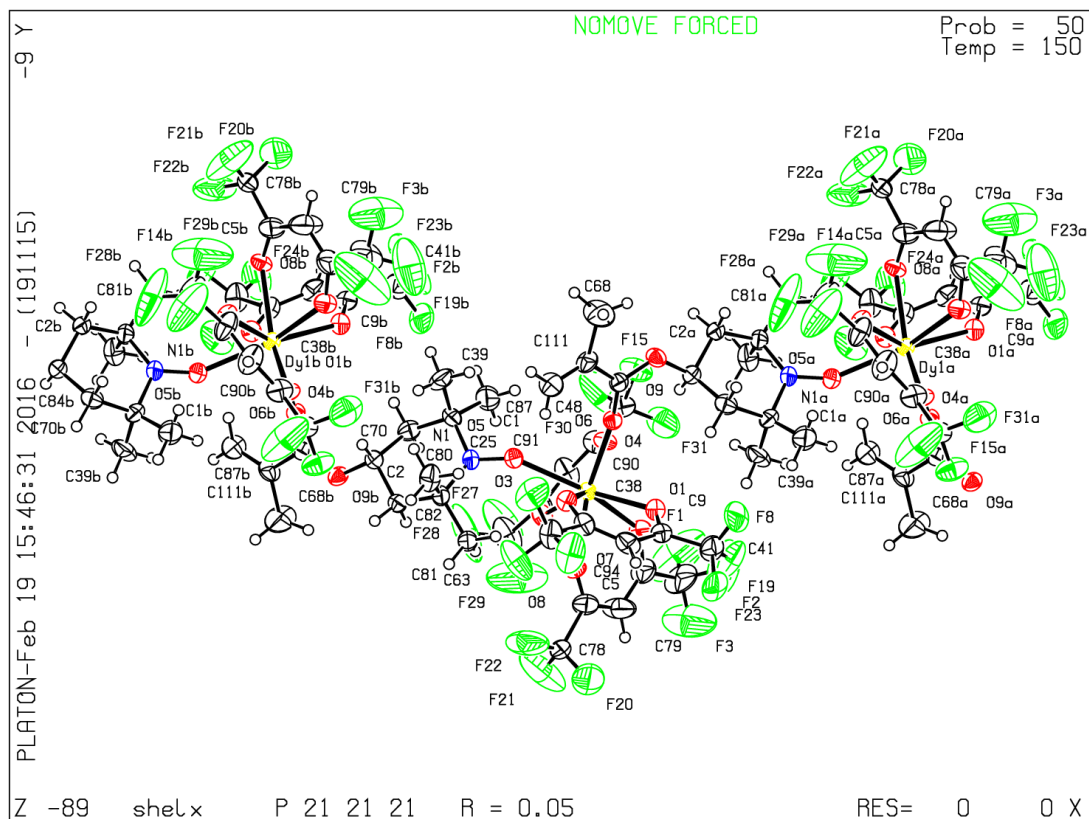
C060	0.2136(3)	0.1288(2)	-0.0543(2)	F027	0.5390(2)	0.1007(2)	0.09310(17)
C061	0.2160(3)	0.2310(2)	0.2934(2)	F028	0.0619(2)	0.23110(17)	0.20563(13)
C062	0.2983(5)	-0.0727(3)	0.0868(3)	F1	0.5448(2)	0.0245(2)	0.0520(2)
C063	0.3804(3)	0.2668(2)	0.2008(2)	F10	-0.0341(2)	0.0695(2)	0.0549(2)
C064	0.3693(4)	0.1401(2)	-0.1738(2)	F2	0.3549(4)	0.10583(18)	0.0730(3)
C065	0.3316(3)	0.1615(3)	0.3728(2)	F3	0.2683(3)	0.09242(18)	0.12809(19)
C066	0.4444(4)	0.0760(3)	0.2569(2)	F4	0.2462(4)	-0.0744(2)	0.0516(2)
C067	0.4215(3)	0.0564(2)	0.07794(19)	F6	0.4907(3)	0.0434(2)	0.2303(2)
C068	0.2302(4)	0.0742(2)	-0.0803(2)	F7	0.4892(3)	0.1034(2)	0.2882(2)
C069	0.2299(3)	0.0900(2)	0.35595(19)	F8	0.0367(4)	0.0070(2)	0.0833(2)
C070	0.3986(4)	0.0016(2)	0.0776(2)	F9	0.0614(3)	0.0443(2)	0.01326(18)
C071	0.5025(3)	0.0690(3)	0.0601(2)	N1	0.1940(2)	0.22638(16)	0.40677(15)
C072	0.1624(4)	-0.0129(3)	0.2094(2)	N2	0.2873(3)	0.08313(19)	0.12143(17)
C073	0.4214(4)	0.0963(3)	-0.0964(2)	N3	0.1901(3)	0.04912(18)	0.27747(16)
C075	0.0370(3)	0.0542(3)	0.0592(2)	N4	0.2675(3)	0.21057(17)	0.01382(15)
C076	0.5238(4)	0.2557(3)	0.0367(3)	O041	0.1958(2)	0.18593(16)	0.37541(15)
C077	0.1578(4)	0.0522(3)	-0.1041(3)	O1	0.2775(2)	0.01805(15)	0.11321(15)
C080	0.2629(5)	0.0322(2)	-0.0423(3)	O13	0.2950(3)	0.04270(18)	0.15246(18)
C1	0.0547(3)	0.1421(2)	0.1065(2)	O2	0.3842(2)	0.09729(15)	0.09071(15)
C2	0.3263(3)	0.1738(2)	0.09003(18)	O3	0.2689(2)	0.16657(15)	0.05942(12)
C20	0.2613(3)	0.2108(2)	0.03582(18)	O4	0.1976(2)	0.08175(15)	0.19891(13)
C26	0.0890(9)	0.3907(12)	0.2473(6)	O5	0.1565(2)	0.08219(15)	0.08665(14)
C3	0.4072(3)	0.1690(2)	0.2261(2)	O6	0.16637(19)	0.17791(14)	0.14559(13)
C66	0.1847(3)	0.0427(2)	0.22818(19)	O7	0.3545(2)	0.08669(16)	0.19356(15)
C9	0.0974(3)	0.1792(2)	0.13404(18)	O8	0.3209(2)	0.19223(15)	0.16125(14)

A7 Additional structural information

C115	0.3269(3)	-0.3412(2)	0.0623(2)	F113	0.5529(2)	-0.05492(17)	-0.37871(16)
C116	0.3680(3)	-0.0490(2)	0.0220(2)	F114	0.5088(3)	-0.1498(2)	-0.3888(3)
C117	0.3656(3)	-0.4333(2)	-0.0065(3)	F115	0.6086(3)	-0.1203(3)	-0.43900(16)
C118	0.2980(3)	-0.0491(2)	-0.2862(2)	F19	0.8674(2)	-0.31662(19)	-0.51452(15)
C119	0.0780(4)	-0.0875(3)	0.0058(3)	F2	0.8872(3)	-0.0582(2)	-0.4534(2)
C120	0.0461(3)	-0.3142(2)	-0.2828(3)	F20	0.8100(3)	-0.24273(19)	-0.56419(15)
C122	-0.0880(3)	-0.1436(3)	-0.1855(2)	F21	0.14849(18)	-0.44688(15)	-0.22449(14)
C124	0.8412(3)	-0.4958(3)	-0.0830(3)	F23	0.7645(2)	-0.03638(17)	-0.19479(15)
C126	0.4362(3)	-0.0523(2)	-0.2173(2)	F24	0.0681(2)	-0.35972(18)	0.03821(14)
C140	0.6887(3)	-0.1210(2)	-0.2346(2)	F26	0.7172(2)	-0.10056(16)	-0.12958(13)
C141	0.5733(4)	-0.1157(3)	-0.3851(3)	F27	0.56542(19)	-0.46300(16)	-0.39586(15)
C311	0.8681(3)	-0.4077(3)	-0.1757(2)	F28	0.03528(19)	-0.43116(15)	-0.02626(15)
C41	0.8011(2)	-0.4030(2)	-0.1400(2)	F3	0.2276(2)	-0.37731(15)	-0.26104(13)
C43	0.4858(2)	-0.2942(2)	0.17969(19)	F300	0.6428(2)	-0.0336(2)	-0.17518(19)
C44	0.6266(3)	-0.1416(2)	-0.3336(2)	F301	-0.0154(2)	-0.3381(2)	-0.0325(2)
C45	0.0195(3)	-0.2481(2)	-0.3041(2)	F32	0.51832(18)	-0.39923(18)	-0.32858(16)
C46	0.3049(3)	-0.0896(2)	-0.2357(2)	F33	0.3169(3)	-0.46874(19)	-0.0383(2)
C48	0.5188(3)	-0.2396(2)	-0.0720(2)	F35	0.43530(19)	-0.05547(17)	-0.00701(16)
C49	0.2078(3)	-0.4084(2)	-0.2099(2)	F36	0.3516(2)	0.01388(16)	0.02140(19)
C51	0.7924(3)	-0.4171(2)	-0.3431(2)	F37	0.5534(2)	-0.36341(19)	-0.41727(18)
C54	0.3312(3)	-0.3656(2)	0.0032(2)	F38	0.3783(3)	-0.46392(18)	0.04567(18)
C59	0.7989(3)	-0.2422(2)	-0.4540(2)	F40	0.2534(3)	-0.2162(2)	0.15336(18)
C60	0.6539(3)	-0.3886(2)	-0.3480(2)	F41	0.3287(3)	-0.2930(2)	0.17985(15)
C62	0.2407(2)	-0.1341(2)	-0.2189(2)	F42	0.3768(2)	-0.2099(2)	0.13780(15)
C63	0.4756(3)	-0.2384(2)	-0.0106(2)	F43	0.4319(2)	-0.42976(19)	-0.0349(2)
C65	0.5867(3)	-0.2879(2)	-0.0671(2)	F44	0.3787(3)	-0.0657(2)	0.07975(16)
C66	0.1884(3)	-0.3623(2)	0.15744(19)	F45	0.0316(2)	-0.0816(2)	-0.0435(2)
C67	0.8258(3)	-0.1433(2)	-0.3992(2)	F46	0.0474(3)	-0.1309(3)	0.0419(3)
C68	0.5719(3)	-0.4047(2)	-0.3725(2)	F47	0.0756(2)	-0.0321(2)	0.0341(2)
C69	0.3739(3)	-0.0912(2)	-0.2009(2)	N1	0.4632(2)	-0.26228(17)	-0.12077(17)
C70	0.7030(3)	-0.0724(2)	-0.1825(2)	N2	-0.0388(2)	-0.22233(18)	-0.25849(17)
C71	0.1165(3)	-0.3455(2)	-0.0627(2)	O1	0.22340(17)	-0.30941(15)	-0.15905(13)

A7 Additional structural information

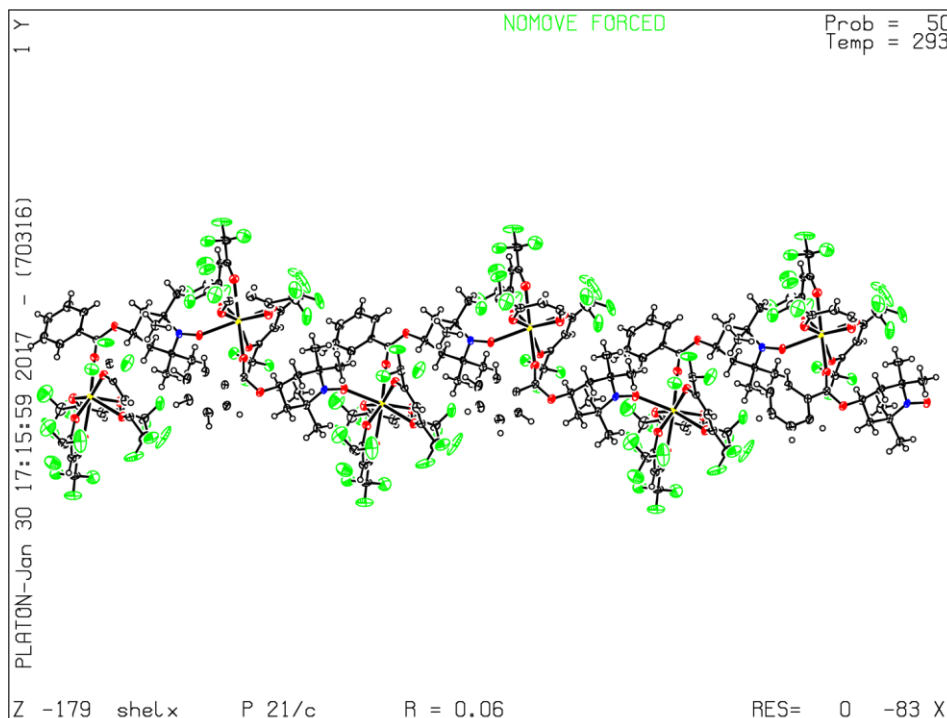
C73	-0.0209(3)	-0.2544(3)	-0.3665(2)	O10	0.81747(18)	-0.36735(15)	-0.31701(15)
C74	-0.0188(3)	-0.1860(2)	-0.2010(2)	O100	0.68257(17)	-0.35169(15)	-0.11711(14)
C76	0.8194(3)	-0.1775(2)	-0.4549(2)	O11	0.77885(19)	-0.27573(15)	-0.40953(14)
C77	0.6200(2)	-0.3052(2)	-0.1290(2)	O12	0.81308(18)	-0.16321(15)	-0.34561(14)
C78	0.8527(3)	-0.0744(2)	-0.4022(2)	O13	0.64930(18)	-0.19790(15)	-0.34130(14)
C79	0.3060(3)	-0.2781(2)	0.0721(2)	O14	0.71953(18)	-0.17513(15)	-0.22678(14)
C80	0.8558(3)	-0.4654(3)	-0.3589(3)	O15	0.74963(18)	-0.31479(15)	-0.19758(13)
C82	0.5573(3)	-0.3369(2)	-0.1679(2)	O16	-0.10657(19)	-0.25054(16)	-0.25864(16)
C83	0.0863(3)	-0.1996(2)	-0.3093(2)	O2	0.14529(18)	-0.29331(16)	-0.04697(14)
C85	0.1617(3)	-0.1075(2)	-0.0132(2)	O3	0.16199(19)	-0.15565(17)	-0.04812(16)
C86	0.7882(3)	-0.4466(2)	-0.0927(2)	O4	0.32327(18)	-0.13111(15)	-0.04426(14)
C88	0.2251(3)	-0.0736(2)	0.0095(2)	O5	0.2816(2)	-0.23757(16)	0.03359(15)
C89	0.6442(3)	-0.1006(2)	-0.2849(2)	O6	0.31417(19)	-0.33748(15)	-0.04661(14)
C91	0.0504(3)	-0.3690(2)	-0.0207(2)	O7	0.39432(18)	-0.23620(15)	-0.12088(15)
C92	0.5032(3)	-0.2433(2)	-0.2285(2)	O8	0.24241(18)	-0.16793(15)	-0.17281(14)
C95	0.7431(2)	-0.3523(2)	0.15446(19)	O9	0.65710(18)	-0.33659(15)	-0.31896(15)
C97	0.5473(3)	-0.1725(2)	-0.0883(2)	O98	0.18224(18)	-0.13520(16)	-0.25844(14)

[Dy(hfac)₃(TEMPO-methacrylate)]_n (12)Table A7.5 Atomic parameters for **12**.

Atom	x/a	y/b	z/c	Atom	x/a	y/b	z/c
C1	1.0693(13)	0.2726(8)	0.6855(8)	F1	0.6819(19)	-0.0284(12)	0.5384(8)
C110	1.0722(10)	0.0658(6)	0.8420(5)	F14	0.5545(11)	0.2245(6)	0.9309(4)
C111	1.1125(12)	0.1163(7)	0.8965(5)	F15	1.1711(7)	0.0391(5)	0.6159(4)
C2	0.7643(10)	0.4139(6)	0.7315(6)	F19	0.6001(10)	-0.1139(5)	0.7959(5)
C25	1.0047(11)	0.3287(6)	0.7264(7)	F2	0.628(2)	-0.1017(8)	0.6098(9)
C38	0.6649(11)	0.1180(6)	0.8983(5)	F20	0.2835(9)	0.1102(6)	0.7359(7)
C39	1.0912(13)	0.3455(8)	0.7873(8)	F21	0.3248(14)	0.1827(9)	0.6622(9)
C41	0.6131(14)	-0.0832(7)	0.8561(7)	F22	0.3748(9)	0.2064(8)	0.7614(10)
C48	1.0814(11)	0.0601(7)	0.5722(5)	F23	0.4999(8)	-0.0884(4)	0.8873(5)
C5	0.4972(11)	0.1154(8)	0.7074(7)	F24	0.5557(11)	0.1395(5)	1.0042(4)
C52	0.6200(15)	0.1703(7)	0.9558(6)	F25	0.7222(11)	0.2007(6)	0.9849(5)

A7 Additional structural information

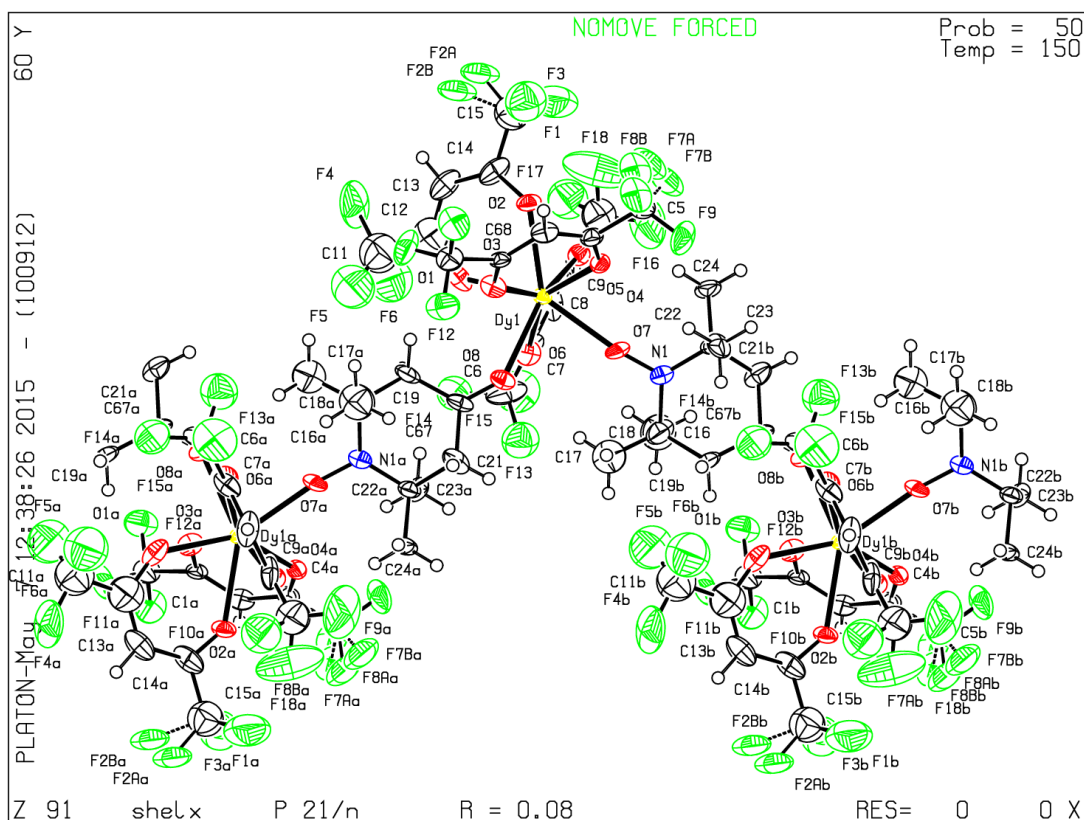
C63	0.730(2)	0.2401(11)	0.5436(7)	F27	0.7806(16)	0.2471(8)	0.4843(5)
C68	1.2357(17)	0.098(1)	0.9326(9)	F28	0.730(2)	0.3044(7)	0.5683(6)
C70	0.9788(11)	0.3963(7)	0.6830(6)	F29	0.6202(17)	0.2240(14)	0.5332(11)
C78	0.3695(13)	0.1543(7)	0.7187(9)	F3	0.4961(14)	-0.0486(11)	0.5618(9)
C79	0.5024(14)	0.0623(10)	0.6544(9)	F30	1.1307(14)	0.0915(9)	0.5216(8)
C80	0.7737(10)	0.3451(6)	0.7774(6)	F31	1.0452(11)	-0.0041(6)	0.5474(6)
C81	0.6512(10)	0.3022(6)	0.7712(6)	F8	0.6910(9)	-0.1217(4)	0.8914(5)
C82	0.8014(14)	0.3623(7)	0.8521(6)	N1	0.8810(7)	0.2983(4)	0.7505(5)
C84	0.8888(11)	0.4510(6)	0.7158(6)	O1	0.7333(7)	0.0064(4)	0.8021(3)
C85	0.8022(16)	0.1863(7)	0.5897(6)	O2	0.7401(7)	0.1465(4)	0.8575(3)
C87	1.0448(13)	0.1725(7)	0.9107(6)	O3	0.7580(8)	0.1850(4)	0.6487(4)
C9	0.6558(11)	-0.0034(6)	0.8495(5)	O4	0.9592(7)	0.0868(4)	0.6674(3)
C90	0.9738(13)	0.1007(8)	0.6049(6)	O5	0.8814(7)	0.2306(4)	0.7682(4)
C91	0.9007(15)	0.1468(7)	0.5633(6)	O6	0.9773(7)	0.0752(4)	0.8070(3)
C94	0.6101(15)	0.0246(8)	0.6382(7)	O7	0.7155(8)	0.0301(4)	0.6652(4)
C96	0.605(2)	-0.0344(12)	0.5826(10)	O8	0.5825(6)	0.1315(4)	0.7455(4)
C99	0.6135(12)	0.0491(7)	0.8979(6)	O9	1.1436(7)	0.0075(4)	0.8341(4)
Dy1	0.79874(4)	0.11352(2)	0.74613(2)	F1	0.6819(19)	-0.0284(12)	0.5384(8)

[Ce(hfac)₃(TEMPO-OCOPh)]_n (13)Table A7.6 Atomic parameters for **13**.

Atom	x/a	y/b	z/c	Atom	x/a	y/b	z/c
C16	-0.3531(4)	0.28659(19)	0.32861(19)	F1	0.2684(3)	0.03589(16)	0.27008(18)
C21	0.1283(4)	0.34542(19)	0.23983(18)	F10	0.2617(3)	0.1026(2)	0.13610(15)
C22	-0.0793(4)	0.1373(2)	0.46640(19)	F11	0.4084(4)	0.17936(18)	0.15499(15)
C23	-0.0994(4)	0.07854(19)	0.3549(2)	F12	0.4663(4)	0.08354(19)	0.17976(16)
C24	0.3244(4)	0.10658(19)	0.37886(19)	F13	0.1748(3)	0.44544(13)	0.18419(14)
C26	0.0356(4)	0.3307(2)	0.18158(18)	F14	0.1807(4)	0.44376(15)	0.29769(15)
C27	-0.4815(4)	0.29939(18)	0.3697(2)	F15	0.3427(3)	0.40027(15)	0.24364(19)
C28	-0.2186(4)	0.36795(18)	0.41954(19)	F16	0.0509(4)	0.2401(2)	0.05728(14)
C30	0.2057(5)	0.4094(2)	0.2413(2)	F17	0.1932(3)	0.31444(16)	0.08199(15)
C33	-0.0392(4)	0.27351(19)	0.17730(19)	F18	0.2285(3)	0.21841(15)	0.11473(14)
C35	-0.4844(4)	0.36592(19)	0.40225(19)	F2	0.0661(3)	0.00452(13)	0.27186(15)
C36	-0.3562(4)	0.37418(19)	0.45466(18)	F3	0.1987(5)	0.02778(15)	0.35368(17)
C38	0.3626(5)	0.1250(2)	0.1807(2)	F4	0.1381(7)	0.0840(2)	0.57072(18)

A7 Additional structural information

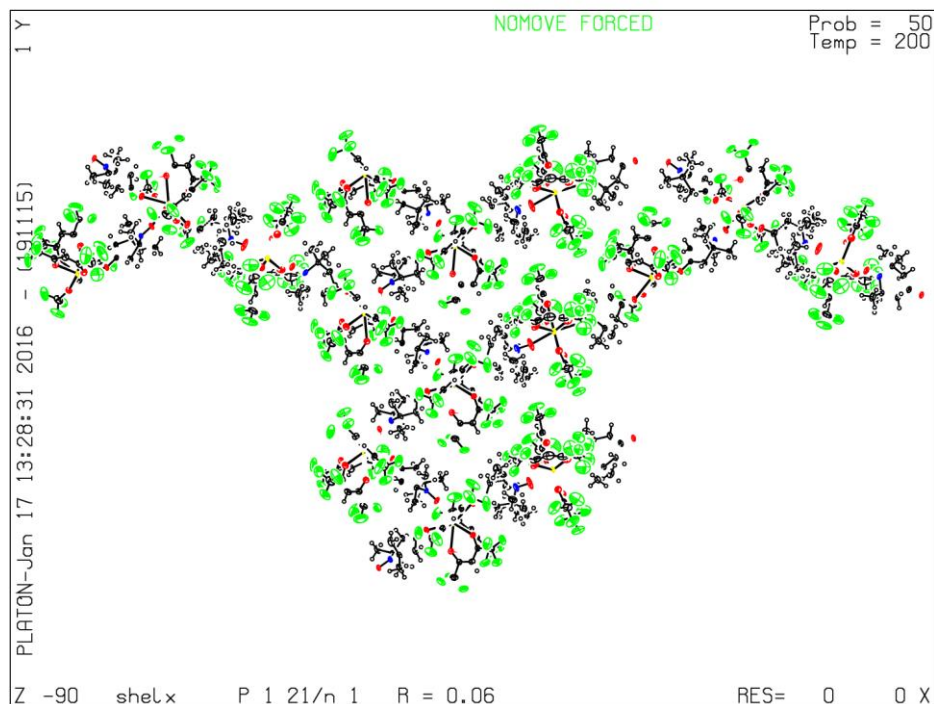
C40	0.3676(4)	0.09778(19)	0.3111(2)	F5	0.0170(5)	0.1678(2)	0.58455(14)
C42	-0.6441(5)	0.4296(2)	0.4668(2)	F6	0.2248(5)	0.1736(4)	0.5503(2)
C44	-0.0969(4)	0.3582(2)	0.4771(2)	F7	0.3110(4)	0.0436(2)	0.4816(2)
C45	-0.1584(5)	0.0191(2)	0.3138(2)	F8	0.4796(4)	0.10833(15)	0.48175(15)
C46	0.3111(4)	0.13522(19)	0.25477(19)	F9	0.4820(4)	0.02351(15)	0.42056(15)
C47	-0.6072(5)	0.4303(2)	0.5443(3)	N1	0.2249(3)	0.30884(15)	0.37282(14)
C48	-0.1169(5)	0.0821(2)	0.4273(2)	O1	0.1938(3)	0.27333(15)	0.43320(14)
C50	-0.1887(5)	0.4264(2)	0.3733(2)	O2	0.1590(3)	0.31168(13)	0.29433(12)
C53	-0.1111(7)	0.1397(3)	0.5448(2)	O3	0.0414(3)	0.22950(12)	0.22237(13)
C54	0.3995(5)	0.0694(2)	0.4411(2)	O4	0.1073(3)	0.29045(13)	0.35147(13)
C59	-0.1303(5)	0.2611(2)	0.1072(2)	O5	0.0251(3)	0.18729(14)	0.44459(13)
C62	-0.3384(4)	0.21399(19)	0.3169(2)	O6	0.0457(3)	0.11942(13)	0.31670(12)
C65	-0.5806(6)	0.4283(3)	0.6059(3)	O7	0.2323(3)	0.14436(14)	0.39699(13)
C67	-0.3618(4)	0.3218(2)	0.25704(19)	O8	0.2216(3)	0.17867(14)	0.25675(13)
Dy	0.07156(2)	0.21654(2)	0.33824(2)	O9	0.6126(3)	0.36880(13)	0.43643(14)

[Dy(hfac)₃(Oxo-TEMPO)]_n (14)Table A7.7 Atomic parameters for **14**.

Atom	x/a	y/b	z/c	Atom	x/a	y/b	z/c
C1	0.4120(12)	0.1169(8)	0.9779(4)	F12	0.5202(8)	0.1064(6)	0.9445(3)
C10	-0.3848(19)	0.3624(14)	0.8520(8)	F13	-0.0764(11)	0.2357(8)	0.6484(5)
C11	-0.149(2)	-0.0020(14)	0.8572(10)	F14	-0.1674(11)	0.1254(7)	0.6838(4)
C12	-0.094(2)	0.0836(12)	0.8915(8)	F15	-0.2997(11)	0.2302(7)	0.6568(4)
C13	-0.1309(13)	0.1071(10)	0.9447(6)	F16	-0.4004(16)	0.4431(10)	0.8410(9)
C14	-0.0857(12)	0.1887(10)	0.9721(6)	F17	-0.5021(12)	0.3102(9)	0.8449(5)
C15	-0.143(2)	0.2175(13)	1.0306(9)	F18	-0.3864(11)	0.3576(15)	0.9071(6)
C16	0.0321(19)	0.4648(13)	0.6841(8)	F2A	-0.2340(16)	0.1633(12)	1.0572(5)
C17	0.2481(17)	0.3841(12)	0.7027(7)	F2B	-0.162(3)	0.1255(13)	1.0521(9)
C18	0.1773(15)	0.4679(9)	0.7173(5)	F3	-0.0378(14)	0.2402(8)	1.0681(6)
C19	0.2366(14)	0.0480(8)	0.7979(5)	F4	-0.2383(12)	-0.0437(7)	0.8957(7)

A7 Additional structural information

C21	0.3858(11)	0.1299(9)	0.7265(5)	F5	-0.0622(15)	-0.0448(10)	0.8356(6)
C22	0.1431(11)	0.5529(7)	0.8147(4)	F6	-0.2131(15)	0.017(1)	0.8101(6)
C23	0.2920(13)	0.5649(8)	0.8484(4)	F7A	0.169(2)	0.4460(14)	1.0407(9)
C24	0.0257(15)	0.5455(9)	0.8568(6)	F7B	0.139(4)	0.475(2)	1.0138(15)
C3	0.3326(12)	0.2742(7)	0.9931(4)	F8A	0.3968(18)	0.4256(11)	1.0542(6)
C4	0.2687(11)	0.3524(7)	0.9735(4)	F8B	0.312(3)	0.4240(17)	1.065(1)
C5	0.2787(14)	0.4356(9)	1.0123(5)	F9	0.3280(12)	0.5038(5)	0.9870(3)
C6	-0.1753(15)	0.2114(13)	0.6832(5)	N1	0.1517(8)	0.4704(6)	0.7806(3)
C67	0.2863(10)	0.1356(8)	0.7750(4)	O1	-0.0221(7)	0.1316(5)	0.8572(4)
C68	0.3283(10)	0.2002(7)	0.9585(4)	O2	-0.0095(8)	0.2466(5)	0.9516(3)
C7	-0.1531(12)	0.2508(8)	0.7445(5)	O3	0.2598(7)	0.1893(5)	0.9105(3)
C8	-0.2680(13)	0.2860(8)	0.7716(7)	O4	0.1984(7)	0.3663(4)	0.9258(3)
C9	-0.2550(14)	0.3225(7)	0.8279(5)	O5	-0.1430(7)	0.3303(5)	0.8586(3)
Dy1	0.08310(4)	0.27035(3)	0.85927(2)	O6	-0.0294(9)	0.2467(6)	0.7650(4)
F1	-0.2388(19)	0.2873(10)	1.0224(7)	O7	0.1371(8)	0.3962(5)	0.8065(3)
F10	0.4669(9)	0.1237(5)	1.0331(3)	O8	0.2462(7)	0.2062(5)	0.7942(3)
F11	0.3371(9)	0.0439(5)	0.9740(4)				

$[\{\text{Ce}(\text{hfac})_3(\text{Oxo-TEMPO})_4\}_n] \text{ (15)}$
Table A7.8 Atomic parameters for **15**.

Atom	x/a	y/b	z/c	Atom	x/a	y/b	z/c
C098	0.3774(4)	0.85851(11)	0.1783(3)	Ce03	1.11642(2)	0.91122(2)	0.27148(2)
C0AA	0.7760(5)	0.56123(12)	0.3816(4)	F013	0.5038(3)	0.66853(7)	0.3957(2)
C1	1.0327(17)	0.6570(5)	0.1968(12)	F031	1.3538(3)	0.93837(9)	0.5531(2)
C10	0.4801(5)	0.86215(12)	0.3577(4)	F035	0.3756(3)	0.68623(8)	0.0515(2)
C100	1.1096(10)	0.6337(3)	0.4932(8)	F036	0.3088(3)	0.69826(8)	0.1513(2)
C102	0.4875(4)	0.81918(10)	0.2349(3)	F037	0.1891(3)	0.77492(8)	0.2964(2)
C103	1.2590(5)	0.60006(11)	0.2277(4)	F039	0.5284(4)	0.78215(9)	0.5774(2)
C104	1.0257(5)	0.90864(12)	0.0889(3)	F040	0.1361(3)	0.73559(8)	0.2808(2)
C106	0.7571(5)	0.65019(12)	0.2780(4)	F041	0.4245(4)	0.79291(9)	0.4855(2)
C107	0.7697(4)	0.82231(12)	0.3757(3)	F042	0.4875(4)	0.69450(8)	0.4856(2)
C108	1.1910(5)	0.46345(11)	0.2662(3)	F043	1.0817(4)	0.84990(8)	0.5063(2)
C11	0.4854(4)	0.8422(1)	0.1824(3)	F044	0.6483(4)	0.78268(9)	0.0058(2)
C110	0.3314(4)	0.74329(11)	0.2951(3)	F048	0.5658(4)	0.81466(8)	0.5100(2)
C111	1.3294(6)	0.94456(15)	0.4828(4)	F052	0.3463(3)	0.67782(8)	0.4322(2)

A7 Additional structural information

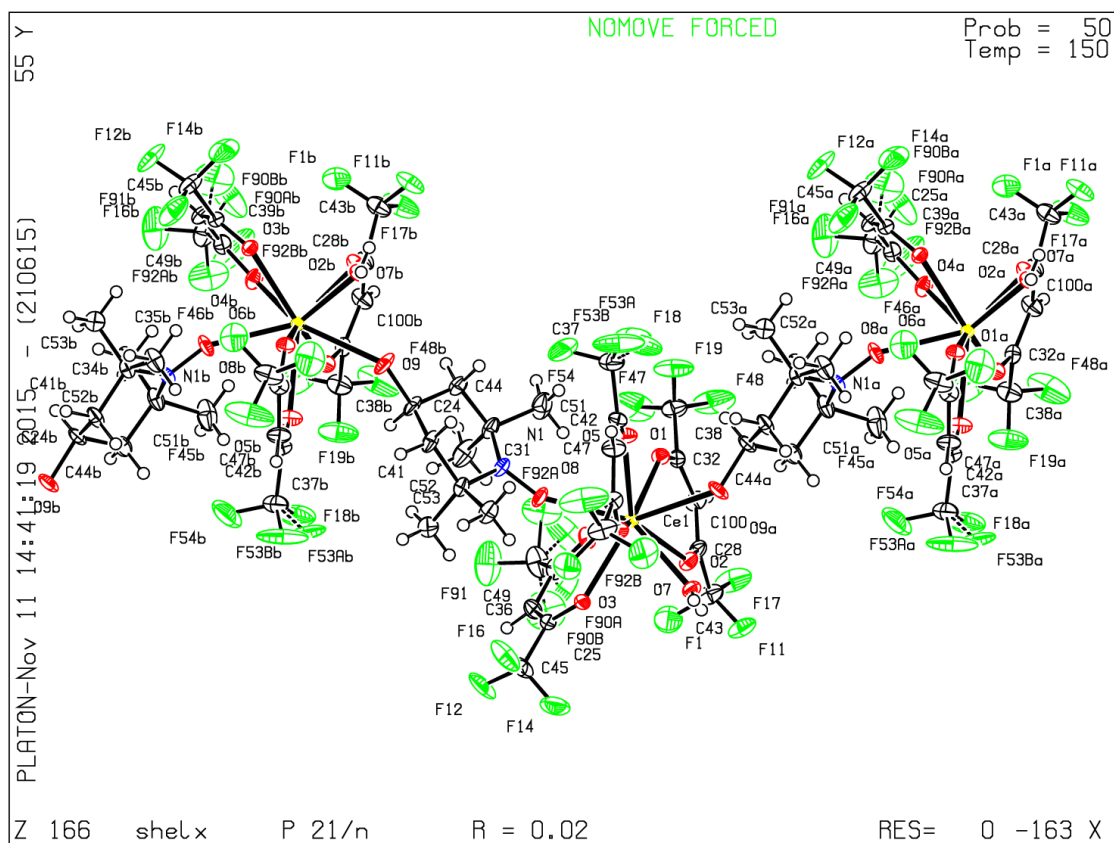
C112	0.4888(4)	0.71322(11)	0.1337(3)	F053	0.8279(4)	0.97789(9)	0.4418(3)
C113	0.8341(5)	0.91923(12)	0.2840(3)	F054	0.4331(4)	0.66909(8)	0.1521(3)
C114	0.4011(5)	0.69159(12)	0.1224(3)	F057	0.5563(3)	0.53661(10)	0.2166(2)
C115	0.9258(7)	0.96854(17)	0.4330(5)	F058	1.2869(4)	0.96892(9)	0.4817(3)
C117	0.3398(5)	0.72120(11)	0.3400(3)	F059	0.6176(4)	0.74620(9)	-0.0504(2)
C118	0.8363(5)	0.93822(12)	0.3378(4)	F060	0.8327(4)	0.72637(9)	0.5596(2)
C12	0.2846(5)	0.84382(12)	0.1357(3)	F063	1.4223(4)	0.94591(10)	0.4489(2)
C120	0.7048(5)	0.55292(11)	0.3251(4)	F064	0.2120(3)	0.75597(10)	0.1948(2)
C122	0.7304(5)	0.55520(12)	0.2520(4)	F066	0.7127(3)	0.88711(9)	0.2320(4)
C123	0.6668(5)	0.75545(11)	0.4895(3)	F1	0.6892(4)	0.52717(13)	0.1530(3)
C124	0.6488(6)	0.54616(18)	0.1917(5)	F10	0.6401(4)	0.91541(13)	0.2933(4)
C126	1.1341(6)	0.59867(13)	0.1197(4)	F11	0.6886(5)	0.92583(12)	0.1982(4)
C127	0.7362(5)	0.74042(11)	0.4471(3)	F12	1.0065(5)	0.99845(9)	0.1401(4)
C13	0.7933(12)	0.6510(3)	0.3719(8)	F122	1.1874(8)	0.64816(19)	0.4648(6)
C130	0.5341(5)	0.72473(12)	0.0731(3)	F123	1.0109(4)	0.64894(8)	0.4926(2)
C131	0.5276(6)	0.79029(14)	0.5084(4)	F124	1.1492(7)	0.62918(19)	0.5636(5)
C132	0.9921(5)	0.95216(12)	0.1373(4)	F13	0.9631(5)	0.95778(11)	0.4947(3)
C133	0.2903(5)	0.84658(12)	0.3746(3)	F14	0.9903(4)	0.98912(10)	0.4210(3)
C134	0.3995(5)	0.88561(11)	0.1424(3)	F15	0.9065(4)	0.98381(9)	0.0544(3)
C135	1.2374(5)	0.48212(11)	0.2118(4)	F16	0.8532(5)	0.98264(11)	0.1612(4)
C136	0.4427(5)	0.68775(12)	0.4198(4)	F17	1.1138(8)	0.66216(16)	0.4088(5)
C137	0.8148(6)	0.72101(15)	0.4888(4)	F18	1.1691(10)	0.6452(3)	0.5156(7)
C139	0.6578(6)	0.75683(16)	0.0127(4)	F2	0.6190(4)	0.56541(12)	0.1467(3)
C14	0.7011(13)	0.6750(3)	0.2601(9)	F23	0.7749(5)	0.69678(9)	0.4845(3)
C140	1.0432(6)	0.87474(14)	0.5076(4)	F24	0.9103(4)	0.72040(11)	0.4604(3)
C146	0.7238(5)	0.91067(15)	0.2483(5)	F25	1.1973(11)	0.52023(19)	0.4675(5)
C148	1.3749(6)	0.60564(17)	0.2607(5)	F25A	1.2561(12)	0.5369(5)	0.4684(8)
C149	1.2381(5)	0.60374(12)	0.1526(4)	F26	1.1887(10)	0.5509(3)	0.5572(6)
C15	0.9337(5)	0.94829(12)	0.3691(3)	F26A	1.1782(13)	0.5366(3)	0.5658(6)
C151	0.7265(11)	0.6323(2)	0.3298(8)	F28	0.7514(5)	0.57796(11)	0.4994(3)
C152	1.2813(5)	0.52351(13)	0.2863(4)	F29	1.1380(6)	0.58151(16)	0.0012(3)
C153	1.2306(6)	0.52637(12)	0.1508(4)	F3	0.6488(4)	0.54632(10)	0.4676(3)

A7 Additional structural information

C154	0.8976(6)	0.69102(13)	0.2213(5)	F30	1.0168(5)	0.61011(13)	0.0171(3)
C155	1.1837(5)	0.90928(11)	0.4865(3)	F31	1.1805(5)	0.62172(14)	0.0119(3)
C156	0.7392(12)	0.6794(3)	0.2899(9)	F33	1.0468(8)	0.5293(3)	0.5161(7)
C157	0.9739(5)	0.93313(13)	0.0838(4)	F33A	1.0993(18)	0.5179(3)	0.4765(10)
C158	0.9350(5)	0.50335(12)	0.3128(4)	F4	0.8127(5)	0.53935(13)	0.4934(3)
C159	1.1239(7)	0.5888(2)	0.4807(5)	F5	1.4454(4)	0.61096(12)	0.2116(3)
C16	0.9617(5)	0.80402(12)	0.3768(3)	F6	1.4135(4)	0.58645(11)	0.3019(3)
C160	1.1150(8)	0.6032(2)	0.0366(5)	F7	1.3753(4)	0.62662(12)	0.3025(3)
C164	0.9644(6)	0.48094(13)	0.1930(4)	F78	0.9494(6)	0.89753(11)	-0.0307(3)
C167	1.1151(5)	0.56420(18)	0.4478(5)	F79	0.9426(5)	0.86870(11)	0.0510(3)
C17	0.9092(4)	0.84524(10)	0.3027(3)	F8	0.9392(4)	0.87301(10)	0.4881(3)
C171	1.1464(9)	0.5395(2)	0.4955(5)	F80	1.0903(5)	0.87750(12)	0.0059(3)
C172	0.7049(12)	0.6424(3)	0.1940(8)	F800	0.7651(4)	0.75191(11)	0.0165(2)
C18	0.8885(4)	0.80421(10)	0.1912(3)	F9	1.0504(5)	0.88244(9)	0.5770(2)
C19	0.9123(4)	0.77645(10)	0.1624(3)	N1	1.0942(4)	0.51462(9)	0.2410(3)
C1A	1.0062(11)	0.6781(3)	0.3294(8)	N2	0.8663(4)	0.64538(10)	0.2539(3)
C1AA	0.5904(5)	0.77298(11)	0.4571(3)	N3	0.8405(3)	0.80168(8)	0.2654(2)
C1B	1.0946(15)	0.6439(4)	0.4567(11)	N9	0.3427(3)	0.86350(8)	0.2548(2)
C2	0.7868(5)	0.69876(12)	0.2433(3)	O1	1.0485(3)	0.59146(8)	0.1508(2)
C20	0.8055(4)	0.81868(11)	0.1407(3)	O10	0.5101(3)	0.71841(7)	0.2006(2)
C21	0.9974(4)	0.81966(10)	0.2006(3)	O11	0.6339(3)	0.75826(7)	0.13898(19)
C22	0.8708(4)	0.81843(10)	0.3307(3)	O12	0.7708(3)	0.78321(7)	0.2736(2)
C23	0.6049(5)	0.74601(12)	0.0812(3)	O13	0.5501(3)	0.80080(7)	0.2268(2)
C24	1.2106(5)	0.51165(12)	0.2229(4)	O14	0.5701(3)	0.77753(7)	0.3900(2)
C25	1.0206(5)	0.49255(11)	0.2625(4)	O15	0.7414(3)	0.73990(7)	0.3793(2)
C26	1.0939(5)	0.47254(11)	0.3060(4)	O16	0.5331(3)	0.71992(7)	0.35488(19)
C3	0.9121(10)	0.6626(2)	0.2005(8)	O17	0.4062(3)	0.75817(7)	0.27412(19)
C3A	0.9620(11)	0.6695(2)	0.2528(8)	O18	1.0798(3)	0.88844(7)	0.3888(2)
C4	1.0901(6)	0.61072(19)	0.4409(6)	O19	1.0658(3)	0.86111(7)	0.2430(2)
C5	0.6721(11)	0.6271(3)	0.2814(9)	O2	0.8977(4)	0.62129(9)	0.2491(3)
C6	0.8626(11)	0.6604(3)	0.1210(7)	O20	1.0894(3)	0.90039(7)	0.1402(2)
C60	0.7473(6)	0.55608(18)	0.4604(5)	O21	1.0427(3)	0.94991(7)	0.1985(2)

A7 Additional structural information

C68	0.2164(5)	0.75209(14)	0.2660(4)	O22	0.9135(3)	0.90678(7)	0.2581(2)
C69	1.0031(7)	0.88856(17)	0.0283(4)	O23	1.0291(3)	0.94302(7)	0.3535(2)
C6A	1.056(2)	0.6603(5)	0.2182(12)	O24	1.2484(3)	0.92646(7)	0.3746(2)
C7	0.4397(5)	0.71152(10)	0.3670(3)	O3	1.0455(4)	0.61268(9)	0.3764(3)
C8	0.4091(5)	0.82005(11)	0.2955(3)	O33	1.2300(3)	0.44133(7)	0.2771(2)
C80	0.9967(4)	0.84399(10)	0.2490(3)	O4	1.0873(3)	0.55743(8)	0.3824(2)
C81	1.1062(5)	0.89225(11)	0.4557(3)	O5	1.0509(3)	0.53772(7)	0.2324(2)
C82	1.2493(5)	0.92521(12)	0.4432(3)	O6	0.8683(3)	0.57201(7)	0.3762(2)
C9	0.3813(4)	0.84794(11)	0.3204(3)	O60	0.2820(3)	0.88377(7)	0.2649(2)
C96	0.9405(7)	0.97994(15)	0.1250(5)	O7	0.8173(3)	0.56419(8)	0.2268(2)
Ce01	0.99719(3)	0.58077(2)	0.27758(2)	O8	1.1931(3)	0.59293(7)	0.2733(2)
Ce02	0.60844(2)	0.75401(2)	0.27382(2)	O9	0.7515(3)	0.72087(7)	0.2356(2)

[Ce(hfac)₃(TEMPO-OH)(H₂O)]_n (16)Table A7.9 Atomic parameters for **16**.

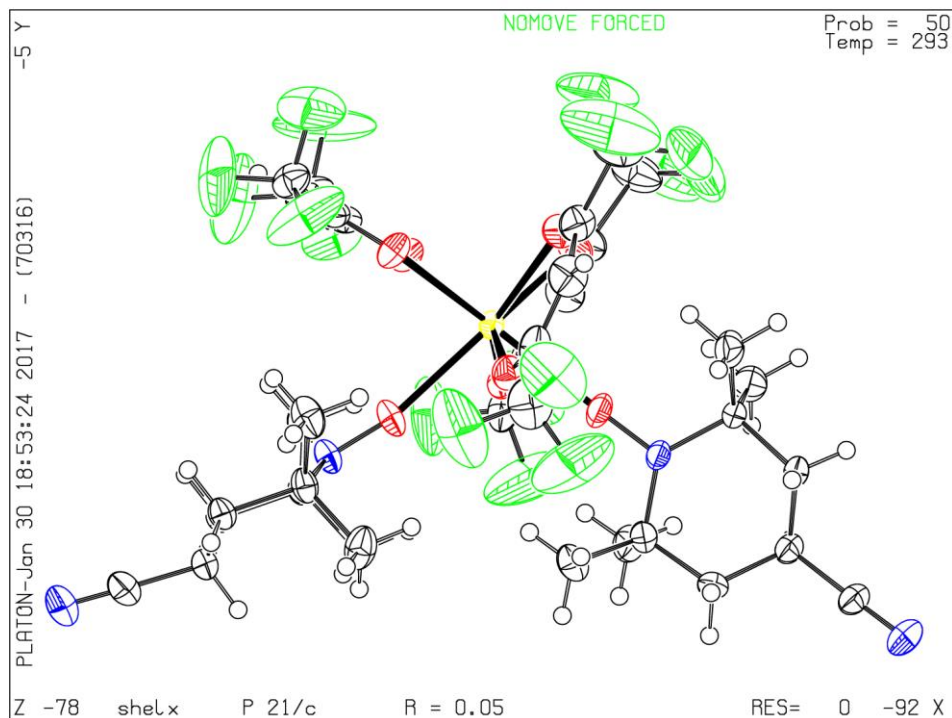
Atom	x/a	y/b	z/c	Atom	x/a	y/b	z/c
C24	1.2334(2)	0.27374(13)	0.93601(16)	F47	0.6002(3)	0.23161(13)	0.79315(14)
C31	1.0365(2)	0.23255(14)	0.86851(16)	F48	0.47264(15)	0.23822(11)	0.6788(2)
C34	1.21576(19)	0.17045(13)	0.82751(15)	F53A	1.0812(12)	0.3866(5)	0.5331(10)
C35	1.2516(2)	0.14725(15)	0.73973(17)	F53B	1.0328(12)	0.3827(6)	0.5054(9)
C41	1.2816(2)	0.23583(14)	0.86272(16)	F54	1.0930(2)	0.36650(11)	0.6603(2)
C44	1.1127(2)	0.29455(14)	0.90111(16)	F90A	0.7249(10)	-0.0183(7)	0.8898(6)
C51	0.9256(2)	0.25901(18)	0.8140(2)	F90B	0.7693(11)	-0.0467(7)	0.8989(7)
C52	1.0123(2)	0.18783(17)	0.94728(18)	F91	0.87230(18)	0.02022(15)	0.97453(12)
C53	1.2344(2)	0.11001(14)	0.89551(18)	F92A	0.7616(8)	0.0898(4)	0.9137(5)
Ce1	0.89087(2)	0.11595(2)	0.61732(2)	F92B	0.7144(13)	0.0562(11)	0.8842(10)
F1	0.61364(17)	-0.05296(10)	0.69795(13)	N1	1.09360(16)	0.18913(10)	0.80680(13)
F10	1.19055(17)	0.11785(11)	0.40179(12)	O1	0.73267(12)	0.18839(8)	0.64568(10)

A7 Additional structural information

F11	0.55539(13)	-0.05609(8)	0.55570(12)	O2	0.71140(12)	0.04653(9)	0.58948(11)
F12	1.12496(17)	-0.11352(10)	0.82961(12)	O3	0.99506(13)	0.00705(8)	0.66988(10)
F14	1.06908(18)	-0.13242(9)	0.68822(13)	O4	0.83294(13)	0.07316(9)	0.75957(10)
F16	1.19582(14)	-0.05583(11)	0.73073(14)	O5	0.94774(14)	0.24049(9)	0.60067(12)
F17	0.45405(14)	-0.00732(9)	0.64103(14)	O6	1.05851(13)	0.12424(8)	0.54289(10)
F18	0.92734(16)	0.37652(9)	0.59213(17)	O7	0.87755(16)	0.0330(1)	0.47866(12)
F19	0.61963(16)	0.29697(9)	0.68546(15)	O8	1.03056(13)	0.14761(9)	0.75226(11)
F45	1.29816(18)	0.19320(11)	0.48018(18)	O9	1.29896(16)	0.33524(9)	0.96442(11)
F46	1.27166(13)	0.09398(10)	0.53568(12)				

A7 Additional structural information

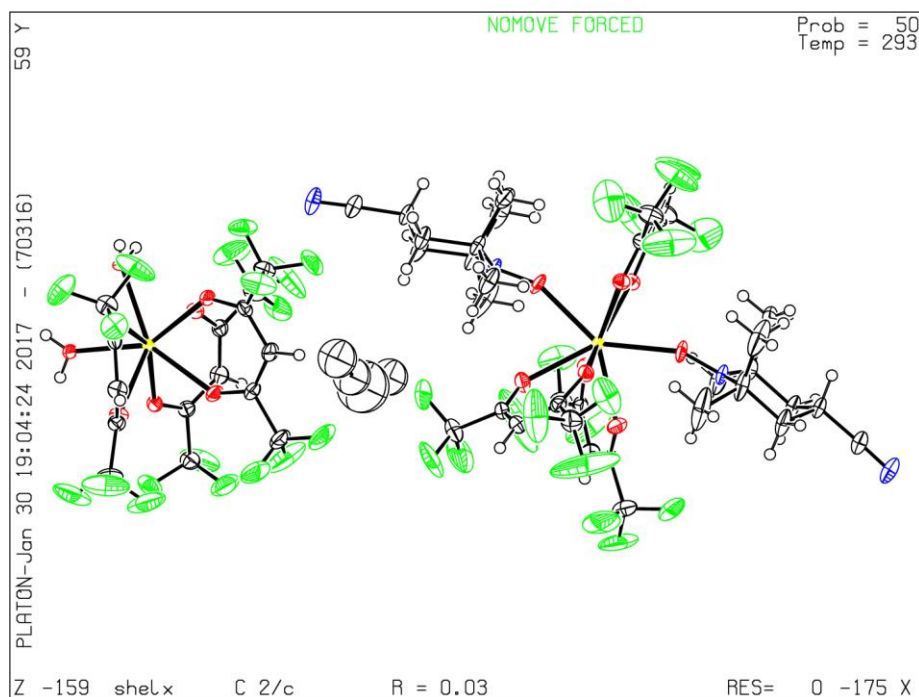
C7	0.4248(2)	0.75	0.4056(4)	O2	0.48137(14)	0.75	0.8527(3)
C8	0.62810(19)	0.75	1.1228(4)	O3	0.51325(12)	0.75	0.5646(2)
C9	0.3696(3)	0.75	0.9152(5)	O4	0.55015(10)	0.62512(13)	0.7524(2)
Dy01	0.58941(2)	0.75	0.75115(2)	O5	0.58440(13)	0.75	1.0023(3)
F1	0.51569(15)	0.47651(16)	0.6507(3)	O6	0.65540(12)	0.75	0.5537(2)
F10	0.78933(11)	0.55989(15)	0.8030(2)				

[Ce(hfac)₃(TEMPO-CN)₂] (20)Table A7.11 Atomic parameters for **20**.

Atom	x/a	y/b	z/c	Atom	x/a	y/b	z/c
C022	0.2583(8)	0.2585(5)	0.5302(3)	C8	-0.0121(9)	0.0918(6)	0.2672(3)
C025	-0.0242(9)	0.2508(5)	0.5396(3)	C9	-0.2046(10)	0.3316(6)	0.3139(4)
C027	0.2431(8)	0.0382(5)	0.3975(3)	Ce01	0.24614(4)	0.24298(2)	0.36816(2)
C029	0.0111(9)	0.2250(5)	0.4906(3)	F1	0.0619(12)	-0.0316(8)	0.4161(4)
C031	0.0857(9)	0.2345(5)	0.5826(3)	F10	0.4525(9)	0.3895(6)	0.2257(3)
C032	0.3293(8)	0.2234(5)	0.2364(3)	F11	0.2747(9)	0.4362(6)	0.2351(4)
C040	0.0054(9)	0.1334(6)	0.4848(4)	F12	0.2891(10)	0.3568(6)	0.1760(4)
C045	0.4400(9)	0.4092(6)	0.4047(4)	F13	0.5956(13)	0.5155(9)	0.4077(5)
C046	0.3518(10)	0.3234(6)	0.5176(4)	F14	0.6216(15)	0.4334(10)	0.4638(6)
C048	0.0436(10)	0.2555(5)	0.6286(4)	F15	0.6651(11)	0.3958(7)	0.4000(4)
C050	0.2119(10)	0.4467(6)	0.3935(4)	F16	0.1578(10)	0.5844(7)	0.4038(4)
C052	0.3295(9)	0.1784(6)	0.5381(4)	F17	0.0228(12)	0.5183(7)	0.3566(4)
C055	-0.0798(12)	0.2648(7)	0.4491(5)	F18	0.0478(12)	0.4966(8)	0.4323(5)

A7 Additional structural information

C058	0.3761(10)	0.0289(6)	0.4140(4)	F2	0.1092(10)	-0.0539(6)	0.3477(4)
C059	0.4574(10)	0.0955(6)	0.4203(4)	F3	0.2211(11)	-0.1050(7)	0.4072(4)
C060	0.3424(10)	0.4670(7)	0.4046(4)	F4	0.6406(10)	0.1285(7)	0.4826(4)
C061	0.3570(11)	0.0762(7)	0.2418(4)	F5	0.6356(12)	0.0132(8)	0.4609(5)
C062	0.1581(9)	-0.0382(6)	0.3931(4)	F6	0.6808(9)	0.1069(6)	0.4131(4)
C063	0.3266(9)	0.3717(6)	0.2220(4)	F7	0.3122(7)	0.0131(5)	0.2623(3)
C064	0.6030(13)	0.0806(8)	0.4421(5)	F8	0.4784(10)	0.0671(7)	0.2389(4)
C065	0.1109(12)	0.5115(8)	0.3968(5)	F9	0.3042(12)	0.0703(8)	0.1950(5)
C066	0.5811(12)	0.4369(8)	0.4192(5)	N1	0.1480(7)	0.2509(4)	0.4884(3)
C1	0.3123(8)	0.2992(5)	0.2551(3)	N2	-0.0656(7)	0.2310(4)	0.2841(3)
C10	-0.0366(10)	0.3715(6)	0.2633(4)	N3	0.0154(10)	0.2701(6)	0.6651(4)
C13	-0.2358(8)	0.2991(5)	0.2242(3)	N4	-0.4713(10)	0.2125(6)	0.1382(4)
C14	-0.2234(8)	0.1487(5)	0.2259(3)	O1	0.4320(6)	0.1667(4)	0.4114(2)
C15	-0.3164(9)	0.2207(5)	0.2220(3)	O2	0.1797(7)	0.2444(3)	0.4463(3)
C2	0.3314(8)	0.1555(5)	0.2649(3)	O3	0.0351(6)	0.2349(4)	0.3183(2)
C29	-0.4057(10)	0.2167(6)	0.1749(4)	O4	0.3137(6)	0.1514(4)	0.3081(2)
C3	0.2052(8)	0.2853(5)	0.5759(3)	O5	0.2901(6)	0.3171(4)	0.2959(2)
C5	-0.1388(8)	0.3088(5)	0.2716(3)	O6	0.1622(6)	0.3791(4)	0.3811(2)
C6	-0.1248(8)	0.1488(5)	0.2741(3)	O7	0.4258(6)	0.3369(4)	0.3963(2)
C7	-0.1829(9)	0.1217(6)	0.3179(4)	O8	0.1802(5)	0.1010(3)	0.3849(2)

{[Dy(hfac)₃(TEMPO-CN)₂][Dy(hfac)₃(H₂O)₂]₂} (**21**)Table A7.12 Atomic parameters for **21**.

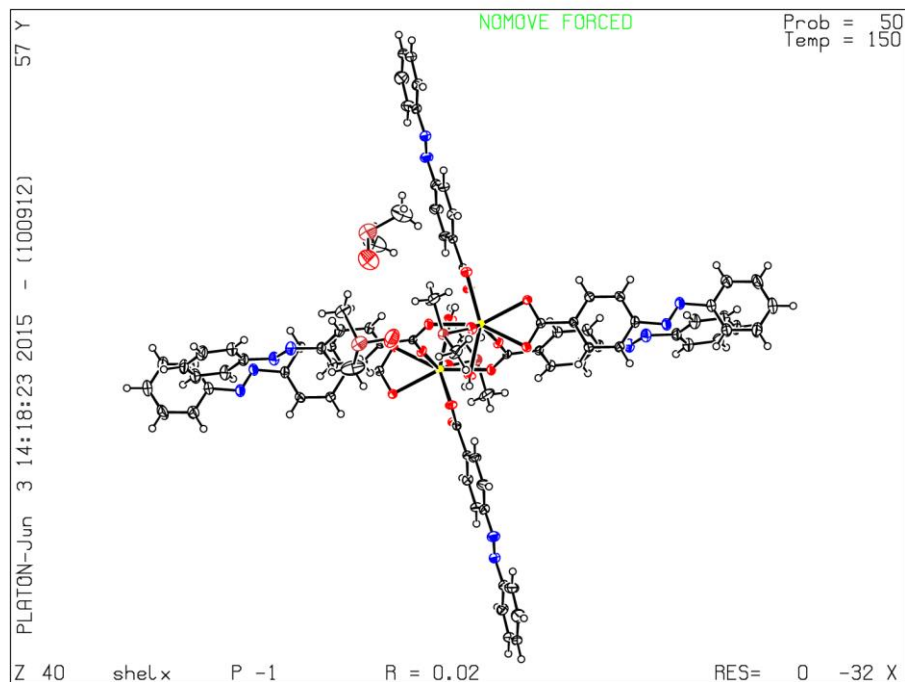
Atom	x/a	y/b	z/c	Atom	x/a	y/b	z/c
C200	0.5688(6)	0.2344(18)	0.5324(9)	F10	0.65779(11)	0.3944(5)	0.7437(3)
C201	0.5430(3)	0.280(1)	0.5321(5)	F13	0.75269(10)	0.4843(3)	0.59980(14)
C202	0.6093(4)	0.2753(12)	0.5399(6)	F14	0.70708(10)	0.4779(3)	0.51568(15)
C29	0.72059(11)	0.3028(3)	0.57771(17)	F2	0.82520(11)	0.2888(3)	0.6485(3)
C3	0.63323(10)	0.6435(5)	0.45007(18)	F20	0.61006(8)	0.3165(3)	0.6880(2)
C300	0.5866(6)	0.248(2)	0.5337(9)	F21	0.6140(1)	-0.1069(3)	0.6961(3)
C36	0.77142(11)	-0.0848(4)	0.63497(18)	F22	0.41694(11)	0.2910(4)	0.10568(16)
C38	0.60279(10)	0.6836(4)	0.39115(17)	F23	0.65705(7)	-0.2094(3)	0.69829(17)
C39	0.64421(11)	0.1101(4)	0.6852(2)	F3	0.86153(8)	0.1627(4)	0.70784(15)
C4	0.80343(10)	0.1011(3)	0.65904(18)	F30	0.40880(13)	0.3775(6)	0.3386(2)
C40	0.63854(11)	-0.1120(4)	0.6752(2)	F31	0.4595(3)	0.3152(7)	0.3909(3)
C41	0.62759(10)	0.6740(4)	0.50753(18)	F32	0.44693(12)	0.4945(4)	0.39146(18)
C42	0.79450(11)	-0.0055(4)	0.62615(18)	F33	0.41984(14)	0.1574(4)	0.1698(2)
C43	0.68634(12)	0.1235(4)	0.54758(19)	F34	0.46386(12)	0.1917(4)	0.1496(2)

A7 Additional structural information

C46	0.45253(10)	0.4191(4)	0.30230(19)	F4	0.73575(12)	-0.2321(4)	0.5696(3)
C48	0.45134(11)	0.3394(4)	0.20799(19)	F40	0.64781(14)	0.0953(4)	0.44278(16)
C49	0.66123(10)	0.0017(4)	0.68971(18)	F41	0.63533(12)	0.0059(5)	0.5096(2)
C51	0.66213(10)	0.2171(4)	0.69581(19)	F42	0.67624(13)	-0.0526(4)	0.4900(2)
C52	0.43808(15)	0.2431(5)	0.1583(3)	F46	0.46490(14)	1.0511(3)	0.3060(3)
C54	0.64229(12)	0.3335(4)	0.6940(3)	F47	0.4615(2)	0.8980(5)	0.3540(3)
C55	0.60247(15)	0.8189(5)	0.3819(2)	F49	0.42478(11)	0.9278(5)	0.2665(3)
C56	0.47971(11)	0.8644(4)	0.27441(19)	F5	0.77511(16)	-0.2918(3)	0.6503(2)
C59	0.44214(14)	0.3998(5)	0.3561(2)	F6	0.78756(14)	-0.2296(4)	0.5780(2)
C63	0.45844(14)	0.9379(4)	0.3016(2)	F7	0.84263(8)	0.1407(3)	0.61139(15)
C68	0.73365(14)	0.4135(4)	0.5548(2)	F8	0.62318(12)	-0.1289(4)	0.61524(17)
C70	0.76817(14)	-0.2109(4)	0.6077(2)	F9	0.64119(15)	0.4014(4)	0.6489(3)
C71	0.44373(11)	0.3286(4)	0.2590(2)	N1	0.56933(8)	0.6465(3)	0.39366(14)
C72	0.83348(11)	0.1750(4)	0.6564(2)	N2	0.68048(11)	0.6068(5)	0.60605(19)
C73	0.65779(12)	0.6376(5)	0.5631(2)	O1	0.69305(7)	-0.0164(2)	0.70301(13)
C74	0.56234(11)	0.6478(6)	0.44988(19)	O10	0.46775(7)	0.5150(3)	0.30292(12)
C80	0.59517(13)	0.6071(5)	0.5050(2)	O11	0.47608(7)	0.7542(2)	0.27732(12)
C86	0.60546(12)	0.6207(5)	0.3367(2)	O12	0.54209(7)	0.6561(3)	0.34296(13)
C89	0.66117(15)	0.0444(5)	0.4961(2)	O2	0.69368(7)	0.2333(3)	0.70668(14)
C93	0.69648(12)	0.2315(4)	0.53254(18)	O3	0.69620(9)	0.0762(3)	0.59905(13)
C94	0.55039(16)	0.7738(8)	0.4589(3)	O4	0.73384(7)	0.2854(2)	0.63385(12)
C96	0.53321(15)	0.5563(9)	0.4407(2)	O5	0.75350(7)	-0.0679(2)	0.66551(13)
C97	0.5	0.9256(5)	0.25	O6	0.79061(7)	0.1429(3)	0.69341(13)
Dy1	0.73617(2)	0.11476(2)	0.69705(2)	O7	0.76580(7)	0.2655(2)	0.76808(13)
Dy2	0.5	0.58640(2)	0.25	O8	0.76435(8)	0.0149(3)	0.79010(12)
F1	0.75250(11)	0.3806(3)	0.52448(18)	O9	0.46789(8)	0.4212(3)	0.19579(14)

A7 Additional structural information

C044	0.3561(4)	-0.0516(4)	0.2243(2)	F21B	0.9628(9)	-0.0022(10)	0.2890(6)
C045	0.6810(4)	-0.0527(4)	0.4135(3)	F22A	1.0520(6)	0.0096(7)	0.1706(4)
C046	0.0169(5)	0.3020(5)	0.4159(3)	F22B	1.032(2)	-0.0132(19)	0.2245(14)
C047	0.6280(5)	-0.5153(4)	0.1239(3)	F3	0.6873(6)	-0.1267(5)	0.0551(3)
C048	0.3611(5)	-0.4748(4)	0.3955(2)	F4	0.7037(5)	0.0294(4)	-0.0383(2)
C049	0.9299(7)	0.1048(7)	0.2156(4)	F5	0.8819(4)	-0.1305(4)	0.0070(2)
C051	0.8274(5)	0.0313(5)	0.1275(3)	N1	0.3624(3)	0.0453(3)	0.2292(2)
C054	0.7477(6)	-0.0460(5)	0.0282(3)	N2	0.4270(3)	-0.4650(3)	0.24146(19)
C1	0.5969(4)	0.0857(4)	0.4281(2)	O1	0.5081(3)	0.1763(3)	0.38765(16)
C2	0.6746(4)	-0.1025(4)	0.3454(3)	O2	0.6022(3)	-0.0381(2)	0.28982(16)
C3	0.1585(4)	0.3813(4)	0.1847(2)	O3	0.5878(3)	0.1164(3)	0.12267(17)
C4	0.0700(4)	0.3701(4)	0.2609(2)	O4	0.6896(3)	0.1775(3)	0.23624(19)
C5	0.3247(4)	-0.3844(4)	0.3132(2)	O5	0.4363(3)	0.4151(2)	0.24379(17)
F002	-0.1146(3)	0.3605(3)	0.40666(17)	O6	0.2881(3)	0.3380(2)	0.17069(15)
F003	0.7039(3)	-0.3139(2)	0.31292(19)	O7	0.2441(3)	0.2607(3)	0.34596(15)
F007	0.8324(4)	-0.3298(3)	0.3946(2)	Tb01	0.46100(2)	0.19594(2)	0.25383(2)

[Dy₂(AZO)₆(DMSO)₂(H₂O)₂]-4DMSO (24)Table A7.14 Atomic parameters for **24**.

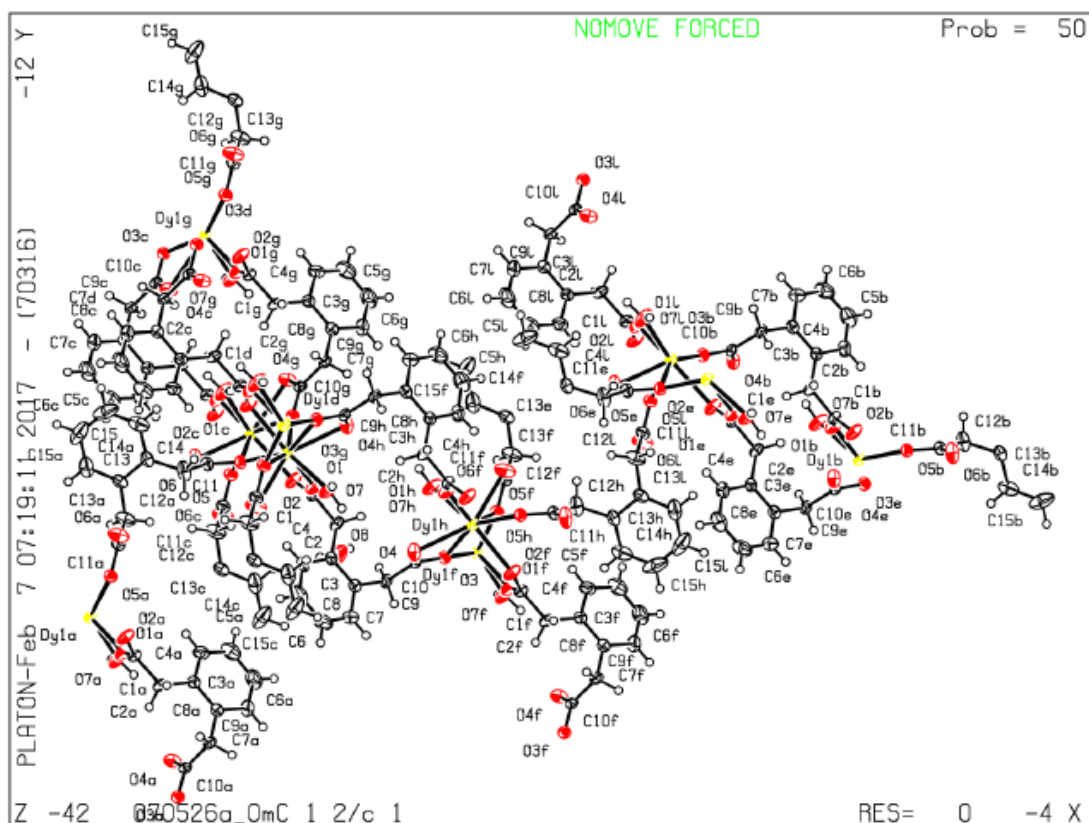
Atom	x/a	y/b	z/c	Atom	x/a	y/b	z/c
C1	-0.5099(3)	0.29529(17)	0.53964(18)	H3	0.363(4)	-0.060(2)	0.5443(18)
C17	-0.0826(3)	-0.07876(15)	0.72765(13)	H38	0.685	0.1381	0.3137
C18	-1.0171(4)	0.62858(19)	0.62540(19)	H39A	0.6005	0.0098	0.7344
C19	-0.9153(4)	0.50367(19)	0.5951(2)	H39B	0.6328	0.0045	0.6481
C2	0.3274(4)	0.1311(2)	0.7204(2)	H39C	0.6358	0.09	0.6653
C20	-1.0417(4)	0.5594(2)	0.6024(2)	H4	0.239(4)	-0.078(2)	0.5213(19)
C22	-0.0388(3)	-0.03179(14)	0.64322(13)	H40	-0.1052	0.3372	0.5854
C24	0.8252(3)	0.44180(17)	-0.01500(15)	H44	0.0042	0.0037	0.7738
C26	-0.1614(3)	-0.15350(16)	0.74756(14)	H45	0.8388	0.2069	0.198
C27	0.5553(3)	0.34846(16)	0.20136(16)	H46	-0.0708	-0.0659	0.9036
C28	-0.3393(3)	0.37816(16)	0.58470(16)	H49	0.6705	0.5403	-0.0431
C29	-0.2245(3)	0.25944(14)	0.54599(14)	H5	1.0514	0.5453	-0.2067
C30	-0.7622(3)	0.51855(17)	0.61160(15)	H50	-0.2654	-0.2436	0.8384
C31	0.5126(3)	0.22892(15)	0.31304(14)	H51	-0.338	-0.2995	1.2396

A7 Additional structural information

C33	0.4065(3)	0.18357(14)	0.38497(14)	H53	-0.5268	-0.3638	1.0336
C34	-0.1798(3)	-0.16015(17)	0.88357(14)	H55	0.3753	0.3344	0.2902
C35	-0.0792(3)	0.20563(14)	0.53235(14)	H56	-0.3887	0.1998	0.5103
C38	0.6527(3)	0.19072(16)	0.28557(15)	H58	-0.8497	0.6884	0.6583
C39	0.5849(3)	0.0375(2)	0.68112(17)	H6	0.8125	0.6044	-0.1631
C40	-0.2065(3)	0.32678(16)	0.57398(15)	H60	1.0087	0.3559	-0.0109
C42	0.6934(3)	0.30940(16)	0.17297(14)	H61	-0.5137	-0.4074	1.2636
C43	-0.4911(3)	0.36180(17)	0.56795(16)	H65	1.148	0.4213	-0.1311
C44	-0.0493(3)	-0.04593(16)	0.78671(14)	H66	-0.6355	0.5958	0.6475
C45	0.7439(3)	0.23166(16)	0.21586(15)	H68	-0.2534	-0.2233	1.1118
C46	-0.0958(3)	-0.08709(18)	0.86428(15)	H69A	0.1766	-0.0337	1.0143
C49	0.7666(4)	0.51619(19)	-0.06065(18)	H69B	0.2582	0.0514	0.9736
C5	0.9942(4)	0.5193(2)	-0.15862(17)	H69C	0.1671	0.0089	0.9251
C50	-0.2114(3)	-0.19416(16)	0.82531(15)	H72	-0.6127	-0.4379	1.1615
C51	-0.3749(4)	-0.3123(2)	1.19795(17)	H74A	-0.1542	0.3309	0.7632
C53	-0.4882(4)	-0.3513(2)	1.07495(17)	H74B	0.0146	0.3128	0.7959
C55	0.4668(3)	0.30826(16)	0.27098(16)	H74C	-0.0193	0.2783	0.7276
C56	-0.3765(3)	0.24455(16)	0.52902(17)	H77A	0.2775	-0.1699	0.9636
C58	-0.8657(4)	0.64220(18)	0.64242(17)	H77B	0.2545	-0.1093	0.8812
C59	-0.3790(3)	-0.28811(18)	1.06028(15)	H77C	0.4158	-0.1628	0.8936
C6	0.8518(4)	0.5545(2)	-0.13247(18)	H78A	-0.3449	0.2028	0.7692
C60	0.9689(4)	0.40578(19)	-0.04126(17)	H78B	-0.1827	0.1671	0.734
C61	-0.4815(4)	-0.3768(2)	1.21239(17)	H78C	-0.2884	0.1113	0.8067
C65	1.0520(4)	0.4451(2)	-0.11313(18)	N1	-0.3312(3)	-0.2499(15)	0.9789(13)
C66	-0.7376(4)	0.58696(18)	0.63580(16)	N2	-0.2268(3)	-0.1962(15)	0.96565(13)
C68	-0.3234(4)	-0.26690(19)	1.12168(16)	N3	0.7288(3)	0.40711(15)	0.05782(13)
C69	0.2338(4)	-0.0005(2)	0.9667(2)	N4	0.7906(3)	0.34359(14)	0.10043(13)
C72	-0.5395(4)	-0.3957(2)	1.15142(18)	N5	-0.6173(3)	0.46884(14)	0.60369(13)
C74	-0.0668(6)	0.2908(3)	0.7747(3)	N6	-0.6370(3)	0.41128(15)	0.57638(15)
C77	0.3318(5)	-0.1329(3)	0.9174(3)	O1	0.0411(2)	0.03271(11)	0.62919(10)
C78	-0.2522(6)	0.1664(3)	0.7814(3)	O2	0.0526(2)	0.21099(11)	0.55761(11)
Dy1	0.17628(2)	0.09745(2)	0.50570(2)	O3	0.2787(2)	-0.0396(11)	0.52776(11)

A7 Additional structural information

H1	-0.6111	0.285	0.528	O4	0.3666(2)	0.09623(11)	0.58665(10)
H18	-1.1029	0.666	0.6294	O5	0.2814(2)	0.21974(11)	0.40946(10)
H19	-0.932	0.4573	0.5796	O7	0.43820(19)	0.10844(10)	0.41871(10)
H20	-1.1446	0.5503	0.5917	O8	-0.0861(2)	-0.0581(11)	0.59179(10)
H26	-0.1807	-0.1764	0.7085	O9	-0.0924(2)	0.15476(11)	0.49341(11)
H27	0.5233	0.4012	0.1735	O90	-0.0030(4)	0.1398(2)	0.8596(2)
H28	-0.3272	0.4233	0.603	O91	0.5014(4)	0.0016(2)	0.86921(17)
H2A	0.3294	0.1079	0.7757	S2	0.37337(7)	0.05237(4)	0.67294(4)
H2B	0.4069	0.1733	0.7007	S3	0.41985(10)	-0.05306(6)	0.94291(5)
H2C	0.2211	0.1547	0.7106	S4	-0.1434(13)	0.1993(7)	0.84398(7)

$[\text{Dy}_2(\text{o-PDA})_3(\text{H}_2\text{O})_2] \cdot 2\text{H}_2\text{O}]_n$ (28)Table A7.15 Atomic parameters for **24**.

Atom	x/a	y/b	z/c	Atom	x/a	y/b	z/c
C1	0.1821(1)	0.3354(2)	0.6848(3)	H15	0.0389	0.8683	0.8275
C10	0.2305(1)	0.0514(2)	0.7430(3)	H2	0.1823	0.3424	1.3255
C11	0.0903(1)	0.5598(2)	0.7268(3)	H2A	0.2153	0.2199	0.6865
C12	0.0517(1)	0.5887(2)	0.8519(4)	H2B	0.182	0.2372	0.5137
C13	0.0240(1)	0.6668(2)	0.7968(3)	H3	0.157(3)	0.190(6)	0.088(10)
C14	0.0465(1)	0.7443(2)	0.8386(5)	H4	0.0977	0.2886	0.7968
C15	0.0232(2)	0.8181(2)	0.7954(6)	H5	0.034	0.209	0.9089
C2	0.1832(1)	0.2432(2)	0.6402(3)	H6	0.0371	0.0652	0.8917
C3	0.1397(1)	0.1928(2)	0.7111(3)	H7	0.1025	0.0008	0.7561
C4	0.0991(1)	0.2306(2)	0.7894(4)	H8	0.1979(16)	0.159(5)	0.111(10)
C5	0.0608(1)	0.1831(3)	0.8563(5)	H9A	0.1729	0.0064	0.5779
C6	0.0625(1)	0.0972(3)	0.8452(5)	H9B	0.1941	0.0922	0.5154

A7 Additional structural information

C7	0.1019(1)	0.0587(2)	0.7651(5)	O1	0.1840(1)	0.3539(1)	0.8437(2)
C8	0.1408(1)	0.1059(2)	0.6974(4)	O2	0.1797(1)	0.3874(1)	0.5600(2)
C9	0.1844(1)	0.0612(2)	0.6172(4)	O3	0.2700(1)	0.0131(1)	0.6911(2)
Dy1	0.1782	0.4627	1.0342	O4	0.2314(1)	0.0788(1)	0.8951(2)
H1	0.1781	0.2835	1.191	O5	0.1272(1)	0.5123(1)	0.7873(2)
H12A	0.0269	0.5445	0.8646	O6	0.0885(1)	0.5813(2)	0.5716(3)
H12B	0.0689	0.5979	0.9659	O7	0.1802(1)	0.3374(1)	1.2123(2)
H14	0.0784	0.7453	0.8979	O8	0.1740(2)	0.1680(2)	0.1475(4)

List of publications

Jung, J.; Yi, X.; Huang, G.; Calvez, G.; Daiguebonne, C.; Guillou, O.; Cador, O.; Caneschi, A.; Roisnel, T.; Le Guennic, B.; Bernot, K., Analysis of the electrostatics in Dy^{III} single-molecule magnets: the case study of Dy(Murex)₃. *Dalton Transactions* 2015, 44 (41), 18270-18275.

Selvanathan, P.; Huang, G.; Guizouarn, T.; Roisnel, T.; Fernandez-Garcia, G.; Totti, F.; Le Guennic, B.; Calvez, G.; Bernot, K.; Norel, L.; Rigaut, S., Highly Axial Magnetic Anisotropy in a N₃O₅ Dysprosium(III) Coordination Environment Generated by a Merocyanine Ligand. *Chemistry – A European Journal* 2016, 22 (43), 15222-15226.

Khelifa, A. B.; Belkhiria, M. S.; Huang, G.; Freslon, S.; Guillou, O.; Bernot, K., Single-molecule magnet behaviour in polynuclear assembly of trivalent cerium ions with polyoxomolybdates. *Dalton Transactions* 2015, 44 (37), 16458-16464.

Fan, X.; Freslon, S.; Daiguebonne, C.; Pollès, L. L.; Calvez, G.; Bernot, K.; Yi, X.; Huang, G.; Guillou, O., A Family of Lanthanide-Based Coordination Polymers with Boronic Acid as Ligand. *Inorganic Chemistry* 2015, 54 (11), 5534-5546.

Yi, X.; Shang, J.; Pan, L.; Tan, H.; Chen, B.; Liu, G.; Huang, G.; Bernot, K.; Guillou, O.; Li, R.-W. "Reversible Luminescence Modulation upon an Electric Field on a Full Solid-State Device Based on Lanthanide Dimers". *ACS Applied Materials & Interfaces*, 2016. 8 (24), 15551-15556.

AVIS DU JURY SUR LA REPRODUCTION DE LA THESE SOUTENUE

Titre de la thèse:

Synthèse, études cristallographiques et magnétiques d'édifices moléculaires à base de lanthanides

Nom Prénom de l'auteur : HUANG GANG

Membres du jury :

- Monsieur GUILLOU Olivier
- Monsieur BERNOT Kevin
- Monsieur RIGAUT Stéphane
- Monsieur TRIKI Smail
- Madame CATALA Laure
- Madame MATHONIERE Corine

Président du jury : S. RIGAUT

Date de la soutenance : 31 Mars 2017

Reproduction de la these soutenue

Thèse pouvant être reproduite en l'état
~~Thèse pouvant être reproduite après corrections suggérées~~

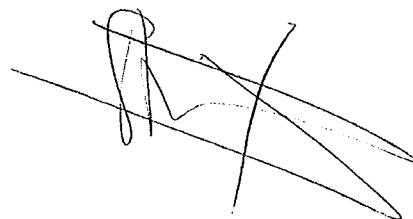
Fait à Rennes, le 31 Mars 2017

Signature du président de jury

Le Directeur,



M'hamed DRISSI



Les molécules-aimants ou Single-Molécule Magnets (SMM) ont attiré une attention croissante au cours des dernières années en raison de leur potentiel attrayant en tant que dispositifs de stockage magnétique à haute densité. Beaucoup d'efforts ont été faits pour améliorer la performance magnétique de ces molécules à l'aide des techniques de chimie de coordination.

Dans cette thèse, le travail est organisé en deux parties principales. La première partie est constituée des chapitres 2 et 3 qui se concentrent principalement sur les familles Lanthanide-radicaux zéro- et mono-dimensionnelles. La deuxième partie contient les chapitres 4 et 5, où des ligands diamagnétiques sont utilisés afin concevoir des matériaux multifonctionnels.

Dans la première partie, neuf radicaux TEMPO-R (R représente le substituant) sont utilisés. Leur structure cristalline, ainsi que leurs propriétés magnétiques ont été caractérisées. Dans le chapitre 2, quatre radicaux (TEMPO-OCH₃, TEMPO-NH₂, TEMPO-Acetamido et TEMPO-OCH₂CCH) sont utilisés pour synthétiser des complexes zéro-dimensionnels, dont trois présentent des propriétés de SMM. Dans le cas particulier de TEMPO-OCH₃, un très rare comportement de SMM avec lanthanides légers est observé (Ce^{III}, Pr^{III} et Nd^{III}). La première SMM à base de Pr^{III} est ainsi reportée. Dans le chapitre 3, l'objectif est de concevoir des SMM organisés mono-dimensionnellement dans l'empilement cristallin. Cinq autres radicaux sont utilisés: TEMPO-Méthacrylate, TEMPO-OCOPh, TEMPO-oxo, TEMPO-OH et TEMPO-CN. Parmi toutes les chaînes obtenues, [Pr(hfac)₃(H₂O)(TEMPO-OH)]_n (17), [Dy(hfac)₃-TEMPO-OH]_n (18) et [Tb(hfac)(TEMPO-CN)]_n (22) sont identifiés comme SMM. 22 présente la relaxation magnétique la plus lente parmi tous les SMM 4f-2p obtenues dans cette thèse, avec une hystérèse magnétique à basse température. Son analogue à base Gd^{III} (23) présente une des plus grandes valeurs d'échange dans les composés de Gd-2p. Enfin un très rare exemple de réseau bidimensionnel 4f-2p de formule [(Ce(hfac)₃)₃(Oxo-TEMPO)₄]_n (15) est obtenu.

Dans la deuxième partie, une chaîne de dimère est obtenue par réaction d'un ligand carboxylique photo-commutable avec des sels d'ions Ln^{III}. La photo-sensibilité du ligand sous irradiation UV a été testée et des mesures magnétiques en solution ont été entreprises. En outre, un composé de type Metal-Organic-Framework (MOF) présentant un comportement de SMM de {[Dy₂(o-PDA)₃(H₂O)₂]₂H₂O}_n (28) a été conçu et caractérisé. Une interaction ferromagnétique Ln-Ln a été observée dans ce MOF-SMM et le dopage diamagnétique démontre que, contrairement à ce qui est observé sur [Ln₂(AZO)₆(DMSO)₂(H₂O)₂]₂·4DMSO, cette interaction favorise le comportement de SMM.

Single-molecule-magnet (SMM) has attracted increasing attention in recent years due to their appealing potential for high-density storage devices. Much effort has been made to improve the magnetic performance through flexible coordination chemistry strategy. In this thesis, the work is organized in two main parts. The first part is constituted of chapter 2 and chapter 3, primarily focus on the Ln-Radical families aiming at designing zero-dimensional and one-dimensional single-molecule-magnet (SMM). The second part contains chapter 4 and chapter 5, in which the ligands are replaced by diamagnetic ones for the purpose of designing the multifunctional materials.

In the first part, nine TEMPO-R (R represents the substituent) radicals are employed to construct zero-dimensional and one-dimensional complexes. These kinds of compounds were prepared by reactions in the dichloromethane/n-heptane co-solvents between the precursor [Ln(hfac)₃(H₂O)₂] and TEMPO radicals. Subsequently their molecular structure as well as magnetic properties have been characterized and described. In chapter 2, four radicals (TEMPO-OCH₃, TEMPO-NH₂, TEMPO-Acetamido and TEMPO-OCH₂CCH) are used to synthesize monometallic or dimetallic complexes, among which three are successful to construct the SMM. For the special case of TEMPO-OCH₃ a rare light lanthanide ions (Ce^{III}, Pr^{III} and Nd^{III}) SMM behavior is reported. The Pr^{III} derivative is the first Pr^{III}-based SMM ever reported. In chapter 3, the target is to design SMM in one dimension by using another five radicals: TEMPO-Methacrylate, TEMPO-OCOPh, TEMPO-oxo, TEMPO-OH and TEMPO-CN. Among all the chains, [Pr(hfac)₃(H₂O)(TEMPO-OH)]_n (17), [Dy(hfac)₃-TEMPO-OH]_n (18) and [Tb(hfac)₃(TEMPO-CN)]_n (22) are identified as chains of SMM. 22 exhibits the slowest magnetic relaxation among all the 4f-2p SMMs obtained in this thesis, with a small opening of magnetic hysteresis. Its analogue of [Gd(hfac)₃(TEMPO-CN)]_n (23) even exhibits one of the largest exchange values in Gd-2p compounds. Last a very rare example of bidimensional 4f-2p network of formula [(Ce(hfac)₃)₃(Oxo-TEMPO)₄]_n (15) is obtained.

In chapter 4, the salt of a photo-switchable carboxylic ligand was reacted with Ln^{III} ions to afford a chain-like arrangement of dinuclear complexes of formula [Ln(AZO)₃(DMSO)(H₂O)]₂·4DMSO. Photo-sensitivity of the ligand under the irradiation of UV has been tested together with magnetic measurements in solution. In chapter 5, a Metal-Organic-Framework (MOF) (28) has been designed and characterized. Ln-Ln ferromagnetic interaction has been observed and diamagnetic doping highlight that, contrary to what observed on [Ln₂(AZO)₆(DMSO)₂(H₂O)₂]₂·4DMSO, this interaction promote SMM behavior in a so-called MOF-SMM.